Towards a Cognitive Millimeter-wave Radio-over-Fiber Centralized Radio Access Network for Future Generation Small Cell Deployment

by

Th'ng Guo Hao

A thesis submitted for the degree of
Doctor of Philosophy

Monash University
School of Engineering
Electrical and Computer Systems Engineering

June 2021

© Th'ng Guo Hao (2021). Except as provided in the Copyright Act 1968, this thesis may not be reproduced in any form without the written permission of the author.

I certify that I have made all reasonable efforts to secure permissions for third-party content included in this thesis and have not knowingly added copyright content to my work without the owner's permission.

Abstract

Millimeter-wave base stations are expected to be deployed within the 5G cellular network to increase data rate and network capacity. The proposal of the use of millimeter-wave range radio frequency (RF) is motivated by the ever-increasing demand of data throughput, congestion of the lower sub-3 GHz radio frequency band, and the relatively larger available bandwidth in millimeter-wave frequency bands. However, higher frequency range signals have higher path loss and are susceptible to atmospheric absorption caused by water moisture and oxygen. Hence, millimeter-wave signals have a relatively shorter reliable transmission range which means that more base stations are needed to achieve the same coverage area compared to the existing sub-3 GHz base stations. Besides, conventional RF-based fronthaul solutions might not be sufficient for sustained Gigabit transmission for future generation communication due to limited bandwidth and reliable transmission range. The proposal of analog radio-over-fiber (ARoF) replaces traditional RF-based link between the central office and the base station with fiber, providing more bandwidth, lower propagation loss, and is immune to RF interference. ARoF also increases spectral efficiency and overcomes the data rate constraints of common public radio interface (CPRI) based digital radio-over-fiber (DRoF). However, ARoF systems are sensitive to phase noise contributed by the optical transmitter and non-linear effects of the fiber. While the increase in the number of base stations allows aggressive frequency reuse, it requires significantly more overhead and processing capability to perform large-scale coordination and scheduling for beamforming, beam alignment, and coordinated multipoint transmission (CoMP).

In this thesis, investigations on proposed differential encoded data and differential demodulation methods are carried out to evaluate the performance of proposed differential encoding based RoF schemes using varying levels of optical receiving power, intensity noise, and phase noise. The differentially encoded data is modulated onto an unlock heterodyning RoF scheme. Compared to self-homodyning-based RoF schemes, the proposed DPSK and DQPSK schemes can directly detect phase-modulated signals and convert millimeter-wave signal to baseband signal in a single stage while remaining relatively phase noise tolerant. Compared to oscillator-based RoF receivers, the proposed M-DPSK schemes' performance falls between a conventional phase-coherent RoF link and an unlocked heterodyning RoF link. The proposed schemes show minimal degradation in detection performance up to 1 MHz range lasers.

Investigation on the use of deep learning in downlink joint transmission CoMP has been carried out using three different approaches in two different scenarios with varying number of base stations. In the three approaches, the deep learning algorithm is used

to select additional base stations, provide all possible base station options, and act as a trigger for downlink joint transmission. Results obtained show that different deep learning algorithms and architecture can yield different results in different approaches. In general, the deep learning algorithms used performed better than support vector machine (SVM) algorithm, and can provide an increase in prediction accuracy of up to 26 percent.

Two deep learning based phase noise tolerant millimeter-wave RoF receivers was developed. The proposed deep learning based receivers are bandwidth-efficient and adaptable to various RoF links. The proposed receivers detect signals using two different approaches: direct detection of phase corrupted signals, and detection of phase corrupted signals with reference tone. The proposed deep learning architecture used for the receivers are based long short-term memory (LSTM) and autoencoder. The receivers' performance is compared with direct threshold detection, self-homodyning-based receiver, and various deep learning algorithms such as multilayer perceptron (MLP), convolutional neural network (CNN), and CNN+LSTM. Results obtained show that for direct detection, denoising autoencoder based receiver performs better than direct threshold detection and other deep learning algorithms in the presence of phase noise. For detection with reference tone, when the frequency gap between the unmodulated reference tone and the main data signal is sufficient, the self-homodyning-based receiver performs the best. However, when the gap reduces, the proposed LSTM based receiver performs better than the self-homodyning-based receiver. In general, the proposed deep learning based receivers can improve detection accuracy by up to 34 percent for direct detection, and reduce bit-error-rate from 10^{-3} to 10^{-5} for detection with reference tone.

The proposed differential encoding methods and deep learning based phase noise tolerant RoF receivers have shown potential in reducing the overall system complexity of ARoF links while being relatively phase noise tolerant. Furthermore, the results obtained from applying deep learning in CoMP and phase noise tolerant RoF receivers demonstrated the ability of deep learning algorithms and the possibility to implement deep learning in future generation cognitive-communication networks.

Declaration

This thesis is an original work of my research and contains no material which has been accepted for the award of any other degree or diploma at any university or equivalent institution and that, to the best of my knowledge and belief, this thesis contains no material previously published or written by another person, except where due reference is made in the text of the thesis.

Signed: ________________________________

Date: ________________________________

Acknowledgements

This work would not have been possible without the advice and support given by a number of individuals. I would like to express my utmost gratitude to my supervisors, especially Dr Mohamed Hisham Jaward and Dr Masuduzzaman Bakaul for being supportive and inspiring me throughout my candidature. Their research knowledge and insightful comments have helped me to develop and improve my understanding on my research topic. I would also like to thank Associate Professor Lan Boon Leong, head of discipline of Electrical and Computer Systems Engineering, for his kind support in procuring research equipment, and making sure I remained on track and making progress when there was a transition in the supervisory team.

I wish to acknowledge the help provided by the lab technicians for their assistance especially during the movement control order (MCO) period in response to the COVID-19 pandemic. I would also like to thank my lab-mates: Somayeh Ebrahimkhani, Andrea Lim Mei Wern, and Kelvin Shak Jian Ming, for their support and assistance.

Special thanks to my friends, especially Chew Yi Hao, Goh Wen Yan, Adwin Ying, Siao Wei Shiuan, Rachel Saw, and Pamela Chia, for their assistance and encouragement during difficult times. Lastly, I would like to thank my parents for their love, support, patience, and guidance throughout this journey.

Contents

List of Figures

List of Tables

Abbreviations

3GPP	Third Generation Partnership Project
3GPP2	Third Generation Partnership Project 2
AI	Artificial Intelligence
ANN	Artificial Neural Network
ARoF	Analog Radio-over-Fiber
ASK	Amplitude-Shift-Keying
BBU	Baseband Unit
BCE	Binary Cross-Entropy
BER	Bit Error Rate
BLER	Block-Error-Rate
BS	Base Station
BW	Bandwidth
CCE	Categorical Cross-Entropy
CDMA	Code Division Multiple Access
CNN	Convolutional Neural Network
CO	Central Office
CO2	Carbon Dioxide
CoMP	Coordinated Multipoint
CP	Consumer Premise
CPRI	Common Public Radio Interface
CPU	Central Processing Unit
CQI	Channel Quality Index

CRAN	Centralized/Cloud Radio Access Network
CSI	Channel State Information
CSRZ	Carrier-Supressed Return-to-Zero
CT	Computerized Tomography
CW	Continuous Wave
DAE	Denoising Autoencoder
DAM	Delay-and-multiply
D-AMPS	Digital Advanced Mobile Phone System
DCR	Direct Conversion Receiver
DD-MZM	Dual-Drive Mach-Zehnder Modulator
DFB	Distributed Feedback Laser
DLDD	Deep Learning based Direct Detection
DLD-RT	Deep Learning based Detection with Reference Tone
DNN	Deep Neural Network
DPMZM	Dual-Parallel Mach-Zehnder Modulator
DPS	Dynamic Point Selection
DPSK	Differential Phase-Shift Keying
DQN	Deep Q-Network
DQPSK	Differential Quadrature Phase-Shift Keying
DRL	Deep Reinforcement Learning
DRoF	Digital Radio-over-Fiber
EAM	Electro-Absorption Modulator
EIRP	Effective Isotropic Radiated Power
ELBO	Evidence Lower Bound
FCC	Federal Communications Commissions
FM	Frequency Modulation
FSPL	Free Space Path Loss
GB	Guard Band
GPU	Graphic Processing Unit

GSM	Global System for Mobile Communication
ICNIRP	International Commission on Non-Ionizing Radiation Protection
IF	Intermediate Frequency
IF-RoF	Intermediate Frequency Radio-over-Fiber
JLS	Joint Leakage Suppression
KL	Kullback-Leibler
LO	Local Oscillator
LOS	Line-of-Sight
LSTM	Long Short-Term Memory
LTE	Long-Term Evolution
LTE-A	Long Term Evolution Advance
MCMC	Malaysia Communications and Multimedia Commission
MIMO	Multiple-Input Multiple-Output
ML	Machine Learning
MLP	Multilayer Perceptron
mMIMO	Massive Multiple-Input Multiple-Output
MRI	Magnetic Resonance Imaging
MSE	Mean Square Error
MZI	Mach-Zehnder Interferometer
MZM	Mach-Zehnder Modulator
NR	New Radio
NRZ	Non-Return-Zero
OCSR	Optical Carrier-to-Sideband Ratio
ODSB	Optical Double-Sideband
ODSB+C	Optical Double-Sideband with Carrier

ODSB+SC	Optical Double-Sideband with Suppressed Carrier
OFDM	Orthogonal Frequency-Division Multiplexing
OOK	On-Off-Keying
OSSB	Optical Single-Sideband
OSSB+C	Optical Single-Sideband with Carrier
PD	Photodetector
PDC	Personal Digital Communication
PDM	Polarization Division Multiplexing
PON	Passive Optical Netowrk
PRBS	Pseudo Random Bit Sequence
QAM	Quadrature Amplitude Modultion
QPSK	Quadrature Phase-Shift Keying
RF	Radio Frequency
RIN	Relative Intensity Noise
RNN	Recurrent Neural Network
RoF	Radio-over-Fiber
RRH	Remote Radio Head
RZ	Return-to-Zero
SDN	Software-Defined Network
SER	Symbol Error Rate
SH	Self-Homodyning
SMF	Single-Mode Fiber
SNR	Signal-to-Noise Ratio
SON	Self-Organizing Network
SR	Symbol Rate
SVM	Support Vector Machine
UE	User Equipment
UMB	Ultra Mobile Broadband

UMFUS	Upper Microwave Flexible Use Service
UV	Ultraviolet
VAE	Variational Autoencoder
WIMAX	Worldwide Interoperability for Microwave Access
ZFBF	Zero-Forcing Beamforming

Chapter 1

Introduction

Wireless communication has become an inseparable part of modern society since the commercialization of the first wireless communication system in the early 1900 [1]. Since then, the wireless industry has evolved from point-to-point technologies to broadcasting and finally to wireless networks that we have today. Although wireless communication was introduced in the early 1900s, the widespread adoption of the masses only started over the past twenty years due to the extensive development in cellular networks and local area networks. Increasing purchasing power in conjunction with global economic growth and the reduced cost of adoption also contributed to wireless communication's widespread adoption.

Wireless mobile communication technologies are divided into generations, with each mobile generation transition occurring approximately every decade. Analog mobile radio systems were introduced in the first generation (1G) of mobile communication in 1980 and predominantly operated in the 450 MHz radio frequency (RF) band using analog frequency modulation (FM). The move towards digital mobile systems occurred in the second generation (2G) of mobile communication. The move from analog to digital modulation allows error-correcting codes to be used, which substantially improved speech quality. There were three main technologies that were used in commercial 2G communication systems: global system for mobile communication (GSM), code division multiple access (CDMA), digital advanced mobile phone system (D-AMPS), and personal digital communication (PDC). GSM was first developed in Europe in the 1980s and was later widely adopted by multiple countries except for the North America region and Japan [2]. CDMA and D-AMPS were mainly used in North America, while PDC was mainly deployed in Japan. 2G networks were initially rolled out at 900 MHz RF range and was later extended to include 2 GHz range RF. The move to a higher RF from 450 MHz used in 1G led to an increase in path loss, making the initial base station (BS) infrastructure deployment more expensive as more BSs are required. Broadband data communication using mobile systems was introduced in 3G, and Long-Term Evolution (LTE) was introduced in 4G [3]. There were two main bodies that were developing 3G wireless communication standards: Third Generation Partnership Project (3GPP) and Third Generation Partnership Project 2 (3GPP2). While 3GPP worked on a 3G standard based on GSM, and 3GPP2 intended to develop a 3G standard based on 2G IS-95 CDMA standards, both bodies ultimately converged towards using CDMA for 3G. There were three competing technologies in the early days of 4G: LTE, Worldwide Interoperability for Microwave Access (WIMAX), and Ultra Mobile Broadband (UMB). However, LTE was the predominant standard used for 4G [4–6].

Currently, 5G-enabled based stations are being deployed worldwide where higher frequency bands ranging from 4GHz up to 70 GHz are being considered. The move to higher frequency bands, especially in the millimeter-wave range (30 GHz - 300 GHz), is mainly driven by bandwidth availability in these bands and lower frequency bands' congestion. The candidate millimeter-wave bands are: 24.25 GHz - 27.5 GHz, 37 GHz - 43.5 GHz, 45.5 GHz - 47 GHz, 47.2 GHz - 48.2 GHz, and 66 GHz - 71 GHz. These bands have been determined in the World Radiocommunication Conference 2019 (WRC-19) for 5G mobile services [7]. In the millimeter-wave band, up to 400MHz of bandwidth can be offered to mobile operators compared to the 20MHz bandwidth being used in current LTE systems [8]. Research in millimeter-wave started long before the commercialization of wireless communication systems. The first 60GHz transmission and reception system over 23 meters was demonstrated in 1895 by Jagadish Chandra Bose [9]. In the same year, transmission and propagation of millimeter-wave were studied by Ryotr N. Lebedew [10], a Russian physicist. In the early days of millimeter-wave communication, especially in the 60GHz range, it is viewed as a wired backhaul replacement [11] due to the requirement for highly directional antennas and high-power amplifier to achieve error-free transmission due to the high propagation loss of millimeter-wave. However, these equipment are expensive, and due to the short reliable transmission range of millimeter-wave, the cost of deployment increases drastically as more base stations are required to cover the same area as traditional lower frequency base stations. The increased number of base stations would also increase network management's difficulty for optimization of beamforming, coordinated multipoint (CoMP), and multiple-input multiple-output (MIMO) transmissions.

Power consumption of each base station due to high power amplifiers needed to overcome the high path loss of millimeter-wave signals is also a concern. For mobile carriers, an increase in power consumption will affect the network's operational cost. From an environmental point of view, an increase in base station needed, could increase power consumption, which could lead to an increase in global carbon dioxide (CO2) output, as power generation methods are still predominantly fossil-fuel based. According to [12], worldwide technology devices consumes approximately 600 TWh of power, and 9% of the total power consumption is contributed by telecommunication radio networks [13]. And according to [14], only approximately 10% of the power consumption is associated with the end-user equipment (UE) while the remaining 60% and 30% is used by the base stations and other network components respectively. Amplifying the RF signal and cooling the base station can consume up to approximately 35% of the total base station power consumption, with cooling consuming up to 13% and power amplifier consuming 22% of power [12].

The conventional wireless access network has the remote radio head (RRH) unit and the baseband processing unit located at the cell site. The increase in density of base stations within a network due to short transmission length of high-frequency signals will rapidly increase the cost of deployment of such architecture. Centralized/cloud radio access network (CRAN) proposes separating the baseband unit (BBU) and the radio equipment unit [15]. The baseband units will be located in a centralized location (e.g central office), and the radio equipment will be located at the base station. The usage of optical fibers in CRAN to connect base stations with the central office enables high capacity and low loss transmissions.

There are two competing technologies in CRAN: Common Public Radio Interface (CPRI) based digital Radio-over-Fiber (DRoF) and analog Radio-over-Fiber (ARoF). The main difference between both RoF technologies is the signal transmitted within the fiber connection between the central office and the base stations. In DRoF, the radio signals are digitized before optical modulation. Therefore, the received signal at the base station has to be upconverted to the desired millimeter-wave range frequency before wireless transmission. In ARoF, the radio signals are directly modulated onto the optical carrier generating optical double-sideband signals (ODSB) or optical single-sideband signals (OSSB). The base station signal will already be in the millimeter-wave range after photodetection. Hence, the base station will act as a relay as no further processing is required. The main advantage DRoF has over ARoF is the simplicity in optical transmitter configuration needed as the signal transmitted is in baseband. However, due to the radio signal's digitization, which involves a large number of quantization bits and baseband signal transmission, CPRI based DRoF schemes are not spectrally efficient [16]. Efforts to improve the bandwidth efficiencies of CPRI have been made. For example, introducing the use of pulse amplitude modulation [17], CPRI compression [18–21], and enhanced CPRI [22]. However, these methods either increases configuration complexity or are limited by the system compression ratio [16, 23]. Furthermore, the base stations of DRoF have a more complex configuration and require a high frequency RF oscillator compared to ARoF.

Artificial intelligence (AI) has garnered attention from the general public and research community ever since the news of AlphaGo [24, 25], an AI-based program developed by Google DeepMind, beating professional Go players such as Fan Hui and Ke Jie. Journal papers published regarding AlphaGo [24, 25] had been accessed more than a hundred thousand times and cited more than nine thousand times. However, the field of AI is not new. The origin of AI's conceptualization can be traced back to the year 1950 [26]. Nevertheless, computers back then are limited by their computational power. In the past decade, the rapid improvement in the processing capability of the central processing unit (CPU) and graphic processing unit (GPU) has enabled the use of deep learning algorithms that were deemed too computationally intensive to be used in the 20th century [27]. The use of machine learning algorithms had been successfully demonstrated in various fields. For example, image processing for magnetic resonance imaging (MRI) [28] and computerized tomography (CT) scan [29], and audio processing for corrupted audio documents [30, 31], speech activity detection and recognition [32–34]. Machine learning algorithms have also been explored in optical and wireless communication for network traffic control [35, 36], optical performance monitoring [37, 38], and proactive fault detection [39, 40]

1.1 Research Focus

Generally, ARoF is more bandwidth efficient than DRoF due to direct radio signal modulation. In wireless communication, phase modulated radio signal such as quadrature phase-shift keying (QPSK) and quadrature amplitude modulation (QAM) are usually used. Therefore, in ARoF, the signal modulated onto the optical carrier will be QPSK or QAM signals. Hence, the transmitted optical signal in ARoF is more susceptible to nonlinear distortion contributed by the optical transmitter. In contrast, the baseband transmission used in DRoF is less susceptible to optical nonlinear distortion due to baseband signal transmission. Therefore, longer fiber length can be used for DRoF compared to ARoF [16].

To overcome some of the distortions caused by the optical transmitter and fiber, narrow linewidth lasers, OSSB signals, and phase-coherent optical tones were used. The use of narrow-linewidth lasers and phase-coherent optical tones reduces optical phase noise propagating from the optical system to the wireless receiver after heterodyne detection. OSSB signals are more resilient to RF power fading and bit walk-off as a result of fiber chromatic dispersion compared to ODSB+C, and ODSB+SC signals [41]. Conventional phase-coherent optical tone generation methods demonstrated in [42–63] requires high speed optoelectronics and RF oscillators. The higher the RF frequency used, the higher the components' speed requirement. While optical frequency multiplication reduces the speed and frequency requirements of optical modulators and oscillators used, it is limited by the harmonic generation efficiency and modulator used [64]. Optical tone generation using uncorrelated optical sources reduces the optical transmitter complexity and the number of high-frequency components used. However, the uncorrelated optical sources are not phase-locked and will lead to phase noise propagating from the optical transmitter to the wireless receiver. The use of self-homodyning (SH) based receivers demonstrated in [65] using amplitude modulation has shown its capability in improving optical phase noise tolerance of the wireless receivers. But SH-based receivers cannot be used directly to detect and downconvert phase modulated signals to baseband as the signal's phase integrity will be affected. Therefore, in this thesis, differential encoded millimeter-wave RoF schemes are proposed in chapter 3 and chapter 4 to maintain phase integrity of phase-modulated signals during detection while maintaining relatively phase noise tolerant. In addition, deep learning based phase noise tolerant millimeter-wave RoF receivers are proposed in chapter 6.

Densification of base stations in the network, led by the low reliable transmission range of millimeter-wave due to high propagation loss and weak penetration power relative to lower RF, enables aggressive frequency reuse and lower interference. The proposal of massive MIMO (mMIMO) antenna allows base stations to exploit the benefit of beamforming. The short-wavelength nature of millimeter-wave allows the antenna elements within the mMIMO antenna to be packed in a relatively dense package, occupying a relatively small footprint [66–68]. However, the increase in antenna elements within the antenna array and the number of base stations increases the network management complexity, as significantly more signaling and feedback between the network elements and computational capacity are required for large-scale coordination and scheduling of beamforming and CoMP. Following the development of AI in various fields, as it progresses in tackling complex problems such as real-time obstacle detection for autonomous driving, human-like text generation using GPT-3, and quantum computing, a fully AI-managed network might be possible in the future. Hence, a deep learning based CoMP is explored and discussed in chapter 5 with a discussion on the challenges faced in CoMP provided in chapter 2.

Fig. 1.1 shows how each chapter fits in a CRAN. In a fiber-connected CRAN, the BBU and RRH are separated, and the optical signal is generated and transmitted from the CO where the BBUs are located. In chapter 3 and chapter 4, a novel approach in implementing differential encoding in ARoF links with an incoherent M-DPSK detector was proposed. Therefore, in the figure, both chapters are highlighted at the CO and the mobile receiver. In chapter 5, we explore the use of deep learning algorithms in CoMP. And CoMP is used to reduce cell edge interference and improve cell edge data throughput. Hence, the cell edge is highlighted in the figure for chapter 5. In chapter 6, novel deep learning based phase noise tolerant receivers were proposed, and therefore in the figure, chapter 6 is highlighted at the mobile receiver.

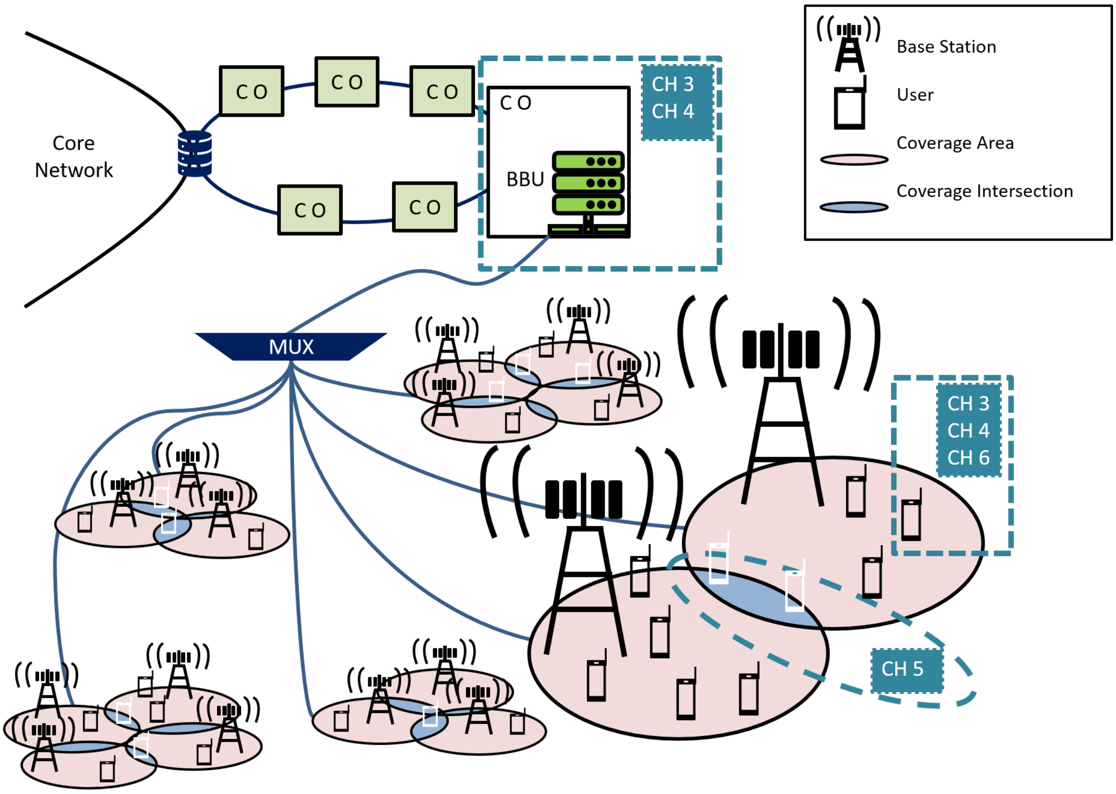

FIGURE 1.1: Centralized fiber wireless access network architecture

This thesis identifies challenges faced in fronthaul centralized radio access network, focusing on ARoF systems with reduced reliance on high-speed optoelectronics and RF oscillators, and explore the use of deep learning for the future generation wireless communication. The objectives of this thesis are:

- Investigate the feasibility of uncorrelated analog millimeter-wave RoF systems using differentially encoded data through simulations and theoretical analysis.
- Analyze and compare the performance of proposed millimeter-wave RoF systems with existing millimeter-wave RoF alternatives.
- Develop a deep learning based phase noise tolerant receiver.
- Propose and investigate the use of deep learning in CoMP.

1.2 Thesis Contribution

Following the research objectives, three M-ary differential phase-shift keying (M-DPSK) modulated millimeter-wave RoF fronthaul downlink schemes are proposed and demonstrated experimentally. The proposed links are analyzed theoretically and experimentally through software simulation and are evaluated through varying receive optical power, laser linewidth, and relative intensity noise. The proposed schemes are compared to a phase correlated conventional millimeter-wave RoF scheme and two intermediate frequency (IF) RoF alternatives. Proposed links reduce system reliance on high-speed optoelectronics, RF oscillators, and complex phase lock system. The differential encoding in M-DPSK modulated signal encodes bits information using phase differences between successive signal transmission. The use of incoherent detection for differential phase-shift keying (DPSK) and differential QPSK (DQPSK) allows phase noise to be reduced through delayed and phase-shifted multiplication of the signal while remaining spectrally efficient.

A deep learning based centrally managed CoMP is proposed and demonstrated. The deep learning algorithms were tested in two different scenarios with varying cell sizes. The deep learning algorithm is used as a trigger to activate or deactivates a CoMP algorithm, to provide all possible base stations for CoMP joint transmission, and to select an additional base station that fulfills predefined criteria for CoMP transmission. Varying user distributions were used to test the performance of different deep learning algorithms used in the deep learning based CoMP. Results show that the multilayer perceptron and long short-term memory (LSTM) based deep learning CoMP performs better than support vector machine (SVM) algorithm.

Two phase noise tolerant receivers employing deep learning algorithm was proposed. The proposed receivers use autoencoder and long short-term memory (LSTM) based deep learning architecture. The receivers are demonstrated using unlock heterodyning RoF downlink using oscillator-based receivers. Traditionally, the autoencoder is trained with the aim of having the output be the same as the input wherein the encoder encodes the input and the decoder decodes the encoded input to obtain the original input. The autoencoder-based receiver is tasked to predict the uncorrupted signal from a phase corrupted input. By defining the output of the encoder to have a smaller dimension than the input, the encoder is forced to only extract essential features from the noisy input that is sufficient for the decoder to reconstruct the original uncorrupted signal. For the LSTM based receiver, an additional reference input is used. The receiver detects the signal based on the phase corrupted input and the reference input. Due to unlocked heterodyning, the phase noise from the transmitter causes phase rotation in the received signal. Hence, the LSTM based receiver detects the transmitted signal based on the reference input changes. The reference input changes are caused by homodyning of the reference signal with an oscillating signal of the same frequency. The phase difference between the reference signal (due to phase rotation caused by the optical transmitter phase noise) and the RF oscillator causes amplitude changes. Therefore, the reference signal can be used as a reference point for the receiver to detect the phase corrupted signal. Compared to self-homodyning-based intermediate frequency RoF systems, the proposed LSTM receiver can improve overall bandwidth efficiency while remaining phase noise tolerant. Furthermore, the proposed receivers using autoencoder and LSTM algorithms can detect phase corrupted signals better than MLP and CNN-based receivers.

As discussed above, the contributions of this thesis can be summarised as follow:

- Proposed and demonstrated the use differential encoding in ARoF links using optical baseband M-DPSK modulation
- Provided theoretical analysis on three M-DPSK millimeter ARoF links and two downlink IF-RoF systems
- Compared link performance of three proposed M-DPSK millimeter-wave RoF links to two QPSK IF-RoF links and a phase correlated conventional millimeter-wave RoF scheme
- Proposed and explored the use of MLP and LSTM algorithms in downlink joint transmission CoMP
- Proposed, demonstrated, and evaluated the use of autoencoder and LSTM algorithms for deep learning based phase noise tolerant receiver for millimeter-wave RoF system
- Compared detection performance of proposed deep learning based receivers to self-homodying based receiver, and other deep learning based receivers using MLP and CNN algorithms.
- Improved overall spectral efficiency of RoF receivers relative to SH based IF-RoF receivers through
  - reducing required frequency spacing between RF frequencies using proposed LSTM based receiver
  - using proposed differential encoding and incoherent detection.

The contributions described above have resulted in the following journal and conference papers:

- T. G. Hao, M. Bakaul and M. Boroon, "Incoherent Heterodyning of Phase Modulated Signal for Low-cost Millimeter-wave RoF Link," 2018 IEEE International RF and Microwave Conference (RFM), Penang, Malaysia, 2018, pp. 159-161
- G. H. Th'ng, M. Bakaul, and M. H. Jaward,"Differential Encoding for Unlock Heterodyning Millimeter-wave RoF Link," Submitted to Optics Communications [Status: Accepted]
- G. H. Th'ng, M. H. Jaward, and M. Bakaul, "Deep Learning based Phase Noise Tolerant Radio-Over-Fiber Receiver," Submitted to Journal of Optical Communications and Networking [Status: Under Review]

1.3 Thesis Outline

This thesis is organized as follows. Chapter 2 provides a review based on the research focus. This includes challenges faced in CoMP, different ARoF optical tone generation methods, optical fiber impairments, and millimeter-wave characteristics. The consecutive chapters present the research's contribution and the details on the research methodology, data generation, results, and discussion. Chapter 3 presents two DPSK modulated millimeter-wave RoF schemes. The chapter demonstrates the proposed scheme's ability to directly detect phase-modulated data while remaining phase tolerant and bandwidth-efficient. Chapter 4 extends the demonstration of the use of differential encoded data in a DQPSK setup. The chapter includes a theoretical analysis and performance comparison of the proposed DQPSK scheme with two IF-RoF schemes. The deep learning based CoMP is presented in chapter 5. Chapter 6 presents two deep learning based phase noise tolerant millimeter-wave RoF receivers. And chapter 7 concludes the thesis and highlights a few future research directions.

Chapter 2

Millimeter-Wave Analog Radio-over-Fiber Centralized Radio Access Networks

2.1 Introduction

For future generation communication, 5G and beyond, the use of higher radio frequency (RF) band, discrete spectral band, and small-cells are being considered to improve latency and data rate for wireless communication. The use of smaller cells and higher RF in populated areas allow more aggressive carrier aggregation and lead to densification of cells. Densification of cells that could go up to 1000 cells per square kilometer allows aggressive spectrum reuse but also incurs new technical challenges [69]. The transition between cells occurs more frequently due to smaller coverage area of a single cell, which means CoMP transmission and beamforming are needed to optimize network performance. CoMP is needed to manage interference between network elements and to increase cell edge data throughput. However, due to the densification of cells, such operation requires an immense amount of processing power and speed from the baseband unit to be able to perform large-scale coordination and scheduling, and at the same time, need to be cost and power-efficient. A cloud radio access network (CRAN) has been proposed to address the aforementioned challenges, using fiber as a transmission medium between CO and base stations [15]. Fiber as an enclosed transmission medium can provide more bandwidth, lower latency, lower attenuation, and immune to RF interference. However, the use of fiber and millimeter-wave signals can pose several challenges, which will be further discussed in this chapter.

As discussed in section 1.1, this thesis focuses on millimeter-wave ARoF systems and exploring the use of deep learning for future generation wireless communication. Following the research objectives of this thesis, three ARoF links using differential encoding and incoherent detection are proposed. In addition, deep learning based centrally managed CoMP is proposed and demonstrated using MLP and LSTM algorithms. Furthermore, two novel deep learning based phase noise tolerant millimeter-wave receivers were proposed and demonstrated using autoencoder and LSTM algorithms. Therefore, this chapter provides essential background information related to the research topics presented in subsequent chapters. In section 2.2, regulations and characteristics of millimeter-wave signals are presented. Section 2.3.1 presents signal impairments caused by the optical delivery system, focusing on ARoF signals. ARoF optical tone generation methods are discussed in section 2.3.2. Section 2.4 presents the challenges of CoMP implementations. Section 2.5 presents an overview of AI implementations in millimeter-wave RoF.

2.2 Millimeter-wave Characteristics, Standards and Regulation

The usage of RF frequency bands are usually regulated by local authorities of each country. For example, the regulatory body in the United States (US) of America is the Federal Communications Commission (FCC), and the Malaysian Communications and Multimedia Commission (MCMC) is the regulatory body in Malaysia. For upper microwave flexible use service (UMFUS) with a frequency range of 24.25 GHz -48.2 GHz, FCC specifies a limit of up to 43 dB average effective isotropic radiated power (EIRP) for mobile stations [70]. In addition to the 43dB EIRP limit, FCC expects that upper microwave flexible use service (UMFUS) devices to comply with FCC's radiofrequency radiation exposure rules as these rules have more stringent exposure limits for devices within 20cm from the human body, which would limit the power of such device to be below the 43 dBm limit [71–73]. For fixed point-to-point transmission at 57 GHz to 71 GHz RF, FCC specifies a maximum average power of 82 dBm, with a 2 dB reduction for every dB if the antenna gain of the transmitter is below 51 dBi [74]; for 27.5 GHz to 28.35 GHz and 38.6 GHz to 40 GHz RF bands the maximum allowable EIRP is 85 dBm [75]. Initially, a 62dBm/100MHz transmission power limit for UMFUS base stations was specified by FCC, but that limit was increased to 75 dBm/100MHz EIRP [70, 76]. The increase in maximum average power limit increases UMFUS base stations' link reliability in dense urban areas and during weather events [71].

On the other hand, third-generation partnership project (3GPP) specifies a maximum total radiated power of 47 dBm and 33 dBm for medium-range BS and local area BS respectively [77]. However, an upper limit for the total radiated power for wide-area BS was not specified. For wireless user equipment (UE), 3GPP guidelines categorize them into four different classes:

- Power Class 1: Fixed wireless access
- Power Class 2: Vehicular UE
- Power Class 3: Handheld UE
- Power Class 4: High power non-handheld UE

The maximum EIRP specified by 3GPP for power class 1 is 55 dBm [78]. For the remaining three classes, the maximum EIRP is 43 dBm [78]. The power limits specified are for RF signal that falls within the 24 GHz - 40 GHz RF range.

While millimeter-waves are non-ionizing, where the risk of cancer due to prolong exposure should not be an issue as compared to ionizing radiation such as ultraviolet (UV), X-rays, and Gamma rays. The radiation energy of millimeter wave is way below the energy required, which is typically 12 eV, to displace an electron from a molecule, to create free-radicals that can lead to cancer [80–82]. While millimeter-waves are non-ionizing, the primary cancer risk will be heating due to the human body absorbing millimeter-waves, especially the eyes and skin of the human body [80, 81]. Hence, the guidelines for the emission power of RF waves should be designed to protect against such risk [83–86]. In the International Commission on Non-Ionizing Radiation Protection (ICNIRP) guideline for the year 2020 [87], the RF power density exposure limits for the general public is $55f_{GHz}^{-0.177}\frac{\mathrm{W}}{\mathrm{m}^2}$ for 6 GHz to 300 GHz RF range. f_{GHz} is the RF measured in GHz. The incident power density is averaged over a square surface of 4 cm^2 of the body surface exposed to RF. If the RF frequency is above 30 GHz with an upper limit of 300 GHz, the incident power density limit averaged over a smaller square surface of 1 cm^2 should not exceed $110f_{GHz}^{-0.177}\frac{\mathrm{W}}{\mathrm{m}^2}$. The IEEE *dosimetric reference limits* has a similar incident power limit as well [88]. The FCC specifies a maximum permissible exposure of 10 $\frac{\mathrm{W}}{\mathrm{m}^2}$ averaged over a 4 cm^2 surface [89, 90]. For 1 cm^2 surface, FCC has recently proposed a maximum local power density limit of 40 $\frac{\mathrm{W}}{\mathrm{m}^2}$ [91].

When a signal is transmitted wirelessly, it will be affected by what is present in the propagation channel space at a given time. RF signal traveling through air will experience attenuation, scattering, and diffraction; most of it is frequency-dependent. The signal's attenuation is contributed by free-space path loss (FSPL), atmospheric gas attenuation, which is mainly contributed by water vapor and oxygen, precipitation attenuation, sand

and dust storm, and foliage blockage. The FSPL can be defined as

$$\text{Free Space Path Loss (FSPL)} = 10\log_{10}\left(\frac{4\pi df}{c}\right)^2 \text{dB} \tag{2.1}$$

where d is the distance between the transmitting and receiving antenna measured in meters, f is the frequency of the RF signal in Hz, c is the speed of light in m/s. Fig. 2.1 [79] shows the attenuation caused by the presents of water and oxygen at sea level (1013 hPa) with a temperature of 15 degree Celsius. From 10 GHz to 100 GHz range, the attenuation contributed by atmospheric absorption peaks around 60 GHz [93, 94]. The lowest attenuation for the millimeter-wave frequency range is at 30 GHz to 40 GHz. Fig. 2.2 [92] shows the specific attenuation of RF signal from 1 GHz to 1000 GHz due

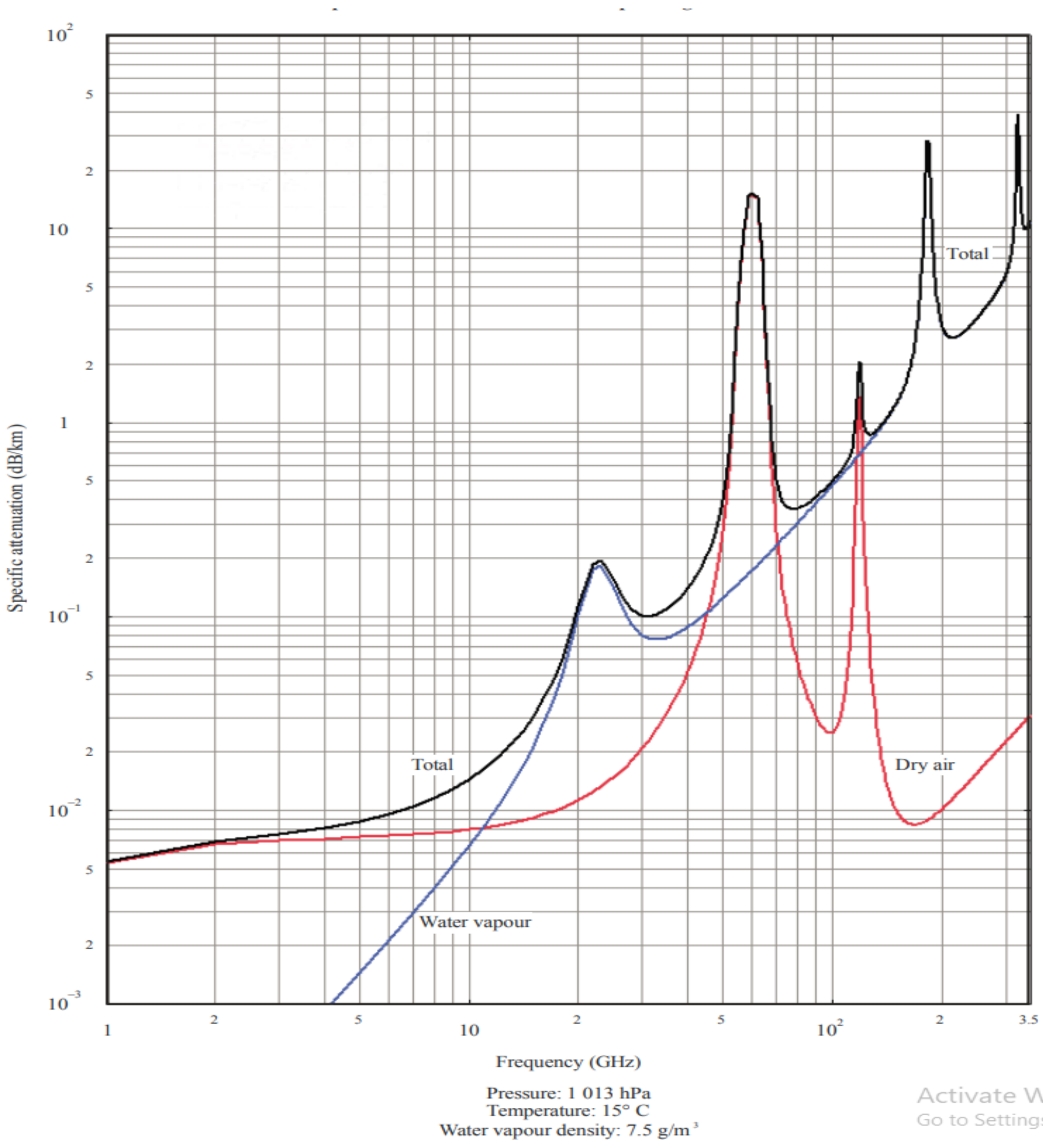

Activate Windows
Go to Settings to act

FIGURE 2.1: Specific attenuation of RF signal at sea-level for dy air and water vapour (7.5 g/m^3) [79]. (Reproduced, with permission, from ["Attenuation by atmospheric gases and related effects," Recommendation ITU-R P.676-12, Tech. Rep., 08 2019.])

to rain. Interestingly, the attenuation curve gradient flattens around 100 GHz, which means that the specific attenuation experienced by an RF signal at 1000 GHz is similar to the specific attenuation at 100 GHz.

As discussed in the previous paragraphs, constituents of the atmosphere can absorb electromagnetic energy and cause attenuation. At the same time, they can also radiate electromagnetic energy. The radiated signals are noise-like, which can degrade communication link performance. Sky noise is a concern for the space industry and is usually considered for satellite communications [96]. When an antenna on earth is pointed upwards with a high elevation angle aimed towards a satellite, the signal sent will be impinged by sky noise emitting from the atmospheric constituents and other sources [97]. This is referred to as brightness temperature or sky noise temperature. In contrast, if the elevation angle of the antenna is low, the dominant sky noise will be from the terrain [97]. If sky noise is considered in a system, it will normally be included in the

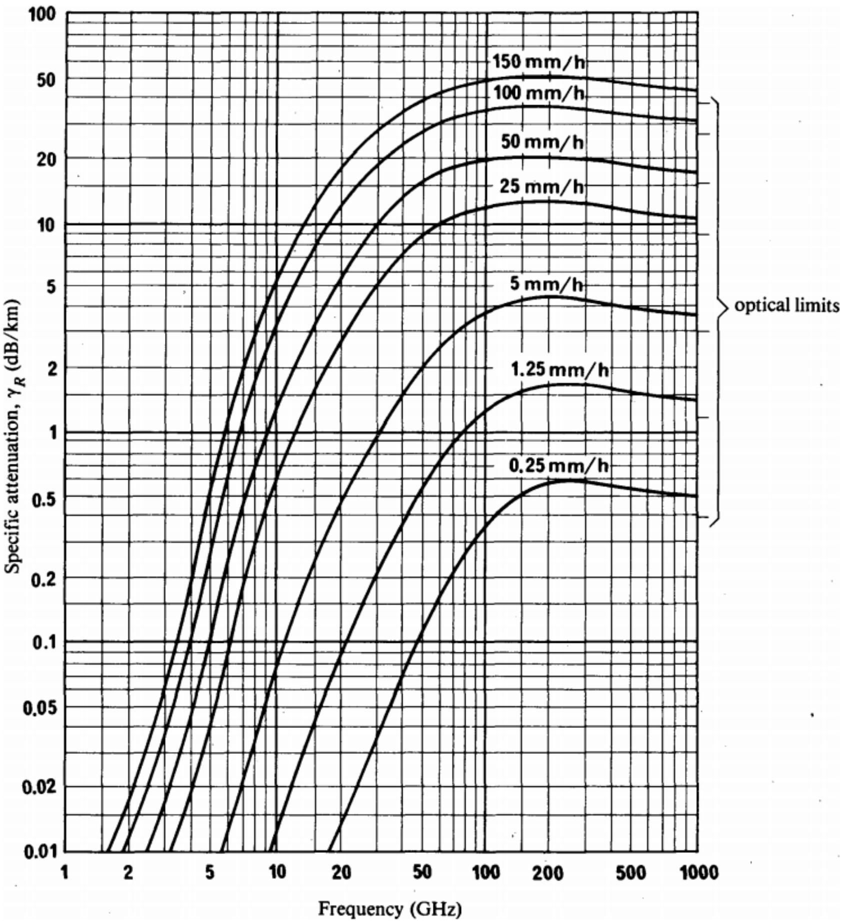

FIGURE 2.2: Specific attenuation of RF signal due to rain [92]. (Reproduced, with permission, from ["Attenuation by hydrometeors, in particular precipitation, and other atmospheric particles," CCIR, Geneva, Switzerland, Report 721-2, 1986])

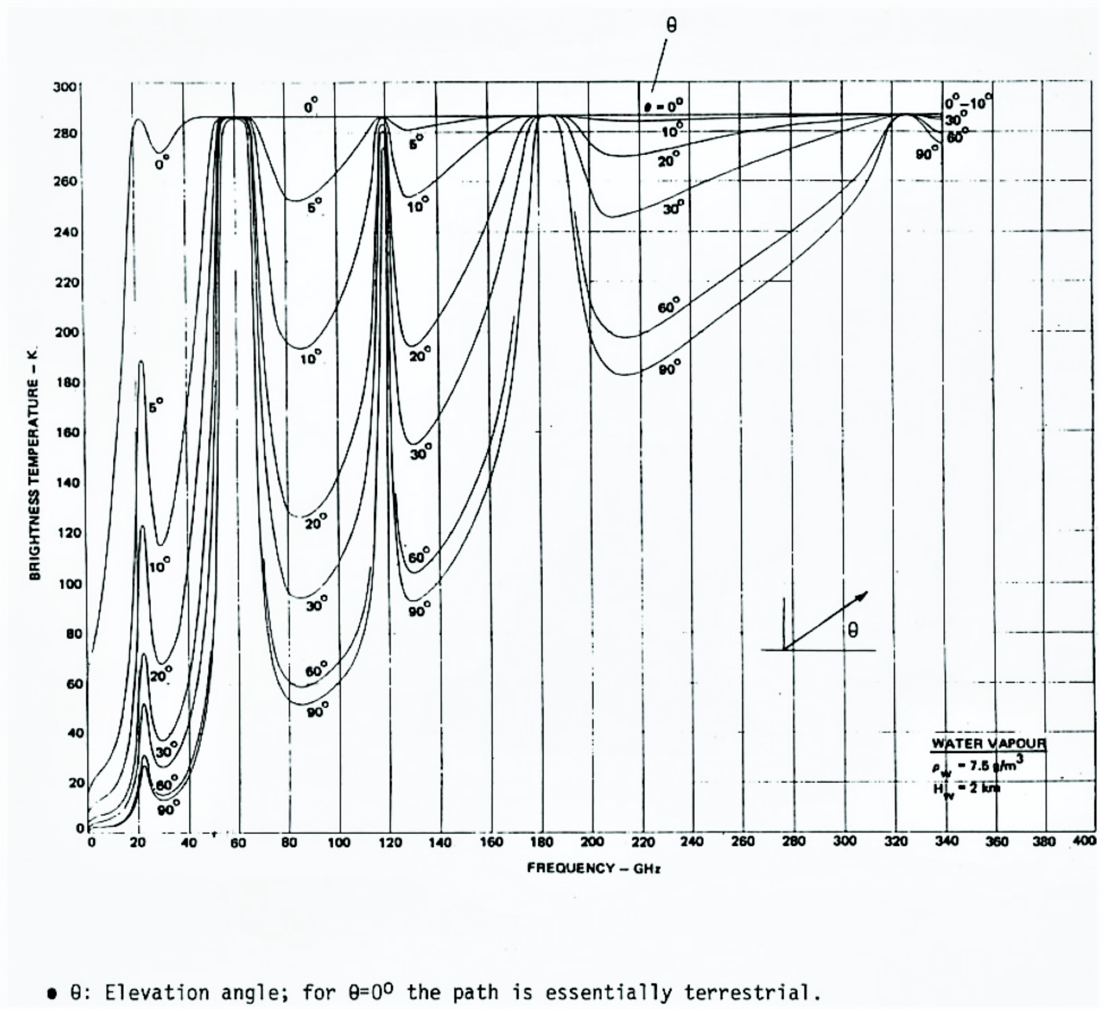

FIGURE 2.3: Sky noise temperature for RF range of 1 Hz to 340 GHz at a water moisture concentration of 7.5 g/m^3 [95]. (Reproduced, with permission, from [E.K. Smith, "Centimeter and Millimeter Wave Attenuation and Brightness Temperature due to Atmospheric Oxygen and Water Vapor," Radio Science, Vol. 17, Dec. 1982])

antenna noise temperature. Fig. 2.3 shows the sky noise temperature for corresponding RF frequency ranges from 1 Hz to 340 GHz.

Foliage is a collective bunch of leaves on a plant. Foliage loss is due to RF signal propagating through one or more plants, mainly trees. If the foliage depth, denoted by R, is less than 400 meters, foliage loss can be estimated using the ITU-R model as shown below [98]:

$$\text{Foliage Loss} = 0.2 {f_{MHz}}^{0.3} R^{0.6} \tag{2.2}$$

where f_{MHz} is the RF signal in MHz. The equation shown above is valid for a frequency range of 0.2 GHz to 95 GHz. However, it is important to note that the foliage loss is also affected by the type of plant as different plants have different trunk, branch, and leave sizes, which can influence the propagation of the RF signal through the vegetation [99–101].

For an RF signal, even if the path between the transmitting and receiving antenna is not a line-of-sight (LOS) path, the signal can still be transmitted and received by receiving antenna through reflections of obstacles and objects via diffraction. There are two kinds of reflections, diffused or specular. The difference between these two reflections is frequency-dependent. A reflective surface appears "rougher" when the incident signal is of higher frequency as the signal has a shorter wavelength. This results in a relatively more diffused reflection in contrast to specular reflections, depending on the angle of incident [102, 103]. Hence, the reflection loss of millimeter-wave may be higher due to its shorter wavelength. However, if the incident angle is large, the scattering loss is small [103, 104]. The larger incident angle leads to a smaller angular spread [103].

Table 2.1: Penetration attenuation for different matterials

		Attenuation, dB			
Material	Thickness, cm	sub-3 GHz [105, 106]	28 GHz [107]	40 GHz [108]	60 GHz [105]
Dry Wall	2.5, 38.1	5.4	6.84 (38.1 cm)	-	6.0
Office Whiteboard	1.9	0.5	-	-	9.6
Clear Glass	<1.3	6.4	3.6	2.5	3.6
Mesh Glass	0.3	7.7	-	-	10.2
Tinted Glass	3.8	-	40.1	-	-
Chipwood	1.6	-	-	0.6	-
Wood	0.7	5.4	-	3.5	-
Plaster board	1.5	-	-	2.9	-
Mortar	10	-	-	160	-
Brick Wall	10, 185.4	-	38.3 (185.4 cm)	178	-
Concrete	10	17.7	-	175	-

While existing sub-3 GHz RF used in current wireless communication can penetrate through buildings with relatively low attenuation loss, millimeter-wave signals do not penetrate obstacles very well. Table 2.1 shows the tabulated penetration attenuation values for different materials at different RF frequencies [105–108]. In general, the penetration loss for millimeter-wave signals is higher than sub-3 GHz RF signals.

2.3 Analogue Radio-over-Fiber

In Radio-over-Fiber, fiber is used to connect the base stations to the central office. Contrary to wireless fronthaul solutions, such as conventional RF-based fronthaul links and free-space optics (FSO) based fronthaul links, fiber as an enclosed transmission medium is immune to RF interference, less susceptible to weather conditions, have relatively low propagation loss, and have more available bandwidth. Fronthaul based on RF links are either limited by available frequency bands or high propagation loss. As discussed in Chapter 1 and Section 2.2, lower RF bands are congested, and while millimeter-wave provides more available bandwidth, it has high propagation loss due to atmospheric absorption and high obstacle penetration loss. On the other hand, FSO based fronthaul link is highly susceptible to weather conditions and temperature fluctuations [109, 110]. In the presence of thick fog, an FSO link's performance degrades greatly due to signal absorption caused by water molecules suspended in the environment [111]. Temperature variations around the FSO link cause variations in the reflective index due to a change in air density and can lead to fluctuations in the received signal's amplitude [109]. Besides, the wireless link between the FSO transmitter and receiver can be temporarily obstructed by flying objects such as flying birds and foliage. Therefore, an enclosed transmission medium such as fiber can provide a more reliable and consistent transmission performance compared to wireless solutions.

In general, RoF can be categorized into two categories: digital RoF (DRoF) and analog RoF (ARoF). In a millimeter-wave DRoF link based on CPRI, the signal transmitted from CO is in baseband and will be upconverted to millimeter-wave signal in the BS. In contrast, in analog RoF (ARoF) the base station acts solely as a relay, and the millimeter-wave signal is generated in the central office. Hence, the base stations in ARoF can be simplified as it no longer performs RF upconversion and modulation as opposed to DRoF. Fig. 2.4 shows an example of fiber connections linking base stations to the central office. The millimeter-wave signal in ARoF is generated by heterodyning two optical tones at the photodiode, where the difference in frequency between the two optical tones will be the millimeter-wave frequency generated. Optical tones can be generated using multiple optical sources or optical modulation. The optical tones generated can be correlated in phase, frequency locked, or both.

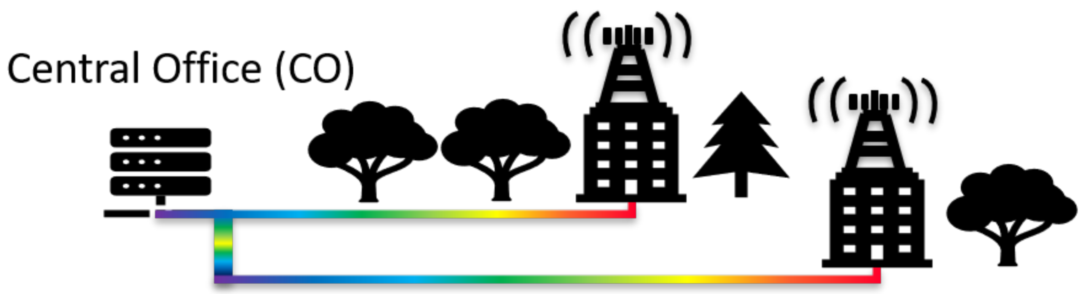

FIGURE 2.4: Illustration of fiber connection used for linking base stations and central office (CO) for DRoF or ARoF.

2.3.1 Optical Transmission Impairments

Compared to wireless backbone networks, the introduction of fiber in RoF provides more bandwidth, lower attenuation, and immunity to RF interference. The high bandwidth fiber allows higher data throughput and improved latency. In RoF, the transmitted signal's quality and integrity can be affected by phase noise, intensity noise, and dispersion. These impairments are contributed by the use of fiber, amplifier, photodiode, and laser.

In an optical transmitter, optical phase noise originates from the optical source and optical amplifier. For the optical amplifier, nonlinear phase noise is generated by the amplified spontaneous emission noise interacting with Kerr non-linearity in fibers [112, 113]. Furthermore, in the optical source, the phase noise originates from spontaneous photon emissions, which causes phase fluctuations. Besides, Ker non-linearity is also affected by the intensity of emitted photons. When the optical intensity increases, the phase delay in fiber increases due to a change in refractive index [114]. Phase noise contributed by the optical amplifier and optical source leads to spectrum broadening. In ARoF, the signal modulation, dictated by the desired wireless signal modulation corresponding to the wireless channel quality, is carried out in the central office. In wireless communication, phase-modulated signals such as QPSK and M-QAM are popular modulation formats. The phase noise contributed by the optical transmitter can significantly degrade the receiver's detection performance. While phase-coherent optical tones can help with reducing optical phase noise through locked heterodyne detection, phase noise from the optical transmitter should be controlled and monitored closely. As high order modulation such as 1024 QAM is being proposed in 5G [8], the margin for phase fluctuations to ensure an error-free transmission is very tight.

Aside from phase noise, spontaneous emission photons can also lead to optical intensity noise [115]. At the photodetector, the unstable rate of photons' emission, shot noise, can cause intensity fluctuations in the electrical signal [116]. On the other hand, the phase change due to chromatic dispersion can cause intensity fluctuations as well [117]. Relative intensity noise (RIN) of a laser limits the maximum achievable SNR of a given optical link as RIN is contributed by the transmitter [118–123]. This means that the second the laser is turned on, the SNR of the signal is degraded, and amplifying the signal with an optical amplifier will not change the maximum achievable SNR. The use of a single photodiode direct detection in RoF does not have the ability to cancel out the RIN and beat noise of detected signal compared to balanced photodiode detection [124]. Therefore, during the design stage of an ARoF link, the link power budget should account for RIN, and a low RIN optical source should be used as other noise sources contributes to the larger fraction of the noise budget [124].

Fiber chromatic dispersion can convert optical phase fluctuations to intensity fluctuations and also convert intensity modulation to phase modulation [118]. Chromatic dispersion occurs due to frequency-dependent refraction index of the fiber. Hence, optical signals at various frequencies have different paths and speeds. In ARoF, signals transmitted from the central office to the base station can be generally categorized in three forms: optical double sideband with carrier (ODSB+C), optical double sideband with suppressed carrier (ODSB+SC), and optical single sideband with carrier (OSSB+C). It was found that chromatic dispersion causes RF power fading in ODSB signals [125–128]. The power fading can cause a drop in SNR, degrading the overall link performance. The RF power degradation changes with different fiber lengths and frequency gaps. The frequency gap is the frequency difference between the optical carrier and one of the optical sideband. In general, a wider frequency gap will lead to a higher the power degradation [126]. In contrast, OSSB signals are immune to RF power fading [41, 126]. The RF power generated from OSSB signals remains relatively flat compares to ODSB signals wherein the RF power generated fluctuates with different fiber length [129].

2.3.2 Optical Tone Generation

In ARoF, optical tones are generated in the CO before transmitting to the BS. The optical tones generated can be uncorrelated, phase-locked, frequency-locked, or phase and frequency locked depending on the generation method used. In this section, optical tones generated through directly modulated laser, multiple optical sources, and external modulation are presented.

The optical generation methods can be categorized into three categories: conventional optical tone generation, uncorrelated optical tone generation Optical injection locking requires three lasers, a master laser, and two slave lasers to generate two optical coherent tones, as shown in Fig. 2.5. The master laser is modulated with an RF reference using frequency modulation, which generates an optical carrier with multiple sidebands. The sideband to carrier spacing is equal to the integer multiples of the modulating frequency. If the slave lasers' wavelength is set to the frequency of the 2nd sideband [42], let's say +2nd order and -2nd order, it will generate a beat note of four times of the RF reference. If the wavelength is set to the 3rd sideband [43], the RF frequency generated after photodiode detection will be six times the RF reference. Optical injection locking is achieved when the slave lasers operating frequency is equivalent to the sideband of the frequency-modulated optical signal [42]. The two slave lasers can also be replaced with a multi-longitudinal-mode slave laser to simplify the overall configuration [43].

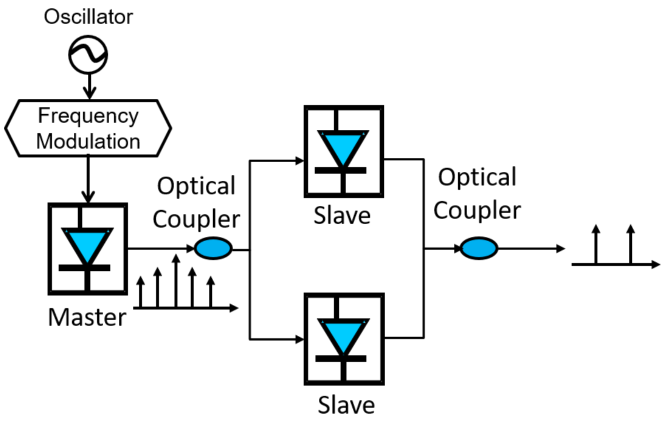

FIGURE 2.5: Optical injection locking with a master laser and two slave lasers

Optical frequency locked loops [44, 45] generates optical tones that are frequency locked. However, the optical tones lack phase coherence. This would lead to the millimeter-wave signal generated after heterodyne photodiode detection to inherit phase noise from the optical transmitter. Frequency-locked optical tones are generated using a master laser and a slave laser. The frequency locking is achieved through the feedback loop, as shown in Fig. 2.6. The frequency discriminator converts the frequency variations into voltage variation. The loop compares the frequency of the controlled oscillator to the reference and increases or lowers the frequency of the slave laser until the frequency matches the reference oscillator's frequency.

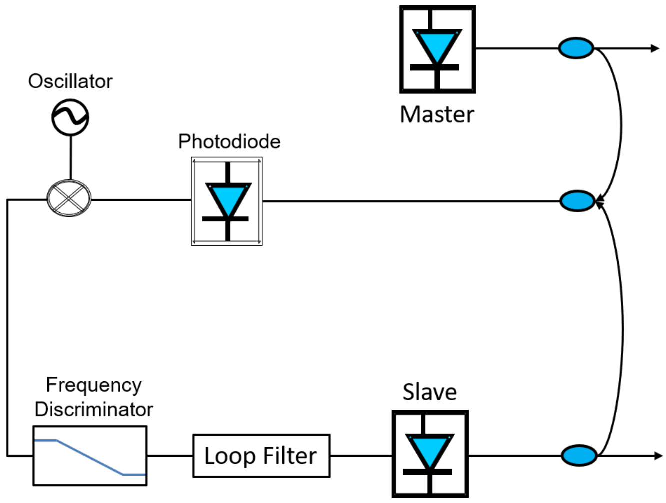

FIGURE 2.6: Optical frequency-locked loop

Phase coherent optical tones can also be generated using optical phase-lock loop [46–48]. The configuration of an optical phase lock loop is shown in Fig. 2.7. This approach achieves phase coherence by actively locking one of the laser's phase to the other using an optical phase lock loop. RF signal generated through the optical phase-lock loop approach can achieve a linewidth of less than 1mHz [46, 48]. However, narrow linewidth

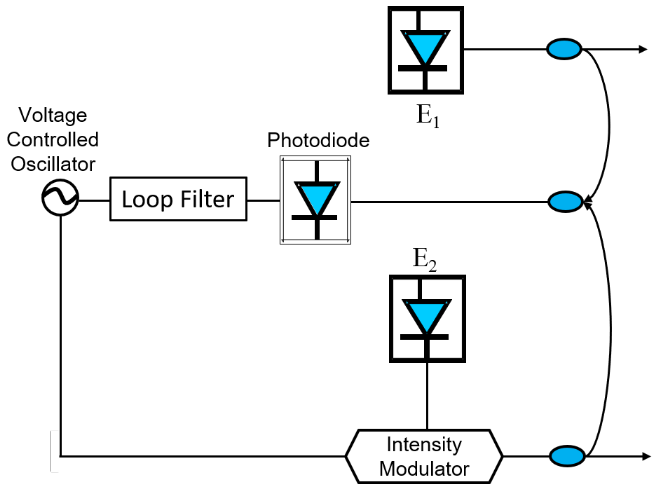

FIGURE 2.7: Optical phase-locked loop

lasers are required to reduce the optical phase-lock loop complexity, as the phase fluctuations of narrow linewidth lasers are at low frequencies.

Optical tone generation discussed in previous paragraphs separates the process of optical tone generation and data modulation. A directly modulated laser can produce optical tones through modulating the downlink data signal at the desired millimeter-wave frequency directly. The downlink data needs to be upconverted from baseband using a quadrature modulator with an oscillator functioning at millimeter-wave frequency. While this setup is relatively simple and cost-effective compared to previously discussed methods, the maximum frequency is limited by the laser resonance peak, and the performance is impaired by frequency chirp, non-linearity, and relative intensity noise of a directly modulated laser [49–54].

An external optical modulator can be used to avoid impairments of a directly modulated laser. Optical tones used to generate millimeter-wave through heterodyning is generated using an continuous wave (CW) laser, RF oscillator, and external modulators such as Mach-Zehnder modulator (MZM), electro-absorption modulator (EAM), or optical phase modulators [55–59]. The simplest method to generate correlated optical tones using an external modulator is intensity modulation. The external modulator modulates the optical output of the CW laser using the downlink data signal at millimeter-wave frequency. This method requires an RF oscillator operating in the millimeter-wave frequency range and a high-speed optical modulator capable of modulating the high-speed RF signal onto the optical carrier. The optical tone generated is in the form of an optical double-sideband (ODSB) signal. However, ODSB signals are heavily affected by fiber chromatic dispersion [125–128]. As the spectral components within the ODSB signal travel at different speeds and different paths, the spectral components detected at the photodiode will have different phases, which would lead to power degradation of the generated RF signal. The dispersion effect can be mitigated through the use of optical single-sideband (OSSB) signal. An OSSB signal can be generated using an optical filter to suppress one of the sidebands of an ODSB signal, or using dual parallel MZM or a single dual-electrode MZM by varying the operating point of the MZM and phase difference between the modulator arms [60–63]. Fig. 2.8 shows the methods used to generate OSSB and ODSB signals.

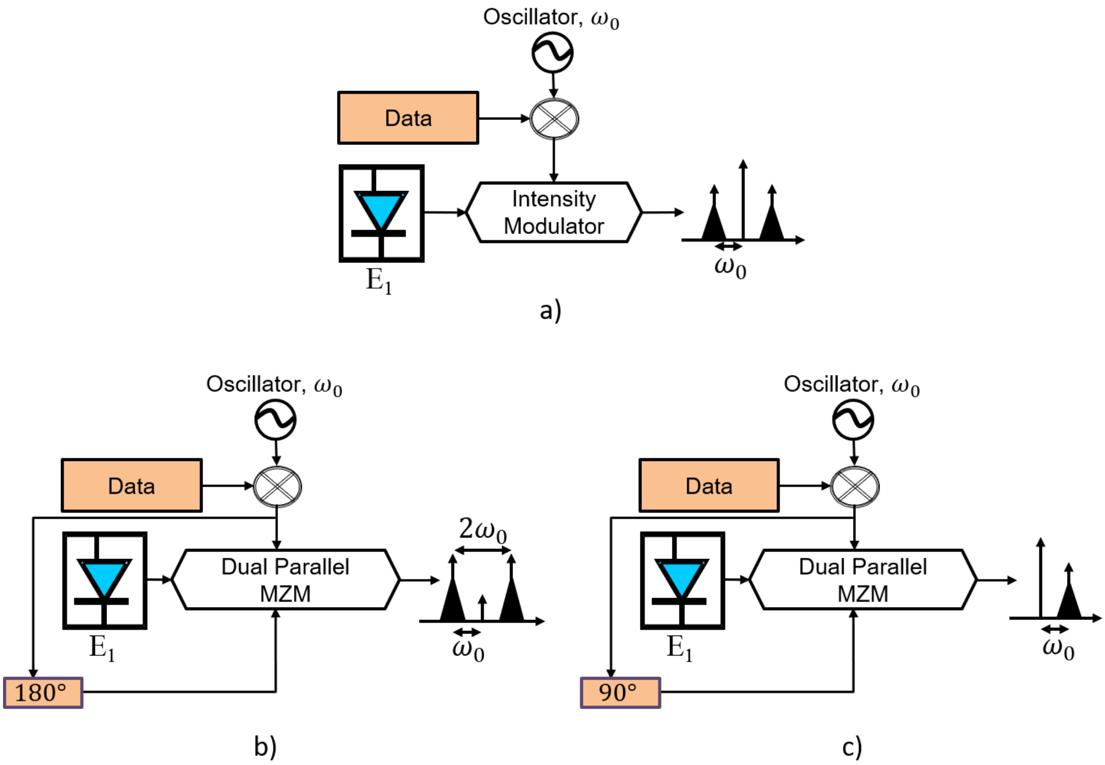

FIGURE 2.8: Conventional ARoF optical tone generation method for a) optical double sideband with carrier b) Optical double sideband with suppressed carrier and c) Optical single sideband

Contrary to previous generation methods discussed, where the optical tones generated are correlated in terms of phase, frequency, or both, uncorrelated ARoF optical tones can be generated using two individual free-running laser. An uncorrelated millimeter-wave RoF scheme, as shown in Fig. 2.9, was proposed in [130–133] and demonstrated using ASK data [65, 134]. The optical tones with a frequency gap equivalent to the desired millimeter-wave frequency are generated using two free-running optical lasers. This method simplifies the optical tone generation method compared to other methods discussed above and does not require a high-speed optical modulator. However, optical tone generated through this method suffers from phase noise inherited from the optical transmitter due to unlock heterodyning of incoherent optical tones. As opposed to coherent optical tones, where the phase of the optical tones are correlated or the same at any given time, uncorrelated optical tones have varying optical phases. During heterodyne detection at the photodiode, optical phase noise is reduced if the tones are correlated, and the opposite is true for uncorrelated optical tones. Therefore, narrow-linewidth lasers are required for such a method.

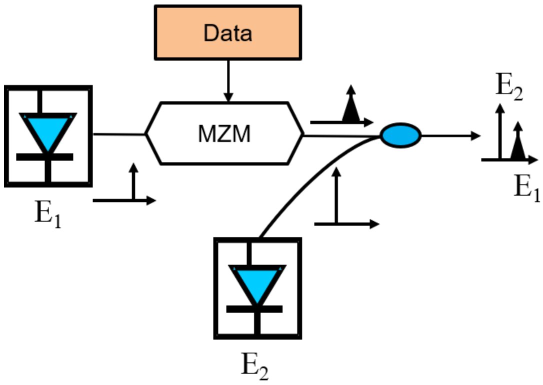

FIGURE 2.9: Optical tone generation using multiple optical sources

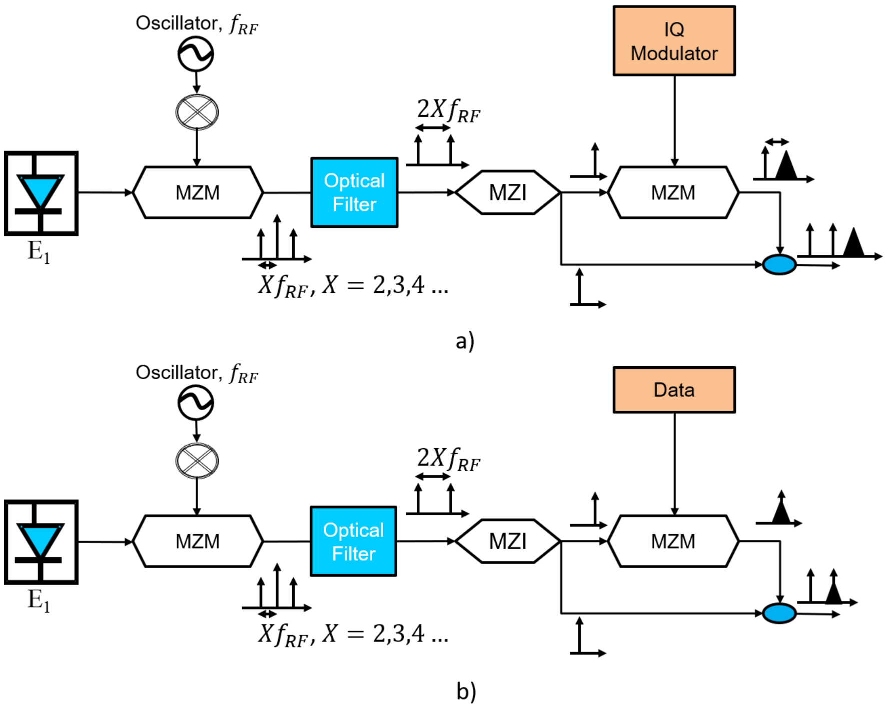

FIGURE 2.10: Optical frequency multiplication optical tone generation using filter with a) intermediate frequency data modulation b) baseband data modulation

The cost of a millimeter-wave analog RoF link is closely related to the number of high-speed components used. As the required speed of the optical modulators and RF oscillators increases, the cost increases, as lower frequency components are less costly than higher frequency components. Optical frequency multiplication method was proposed to generate millimeter-wave signal using lower frequency oscillators and an external modulator. The external modulator used can have a lower bandwidth or speed compared to the desired millimeter-wave signal. Optical frequency multiplication can be achieved using two methods, one of which requires an optical filter while the other uses carrier suppression modulation, as shown in Fig. 2.10 and Fig. 2.11. The first method achieves optical frequency multiplication by filtering the ODSB signal's optical carrier using an optical filter, or optical interleaver [135–138]. Using proper modulator biasing and modulation index, a frequency separation between the two sidebands can be more than twice the frequency of the oscillator used and limited by the harmonic generation efficiency and modulator used [64]. The second method implements optical frequency multiplication through optical double sideband with suppressed carrier modulation achieved by varying the biasing voltage and phase difference between the two arms of a dual-electrode MZM [139, 140] or multiple cascaded MZMs [141].

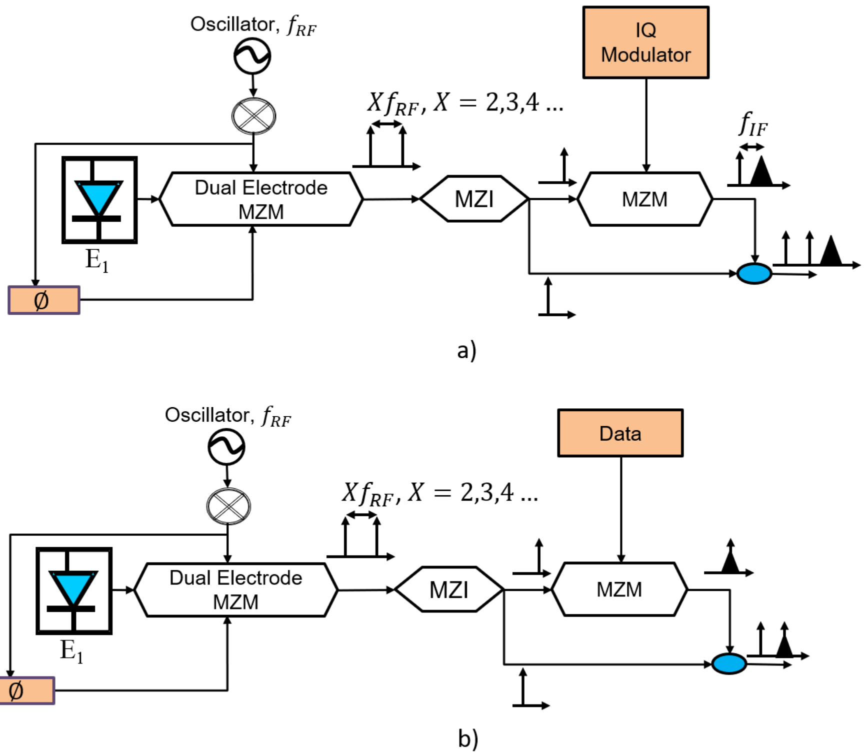

FIGURE 2.11: Optical frequency multiplication optical tone generation using carrier suppressed modulation with a) intermediate frequency data modulation b) baseband data modulation

Table 2.2 provides a comparison comparing the advantages and disadvantages of each optical tone generation method discussed above.

Table 2.2:
Comparison of optical tone generation methods

Techniques	Advantage(s)	Disadvantage(s)
Optical Injection Locking [42, 43]	Stable frequency separation between optical tones Narrow linewidth optical tone	Requires narrow linewidth master laser
Optical Frequency/Phase Locked Loop [44–48]	Optical tones generated are frequency locked, phase locked or both Low phase noise due to locked heterodyning	Requires millimeter-wave frequency components
Direct Modulation [49–54]	Simple configuration Stable frequency separation between optical tones	Requires millimeter-wave frequency components Poor link performance due to nonlinearities, noise and frequency chirp
External Modulation without Optical Frequency Multiplication [55–59]	Correlated optical tones Stable frequency separation between optical tones	Requires millimeter-wave frequency components High cost for high frequency operation
External Modulation with Optical Frequency Multiplication [64, 135–141]	Correlated optical tones Stable frequency separation between optical tones Millimeter-wave frequency are generated using lower frequency components	May require optical filtering Millimeter-wave frequency generated are limited by harmonic generation efficiency and modulator used
Uncorrelated Lasers[65, 130–134]	Simple configuration Does not require high speed optoelectronics and RF components	Frequency gap between optical tones may fluctuate Heterodyning of unlocked optical tones causes generated millimetwer-wave signal to inherit phase noise from optical transmitter Low phase noise requires narrow linewidth lasers

2.4 Coordinated Multipoint

In March 2008, 3GPP initiated a study item focusing on radio interface enhancements for Long Term Evolution-Advance (LTE-A) and was published in [142]. To fulfill these requirements, CoMP has been identified as a critical component for physical layer enhancements [143], and a feasibility study was released in 3GPP Release 11 [144]. In CoMP, transmissions between base stations and mobile users are coordinated to reduce interference and to improve overall data throughput. Interference between base stations and mobile users can be managed through coordinated scheduling or coordinated beamforming. For example, to manage interference in a downlink CoMP, base stations are coordinated in which data transmission to the user originates from a single base station at a time. For uplink CoMP interference management, mobile users are coordinated such that the user data is received by one recipient point (or base station) at a given time. On the other hand, in joint transmission downlink CoMP, data is simultaneously transmitted from multiple base stations to a single mobile user to improve received signal quality and/or data throughput. However, several challenges such as cluster size, fault detection and mitigation, efficiency, and backhaul bandwidth have to be addressed to exploit the full benefit of CoMP.

The network performance using coordinated multipoint is closely related to the cluster size. The cluster's size is determined by the total number of base stations involved in a coordinated multipoint transmission. A CoMP cluster that is too small will lead to a failure in achieving the full potential of CoMP. On the other hand, an oversize cluster would increase overhead due to Channel State Information (CSI) feedback and increase the load on the backhaul network [145]. An increase in cluster size results in a better-weighted sum-rate at the cost of additional signal processing, increased feedback and signaling, and power consumption [146, 147]. A dynamic clustering scheme demonstrated in [148] shows no spectral efficiency gain in employing CoMP in a high signal-to-interference-plus-noise ratio (SINR) region due to an increase in the overhead required for CoMP. The CSI collection relies on the backhaul network of CoMP; when the CoMP feedback and signaling increases, the bandwidth required to collect the CSI increases. If the backhaul network relies on wireless transmission wherein bandwidth is limited, the increase in overhead can reach a point where most bandwidth is used for CoMP feedback and signaling instead of actual data transmission.

Self-Organizing Network (SON) in telecommunication aims to automate the operation task to simplify the system and reduce latency. SON is a part of 3GPP LTE and LTE-A standards starting from Release 8 with further improvement introduced until Release 12 [149]. SON aims to automated new site configuration, initial automated neighbor relations, optimize network performance through monitoring to reduce operational costs and improves overall network Quality of Service (QoS) and network capacity [150, 151]. SON also aims to detect, analyze, diagnose, and clear faults in network elements [152]. Ideally, suppose a fault is detected in one of the cooperating base stations within a given cluster. The network should be able to detect the fault and re-route network traffic to other base stations while optimizing for coordinated multipoint transmission to maximize transmission rate or avoiding interference between base stations.

There are three main clustering types in CoMP: static clustering, semi-dynamic clustering, and dynamic clustering. Static clustering forms clusters based on topology and does not change according to network traffic changes. The method offers a relatively low complexity solution as clusters are static; hence no data exchange between sites is required. However, the advantage of static clustering is also its downside; the static nature of this method makes it not able to respond to network profile changes throughout the day [153, 154]. Hence, the throughput gain from static clustering is limited, and its effectiveness to handle different degrees of interferences is limited as well. An effort to improve such a situation is demonstrated in [145], where overlapping clusters are formed, but this increases complexity with increasing network cluster size. On the other hand, dynamic clustering [155–157] is more flexible. Cluster sets change with time according to changes in user density. A change in user density increases or decreases network traffic within an area. Dynamic clustering requires frequent channel state information (CSI) transmission to coordinate and manage clusters sets and sizes that are constantly changing. A semi-dynamic clustering CoMP falls between static clustering and dynamic clustering. While static clustering is simple to be implemented and dynamic clustering provides flexibility but requiring more overhead, a semi-dynamic clustering scheme demonstrated in [158], requires lower overhead and clustering complexity compared to dynamic clustering. Furthermore, providing more flexibility compared to static clustering. The added flexibility of semi-dynamic clustering and dynamic clustering can have scalability issues due to increased in complexity, computational intensity and backhaul bandwidth [159–166].

As discussed in Chapter 1, the introduction of millimeter-wave frequency bands to commercial wireless communication enables higher data throughput due to higher bandwidth availability than lower RF bands. However, higher frequency bands lead to higher propagation loss, as discussed in Section 2.2. This leads to needing more base stations to service the same area compared to using lower RF base stations. While having more base stations in closer proximity allows aggressive frequency reuse, it increases the load on the backbone network. More base stations mean more scheduling and coordination needed, and these are carried out through feedback and signaling between network elements. Since base stations are densely distributed, users' movement from one cell site to the other is shorter. Besides, cooperating base stations involved in CoMP have to be synchronized [167]. Hence, the network has to be able to process the immense amount of feedback and signaling from network elements fast for large-scale synchronization, scheduling, and coordination for CoMP and beamforming. The use of CRAN can be an effective solution for the latency and heavy processing requirements to perform CoMP for densely distributed base stations. The centrally located baseband units in CRAN enable more efficient resource allocation and distribution, and easier information sharing as all the signals are transmitted back to the central office. Several research has been carried out using CRAN for CoMP. Space-frequency block coding based CoMP demonstrated using an RoF link presented in [168] shows an improvement of 3 dB in optical receiver sensitivity. The performance of the demonstrated link is evaluated using only two radio head units. Besides, the impact of uplink performance and synchronization still needs to be evaluated. A demonstration of a polarization division multiplexing (PDM) based coordinated multipoint transmission RoF link was presented in [169], showing a polarization track-free mechanism at the receiver in which requires no additional latency for PDM demultiplexing. However, similar to [168], the demonstration was only carried out using a downlink system with two radio head units. A study on the balancing of cooperative gain of CoMP and bandwidth consumption and resource allocation optimization for delay-sensitive traffic in CRAN is carried out in [170]. In [170], a hybrid CoMP scheme has been proposed to balance between cooperation gain and fronthaul consumption to minimize transmission delay in CRAN. The simulation results show that the proposed hybrid CoMP [170] achieves a significant delay performance gains against coordinated beamforming CoMP and joint processing CoMP. However, the demonstration did not evaluate the impact of processing and radio parameters on energy consumption and delay of user-requested service. A software-defined network (SDN) based orchestration of CoMP on a cloud radio-over flexible optical fronthaul network was demonstrated in [171]. The SDN-based orchestration [171] reduces traffic between baseband units through lightpath reconfiguration without impacting the download rate of cell-edge users. While a latency of hundreds of milliseconds was reported in [171], the lightpath setup time is ignored, assuming that the lightpath has already been configured. To cope with network traffic changes due to changes in user density throughout the network, and to reduce power consumption, spectral width and bit rate of the lightpaths need to be dynamically configured. In a fixed-grid network, the number of wavelengths available is limited due to the fixed channel spacing. The limited number of wavelengths limits the number of possible lightpaths, limiting the flexibility in dynamically assigning RRH and BBU pairs. Consequently, the fixed grid network will impede the applicability of the SDN-based orchestration demonstrated in [171].

2.5 Deep Learning in Millimeter-Wave Radio-over-Fiber

In recent years, AI has garnered attention and interest of the research community, and has motivated research in AI application in telecommunication problems. In RoF, the use of AI has been explored to be used as a decoder [172–176] ,and equalizer[177–179]. In addition, the use of AI has also been explored in network management [180–186]. The algorithms used in [172–186] are mainly k-nearest neighbors [177], SVM [178, 179], feed-forward neural network [172–174], CNN [175, 176], LSTM [184, 185], Hopfield neural network [186]. While most studies are carried out using neural networks are mainly shallow neural networks in which only a single hidden layer is used [172–174, 180], only limited number of experiments are carried out using deep learning algorithms.

A multilayered feed-forward neural network has been proposed for traffic prediction and resource allocation in a time-division multiplexing passive optical network based CRAN RoF [183]. The demonstration results suggest that the proposed deep learning method outperforms conventional passive optical network compliant dynamic bandwidth allocation methods in terms of delay time, packet loss ratio, and efficient use of upstream bandwidth. In addition, LSTM has been utilized for traffic prediction, and resource allocation in CRAN [184, 185]. The use of LSTM increases network throughput by 7% [184], reduces required processing resources [184, 185], and improves power efficiency [185]. Besides, the use of deep learning algorithms such as CNN [175, 176] has been explored and demonstrated as a nonlinear decoder. The use of CNN improves link sensitivity while requiring less computation compared to feed-forward neural network based decoder. The demonstrations are carried out using correlated optical tones, which reduces phase noise incurred by the optical transmission system through lock heterodyning. Although numerous studies on AI application in RoF CRAN have been carried out, only a few experimental demonstrations were carried out using deep learning in ARoF CRAN. Hence, more research can be carried out to explore the use of deep learning on problems discussed in section 2.3 and section 2.4.

2.6 Conclusions

Millimeter-wave band frequency can provide more bandwidth compared to sub-3GHz RF bands used in 4G LTE to meet future generation wireless communication data throughput requirements. However, such high-frequency signal suffers from high path loss, high specific attenuation in the presence of water and moisture, high specific attenuation when it is raining, and high penetration loss, especially for concrete walls. The introduction of fiber helps solve the increased bandwidth utilization for signaling and feedback between network elements and provides more bandwidth to the base stations to meet the tenfold increase in data throughput requirement for 5G wireless communication. However, the maximum range of optical signal transmission is heavily dependent on the signal modulation used due to impairments caused by the fiber and the optical source. Hence, the maximum distance from the central office and the base station is limited. Coordinated multipoint helps improve cell edge data throughput and reduce interference between base stations. The extent of the diversity gain of CoMP depends on how well the network can optimize for the size of each cell, the degree of freedom in clustering, power consumption, and bandwidth utilization.

Moreover, the densification of base stations due to high propagation loss increased the optimization complexity of CoMP. While ARoF is spectrally more efficient than DRoF, the ARoF link's performance can be severely degraded due to fiber impairments. Conventional ARoF phase-coherent optical tone generation methods rely on high-speed optoelectronics and oscillators and are generally more complex than phase uncorrelated generation methods.

The problems discussed in this chapter mainly arise from the use of high-frequency RF, and the solutions to those problems also cause new challenges. However, it is not limited to the current transmission from lower sub-3 GHz RF to millimeter-wave range signals. As long as the demand for higher data throughput remains, the move to higher frequency RF will continue, and similar problems will arise again.

Chapter 3

Differential Encoding for Unlock Heterodyning Millimeter-wave Radio-over-Fiber

3.1 Introduction

The ever-increasing demand in bandwidth by wireless end-users and connected IoT devices has poised to set the future wireless communications in millimeter-wave and sub-THz bands. These high-frequency bands offer much higher aggregate bandwidth, but signals at such frequencies have high propagation loss. To overcome this problem, wireless base stations (BS) at these frequencies are expected to be networked by low-loss fiber backhaul networks, such as radio-over-fiber (RoF). RoF connects the BSs to the central office (CO) via a fiber feeder network, predominantly utilizing the widely deployed last-mile fiber infrastructure [187].

Traditionally, the generation of millimeter-wave RoF signal relies on the generation of two correlated/coherent optical tones by using either various frequencies, modes or phase locking mechanisms of the laser, or advanced external modulations, such as optical single-sideband with carrier or optical double sidebands with suppressed carrier [188–190]. These locked optical tones will be heterodyned at the photodetector (PD) to be downconverted to the desired millimeter-wave wireless frequency. The principal drawbacks of these approaches are their complexity, delicacy, and cost, which are far too high compared to other access technologies such as CPRI. Therefore, a scheme having a pair of free running optical tones separated by the desired millimeter-wave frequency at the CO, one of which is modulated with data, has been proposed [133, 191]. The tones are heterodyned at the BS for wireless transmission and directly detected by a

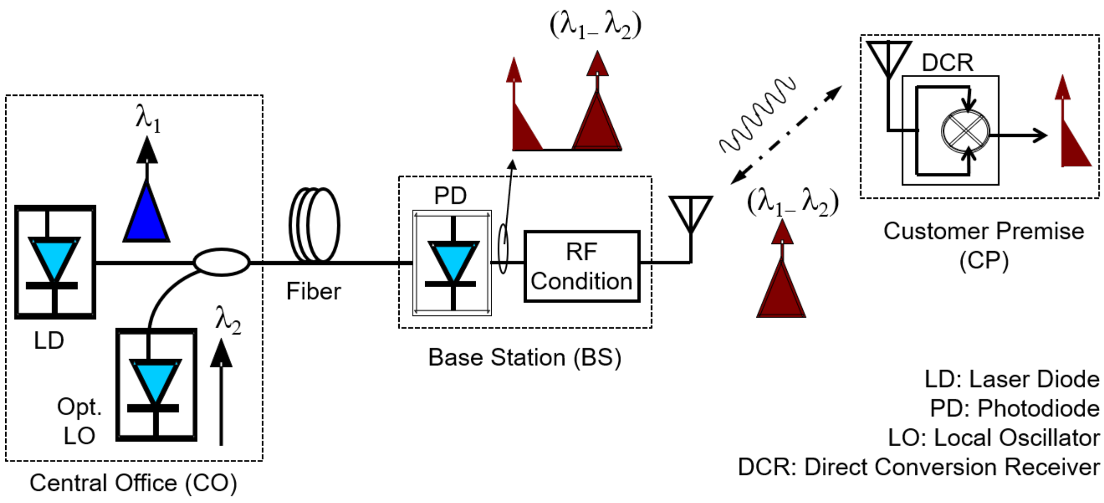

FIGURE 3.1: Uncorrelated Millimeter-wave Radio-over-Fiber

phase noise-tolerant direct conversion receiver (DCR) (also known as a self-homodyning receiver) at the customer premise (CP) for baseband downconversion, as shown in Fig. 3.1. Hence, the scheme can reduce the amount of high-speed optoelectronic and RF components in a typical RoF link to make it simple and independent of electrical local oscillators. The scheme can potentially be designed as a subset of current passive optical network (PON) deployments. Along with modulated optical carrier, an optical tone with the correct wavelength spacing can be added for the provision of RoF. A scheme similar to Fig. 3.1 was successfully demonstrated experimentally for both single and multi-level amplitude-shift-keyed (ASK) modulations employing DCR [65, 192].

However, direct detection using DCR, as demonstrated in ASK, is not directly applicable to phase-sensitive data such as in QPSK and QAM as it would affect the detected signal's phase integrity. Methods demonstrated in [67, 193] used QAM on an intermediate frequency radio-over-fiber link (IF-RoF), managed to maintain phase information, and avoid beating interference after heterodyning and direct DCR detection through the presence of an additional intermediate frequency (IF) tone made available at CP. However, additional bandwidth is required to transmit IF tone for self-homodyning detection.

This chapter extends the previous ASK investigations to phase-sensitive data while maintaining bandwidth efficiency and relative phase noise tolerant without IF pilot tone. We propose the use of differential encoding and baseband optical modulation for millimeter-wave RoF link. The proposed method is demonstrated in this chapter using an optical baseband modulated DPSK system and is extended to include an optical baseband DQPSK system in Chapter 4. While it is possible for the proposed method to be implemented in high-order modulations such as Differential QAM, it is not the focus of this thesis and can be explored in the future. During demodulation of a differential encoded signal such as DPSK, the actual bit is recovered using the received signal with a delayed version of the received signal. Hence, the phase noise can be reduced through multiplication of the received signal and the delayed signal. Therefore, an IF tone is no longer required at CP and thus increases overall bandwidth efficiency. The proposed model is compared with two different RoF links: a Mach-Zehnder interferometer (MZI) demodulated DPSK RoF link, and a conventional OSSB+C RoF link. The proposed model is analyzed through theoretical analysis and software simulations.

The main contributions of this chapter are as follows:

- Develop a theoretical analysis of differential encoding in RoF links using optical baseband DPSK modulation
- Increase overall spectral efficiency through incoherent detection without the need of IF tone for phase noise tolerant receiver.

In this chapter, the theoretical analysis of the proposed optical DPSK RoF scheme and the alternative optical demodulated DPSK scheme are provided in section 3.2. Section 3.3 presents the theory of operation of a conventional phase-locked RoF link. The simulation results and system performance comparison between the proposed optical DPSK scheme, optical demodulated DPSK scheme, and conventional phase-locked RoF link are provided in section 3.4. Section 3.5 summarizes the chapter.

3.2 Proposed DPSK Millimeter-wave Radio-over-Fiber Schemes

In this section, two DPSK schemes using differential encoding and baseband optical modulation are presented. The two schemes are the following:

- Proposed Optical DPSK Scheme (Scheme A)
- Optical Demodulated DPSK Scheme (Scheme B)

The two schemes share the same optical transmission configuration while having different BS and CP configurations. In Scheme A, the DPSK signal is demodulated and downconverted to baseband at the CP. However, in Scheme B, the DPSK signal is converted to OOK at the BS and downconverted to baseband at the CP.

3.2.1 Proposed Optical DPSK Scheme

Fig. 3.2 shows the configuration of the proposed optical baseband DPSK modulated millimeter-wave RoF scheme (Scheme A) for downlink communication that employs an electrical delay-and-multiply (DAM) type DPSK receiver at the CP to demodulate data asynchronously. Fig. 3.3 shows the optical and radio frequency spectra of the signal at points stated in Fig. 3.2.

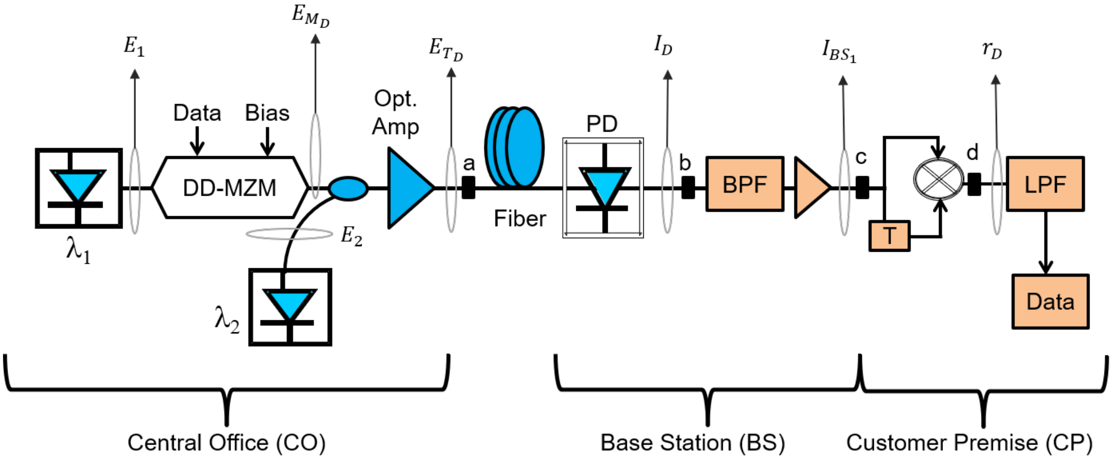

FIGURE 3.2: Optical Modulated OSSB+C NRZ-DPSK RoF

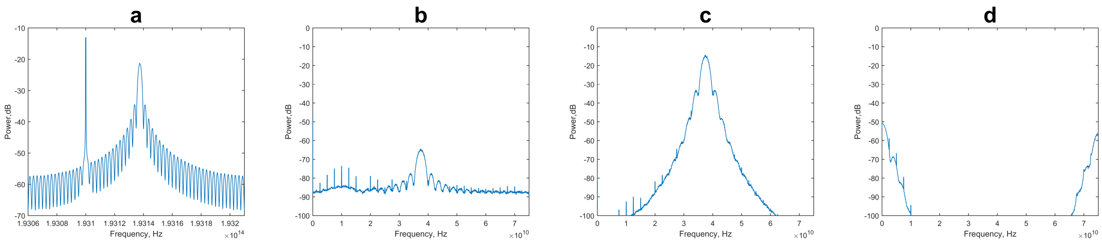

FIGURE 3.3: Optical spectrum of at point a; RF spectra at respective points b to d shown in Fig. 3.2

The structure of the DAM receiver is similar to an SH receiver. In an SH receiver, the received signal at millimeter-wave range is downconverted to baseband through self-multiplication. In a DAM receiver, the received signal is demodulated from DPSK to OOK and downconverted to baseband through multiplying the received signal with a delayed version of the received signal. Comparing the DAM receiver shown in Fig. 3.2 and the SH receiver shown in Fig. 3.1, the DAM receiver has an additional time delay at one of the arm. The proposed DAM receiver should remain relatively tolerant to phase noise compared to LO-based receivers without the need for an additional phase-locked loop for synchronization [12]. As shown in Fig. 3.2, the optical tone from the first laser will be modulated with DPSK encoded data using a dual-drive Mach-Zehnder modulator (DD-MZM). The output signal from the DD-MZM will be coupled with the output optical tone from the second laser. An optical amplifier will be used to amplify the coupled signal before fiber transmission. The output signal from the fiber is received at the BS and directly detected using a photodiode. The received signal will undergo optical heterodyning to produce a millimeter-wave signal with a frequency equivalent to the two optical sources' frequency difference. Before RF transmission from the BS, the signal is filtered and amplified. At CP, the received signal from BS will be demodulated from DPSK to OOK and downconverted to baseband using the proposed DAM receiver.

Given the output of two lasers and modulator used is represented by

$$E_1(t) = e^{j(\omega_1 t+\phi_{1l}(t))} \tag{3.1}$$

$$E_2(t) = e^{j(\omega_2 t+\phi_{2l}(t))} \tag{3.2}$$

$$E_{M_D}(t) = \frac{E_{in}(t)}{10^{\frac{l_i}{20}}}\left[\gamma e^{j(\frac{\pi v_2(t)}{V_{\pi RF}}+\frac{\pi v_{bias2}}{V_{\pi DC}})} + (1-\gamma)e^{j(\frac{\pi v_1(t)}{V_{\pi RF}}+\frac{\pi v_{bias1}}{V_{\pi DC}})}\right] \tag{3.3}$$

where:
- $E_1(t)$ and $E_2(t)$ are the lasers used shown in Fig. 3.2
- ω_1 and ω_2 are the angular frequency of the lasers.
- $\phi_{1l}(t)$ and $\phi_{2l}(t)$ are the phase noise representation of the lasers. As the lasers used are not phase-locked, separate notations are used.
- $E_{M_D}(t)$ is the output equation for a dual arm MZM (or DD-MZM) [194–196].
- $E_{in}(t)$ is the input optical signal to a MZM.
- l_i is the parameter insertion loss
- $v_1(t)$ and $v_2(t)$ are the input electrical signal voltages for the upper and lower modulator arms respectively.
- v_{bias1} and v_{bias2} are the biasing voltage driving the two MZM arms.
- $V_{\pi RF}$ is the switching modulation voltage.
- $V_{\pi DC}$ is the switching bias voltage.
- γ is the power splitting ratio between the two MZM arms, and it is given by:

$$\gamma = \frac{(1-\frac{1}{\sqrt{\epsilon_r}})}{2} \tag{3.4}$$

$$\epsilon_r = 10^{\frac{r_e}{10}} \tag{3.5}$$

where r_e is the extinction ratio of the MZM to turn the modulator on or off.

Assuming that the signal is transmitted in the form of non-return-zero (NRZ) DPSK, only one dual drive MZM is used with $v_1(t) = v_2(t)$, and assuming $v_{bias1} = v_{bias2}$ and

$\gamma = \frac{1}{2}$. The output of the modulator for Scheme A can be represented by

$$E_{M_D}(t) = \frac{E_{in}(t)}{10^{\frac{l_i}{20}}} \left[e^{j(\frac{\pi v_2(t)}{V_{\pi RF}} + \frac{\pi v_{bias2}}{V_{\pi DC}})} \right] \tag{3.6}$$

If $E_1(t)$ is the MZM input and $s_D(t)$ is the electrical DPSK signal, equation (3.6) can be rewritten as

$$\begin{aligned} E_{M_D}(t) &= \frac{E_1(t)}{10^{\frac{l_i}{20}}} \left[e^{j(\frac{\pi s_D(t)}{V_{\pi RF}} + \frac{\pi v_{bias2}}{V_{\pi DC}})} \right] \\ &= \frac{e^{j(\omega_1 t + \phi_{1l}(t))}}{10^{\frac{l_i}{20}}} \left[e^{j(\frac{\pi s_D(t)}{V_{\pi RF}} + \frac{\pi v_{bias2}}{V_{\pi DC}})} \right] \\ &= \frac{e^{j(\omega_1 t + \frac{\pi s_D(t)}{V_{\pi RF}} + \phi_{1l}(t) + \frac{\pi v_{bias2}}{V_{\pi DC}})}}{10^{\frac{l_i}{20}}} \\ &= A_1 e^{j(\omega_1 t + \frac{\pi s_D(t)}{V_{\pi RF}} + \phi_1(t))} \end{aligned} \tag{3.7}$$

where $A_1 = \frac{1}{10^{\frac{l_i}{20}}}$ and $\phi_1(t) = \phi_{1l}(t) + \frac{\pi v_{bias2}}{V_{\pi DC}}$.

Since optical baseband modulation is used, the output of the MZM only contains a single optical tone centered around the operating frequency of the laser ($E_1(t)$) used. In RoF, millimeter-wave RF signals are generated through heterodyning of optical tones at the photodiode. Therefore, the output of the DD-MZM is coupled with a second laser using a 3 dB optical coupler to generate an OSSB+C signal.

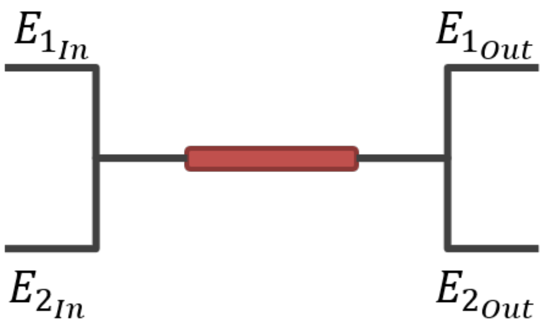

FIGURE 3.4: Optical Coupler

Fig. 3.4 shows an optical coupler, where the output of the coupler can be represented as follows [197, 198]:

$$E_{coupler} = \begin{bmatrix} E_{1_{Out}} \\ E_{2_{Out}} \end{bmatrix} = \alpha \begin{bmatrix} \sqrt{1-c} & pj\sqrt{1-c} \\ pj\sqrt{1-c} & \sqrt{1-c} \end{bmatrix} \begin{bmatrix} E_{1_{In}} \\ E_{2_{In}} \end{bmatrix} \tag{3.8}$$

$$E_{coupler} = \begin{bmatrix} E_{1_{Out}} \\ E_{2_{Out}} \end{bmatrix} = \alpha \begin{bmatrix} \sqrt{\frac{1}{2}} & -j\sqrt{\frac{1}{2}} \\ -j\sqrt{\frac{1}{2}} & \sqrt{\frac{1}{2}} \end{bmatrix} \begin{bmatrix} E_{1_{In}} \\ E_{2_{In}} \end{bmatrix} \tag{3.9}$$

where:

- $E_{1_{In}(t)}$ and $E_{2_{In}(t)}$ are the inputs of the optical coupler
- $E_{1_{Out}(t)}$ and $E_{2_{Out}(t)}$ represent the outputs of the optical coupler
- α is the insertion loss of the coupler
- c being the coupling coefficient. Since a 3 dB coupler is used, $c = 0.5$
- p controls the phase difference between the two outputs of the coupler at $\pm 90\,\mathrm{deg}$

$$\begin{aligned}
\begin{bmatrix} E_{1_{Out}} \\ E_{2_{Out}} \end{bmatrix} &= \alpha \begin{bmatrix} \sqrt{\frac{1}{2}} & -j\sqrt{\frac{1}{2}} \\ -j\sqrt{\frac{1}{2}} & \sqrt{\frac{1}{2}} \end{bmatrix} \begin{bmatrix} E_{M_D}(t) \\ E_2(t) \end{bmatrix} \\
&= \alpha \begin{bmatrix} \sqrt{\frac{1}{2}} & -j\sqrt{\frac{1}{2}} \\ -j\sqrt{\frac{1}{2}} & \sqrt{\frac{1}{2}} \end{bmatrix} \begin{bmatrix} A_1 e^{j(\omega_1 t + \frac{\pi s_D(t)}{V_{\pi RF}} + \phi_1(t))} \\ e^{j(\omega_2 t + \phi_{2l}(t))} \end{bmatrix} \\
&= \alpha \begin{bmatrix} \sqrt{\frac{1}{2}}[A_1 e^{j(\omega_1 t + \frac{\pi s_D(t)}{V_{\pi RF}} + \phi_1(t))}] - j\sqrt{\frac{1}{2}}[e^{j(\omega_2 t + \phi_{2l}(t))}] \\ -j\sqrt{\frac{1}{2}}[A_1 e^{j(\omega_1 t + \frac{\pi s_D(t)}{V_{\pi RF}} + \phi_1(t))}] + \sqrt{\frac{1}{2}}[e^{j(\omega_2 t + \phi_{2l}(t))}] \end{bmatrix}
\end{aligned} \tag{3.10}$$

Letting $A_1 = 1$ for simplicity and assuming the signal transmitted from the CO is $E_{1_{Out}}$, the transmitted signal (in the form of an OSSB+C signal) from the CO can be represented as

$$\begin{aligned}
E_{T_D}(t) = E_{1_{Out}} &\propto e^{j(\omega_1 t + \frac{\pi s_D(t)}{V_{\pi RF}} + \phi_1(t))} - je^{j(\omega_2 t + \phi_{2l}(t))} \\
&\propto e^{j(\omega_1 t + \frac{\pi s_D(t)}{V_{\pi RF}} + \phi_1(t))} + e^{j(\omega_2 t + \phi_{2l}(t) + \frac{3}{2}\pi)} \\
&\propto e^{j(\omega_1 t + \frac{\pi s_D(t)}{V_{\pi RF}} + \phi_1(t))} + e^{j(\omega_2 t + \phi_2(t))}
\end{aligned} \tag{3.11}$$

where $\phi_2 = \phi_{2l} + \frac{3}{2}\pi$.

The optical signal is received by the photodiode at the base station, and the photocurrent output can be represented as :

$$\begin{aligned}
I_D(t) &\propto E_{T_D}(t) \times E^*_{T_D}(t) \\
I_D(t) &\propto 2 + 2\cos\left(2\pi f_{mm} t + \Delta\phi(t) + \frac{\pi s_D(t)}{V_{\pi RF}}\right)
\end{aligned} \tag{3.12}$$

Here, $E^*_{T_D}(t)$ is the conjugate of $E_{T_D}(t)$, f_{mm} is the millimeter-wave frequency where $2\pi f_{mm} = \omega_1 - \omega_2$, and $\Delta\phi(t)$ is the phase noise contributed by two laser source where $\Delta\phi(t) = \phi_1(t) - \phi_2(t)$. The signal will then be amplified and filtered before transmission from the BS, as shown in Fig. 3.2. The output signal from the BS can be represented by

$$I_{BS_1}(t) \propto 2\cos\left(2\pi f_{mm} t + \Delta\phi(t) + \frac{\pi s_D(t)}{V_{\pi RF}}\right) \tag{3.13}$$

In our proposed configuration, the received DPSK signal will be demodulated using a DAM receiver. After DAM receiver detection, the signal can be represented as

$$\begin{aligned}
r_D(t) &= I_{BS}(t) \times I_{BS}(\Delta t) \\
r_D(t) &\propto \cos\left(2\pi f_{mm}t + \Delta\phi(t) + \frac{\pi s_D(t)}{V_{\pi RF}}\right) \times \\
&\quad \cos\left(2\pi f_{mm}\Delta t + \Delta\phi(\Delta t) + \frac{\pi s_D(\Delta t)}{V_{\pi RF}}\right) \\
&\propto \cos\left(2\pi f_{mm}t + \Delta\phi(t) + \frac{\pi s_D(t)}{V_{\pi RF}}\right) \times \\
&\quad \cos\left(2\pi f_{mm}\Delta t + \phi_d(\Delta t) + \frac{\pi s_D(\Delta t)}{V_{\pi RF}}\right)
\end{aligned} \tag{3.14}$$

The term Δt is the shifted time; it can be represented by $t - \tau_1$ where τ_1 is a bit time. The delayed phase noise is defined as $\Delta\phi(\Delta t) = \phi_d(\Delta t)$. After lowpass filtering, the signal before sampling $Y(t)$ will be:

$$Y(t) \;\propto\; \cos\left(2\pi f_{mm}\tau_1 + \frac{\pi}{V_{\pi RF}}[s_D(t) - s_D(\Delta t)] + \Delta\phi(t) - \phi_d(\Delta t)\right) \tag{3.15}$$

As shown in equation (3.15), the DAM receiver reduces phase noise through subtracting the phase noise inherited from the optical transmission system ($\Delta\phi(t)$) with its delayed version ($\phi_d(\Delta t)$). The phase noise residual after subtraction is denoted as $\phi_r(t)$ where $\phi_r(t) = \Delta\phi(t) - \phi_d(\Delta t)$. If the phase fluctuation between time t and Δt increase, there will be an increase in phase noise residual $\phi_r(t)$. The increase in $\phi_r(t)$ will lead to a drop in detection accuracy. The effects of signal impairment due to phase noise residual is demonstrated and discussed in section 3.4.

3.2.2 Optical Demodulated DPSK Scheme

Fig. 3.5 and Fig. 3.6 presents an alternative DPSK scheme (Scheme B) and the optical and RF spectra at respective points. In Scheme B, the DPSK signal is demodulated to OOK using an MZI at the BS and downconverted to baseband using DCR at CP. This scheme simplifies the receiver by replacing DAM with DCR while maintaining the advantage of optical DPSK modulation over On-Off-Keying (OOK) optical modulation.

Since the configuration of the CO is the same for both schemes, the transmission signal can be represented by equation (3.11). At the BS, the received optical signal will pass through an MZI, with its outputs being denoted by $E_3(t)$ and $E_4(t)$, to be converted from DPSK to OOK. As DPSK and OOK transmit the same number of bits per symbol, the overall bandwidth efficiency will not be affected. An MZI can be composed of two optical couplers, and an optical delay line [197, 198]. In this case, the MZI transfer function can

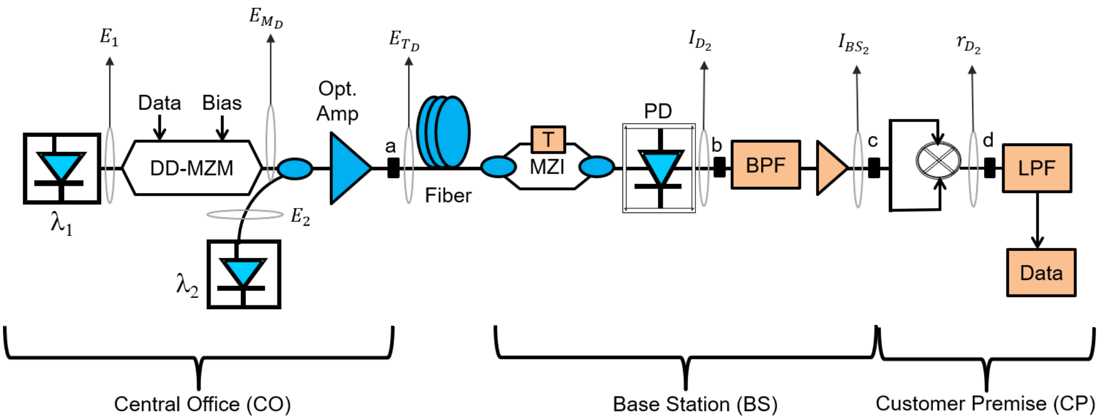

FIGURE 3.5: Alternative Optical demodulated DPSK RoF

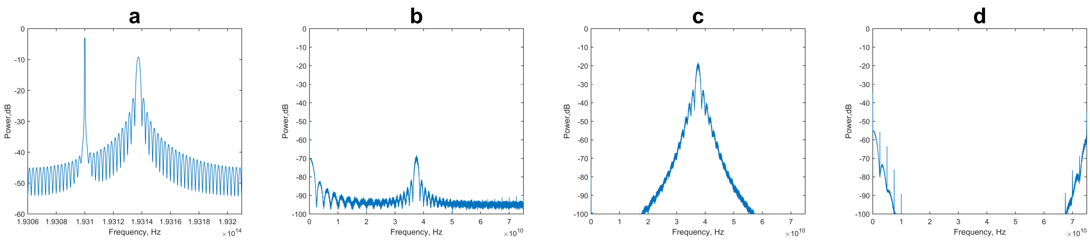

FIGURE 3.6: Optical spectrum of at point a; RF spectra at respective points b to d shown in Fig. 3.5

be obtained by cascading each optical coupler and optical delay line's transfer function.

$$H_I = H_c.\, H_d.\, H_c$$

$$H_c = \begin{bmatrix} \sqrt{0.5} & -j\sqrt{0.5} \\ -j\sqrt{0.5} & \sqrt{0.5} \end{bmatrix} \tag{3.16}$$

$$H_d = \begin{bmatrix} e^{-j2\pi f\tau} & 0 \\ 0 & 1 \end{bmatrix} \tag{3.17}$$

$$\begin{aligned} H_I &= \begin{bmatrix} \sqrt{0.5} & -j\sqrt{0.5} \\ -j\sqrt{0.5} & \sqrt{0.5} \end{bmatrix} \begin{bmatrix} e^{-j2\pi f\tau} & 0 \\ 0 & 1 \end{bmatrix} \begin{bmatrix} \sqrt{0.5} & -j\sqrt{0.5} \\ -j\sqrt{0.5} & \sqrt{0.5} \end{bmatrix} \\ &= \begin{bmatrix} \sqrt{0.5}\; e^{-j2\pi f\tau} & -j\sqrt{0.5} \\ -j\sqrt{0.5}\; e^{-j2\pi f\tau} & \sqrt{0.5} \end{bmatrix} \begin{bmatrix} \sqrt{0.5} & -j\sqrt{0.5} \\ -j\sqrt{0.5} & \sqrt{0.5} \end{bmatrix} \\ &= \begin{bmatrix} 0.5\; e^{-j2\pi f\tau} - 0.5 & -j0.5\; e^{-j2\pi f\tau} - j0.5 \\ -j0.5\; e^{-j2\pi f\tau} - j0.5 & -0.5\; e^{-j2\pi f\tau} + 0.5 \end{bmatrix} \\ &= \frac{1}{2} \begin{bmatrix} e^{-j2\pi f\tau} - 1 & -je^{-j2\pi f\tau} - j \\ -je^{-j2\pi f\tau} - j & -e^{-j2\pi f\tau} + 1 \end{bmatrix} \end{aligned} \tag{3.18}$$

with H_I representing the transfer function of MZI, H_d representing the transfer function of the optical delay line, and H_c representing the transfer function of the optical coupler. By obtaining H_I, output of the MZI can be represented by:

$$
\begin{aligned}
E_I &= \begin{bmatrix} E_3(t) \\ E_4(t) \end{bmatrix} = H_I \begin{bmatrix} E_{1_{in}}(t) \\ 0 \end{bmatrix} \\
E_I &= \begin{bmatrix} E_3(t) \\ E_4(t) \end{bmatrix} = \frac{1}{2} \begin{bmatrix} e^{-j2\pi f\tau} - 1 & -je^{-j2\pi f\tau} - j \\ -je^{-j2\pi f\tau} - j & -e^{-j2\pi f\tau} + 1 \end{bmatrix} \begin{bmatrix} E_{1_{in}}(t) \\ 0 \end{bmatrix} \\
\begin{bmatrix} E_3(t) \\ E_4(t) \end{bmatrix} &= \frac{1}{2} \begin{bmatrix} e^{-j2\pi f\tau} - 1 & -je^{-j2\pi f\tau} - j \\ -je^{-j2\pi f\tau} - j & -e^{-j2\pi f\tau} + 1 \end{bmatrix} \begin{bmatrix} E_{1_{in}}(t) \\ 0 \end{bmatrix} \\
&= \frac{1}{2} \begin{bmatrix} E_{1_{in}}(t)\left(e^{-j2\pi f\tau} - 1\right) \\ E_{1_{in}}(t)\left(-je^{-j2\pi f\tau} - j\right) \end{bmatrix}
\end{aligned} \tag{3.19}
$$

Using $\mathcal{F}\{g(t-\tau)\} = e^{-j2\pi f\tau}G(f)$ where $\tau = \tau_1$, equation (3.19) can be rewritten as

$$
\begin{bmatrix} E_3(t) \\ E_4(t) \end{bmatrix} = \frac{1}{2} \begin{bmatrix} E_{1_{in}}(t-\tau_1) - E_{1_{in}}(t) \\ e^{-j\frac{1}{2}\pi} E_{1_{in}}(t-\tau_1) + e^{-j\frac{1}{2}\pi} E_{1_{in}}(t) \end{bmatrix} \tag{3.20}
$$

Let $\Delta t = t - \tau_1$, and substituting equation (3.11), equation (3.20) can be rewritten as:

$$
E_3(t) = \frac{1}{2}\left(\begin{array}{c} e^{j(2\pi f_1 \Delta t + \phi_1(\Delta t) + \frac{\pi s_D(\Delta t)}{V_{\pi RF}})} + e^{j(2\pi f_2 \Delta t + \phi_2(\Delta t))} - \\ e^{j(2\pi f_1 t + \phi_1(t) + \frac{\pi s_D(t)}{V_{\pi RF}})} - e^{j(2\pi f_2 t + \phi_2(t))} \end{array} \right) \tag{3.21}
$$

$$
E_4(t) = \frac{1}{2}\left(\begin{array}{c} e^{j(2\pi f_1 \Delta t + \phi_1(\Delta t) + \frac{\pi s_D(\Delta t)}{V_{\pi RF}} + \frac{3}{2}\pi)} + e^{j(2\pi f_2 \Delta t + \phi_2(\Delta t) + \frac{3}{2}\pi)} - \\ e^{j(2\pi f_1 t + \phi_1(t) + \frac{\pi s_D(t)}{V_{\pi RF}} + \frac{3}{2}\pi)} - e^{j(2\pi f_2 t + \phi_2(t) + \frac{3}{2}\pi)} \end{array} \right) \tag{3.22}
$$

Here, τ_1 is the time delay introduced by the MZI. Assuming $E_4(t)$ is being detected, the output signal from the photodetector can be:

$$
\begin{aligned}
I_{D2}(t) \propto\ & 2 + \cos(2\pi f_{mm} t + \frac{\pi s_D(t)}{V_{\pi_{RF}}} + \Delta\phi(t)) + \\
& \cos(2\pi f_1 \tau_1 + \frac{\pi s_D(t)}{V_{\pi_{RF}}} - \frac{\pi s_D(\Delta t)}{V_{\pi_{RF}}} + \phi_1(t) - \phi_1(\Delta t)) + \\
& \cos(2\pi f_{mm} t + 2\pi f_2 \tau_1 + \frac{\pi s_D(t)}{V_{\pi_{RF}}} + \phi_1(t) - \phi_2(\Delta t)) + \\
& \cos(2\pi f_2 \tau_1 + \phi_2(t) - \phi_2(\Delta t)) + \cos(2\pi f_{mm} \Delta t + \frac{\pi s_D(\Delta t)}{V_{\pi_{RF}}} + \phi_d(\Delta t)) + \\
& \cos(-2\pi f_{mm} t + 2\pi f_1 \tau_1 - \frac{\pi s_D(\Delta t)}{V_{\pi_{RF}}} + \phi_2(t) - \phi_1(\Delta t))
\end{aligned} \tag{3.23}
$$

Before tranmitting out of the BS, the signal will be filtered and amplified. The output signal from the BS can be represented as

$$
\begin{aligned}
I_{BS_2}(t) \quad \propto \quad & \cos(2\pi f_{mm}t + \frac{\pi s_D(t)}{V_{\pi_{RF}}} + \Delta\phi(t)) + \\
& \cos(2\pi f_{mm}t + 2\pi f_2\tau_1 + \frac{\pi s_D(t)}{V_{\pi_{RF}}} + \phi_1(t) - \phi_2(\Delta t)) + \\
& \cos(-2\pi f_{mm}t + 2\pi f_1\tau_1 - \frac{\pi s_D(\Delta t)}{V_{\pi_{RF}}} + \phi_2(t) - \phi_1(\Delta t)) + \\
& \cos(2\pi f_{mm}\Delta t + \frac{\pi s_D(\Delta t)}{V_{\pi_{RF}}} + \phi_d(\Delta t))
\end{aligned}
\tag{3.24}
$$

At the CP, the received millimeter-wave signal will be downconverted to baseband using DCR. The signal after DCR detection can be represented by

$$
\begin{aligned}
r_{D2}(t) \quad &= \quad I^2_{BS_2} \\
r_{D2}(t) \quad &\propto \quad \cos(A)^2 + \cos(B)^2 + \cos(C)^2 + \cos(D)^2 + 2\cos(A)\cos(B) + \\
& \quad 2\cos(A)\cos(C) + 2\cos(B)\cos(C) + 2\cos(A)\cos(D) + 2\cos(B)\cos(D) + \\
& \quad 2\cos(C)\cos(D)
\end{aligned}
\tag{3.25}
$$

where

$$
\begin{aligned}
A &= 2\pi f_{mm}t + \frac{\pi s_D(t)}{V_{\pi_{RF}}} + \Delta\phi(t) \\
B &= 2\pi f_{mm}t + 2\pi f_2\tau_1 + \frac{\pi s_D(t)}{V_{\pi_{RF}}} + \phi_1(t) - \phi_2(\Delta t) \\
C &= -2\pi f_{mm}t + 2\pi f_1\tau_1 - \frac{\pi s_D(\Delta t)}{V_{\pi_{RF}}} + \phi_2(t) - \phi_1(\Delta t) \\
D &= 2\pi f_{mm}\Delta t + \frac{\pi s_D(\Delta t)}{V_{\pi_{RF}}} + \phi_d(\Delta t)
\end{aligned}
$$

Full derivation to obtain the baseband signal $Y_2(t)$ from equation (3.25) is shown in Appendix A.1. After lowpass filtering and simplifying equation (A.3), the baseband signal $Y_2(t)$ can be represented as

$$\begin{aligned} Y_2(t) \propto\ & 2 + 2\cos(\phi_2(\Delta t) - \phi_2(t) - 2\pi f_2 \tau_1) \\ & + \cos(\phi_1(t) - \phi_1(\Delta t) + \frac{\pi s_D(t)}{V_{\pi_{RF}}} + 2\pi f_1 \tau_1 - \frac{\pi s_D(\Delta t)}{V_{\pi_{RF}}}) \\ & + \cos(\phi_1(t) - \phi_2(\Delta t) + \phi_2(t) - \phi_1(\Delta t) + \frac{\pi s_D(t)}{V_{\pi_{RF}}} + 2\pi f_2 \tau_1 + 2\pi f_1 \tau_1 - \\ & \quad \frac{\pi s_D(\Delta t)}{V_{\pi_{RF}}}) \\ & + \cos(\Delta\phi(t) - \phi_d(\Delta t) + \frac{\pi s_D(t)}{V_{\pi_{RF}}} - \frac{\pi s_D(\Delta t)}{V_{\pi_{RF}}} + 2\pi f_{mm} \tau_1) \\ & + \cos(\phi_1(t) - \phi_1(\Delta t) + \frac{\pi s_D(t)}{V_{\pi_{RF}}} + 2\pi f_2 \tau_1 - \frac{\pi s_D(\Delta t)}{V_{\pi_{RF}}} + 2\pi f_{mm} \tau_1) \end{aligned} \tag{3.26}$$

The phase noise propagated from the optical transmitter is converted into additive noise, as shown in the second term of equation (3.26). If the phase fluctuation between time t and time Δt increases, the baseband signal of Scheme B will not only be impaired by the increased phase noise, but also the converted additive noise. Comparing the received baseband signal of Scheme A (equation (3.15)) and Scheme B (equation (3.26)), the additive noise term is not present in baseband signal of Scheme A. Therefore, Scheme B may have a lower detection accuracy compared to Scheme A at the same level of phase noise.

3.3 Conventional Phase Locked Optical DPSK Link

In this section, a theory of operation is provided on a conventional phase-locked RoF link. In a phase-locked millimeter-wave RoF OSSB+C optical DPSK link (Scheme C), the optical tones used are phase-locked. Hence contrary to (3.11), the output signal from the CO can be represented as

$$E_{1_{Out}} \propto e^{j(\omega_1 t + v_{mm}(t) + \phi_1(t))} + e^{j(\omega_1 t + \phi_1(t))} \tag{3.27}$$

where $v_{mm}(t)$ is the millimeter-wave DPSK signal. Correlated phase-locked optical tones can be generated through conventional method using high-speed millimeter-wave oscillators and MZMs, as shown in [199], or frequency quadrupling method shown in [139]. Conventionally, an OSSB+C signal can be generated using a dual-parallel MZM, as shown in Fig. 3.7. The biasing voltages supplied to the DPMZM are used to bias the MZM and control the phase difference between the two MZM outputs within the DPMZM. However, the simulator used for the experiment does not have a dual-parallel MZM. Hence, the OSSB+C signal is generated using two single drive MZM, two optical couplers with a 90 deg phase difference between two output ports, and a phase shifter of −90 deg to mimic a DPMZM, as shown in Fig. 3.8. Therefore, a theoretical analysis is carried out to ensure the individual components used to mimic a DPMZM can generate OSSB+C signals. The alternative shown in [200] simplifies the overall configuration by using only a single dual-drive MZM, but the unwanted sideband suppression ratio is lower than the conventional method. A lower suppression ratio would lead to a drop in system performance due to higher dispersion.

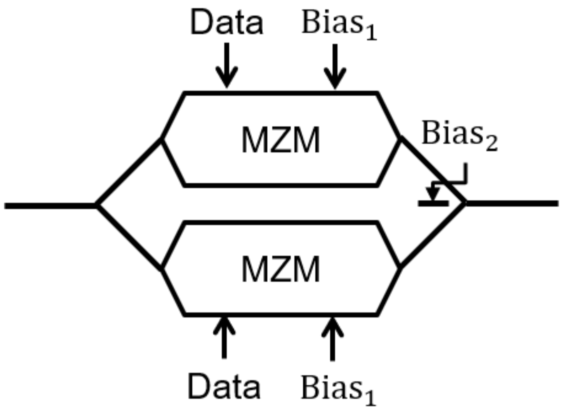

FIGURE 3.7: DPMZM

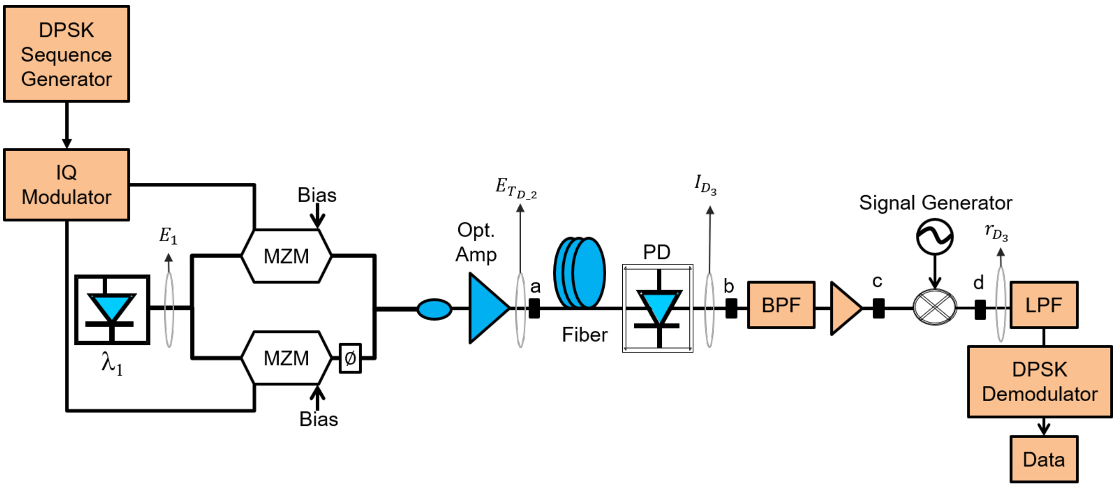

FIGURE 3.8: Conventional DPSK RoF Link

As shown in Fig. 3.8, the laser output is divided using a 3dB optical coupler. Using equation (3.8), the output of the first optical coupler can be represented by

$$
\begin{aligned}
E_{coupler_1} = \begin{bmatrix} E_{1_{Out}} \\ E_{2_{Out}} \end{bmatrix} &= \alpha \begin{bmatrix} \sqrt{\frac{1}{2}} & j\sqrt{\frac{1}{2}} \\ j\sqrt{\frac{1}{2}} & \sqrt{\frac{1}{2}} \end{bmatrix} \begin{bmatrix} E_{1_{In}} \\ E_{2_{In}} \end{bmatrix} \\
= \begin{bmatrix} E_{1_{Out}} \\ E_{2_{Out}} \end{bmatrix} &= \alpha \begin{bmatrix} \sqrt{\frac{1}{2}} & j\sqrt{\frac{1}{2}} \\ j\sqrt{\frac{1}{2}} & \sqrt{\frac{1}{2}} \end{bmatrix} \begin{bmatrix} E_{1_{In}} \\ 0 \end{bmatrix} \\
= \begin{bmatrix} E_{1_{Out}} \\ E_{2_{Out}} \end{bmatrix} &= \begin{bmatrix} \alpha\sqrt{\frac{1}{2}}E_{1_{In}} \\ \alpha j\sqrt{\frac{1}{2}}E_{1_{In}} \end{bmatrix}
\end{aligned}
\tag{3.28}
$$

The outputs of the optical coupler are modulated using two single drive MZM. The output signal of the single drive MZM can be represented by [134]

$$
E_{mod}(t) = \alpha_2 E_{in}(t)[1 + as(t)] \tag{3.29}
$$

where α_2 is the modulation index of the modulator with $a = \frac{\pi}{V_\pi}$. The output of the first modulator is

$$
\begin{aligned}
E_{mod_1}(t) &= \alpha_2\sqrt{\frac{1}{2}}E_{1_{In}}(t)[1 + as_1(t)] \\
&= \alpha_2\sqrt{\frac{1}{2}}E_{1_{In}}(t)[1 + a\cos(2\pi f_{mm}t + \phi_s(t))] \\
&= \alpha_2\sqrt{\frac{1}{2}}E_{1_{In}}(t)[1 + a\frac{1}{2}(e^{j(2\pi f_{mm}t+\phi_s(t))} + e^{-j(2\pi f_{mm}t+\phi_s(t))})]
\end{aligned}
\tag{3.30}
$$

where $s_1(t) = \cos(2\pi f_{mm}t + \phi_s(t))$ is the modulating signal, and $\phi_s(t)$ is the phase change caused by DPSK modulation. The output of the second modulator is

$$
\begin{aligned}
E_{mod_2}(t) &= \alpha_2 j\sqrt{\frac{1}{2}}E_{1_{In}}(t)[1 + as_2(t)] \\
&= \alpha_2 j\sqrt{\frac{1}{2}}E_{1_{In}}(t)[1 + a\cos(2\pi f_{mm}t + \phi_s(t) + \frac{\pi}{2})] \\
&= \alpha_2 j\sqrt{\frac{1}{2}}E_{1_{In}}(t)[1 - a\sin(2\pi f_{mm}t + \phi_s(t))] \\
&= \alpha_2 j\sqrt{\frac{1}{2}}E_{1_{In}}(t)[1 - a\frac{1}{2j}(e^{j(2\pi f_{mm}t+\phi_s(t))} - e^{-j(2\pi f_{mm}t+\phi_s(t))})]
\end{aligned}
\tag{3.31}
$$

The output of the second modulator is phase shifted by $-90\,\deg$ before coupling with the output of the first modulator using an optical coupler. The output representation of the second optical coupler is

$$\begin{aligned}
E_{coupler_2} = \begin{bmatrix} E_{1_{Out}} \\ E_{2_{Out}} \end{bmatrix} &= \alpha \begin{bmatrix} \sqrt{\frac{1}{2}} & j\sqrt{\frac{1}{2}} \\ j\sqrt{\frac{1}{2}} & \sqrt{\frac{1}{2}} \end{bmatrix} \begin{bmatrix} E_{mod_1}(t) \\ -jE_{mod_2}(t) \end{bmatrix} \\
= \begin{bmatrix} E_{1_{Out}} \\ E_{2_{Out}} \end{bmatrix} &= \alpha \begin{bmatrix} \sqrt{\frac{1}{2}}E_{mod_1}(t) + \sqrt{\frac{1}{2}}E_{mod_2}(t) \\ j\sqrt{\frac{1}{2}}E_{mod_1}(t) - j\sqrt{\frac{1}{2}}E_{mod_2}(t) \end{bmatrix}
\end{aligned} \tag{3.32}$$

Assuming $E_{1_{Out}}$ is transmitted from the CO, the signal output from CO can be represented by

$$\begin{aligned}
E_{T_{D_2}} = E_{1_{Out}} &= \alpha\sqrt{\frac{1}{2}}(E_{mod_1} + E_{mod_2}) \\
&= \alpha\alpha_2\frac{1}{2}E_{1_{In}}(t)(1 + a\frac{1}{2}(e^{j(2\pi f_{mm}t+\phi_s(t))} + e^{-j(2\pi f_{mm}t+\phi_s(t))}) \\
&\quad +j[1 - a\frac{1}{2j}(e^{j(2\pi f_{mm}t+\phi_s(t))} - e^{-j(2\pi f_{mm}t+\phi_s(t))})]) \\
&= \alpha\alpha_2\frac{1}{2}E_{1_{In}}(t)([1+j] + ae^{-j(2\pi f_{mm}t+\phi_s(t))}) \\
&= \alpha\alpha_2\frac{1}{2}([1+j]e^{j(\omega_1 t+\phi_{1l}(t))} + ae^{j(\omega_1 t-2\pi f_{mm}t-\phi_s(t)+\phi_{1l}(t))}) \\
&= \alpha\alpha_2\frac{1}{2}(\sqrt{2}[e^{j\frac{\pi}{4}}]e^{j(\omega_1 t+\phi_{1l}(t))} + ae^{j(\omega_1 t-2\pi f_{mm}t-\phi_s(t)+\phi_{1l}(t))}) \\
&= \alpha\alpha_2\frac{1}{\sqrt{2}}e^{j(\omega_1 t+\phi_{1l}(t)+\frac{\pi}{4})} + \alpha\alpha_2\frac{1}{2}ae^{j(\omega_1 t-2\pi f_{mm}t-\phi_s(t)+\phi_{1l}(t))} \\
&= C_1e^{j(\omega_1 t+\phi_{1l}(t)+\frac{\pi}{4})} + D_1e^{j(\omega_1 t-2\pi f_{mm}t-\phi_s(t)+\phi_{1l}(t))}
\end{aligned} \tag{3.33}$$

where $C_1 = \alpha\alpha_2\frac{1}{\sqrt{2}}$ and $D_1 = \alpha\alpha_2\frac{1}{2}a$. As the optical tones are phase locked, as shown in equation (3.33), during heterodyning detection at the photodiode, phase noise from the transmitter is reduced as opposed to unlocked heterodyning shown in equation (3.12). Hence, the signal output of the photodiode will be

$$\begin{aligned}
I_{D_3}(t) &\propto E_{T_{D_2}}(t) \times E^*_{T_{D_2}}(t) \\
I_{D_3}(t) &\propto 2 + 2cos(2\pi f_{mm}t + \phi_s(t) + \frac{\pi}{4})
\end{aligned} \tag{3.34}$$

where $E^*_{T_{D\_2}}(t)$ is the conjugate of $E_{T_{D\_2}}(t)$, and assuming $C = D$ for simplicity, and no optical fiber is present. Comparing the equation above with equation (3.12), it can be observed that the phase noise contributed by the transmitter is no longer present. However, this is based on the assumption that no fiber is present, and the optical tones generated stays coherent throughout the link before heterodyning detection at the photodiode. If the optical tones are no longer coherent, the photodiode's output signal will be similar to equation (3.12). The millimeter-wave DPSK signal is downconverted to baseband using an RF mixer and an RF oscillator operating at millimeter-wave frequency.

The downconverted signal is denoted as $r_{D_3}(t)$.

$$r_{D_3}(t) \quad \propto \quad cos(\phi_s(t) - \phi_{LO}(t)) \tag{3.35}$$

where $\phi_{LO}(t)$ represents the phase noise contributed by the RF oscillator. The baseband DPSK signal can be demodulated using a DPSK demodulator.

3.4 Experiment and Results

The performance of all three schemes are compared using varying levels of optical receiving power, phase noise, and relative intensity noise. In addition, validation tests comparing different signal formats of DPSK, and optical carrier-to-sideband power difference were carried out to optimize the performance of Scheme A and Scheme B. This section is arranged as follows. The simulation setup for all three schemes are provided in section 3.4.1. Validation tests and performance comparison between schemes are provide in section 3.4.2 and section 3.4.3 respectively.

3.4.1 Simulation Setup

All three schemes presented in section 3.2 and section 3.3 are modelled using *OptiSystem 16* software. For Scheme A and Scheme B, a free-running DFB laser operating at 193.1THz is externally modulated by dual-drive Mach-Zehnder Modulator (DD-MZM) with a differential encoded data generated by 2.5Gbps Pseudo Random Bit Sequence (PRBS) fed into an XOR gate with a one-bit delay feedback path. Another free-running optical LO laser operating at 193.1375 THz is coupled with the output of DD-MZM using a 3dB coupler. The linewidth of both lasers is set to 5 MHz, which corresponds to the linewidth found in low-cost laser diodes. The coupled signal is amplified and transported over a 25km single-mode fiber (SMF) to the BS. In Scheme A, received tones from the lasers are directly detected by a PD, and heterodyning occurs to generate a DPSK modulated millimeter-wave signal at 37.5GHz. An MZI is used before the PD in Scheme B with a delay equivalent to one-bit time. For all schemes, a 50-dB gain amplifier with a spectral density of noise current of $2.25 \times 10^{-11} \frac{A}{\sqrt{(Hz)}}$ and a 5GHz bandwidth Bessel bandpass filter centered around 37.5 GHz is used to amplify and filter the millimeter-wave signal.

For Scheme C, a single free-running laser operating at 193.1THz is modulated by a dual-parallel MZM (DP-MZM). The DP-MZM is modeled using two MZM, two optical couplers, and an optical phase change in *Optiwave*^{TM}. The DP-MZM generates an

OSSB+C signal as described in the section 3.3. Before the signal is transmitted, an optical filter is used to improve the optical carrier-to-sideband ratio (OCSR) from -22.742 dB to -11.4 dB. The BS configuration of Scheme C is similar to Scheme A. The 37.5 GHz millimeter-wave signal is downconverted at the receiver, using an oscillator-based receiver operating at the same frequency as the millimeter-wave signal. The DPSK signal is demodulated to OOK signal at the CP.

3.4.2 Validation Test

Optical carrier-to-sideband power difference has a major influence on system performance [201]. In Scheme C, an optical filter is used to improve OCSR. In Scheme A and Scheme B, optical tones are generated using two uncorrelated lasers; hence the optical carrier-to-sideband power difference can be controlled by varying the power of the lasers used. To optimize the performance of uncorrelated multi-optical source RoF, the power of the lasers are varied from -15 dBm to -5 dBm. The power difference is calculated between the MZM output signal power (P_{M1}) and the power of the second LO laser (P_{L2}), and is denoted by $\Delta P = P_{M1} - P_{L2}$. The fiber launch power is fixed at 0 dBm ± 0.001. The received power of Scheme A and Scheme B is fixed at -24 dBm ± 0.002 when $P_{M1} = P_{L2}$. Results for various ΔP are shown in Fig. 3.9 and Fig. 3.10. Based on the results obtained, the optimal point of operation is when $P_{M1} = P_{L2}$.

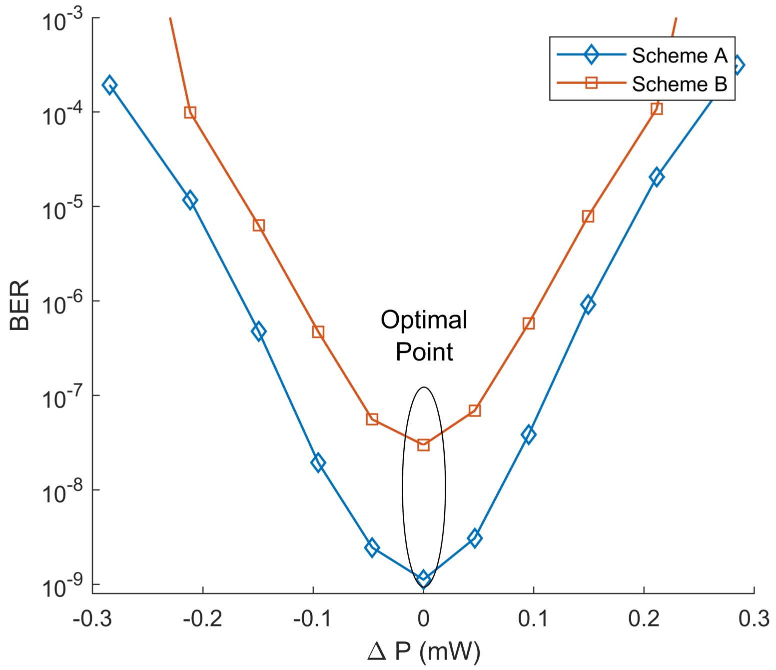

FIGURE 3.9: BER of Scheme A and Scheme B under different ΔP

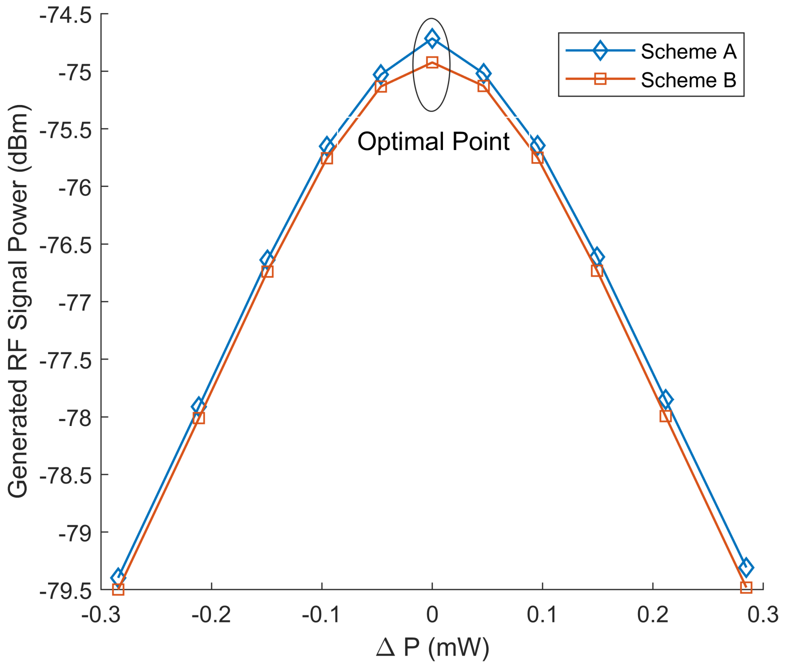

FIGURE 3.10: Generated RF power of Scheme A and Scheme B under different ΔP

Three different signal formats were tested on Scheme A and Scheme B: Return-to-zero (RZ) DPSK, carrier-suppressed return-to-zero (CSRZ) DPSK, and non-return-to-zero (NRZ) DPSK. RZ-DPSK and CSRZ-DPSK demonstrated in [202, 203] have shown lower BER over NRZ-DPSK against fiber nonlinearity, dispersion, and thermal noise in long-haul communication systems. However, both CSRZ-DPSK and RZ-DPSK utilize more bandwidth compared to NRZ-DPSK, and the fiber used in an RoF link is used as a last-mile connection to base stations, which are normally much shorter in length relative to fiber length used in long-haul communication. Hence, these three signal formats are compared in Scheme A and Scheme B to investigate the performance benefit of using RZ and CSRZ over NRZ in a relatively shorter fiber length RoF link.

Configurations of RZ-DPSK and CSRZ-DPSK for Scheme A and Scheme B are shown in Fig. 3.11. Comparing the configurations shown in Fig. 3.11, Fig. 3.2, and Fig. 3.5, two DD-MZM are required to generate RZ-DPSK and CSRZ-DPSK signals as opposed to one DD-MZM used for optical baseband NRZ-DPSK generation. An additional modulator is required for pulse shaping. For the RZ-DPSK setup, the first modulator has the same biasing and configuration as NRZ-DPSK, where both inputs of the DD-MZM are fed with the same data. As for CSRZ-DPSK, both arms have a 180-degree phase difference. The second DD-MZM for both RZ-DPSK and CSRZ-DPSK is fed by a signal generator, generating a sine wave at 1.25 GHz for CSRZ-DPSK, and a cosine wave at the same frequency for RZ-DPSK. Both arms of the second DD-MZM will have a 180-degree phase

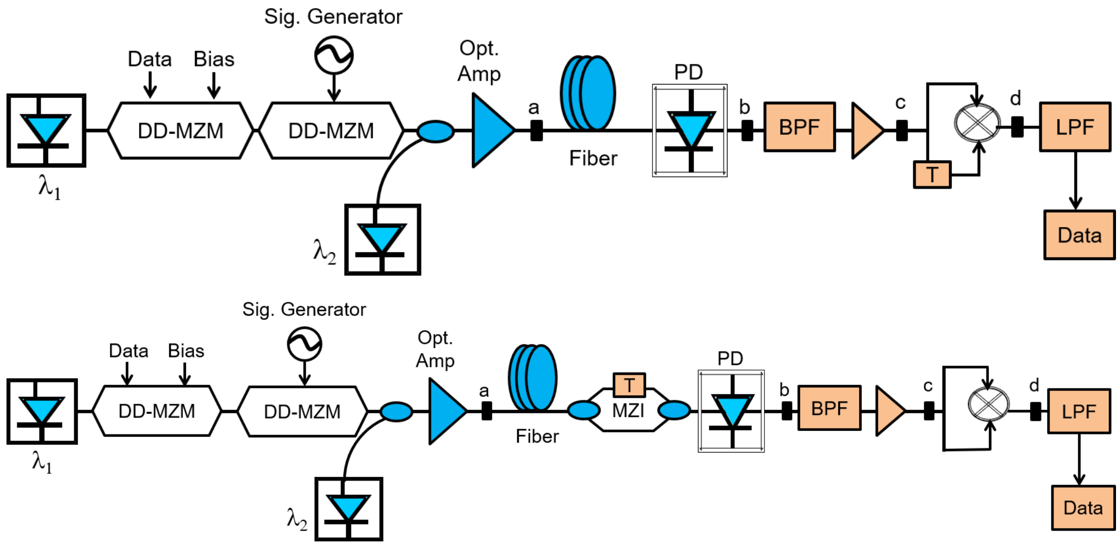

FIGURE 3.11: Configuration of RZ-DPSK and CSRZ-DPSK for Scheme A (top) and Scheme B (bottom)

difference. The output signal of the second DD-MZM is coupled with the output of the LO laser.

Fig. 3.12 shows the performance of 33% RZ-DPSK, CSRZ-DPSK, and NRZ-DPSK at different optical receiving power for Scheme A and Scheme B. As shown in the figure, for both Scheme A and Scheme B, RZ-DPSK performs the best, followed by NRZ-DPSK and CSRZ-DPSK. At BER of 10^{-9}, the performance of CSRZ-DPSK is similar to NRZ-DPSK. While CSRZ-DPSK performs better than NRZ-DPSK at lower BER rates, NRZ-DPSK performs better than CSRZ-DPSK at higher BER rates. Although the performance benefit of RZ-DPSK compared to NRZ-DPSK and CSRZ-DPSK is larger in Scheme B relative to Scheme A, it is still relatively small, at less than 1 dBm measured at 10^{-9} BER. The performance improvement comes at the cost of requiring twice the bandwidth and a relatively more complex transmission setup compared to NRZ-DPSK. In wireless communication, bandwidth is limited, and since both RZ-DPSK and CSRZ-DPSK provides minor performance benefit over NRZ-DPSK, only NRZ-DPSK is used for the consecutive tests.

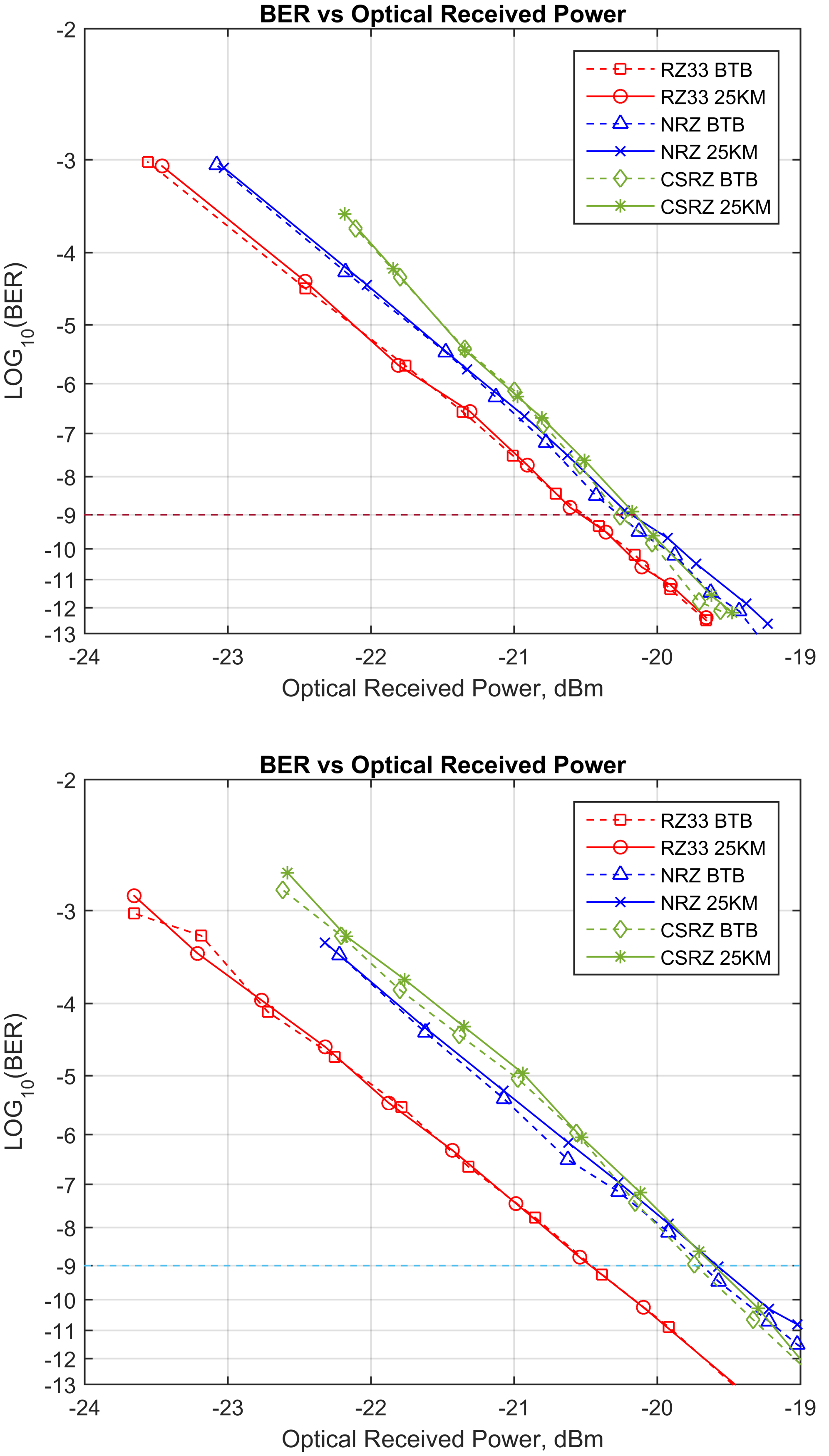

FIGURE 3.12: Performance of Scheme A (top) and Scheme B (bottom) using different signal formats measured using BER with varying optical receiving power

3.4.3 Comparison between Schemes

The main advantage of DPSK over OOK is the lack of modulation depth, which could result in better sensitivity of the system. Even with the use of MZI before the PD, the advantage of using DPSK remains, although the base station's received data has been demodulated to OOK. As shown in Fig. 3.3. and Fig. 3.6. the signal's spectrum after MZI remains the same. However, such configuration takes a slight performance hit of around 0.55 dB compared to Scheme A at the same bit error rate (BER). From Fig. 3.13, we can see that in all scenarios, Scheme C performs better than Scheme A and Scheme B. Scheme C has a power penalty advantage of 1.2dBm over Scheme A, and 1.75dB over Scheme B at BER of 10^{-9}.

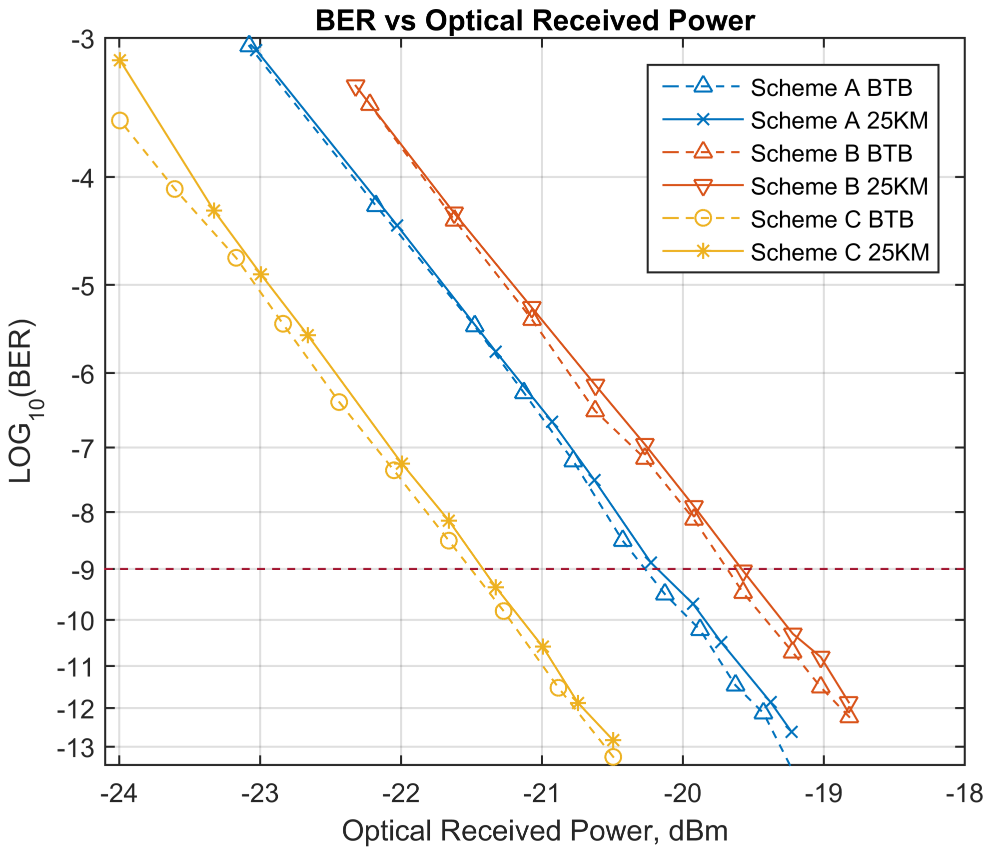

FIGURE 3.13: Performance of Scheme A, Scheme B, and Scheme C at various optical receiving power

Fig. 3.14. shows the power penalty incurred by the laser's relative intensity noise (RIN) on each scheme. The power penalty is calculated relative to the optical received power at -145 dB/Hz with a 10^{-9} BER. The curve of Scheme A and Scheme B is plotted relative to Scheme C. Linewidth of each laser is set to 1kHz to eliminate the effects of laser linewidth while obtaining results. RIN of the data modulated laser source is varied from -145 dB/Hz to -115 dB/Hz. This range is chosen because off-the-shelve laser's RIN falls

within this range, and commercially available distributed feedback (DFB) lasers have a RIN of below -130 dB/Hz [67].

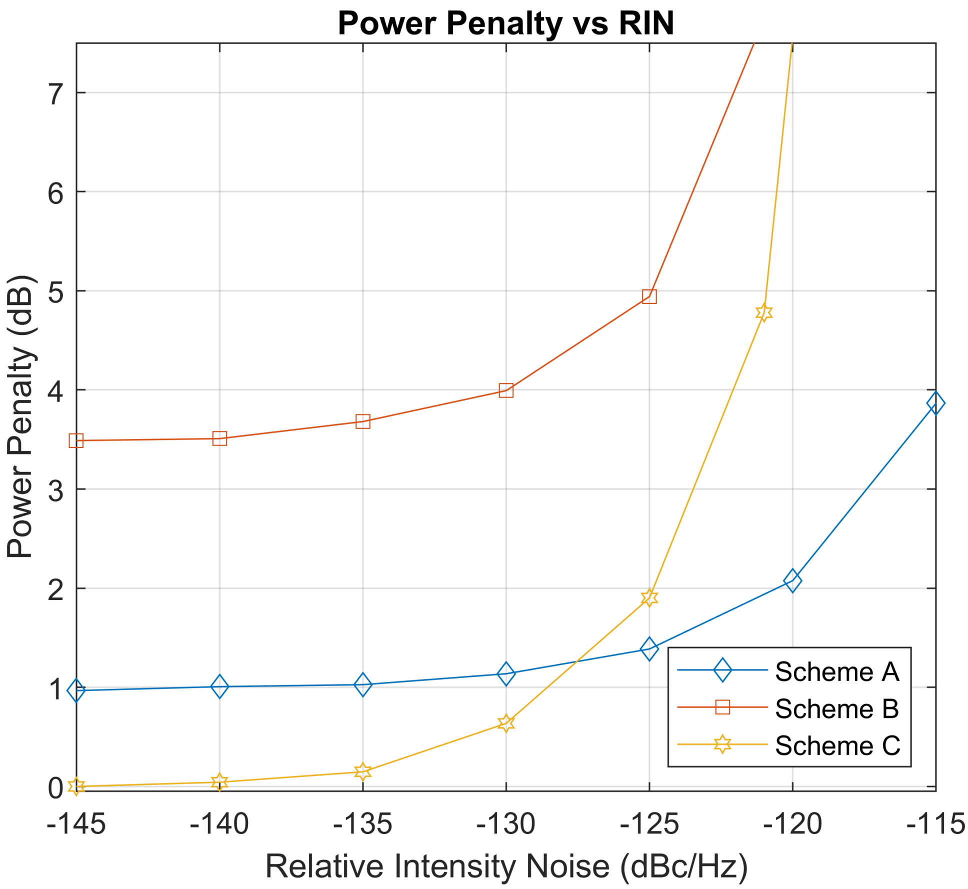

FIGURE 3.14: Power penalty incurred to Scheme A, Scheme B, and Scheme C at different levels of relative intensity noise

Based on the results obtained, a minimal increase in power penalty is observed when RIN is increased from -145 dB/ Hz to -135 dB/Hz for Scheme B, -145 dB/Hz to -130 dB/Hz for Scheme A, and -145 dB/Hz to -140 dB/Hz for Scheme C. From that point onwards, the gradient of the curve increases rapidly, with Scheme C being the fastest, followed by Scheme B and Scheme A. The trend in curves show that Scheme A is more resilient to RIN compared to Scheme B, and proposed DAM receiver is more resilient to RIN compared to oscillator based receiver used in Scheme C. As RIN increases, each scheme's power penalty increases exponentially, which indicates that RIN needs to be monitored while designing and during deployment of ARoF fronthaul link.

Phase noise of a system is affected by the data rate and the linewidth of the laser. Usually, when the linewidth of a laser increases, phase noise increases as well [204, 205]. To quantify the effect of phase noise on each scheme, the first laser's ($E_1(t)$) linewidth is varied from 1 Hz up to 75 MHz while fixing the second LO laser at 1 MHz. A LO-based downconversion technique used in an uncorrelated RoF link (LO2) [206, 207] is added for comparison in addition to the three schemes. The results are shown in Fig. 3.15. The power penalty is calculated based on the lowest optical receiving power to achieve a BER of 10^{-9}, which happens to be the optical receiving power at 1 Hz laser linewidth of the added LO based uncorrelated RoF link. A minimal increase in power penalty is observed from the figure till 10 MHz for Scheme A and Scheme B. While LO2 performs better than the proposed scheme (Scheme A) before 100KHz, it receives a power penalty of 9.25 dB at 200 kHz laser linewidth. In contrast, although Scheme C also uses LO based receiver, the power penalty curve remains relatively flat throughout the test due to using coherent optical tones. This shows the robustness of the proposed scheme's (Scheme A) DAM receiver to high laser linewidth.

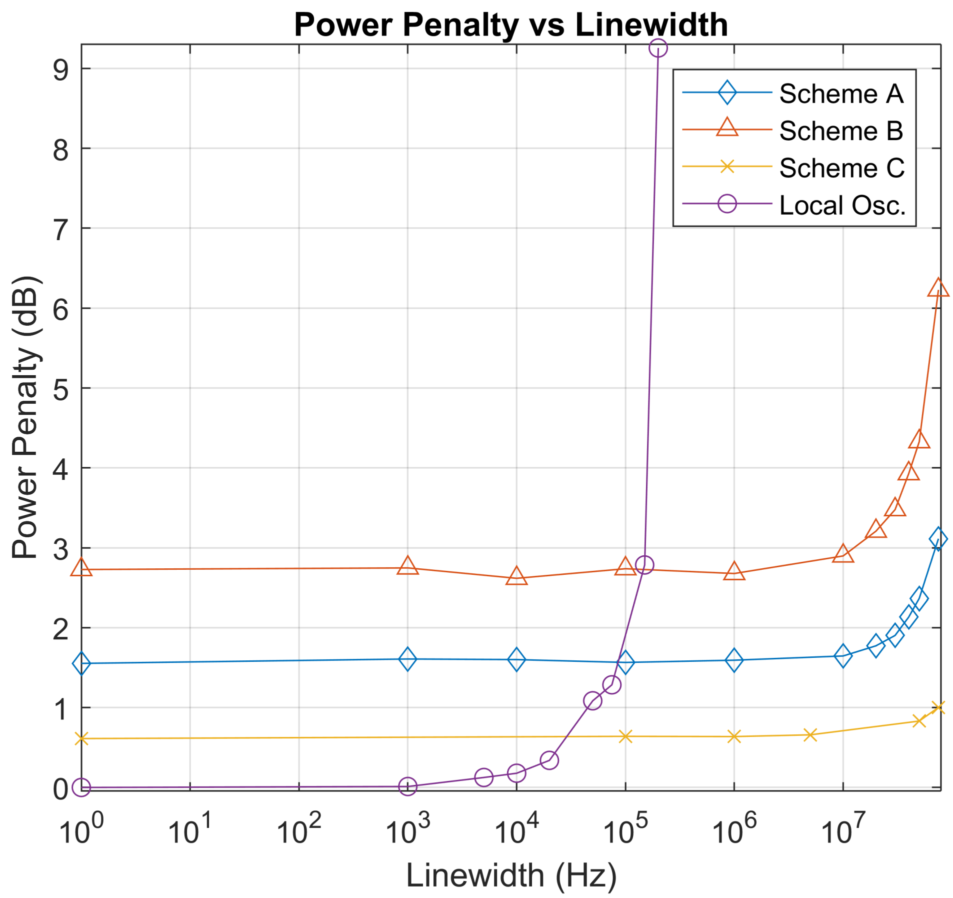

FIGURE 3.15: Power penalty incurred to Scheme A, Scheme B, and Scheme C at different levels of laser linewidth

Beyond 10 MHz, the curves' gradient increases rapidly with Scheme B being faster than Scheme A. At 75 MHz, the power penalty is 3.113 dB for Scheme A and 6.228 dB for Scheme B. Compared to ASK [134], the proposed DPSK scheme power penalty curve increases exponentially while the power penalty curve of ASK remains relatively flat with increasing laser linewidth. As linewidth increases, the coherence time of the signal decreases. Therefore, the phase difference between the signal at current time and the delayed signal (Δt and t) changes with increasing linewidth. This contributes to a higher power penalty for the proposed DPSK model at higher laser linewidth.

3.5 Summary

A novel implementation of differential encoding in an unlocked heterodyning RoF link has been proposed and demonstrated using a DPSK RoF link. Theoretical analysis carried out shows that the proposed DPSK RoF scheme has the potential in reducing phase noise inherited from the optical transmitters, a common problem faced by uncorrelated RoF systems. Simulation results show that the proposed DPSK RoF scheme remains phase noise tolerant up to 10 MHz range laser linewidth. The conventional phase-locked RoF link performs better than the proposed DPSK scheme at low RIN and high phase noise scenarios, while the proposed DPSK scheme performs better than oscillator receiver based unlocked heterodyning RoF link at higher phase noise levels. Besides, the proposed DPSK scheme is more tolerant towards RIN compared to the conventional phase-lock RoF link. Similar to conventional phase-locked RoF links, optical carrier-to-sideband power difference can significantly influence the proposed DPSK scheme's system performance. Results obtained show that the optimal operating point for the proposed DPSK link is when the total carrier power is equal to the total sideband power.

Chapter 4

DQPSK Millimeter-wave Radio-over-Fiber

4.1 Introduction

This chapter extends the previous chapter's investigation to include the use of DQPSK in uncorrelated millimeter-wave RoF. The proposal of millimeter-wave band frequency usage has been driven by the limited availability of bandwidth in the existing 4G sub-3GHz RF band [208]. However, with the increasing number of connected devices, even with the increased available bandwidth with the inclusion of millimeter-wave frequencies, wireless bandwidth should be utilized efficiently. Moving from DPSK to DQPSK doubles the spectral utilization where data are transmitted at a rate of 2 bits/Hz instead of 1 bits/Hz [209, 210]. DQPSK signal can be modulated onto an optical carrier using the same optical transmitter setup as the proposed DPSK scheme in Chapter 3. Hence, no additional changes have to be made to the optical transmitter while doubling the spectral usage. However, the demodulation process of DQPSK signal will cause a drop in detection performance due to higher phase noise residual. The longer time delay used to demodulate DQPSK would lead to a greater difference in phase between the current signal and the delayed signal. As discussed in the previous chapter, the time delay in the DAM receiver will cause an exponential decrease in detection performance when phase noise increases. The impairment would be greater for DQPSK as the time delay used in DQPSK is twice the duration of DPSK [211].

Therefore, this chapter investigates the feasibility of DQPSK in the presence of a relatively higher phase noise residual compared to the phase noise residual present in the proposed DPSK scheme. The proposed DQPSK scheme will be compared to two self-homodyning-based IF-RoF schemes. The two IF-RoF schemes were demonstrated through physical experiments in [67, 193] using QAM-based orthogonal frequency division multiplexing (OFDM) signals and envelop detection. The demonstrated IF-RoF systems managed to maintain phase information and avoid beating interference after heterodyning and self-homodyning detection. However, additional bandwidth is required to transmit IF tone for self-homodyning detection to ensure that the signal's phase integrity is maintained.

The main contributions of this chapter are as follows:

- Develop a theoretical analysis of differential encoding in RoF links using optical baseband DQPSK modulation
- Provide theoretical analysis on two IF-RoF links based on self-homodyning receiver.
- Increase overall spectral efficiency through incoherent detection without the need of IF tone for phase noise tolerant receiver.

In this chapter, the theoretical analysis of the proposed baseband optical modulated DQPSK millimeter-wave RoF scheme is provided in section 4.2. Section 4.3 presents the theoretical analysis on two alternative self-homodyning-based IF-RoF schemes. Simulation results and performance comparison between the proposed schemes and the two IF-RoF alternatives are provided in section 4.4. A summary of the chapter is provided in section 4.5

4.2 Proposed Optical DQPSK Scheme

Fig. 4.1 shows the configuration of the proposed optical baseband DQPSK modulated millimeter-wave RoF scheme. The proposed DQPSK scheme is similar to the DPSK scheme in chapter 3, with the exception of requiring an additional DAM receiver. The two DAM receivers are used to demodulate in-phase and quadrature components of the DQPSK signal respectively. The DQPSK data is modulated optically onto an optical carrier using a dual-drive MZM (DD-MZM). Using the output equation of an MZM defined in Chapter 3, equation (3.3), the output of the dual-drive MZM can be represented by

$$\begin{aligned} E_{M_Q}(t) &= \frac{E_{in}(t)}{10^{\frac{l_i}{20}}}\left[\gamma e^{j(\frac{\pi v_2(t)}{V_{\pi RF}}+\frac{\pi v_{bias2}}{V_{\pi DC}})}+(1-\gamma)e^{j(\frac{\pi v_1(t)}{V_{\pi RF}}+\frac{\pi v_{bias1}}{V_{\pi DC}})}\right] \\ &= \frac{E_1(t)}{10^{\frac{l_i}{20}}}e^{j(\frac{\pi v_2(t)}{V_{\pi RF}})} \end{aligned} \tag{4.1}$$

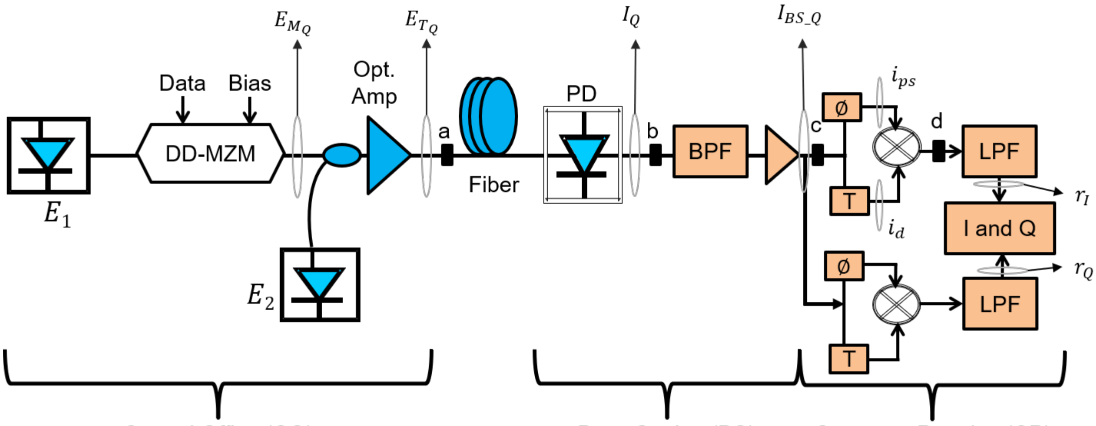

FIGURE 4.1: Proposed Downlink Radio-over-Fiber DQPSK link

where $E_1(t)$ is the input optical carrier from the first laser, and l_i is the insertion loss of the MZM. Assuming both of the modulator arms are symmetric with $\gamma = 0.5$, both arms of the modulator are fed with the same signal $v_1(t) = v_2(t)$, and the biasing voltage of the two arms are the same $v_{bias2} = v_{bias1} = 0$. If the switching voltage of the modulator $V_{\pi_{RF}} = 4V$, the DQPSK signal denoted by $v_2(t)$ will be

$$v_2(t) = 4I(t) + 2Q(t) \tag{4.2}$$

where $I(t)$ and $Q(t)$ are the in-phase and quadrature components of the DQPSK signal. The amplitude of the in-phase component is set to be twice of the quadrature components because when $|V_{\pi_{RF}}| = 4$, $I(t)$ and $Q(t)$ will have a 90 deg phase difference as shown below

$$\begin{aligned} E_{M_Q}(t) &= \frac{E_1(t)}{10^{\frac{l_i}{20}}} e^{j(\frac{\pi v_2(t)}{V_{\pi_{RF}}})} \\ &= \frac{E_1(t)}{10^{\frac{l_i}{20}}} e^{j(\frac{\pi 4I(t)+\pi 2Q(t)}{4})} \\ &= \frac{E_1(t)}{10^{\frac{l_i}{20}}} e^{j(\pi I(t)+\frac{\pi}{2}Q(t))} \end{aligned} \tag{4.3}$$

A change in voltage in $I(t)$ and $Q(t)$ will lead to a change in phase to the input optical carrier. The output of the dual-drive MZM will be coupled with an optical local oscillator using an optical coupler before transmitting out of the CO and is denoted by E_{C_Q}

$$\begin{aligned} E_{C_Q} &= \alpha \begin{bmatrix} \sqrt{\frac{1}{2}} & -j\sqrt{\frac{1}{2}} \\ -j\sqrt{\frac{1}{2}} & \sqrt{\frac{1}{2}} \end{bmatrix} \begin{bmatrix} E_{M_Q} \\ E_2(t) \end{bmatrix} \\ &= \alpha \begin{bmatrix} \sqrt{\frac{1}{2}}E_{M_Q} - j\sqrt{\frac{1}{2}}E_2(t) \\ -j\sqrt{\frac{1}{2}}E_{M_Q} + \sqrt{\frac{1}{2}}E_2(t) \end{bmatrix} \end{aligned} \tag{4.4}$$

where $E_2(t)$ represents the output signal of the second laser, and α is the insertion loss of the optical coupler. Assuming that the first output is transmitted from the CO, and given that the output of the two lasers are

$$\begin{aligned} E_1(t) &= e^{j(\omega_1 t+\phi_{1l}(t))} \\ E_2(t) &= e^{j(\omega_2 t+\phi_{2l}(t))} \end{aligned}$$

the signal output from the CO can be

$$\begin{aligned} E_{T_Q}(t) &= \alpha\left(\sqrt{\frac{1}{2}}E_{M_Q}(t) - j\sqrt{\frac{1}{2}}E_2(t)\right) \\ &= \alpha\sqrt{\frac{1}{2}}\left(\frac{E_1(t)}{10^{\frac{l_i}{20}}}e^{j(\pi I(t)+\frac{\pi}{2}Q(t))} - jE_2(t)\right) \\ &= \alpha\sqrt{\frac{1}{2}}\left(\frac{e^{j(\omega_1 t+\phi_{1l}(t))}}{10^{\frac{l_i}{20}}}e^{j(\pi I(t)+\frac{\pi}{2}Q(t))} - je^{j(\omega_2 t+\phi_{2l}(t))}\right) \\ &= \alpha\sqrt{\frac{1}{2}}\left(\frac{e^{j(\omega_1 t+\phi_{1l}(t)+\pi I(t)+\frac{\pi}{2}Q(t))}}{10^{\frac{l_i}{20}}} + e^{j(\omega_2 t+\phi_{2l}(t)-\frac{\pi}{2})}\right) \\ &= A_2 e^{j(\omega_1 t+\phi_{1l}(t)+\pi I(t)+\frac{\pi}{2}Q(t))} + B_2 e^{j(\omega_2 t+\phi_{2l}(t)-\frac{\pi}{2})} \end{aligned} \tag{4.5}$$

where $A_2 = \frac{\alpha\sqrt{\frac{1}{2}}}{10^{\frac{l_i}{20}}}$ and $B_2 = \alpha\sqrt{\frac{1}{2}}$. For simplicity, let $A_2 = B_2$. At the BS, the signal is directly detected by a photodiode. The photocurrent can be obtained as

$$\begin{aligned} I_Q(t) &\propto E_{T_Q}(t) \times E^*_{T_Q}(t) \\ &\propto (e^{j(\omega_1 t+\phi_{1l}(t)+\pi I(t)+\frac{\pi}{2}Q(t))} + e^{j(\omega_2 t+\phi_{2l}(t)-\frac{\pi}{2})}) \\ &\quad \times(e^{-(\omega_1 t+\phi_{1l}(t)+\pi I(t)+\frac{\pi}{2}Q(t))} + e^{-j(\omega_2 t+\phi_{2l}(t)-\frac{\pi}{2})}) \\ &\propto 1+\cos\left(\omega_1 t - \omega_2 t + \phi_{1l}(t) - \phi_{2l}(t) + \pi I(t) + \frac{\pi}{2}Q(t) + \frac{\pi}{2}\right) \\ &\propto 1+\cos\left(\Delta\omega t + \Delta\phi_l(t) + \pi I(t) + \frac{\pi}{2}Q(t) + \frac{\pi}{2}\right) \end{aligned} \tag{4.6}$$

with the assumption that there is no fiber to distort the signal. Here, $E^*_{T_Q}(t)$ is the conjugate of $E_{T_Q}(t)$, $\Delta\omega t$ represents $\omega_1 t - \omega_2 t$, and $\Delta\phi_l(t)$ represents $\phi_{1l}(t) - \phi_{2l}(t)$. The millimeter-wave carrier (ω_{mm}) is produced through heterodyning of the two optical tones, $\omega_{mm}t = \Delta\omega t$. The transmitted signal from the BS after bandpass filtering and amplification is

$$I_{BS\_Q}(t) \propto \cos\left(\omega_{mm}t + \Delta\phi_l(t) + \pi I(t) + \frac{\pi}{2}Q(t) + \frac{\pi}{2}\right) \tag{4.7}$$

For DQPSK demodulation, the received signal is split into two by a balance power divider with a time delay $\tau_2 = \frac{2}{\text{Bit-Time}}$, and a phase change of $\frac{\pi}{4}$ or $-\frac{\pi}{4}$ at both arms.

The output representation at one of the delay arm,

$$\begin{aligned} i_d(t) &\propto \left(\omega_{mm}\Delta t_2 + \Delta\phi_l(\Delta t_2) + \pi I(\Delta t_2) + \frac{\pi}{2}Q(\Delta t_2) + \frac{\pi}{2}\right) \\ &\propto \left(\omega_{mm}\Delta t_2 + \phi_{l\_d}(\Delta t_2) + \pi I(\Delta t_2) + \frac{\pi}{2}Q(\Delta t_2) + \frac{\pi}{2}\right) \end{aligned} \tag{4.8}$$

where $\Delta t_2 = t - \tau_2$ and the delayed phase noise is defined as $\Delta\phi_l(\Delta t_2) = \phi_{l\_d}(\Delta t_2)$. The output representation at one of the phase shift arm,

$$i_{ps}(t) \propto \cos\left(\omega_{mm}t + \Delta\phi_l(t) + \pi I(t) + \frac{\pi}{2}Q(t) + \frac{3\pi}{4}\right) \tag{4.9}$$

At the receiver, signal demodulation and baseband downconversion is carried out through multiplying delayed signal and the phase-shifted signal at both arms respectively, as shown in Fig. 4.1.

$$r(t) = i_d(t) \times i_{ps}(t)$$

After lowpass filtering, the baseband IQ signal represented by $r_I(t)$ and $r_Q(t)$ are

$$\begin{aligned} r_I(t) &= \cos(-\omega_{mm}\tau + \phi_{l\_d}(\Delta t_2) - \Delta\phi_l(t) + \pi I(\Delta t_2) \\ &\quad -\pi I(t) + \frac{\pi}{2}Q(\Delta t_2) - \frac{\pi}{2}Q(t) - \frac{\pi}{4}) \end{aligned} \tag{4.10}$$

$$\begin{aligned} r_Q(t) &= \cos(-\omega_{mm}\tau + \phi_{l\_d}(\Delta t_2) - \Delta\phi_l(t) + \pi I(\Delta t_2) \\ &\quad -\pi I(t) + \frac{\pi}{2}Q(\Delta t_2) - \frac{\pi}{2}Q(t) + \frac{\pi}{4}) \end{aligned} \tag{4.11}$$

As shown in equation (4.10) and equation (4.11), the DAM receivers reduces the phase noise inherited from the optical transmission system through subtracting the inherited phase noise ($\Delta\phi_l(t)$) with its delayed version ($\phi_{l\_d}(\Delta t_2)$). If the phase difference from time t to Δt_2 is negligible, then the phase noise can be minimized to approximately zero, $\phi_{l\_d}(\Delta t_2) - \Delta\phi_l(t) \approx 0$. However, when the phase difference from time t to Δt_2 increases, residue phase noise increases. This finding is similar to the proposed DPSK scheme. However the time delay used for DPSK demodulation is one bit time (τ_1) while the time delay used for DQPSK demodulation is two bit time (τ_2). The longer time delay used in DQPSK would result in having a larger phase fluctuation between symbols which will cause a drop in detection accuracy of the system. The effects on system performance in the presence of a larger phase noise residue due to having a longer time delay will be explored in section 4.4.

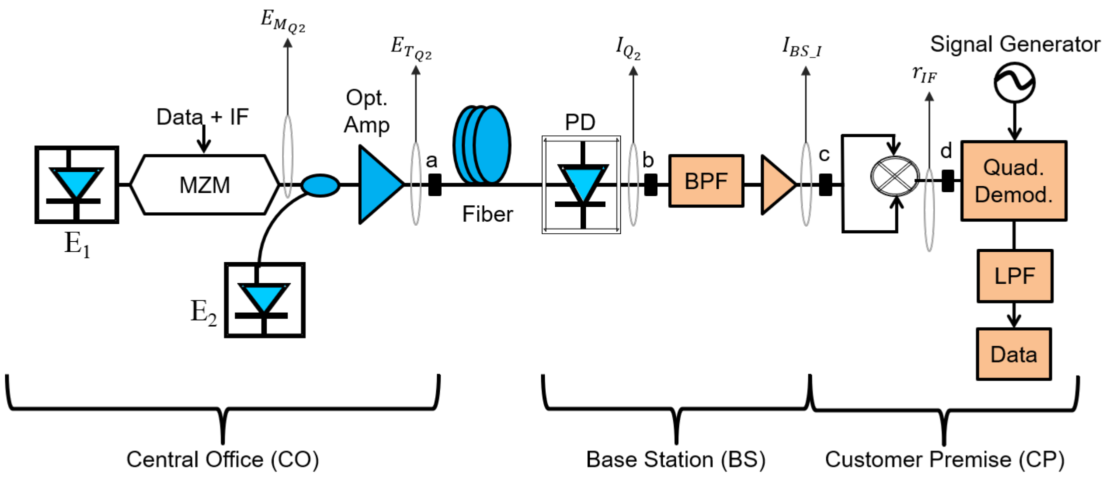

FIGURE 4.2: Downlink of an Uncorrelated Intermediate Frequency Radio-over-Fiber (IF-RoF) Link Using Self-Homodyning (SH) Receiver

4.3 Intermediate Frequency Radio-over-Fiber

A theoretical analysis of two downlink IF-RoF links is provided in this section: unlock heterodyned IF-RoF and remote oscillator IF-RoF. Both IF-RoF schemes were demonstrated in [67, 193]. However, in both papers, a full downlink theoretical analysis was not provided. Therefore, a full downlink theoretical analysis from RoF signal generation to baseband frequency downconversion is carried out in this section.

4.3.1 Unlock Heterodyned IF-RoF

An intermediate frequency (IF) RoF link using unlocked optical heterodyning and envelope detection has been proposed and demonstrated using orthogonal frequency-division multiplexing (OFDM) with quadrature amplitude modulation (QAM) in [193]. The link was analyzed through physical experiments with varying fiber lengths and optical receiving power. However, a theoretical analysis was not provided. Hence, the IF-RoF link in [193] is adapted to use DQPSK signal (Fig. 4.2), and a theoretical analysis is provided in this section.

The DQPSK data is generated using a quadrature modulator using an intermediate frequency that is much lower than the desired millimeter-wave signal. Although RF oscillators operating at IF are required, the physical link configuration is similar to ASK-based uncorrelated RoF link shown in Fig. 3.1. Hence, the number of high-speed optoelectronics and RF components used are still lower than conventional RoF links.

At the transmitter, the output of the modulator is represented by

$$\begin{aligned} E_{M_{Q2}}(t) &= \alpha_2 E_{1_{In}}(t)[1 + a s_2(t)] \\ &= \alpha_2 E_1(t)[1 + a\cos(2\pi f_{IF}t + \phi_{s_2}(t))] \\ &= \alpha_2 e^{j(\omega_1 t + \phi_{1l}(t))}\left[1 + a\frac{1}{2}(e^{j(2\pi f_{IF}t + \phi_{s_2}(t))} + e^{-j(2\pi f_{IF}t + \phi_{s_2}(t))})\right] \\ &= \alpha_2 e^{j(\omega_1 t + \phi_{1l}(t))} + \alpha_2 a\frac{1}{2}(e^{j(2\pi(f_1 + f_{IF})t + \phi_{1l}(t) + \phi_{s_2}(t))} \\ &\qquad + e^{j(2\pi(f_1 - f_{IF})t + \phi_{1l}(t) - \phi_{s_2}(t))}) \end{aligned} \tag{4.12}$$

where $\omega_1 = 2\pi f_1$, f_{IF} is the intermediate frequency used, and $\phi_{s_2}(t)$ is the phase representation of the DQPSK signal. As shown in equation (4.12), the output from the modulator is the form of an optical double sideband with carrier signal (ODSB+C). ODSB+C signals are known to have higher impairments due to dispersion compared to OSSB+C and ODSC+SC signals. The effect of dispersion is also affected by the frequency difference between the carrier and sidebands. The higher the frequency difference, the higher the impairment. Compared to conventional ODSB+C generation method where the frequency difference between carrier and sidebands equals to the desired millimeter-wave frequency, the frequency used in this IF-RoF link is IF. Hence the signal impairment due to dispersion is lower.

Before transmitting out of the CO, the output of the modulator will be coupled with an optical local oscillator using a 3 dB optical coupler. The output of the coupler is denoted by $E_{C_{Q2}}$.

$$\begin{aligned} E_{C_{Q2}} &= \alpha \begin{bmatrix} \sqrt{\frac{1}{2}} & -j\sqrt{\frac{1}{2}} \\ -j\sqrt{\frac{1}{2}} & \sqrt{\frac{1}{2}} \end{bmatrix} \begin{bmatrix} E_{M_{Q2}}(t) \\ E_2(t) \end{bmatrix} \\ &= \alpha \begin{bmatrix} \sqrt{\frac{1}{2}}E_{M_{Q2}}(t) - j\sqrt{\frac{1}{2}}E_2(t) \\ -j\sqrt{\frac{1}{2}}E_{M_{Q2}}(t) + \sqrt{\frac{1}{2}}E_2(t) \end{bmatrix} \end{aligned} \tag{4.13}$$

Assuming the first output of the optical coupler is transmitted, the output from the CO can be represented by

$$\begin{aligned} E_{T_{Q2}}(t) &= \alpha\left(\sqrt{\frac{1}{2}}E_{M_{Q2}}(t) - j\sqrt{\frac{1}{2}}E_2(t)\right) \\ &= \alpha\alpha_2\sqrt{\frac{1}{2}}e^{j(\omega_1 t + \phi_{1l}(t))} + \alpha\alpha_2 a\frac{1}{2\sqrt{2}}(e^{j(2\pi(f_1 + f_{IF})t + \phi_{1l}(t) + \phi_{s_2}(t))} \\ &\quad + e^{j(2\pi(f_1 - f_{IF})t + \phi_{1l}(t) - \phi_{s_2}(t))}) + \alpha\sqrt{\frac{1}{2}}e^{j(\omega_2 t + \phi_{2l}(t) - \frac{\pi}{2})} \end{aligned} \tag{4.14}$$

For simplicity, let the amplitude of each optical tone in $E_{T_{Q2}}(t)$ be one, and assume that no fiber is present. After heterodyning detection at the photodiode, the photocurrent output can be represented by

$$
\begin{aligned}
I_{Q2}(t) &\propto E_{T_{Q2}}(t) \times E^*_{T_{Q2}}(t) \\
&\propto 4 + 2e^{j(2\pi f_{IF}t+\phi_{s_2}(t))} + 2e^{-j(2\pi f_{IF}t+\phi_{s_2}(t))} \\
&\quad + e^{j((\omega_1-\omega_2)t+\phi_{1l}(t)-\phi_{2l}(t)+\frac{\pi}{2})} + e^{j(4\pi f_{IF}t+2\phi_{s_2}(t))} \\
&\quad + e^{j((\omega_1-\omega_2)t+2\pi f_{IF}t+\phi_{1l}(t)-\phi_{2l}(t)+\phi_{s_2}(t)+\frac{\pi}{2})} + e^{-j(4\pi f_{IF}t+2\phi_{s_2}(t))} \\
&\quad + e^{j((\omega_1-\omega_2)t-2\pi f_{IF}t+\phi_{1l}(t)-\phi_{2l}(t)-\phi_{s_2}(t)+\frac{\pi}{2})} \\
&\quad + e^{-j((\omega_1-\omega_2)t+\phi_{1l}(t)-\phi_{2l}(t)+\frac{\pi}{2})} \\
&\quad + e^{-j((\omega_1-\omega_2)t+2\pi f_{IF}t+\phi_{1l}(t)-\phi_{2l}(t)+\phi_{s_2}(t)+\frac{\pi}{2})} \\
&\quad + e^{-j((\omega_1-\omega_2)t-2\pi f_{IF}t+\phi_{1l}(t)-\phi_{2l}(t)-\phi_{s_2}(t)+\frac{\pi}{2})} \\
&\propto 2 + 2\cos(2\pi f_{IF}t + \phi_{s_2}(t)) + \cos\left(\omega_{mm}t + \Delta\phi_l(t) + \frac{\pi}{2}\right) \\
&\quad + \cos(4\pi f_{IF}t + 2\phi_{s_2}(t)) + \cos\left(\omega_{mm}t + 2\pi f_{IF}t + \Delta\phi_l(t) + \phi_{s_2}(t) + \frac{\pi}{2}\right) \\
&\quad + \cos\left(\omega_{mm}t - 2\pi f_{IF}t + \Delta\phi_l(t) - \phi_{s_2}(t) + \frac{\pi}{2}\right)
\end{aligned} \tag{4.15}
$$

where $E^*_{T_{Q2}}(t)$ is the conjugate of $E_{T_{Q2}}(t)$. Due to the usage of SH receiver, in addition to one of the sideband of the double-sideband signal, the carrier of the double-sideband signal has to be present at the receiver to maintain the phase integrity of the signal. Therefore, the signal transmitted from the BS is

$$
\begin{aligned}
I_{BS\_I}(t) &\propto \cos\left(\omega_{mm}t + \Delta\phi_l(t) + \frac{\pi}{2}\right) \\
&\quad + \cos\left(\omega_{mm}t + 2\pi f_{IF}t + \Delta\phi_l(t) + \phi_{s_2}(t) + \frac{\pi}{2}\right)
\end{aligned} \tag{4.16}
$$

At the CP, the signal will be downconverted to IF by the SH receiver, and the IF signal will be downconverted to baseband using RF oscillators. The IF signal after downconversion can be represented by

$$
\begin{aligned}
r_{IF}(t) &\propto I_{BS_5}(t) \times I_{BS_5}(t) \\
&\propto \cos^2\left(\omega_{mm}t + \Delta\phi_l(t) + \frac{\pi}{2}\right) \\
&\quad + 2\cos\left(\omega_{mm}t + \Delta\phi_l(t) + \frac{\pi}{2}\right) \\
&\qquad \cos\left(\omega_{mm}t + 2\pi f_{IF}t + \Delta\phi_l(t) + \phi_{s_2}(t) + \frac{\pi}{2}\right) \\
&\quad + \cos^2\left(\omega_{mm}t + 2\pi f_{IF}t + \Delta\phi_l(t) + \phi_{s_2}(t) + \frac{\pi}{2}\right) \\
&\propto 1 - \frac{1}{2}\cos(2\omega_{mm}t + 2\Delta\phi_l(t)) \\
&\quad + \cos(2\pi f_{IF}t + \phi_{s_2}(t)) - \cos(2\omega_{mm}t + 2\pi f_{IF}t + 2\Delta\phi_l(t) + \phi_{s_2}(t)) \\
&\quad - \frac{1}{2}\cos(2\omega_{mm}t + 4\pi f_{IF}t + 2\Delta\phi_l(t) + 2\phi_{s_2}(t))
\end{aligned} \tag{4.17}
$$

The final baseband IQ signal after lowpass filtering can be represented by

$$r_{I2}(t) \quad \propto \quad \cos(\phi_{s_2}(t) - \phi_{LO}(t)) \tag{4.18}$$

$$r_{Q2}(t) \quad \propto \quad \cos\left(\phi_{s_2}(t) - \phi_{LO}(t) + \frac{\pi}{2}\right) \tag{4.19}$$

where $\phi_{LO}(t)$ is the phase fluctuation of the RF local oscillator used for baseband downconversion, given that the RF local oscillators used have an output of $\cos(2\pi f_{IF}t + \phi_{LO}(t))$ and $\cos\left(\frac{\pi}{2} - 2\pi f_{IF}t - \phi_{LO}(t)\right)$ respectively. As shown in equation (4.17), the term $\Delta\phi_l(t)$ is not present in the signal at IF after SH downconversion. Hence, in the final baseband signal, as shown in equation (4.18) and equation (4.19), the phase noise contributed from the optical transmitter in the CO is no longer present while retaining the DQPSK signal phase information. If the additional carrier tone is not present during SH detection, the signal downconverted will be at baseband instead of IF, and the phase information of the signal will be removed.

4.3.2 Remote Oscillator IF-RoF

The remote oscillator IF-RoF has been demonstrated and evaluated experimentally in [67] using M-QAM signals. While a brief theoretical analysis is provided, it is not complete. Hence, the demonstrated remote IF-RoF link is adapted to use DQPSK (as shown in Fig. 4.3), and an end-to-end downlink theoretical analysis is provided in this section. Comparing Fig. 4.3 and Fig. 4.2, both IF-RoF links are similar while having two differences. At the BS, while unlock heterodyning IF-RoF generates millimeter-wave signal through unlocked heterodyning of the ODSB+C signal and the optical tone from the second laser, remote oscillator IF-RoF generates the desired millimeter-wave signals through mixing of output signals from the two photodiodes. At the CO, the second laser's output is directly coupled with the output of the MZM in unlocked heterodyning IF-RoF, whilst in remote oscillator IF-RoF, the output of the second laser is modulated with an IF signal to generate an ODSB+SC signal.

For remote oscillator IF-RoF, the signal representation of the modulated signal on the first laser's output (E_1) is similar to $E_{M_{Q2}}(t)$. For the second modulator, frequency doubling modulation technique is used, and the output can be represented by

$$\begin{aligned}
E_{M_{Q3}}(t) &= \frac{E_{in}(t)}{10^{\frac{l_i}{20}}}\left[\gamma e^{j\left(\frac{\pi v_2(t)}{V_{\pi RF}}+\frac{\pi v_{bias2}}{V_{\pi DC}}\right)} + (1-\gamma)e^{j\left(\frac{\pi v_1(t)}{V_{\pi RF}}+\frac{\pi v_{bias1}}{V_{\pi DC}}\right)}\right] \\
&= A_1 E_{in}(t)\left[\frac{1}{2}e^{j\left(\frac{\pi v_2(t)}{V_{\pi RF}}+\frac{\pi}{2}\right)} + \frac{1}{2}e^{-j\left(\frac{\pi v_2(t)}{V_{\pi RF}}+\frac{\pi}{2}\right)}\right] \\
&= A_1 E_{in}(t)\cos\left(\frac{\pi v_2(t)}{V_{\pi RF}}+\frac{\pi}{2}\right) \\
&= -A_1 E_{in}(t)\sin\left(\frac{\pi}{V_{\pi RF}}\cos(2\pi f_{IF_2}t)\right) \\
&= -A_1 E_{in}(t)\left(2J_1\left(\frac{\pi}{V_{\pi RF}}\right)\cos(2\pi f_{IF_2}t)\right) \\
&= -A_1 J_1\left(\frac{\pi}{V_{\pi RF}}\right)E_{in}(t)(e^{j(2\pi f_{IF_2}t)} + e^{-j(2\pi f_{IF_2}t)}) \\
&= -A_1 J_1\left(\frac{\pi}{V_{\pi RF}}\right)(e^{j(\omega_2 t+2\pi f_{IF_2}t+\phi_{2l}(t))} + e^{j(\omega_2 t-2\pi f_{IF_2}t+\phi_{2l}(t))})
\end{aligned} \tag{4.20}$$

As shown in equation (4.20), frequency doubling modulation can be carried out using a dual-drive MZM with a biasing voltage equivalent to $\pm\frac{1}{2}V_{\pi DC}$. The signal input fed to the two MZM arms have an inverse polarity, $v_1(t) = -v_2(t)$. The output of the two MZMs are coupled using an optical coupler with an output representation of

$$\begin{aligned}
E_{C_{Q3}} &= \alpha\begin{bmatrix}\sqrt{\frac{1}{2}} & -j\sqrt{\frac{1}{2}} \\ -j\sqrt{\frac{1}{2}} & \sqrt{\frac{1}{2}}\end{bmatrix}\begin{bmatrix}E_{M_{Q2}}(t) \\ E_{M_{Q3}}(t)\end{bmatrix} \\
&= \alpha\begin{bmatrix}\sqrt{\frac{1}{2}}E_{M_{Q2}}(t) - j\sqrt{\frac{1}{2}}E_{M_{Q3}}(t) \\ -j\sqrt{\frac{1}{2}}E_{M_{Q2}}(t) + \sqrt{\frac{1}{2}}E_{M_{Q3}}(t)\end{bmatrix}
\end{aligned} \tag{4.21}$$

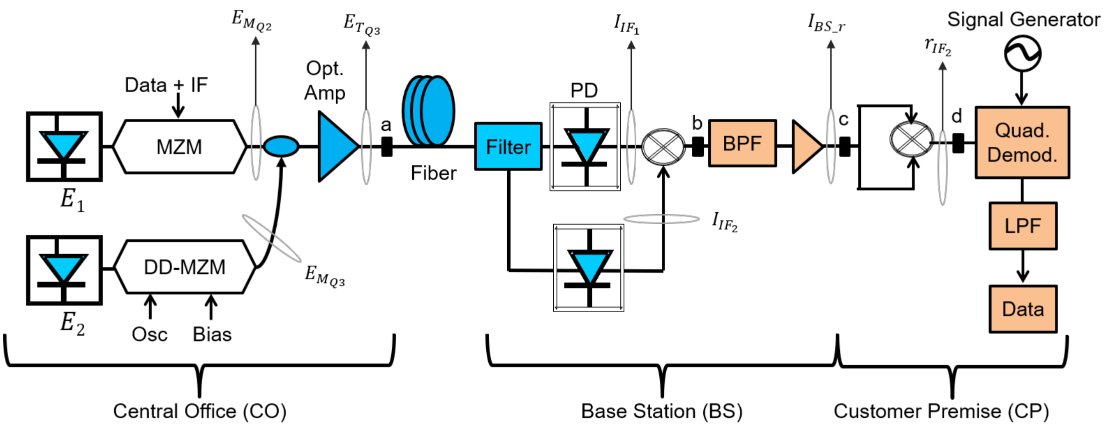

FIGURE 4.3: Downlink of an Remote Oscillator Intermediate Frequency Radio-over-Fiber (IF-RoF) Link Using Self-Homodyning (SH) Receiver

Assuming that the first output of the coupler is transmitted, the transmitted signal from the CO will be

$$\begin{aligned} E_{T_{Q3}}(t) &= \alpha\left(\sqrt{\frac{1}{2}}E_{M_{Q2}}(t) - j\sqrt{\frac{1}{2}}E_{M_{Q3}}(t)\right) \\ &= -\alpha A_1 J_1\left(\frac{\pi}{V_{\pi RF}}\right)(e^{j(\omega_2 t+2\pi f_{IF_2}t+\phi_{2l}(t))} + e^{j(\omega_2 t-2\pi f_{IF_2}t+\phi_{2l}(t))}) \\ &\quad +\alpha\alpha_2\sqrt{\frac{1}{2}}e^{j(\omega_1 t+\phi_{1l}(t))} + \alpha\alpha_2 a\frac{1}{2\sqrt{2}}(e^{j(2\pi(f_1+f_{IF})t+\phi_{1l}(t)+\phi_{s_2}(t))} \\ &\quad +e^{j(2\pi(f_1-f_{IF})t+\phi_{1l}(t)-\phi_{s_2}(t))}) \end{aligned} \tag{4.22}$$

Before photodiode detection, the coupled optical tones are separated using an optical filter. A high-speed photodiode is used to detect $E_{M_{Q3}}$ with its output denoted by I_{IF_2} and a low-speed photodiode is used to detect $E_{M_{Q2}}$ with an output denoted by I_{IF_1}.

$$\begin{aligned} I_{IF_1}(t) &\propto E_{M_{Q2}}(t) \times E^*_{M_{Q2}}(t) \\ &\propto 3 + 2e^{j(2\pi f_{IF}t+\phi_{s_2}(t))} + 2e^{-j(2\pi f_{IF}t+\phi_{s_2}(t))} + e^{j(4\pi f_{IF}t+2\phi_{s_2}(t))} \\ &\quad +e^{-j(4\pi f_{IF}t+2\phi_{s_2}(t))} \\ &\propto 3 + 4\cos(2\pi f_{IF}t + \phi_{s_2}(t)) + 2\cos(4\pi f_{IF}t + 2\phi_{s_2}(t)) \end{aligned} \tag{4.23}$$

$$\begin{aligned} I_{IF_2}(t) &\propto E_{M_{Q3}}(t) \times E^*_{M_{Q3}}(t) \\ &\propto 2 + e^{j(2\pi(2\times f_{IF_2})t)} + e^{-j(2\pi(2\times f_{IF_2})t)} \\ &\propto 2 + 2\cos(2\pi(2\times f_{IF_2})t) \end{aligned} \tag{4.24}$$

Here, $E^*_{M_{Q2}}(t)$ and $E^*_{M_{Q3}}(t)$ are the conjugate of $E_{M_{Q2}}(t)$ and $E_{M_{Q3}}(t)$ respectively.

Referring to equation (4.23) and equation (4.24), $I_{IF_1}(t)$ contains the DQPSK signal $\phi_{s_2}(t)$ at IF whilst $I_{IF_2}(t)$ only contains a signal oscillating at f_{IF_2}. The oscillator frequency used for signal up-conversion is remotely delivered from the CO to the BS, hence the name of the setup: remote oscillator IF-RoF. The output of the two photodiodes are mixed using an RF mixer to generate the desired millimeter-wave signal with its output represented by

$$\begin{aligned} I_{IF_1}(t) \times I_{IF_2}(t) &\propto 3 + 3\cos(2\pi(2\times f_{IF_2})t) + 4\cos(2\pi f_{IF}t + \phi_{s_2}(t)) \\ &\quad +4\cos(2\pi f_{IF}t + \phi_{s_2}(t))\cos(2\pi(2\times f_{IF_2})t) \\ &\quad +2\cos(4\pi f_{IF}t + 2\phi_{s_2}(t)) \\ &\quad +2\cos(4\pi f_{IF}t + 2\phi_{s_2}(t))\cos(2\pi(2\times f_{IF_2})t) \end{aligned}$$

$$\begin{aligned} I_{IF_1}(t) \times I_{IF_2}(t) \quad \propto \quad & 3 + 3\cos(2\pi(2 \times f_{IF_2})t) + 4\cos(2\pi f_{IF} t + \phi_{s_2}(t)) \\ & +2(\cos(2\pi(f_{IF} - 2f_{IF_2})t + \phi_{s_2}(t)) + \cos(2\pi(f_{IF} + 2f_{IF_2})t + \phi_{s_2}(t))) \\ & + \cos(4\pi(f_{IF} - f_{IF_2}t + 2\phi_{s_2}(t))) + \cos(4\pi(f_{IF} + f_{IF_2}t + 2\phi_{s_2}(t))) \\ & +2\cos(4\pi f_{IF} t + 2\phi_{s_2}(t)) \end{aligned} \tag{4.25}$$

Before BS transmission, the signal is filtered to have frequencies at $f_{mm} = f_{IF} + 2f_{IF}$ and $2 \times f_{IF_2}$. If an oscillator based receiver is used, the frequency required for transmission will only be f_{mm}. The BS transmitted signal is

$$I_{BS\_r}(t) \propto 3\cos(2\pi(2 \times f_{IF_2})t) + 2\cos(2\pi(f_{IF} + 2f_{IF_2})t + \phi_{s_2}(t)) \tag{4.26}$$

At the receiver, the signal is detected by the SH based receiver, which can be represented by

$$\begin{aligned} r_{IF_2}(t) \quad & \propto \quad I_{BS_6}(t) \times I_{BS_6}(t) \\ & \propto \quad 9\cos^2(2\pi(2 \times f_{IF_2})t) + 4\cos^2(2\pi(f_{IF} + 2f_{IF_2})t + \phi_{s_2}(t)) \\ & \qquad +12\cos(2\pi(2 \times f_{IF_2})t)\cos(2\pi(f_{IF} + 2f_{IF_2})t + \phi_{s_2}(t)) \end{aligned} \tag{4.27}$$

The signal will then be further downconverted to baseband using RF oscillators and RF mixers. The final baseband IQ signal will be similar to equation (4.18) and equation (4.19).

$$\begin{aligned} r_{I3}(t) \quad & \approx \quad \cos(\phi_{s_2}(t) - \phi_{LO}(t)) \\ r_{Q3}(t) \quad & \approx \quad \cos\left(\phi_{s_2}(t) - \phi_{LO}(t) + \frac{\pi}{2}\right) \end{aligned}$$

Comparing both IF-RoF schemes, at the photodiode, as shown in equation (4.15), equation (4.23) and equation (4.24), in remote oscillator IF-RoF, the phase noise contributed by the optical transmission source is subtracted from the photocurrent output due to optical locked heterodyning. Although both IF-RoF schemes use two uncorrelated optical sources, in remote oscillator IF-RoF the signal is detected separately using two photodiodes. Due to the modulation methods used in remote oscillator IF-RoF, the two signals are in the form of an ODSB+C signal and an optical double sideband with suppressed carrier (ODSB+SC) signal. While these two signals are not correlated, the tones within the ODSB+C and ODSB+SC signals are correlated. Therefore, the optical tones heterodyned at the photodiodes are phase-locked, reducing the phase noise inherited from the optical transmitter. However, this is only possible if the optical tones remain phase-locked at the photodiode after fiber transmission.

4.4 Experimental Results

In this section, the proposed DQPSK scheme's performance is compared to the two IF-RoF alternative schemes at varying levels of optical receiving power, phase noise, and relative intensity noise. A validation test comparing the optical carrier-to-sideband power difference is carried out to optimise the performance of the proposed DQPSK scheme. The simulation setup for the proposed DQPSK scheme and the two IF-RoF schemes are provided in section 4.4.1. Validation test and performance comparisons between schemes are provided in section 4.4.2 and section 4.4.3 respectively. In this section, solid continuous lines in all figures are fitting curves plotted using MATLAB. It is plotted to provide a better illustration of the trend of the results collected for each test.

4.4.1 Simulation Setup

The proposed DQPSK link as shown in Fig. 4.1 is modeled using *OptiSystem 16* software. A free-running continuous wave (CW) laser operating at 193.1 THz is externally modulated by a dual-drive Mach-Zehnder Modulator (DD-MZM) with differential encoded IQ data generated using 2.5 Gbps Pseudo Random Bit Sequence (PRBS) fed into a precoder to generate DQPSK data. Another free-running optical LO laser operating at 193.1375 THz is coupled with the output of the DD-MZM using a 3 dB coupler. The linewidth of both lasers is set to 1 MHz. The coupled signal is amplified before being transported over a 25 km single-mode fiber (SMF) to the BS. A 37.5 GHz millimeter-wave signal is generated through unlocked heterodyning of the received tones. A 50 dB gain amplifier with a spectral density of noise current of $2.25 \times 10^{-11} \frac{A}{\sqrt{Hz}}$ and a 2.5 GHz bandwidth Bessel bandpass filter centered around 37.5 GHz is used to amplify and filter the millimeter-wave signal.

The proposed scheme is compared to two intermediate frequency QPSK setups as shown in Fig. 4.2 and Fig. 4.3. From this point onwards, unlocked heterodyining IF-RoF and remote oscillator IF-RoF will be referred to as IF-RoF1 and IF-RoF2 respectively. The IF used in both schemes is set to 2.5 GHz. In IF-RoF1, a double sideband with carrier (DSB+C) signal is generated by feeding the MZM with a quadrature modulated 2.5 GHz DQPSK signal. The DSB+C signal is coupled with a LO laser tone before transmission. Millimeter-wave signal is generated through unlocked heterodyning of the LO tone and the DSB+C signal. In IF-RoF2, the millimeter-wave carrier is generated at the second photodiode through heterodyning of double sideband with suppressed carrier (DSB+SC) laser tones. The DSB+SC tones are generated using the second DD-MZM shown in Fig. 4.3. The RF carrier is added to the DSB+C IF signal through an RF combiner. For both schemes, the millimeter-wave signal is amplified by 50 dB, and filtered to include the main data signal and the RF reference tone for SH detection.

4.4.2 Optical Carrier-to-Sideband Power

As mentioned in chapter 3, optical carrier-to-sideband power difference can influence system performance drastically. Therefore, before commencing subsequent test, a validation test is carried out to obtain the optimal optical carrier-to-sideband power difference.

In the proposed DQPSK link, two uncorrelated lasers were used. The power of the two uncorrelated sources is varied from -15 dBm to -5 dBm. The power difference is calculated between the output power of the MZM and the power of the second LO laser, denoted by ΔP. The fiber length is fixed at 5 km, and the launch power is fixed at 0 dBm ± 0.001. The results obtained are shown in Fig. 4.4 and Fig. 4.5. Compared to the test carried out on DPSK, as shown in Fig. 3.9 and Fig. 3.10, the DQPSK scheme has the same optimal operating point as the DPSK schemes. At $\Delta P = 0$ dBm, the proposed DQPSK scheme achieves the lowest BER and has the highest RF generated power at the same fiber launch power.

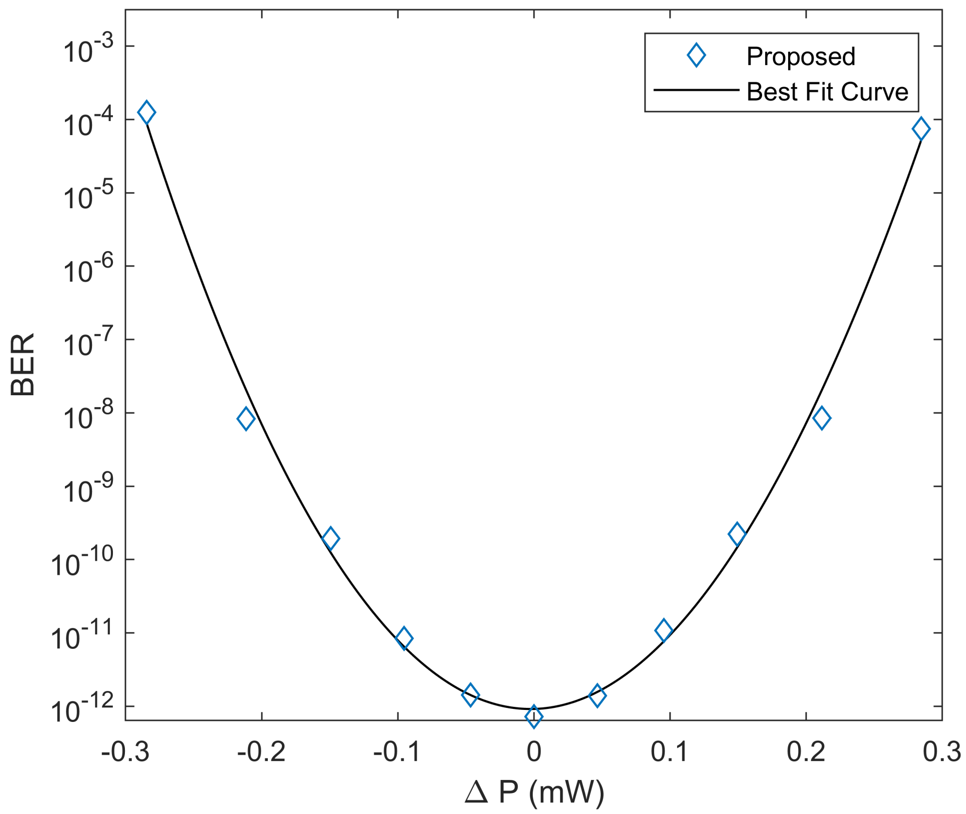

FIGURE 4.4: BER of the proposed DQPSK scheme under different ΔP

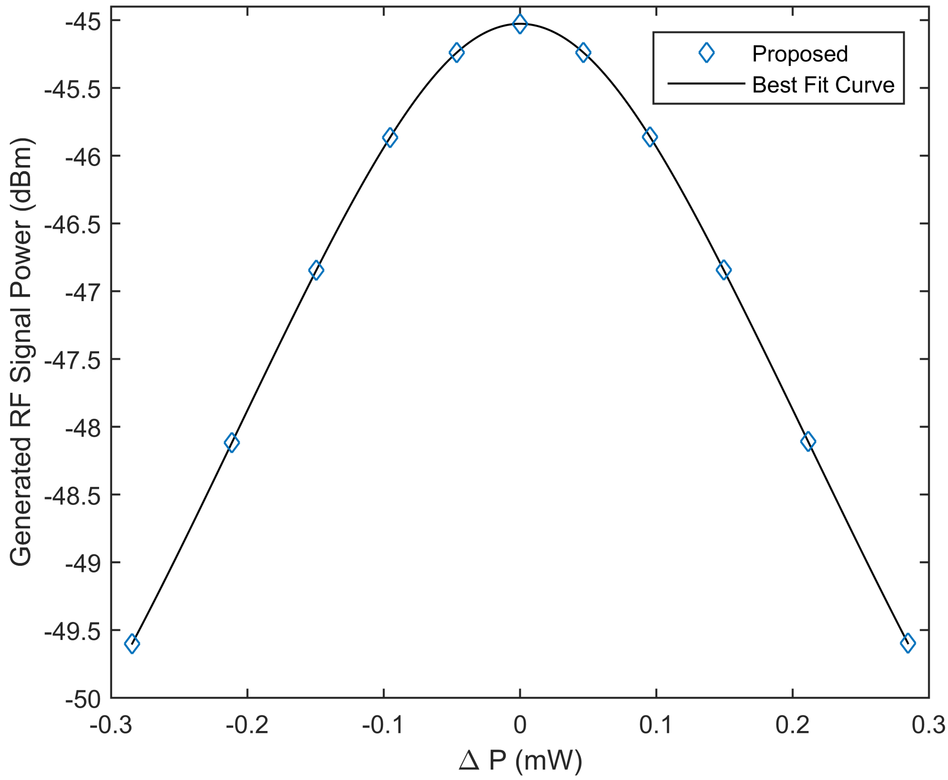

FIGURE 4.5: Generated RF signal power of the proposed DQPSK scheme under different ΔP with the same fiber launch power.

4.4.3 Comparison between the proposed scheme and IF-RoF schemes

Fig. 4.7 shows the performance of the proposed scheme and the two IF-RoF schemes under varying levels of optical receiving power at 25 km fiber length measured using symbol error rate (SER). The SER obtained is estimated using the error vector magnitude of the received signal constellation. In Chapter 3, the results on varying optical receiving power included the results for a back-to-back optical link. However, the back-to-back analysis is not carried out for DQPSK. In millimeter-wave RoF systems, dispersion induced by the fiber can severely limit the transmission distance and performance of a given link, especially when optical double sideband signals are used [125–128]. Hence, the performance of the two IF-RoF schemes and the proposed scheme are measured using SER at a varying fiber length of 0 to 30 km. The fiber launch power is set to maintain at 0 dBm ± 0.001, and the optical receiving power is set to maintain at -13.5 dBm ± 0.002 at all fiber length using an optical attenuator. The results obtained are shown in Fig. 4.6. From the figure, IF-RoF2 reaches its local minima at 25 km while the local minima for IF-RoF1 falls between 25 km and 26 km. The proposed scheme reaches a local minima at 23 km. Furthermore, all three schemes have a much higher

SER at 0 km fiber (back-to-back) relative to the performance of both links at 25 km. For consistency, all three schemes will be compared using a fiber length of 25 km.

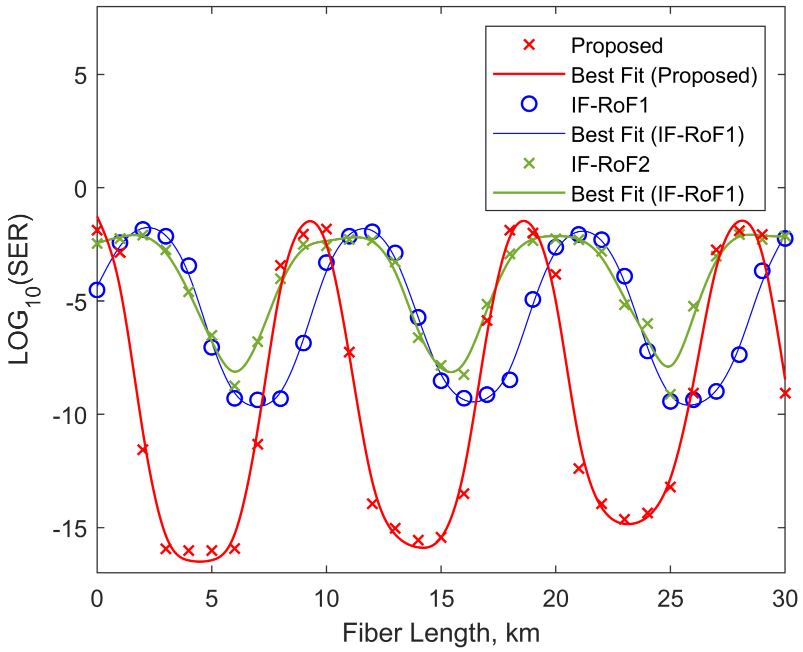

FIGURE 4.6: Effects of fiber dispersion on the proposed DQPSK sheme and two IF-RoF schemes measured using SER

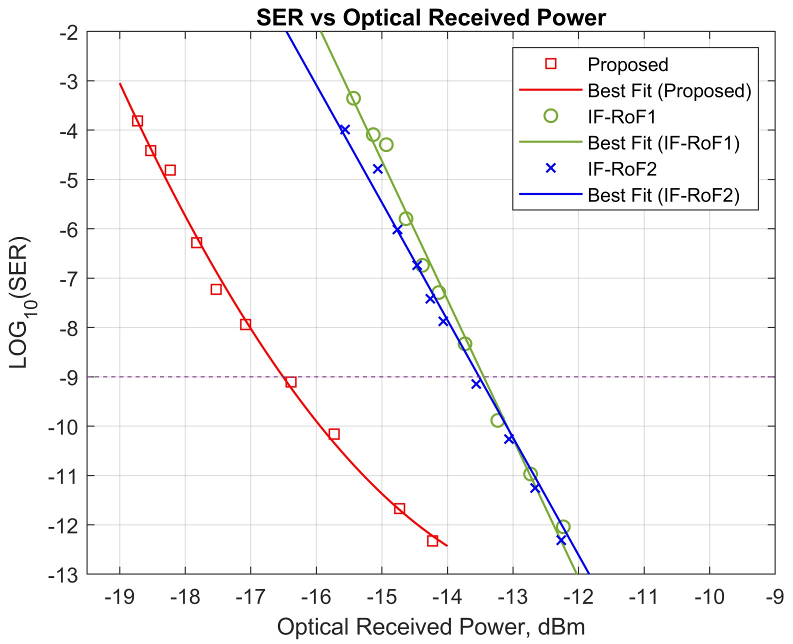

FIGURE 4.7: Performance of the proposed DQPSK sheme and two IF-RoF schemes at various optical receiving power

From Fig. 4.7, the results show that the proposed scheme performs better than both IF-RoF schemes, while IF-RoF1 and IF-RoF2 perform similarly. At a SER of 10^{-9}, the optical receiving powers are -16.75 dBm, -13.5 dBm, and -13.6dBm for the proposed scheme, IF-RoF1, and IF-RoF2 respectively. Additionally, the proposed scheme has an approximate 3 dB power penalty advantage over the other schemes at 1 MHz laser linewidth.

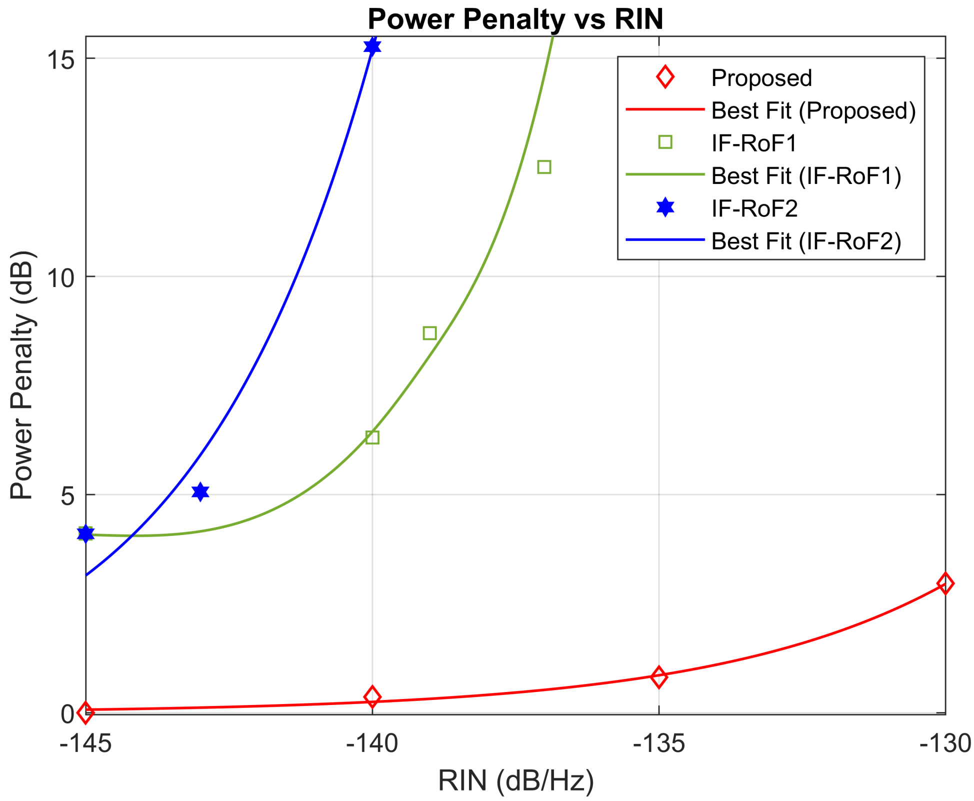

FIGURE 4.8: Power penalty incurred at different levels of relative intensity noise

Fig. 4.8 shows the power penalty incurred by varying levels of relative intensity noise (RIN). RIN is varied from -145 dB/Hz to -130 dB/Hz. The power penalty is calculated relative to the received power at SER 10^{-9} of the proposed scheme at -145 dB/Hz. Based on Fig. 4.8, the proposed DQPSK scheme performs better than IF-RoF1 and IF-RoF2 at all RIN levels. The rate of increase in the gradient of the power penalty curve is much faster for IF-RoF1 and IF-RoF2 compared to the proposed scheme. Compared to Scheme A and Scheme B in Chapter 3, as shown in Fig. 3.14, the proposed DQPSK scheme is more sensitive to RIN, as the gradient of the proposed DQPSK power penalty curve increases much faster than DPSK. At -130 dBc/Hz, Scheme A experienced a power penalty of less than 2 dB, while the proposed DPQSK scheme experienced a power penalty of 2.96 dB. Hence, for higher-order modulation, RIN needs to be controlled and monitored during designing and deployment.

Phase noise effects on detection accuracy, induced by the laser tones, can be quantified by measuring the SER at different laser linewidths. Fig. 4.9 shows the power penalty

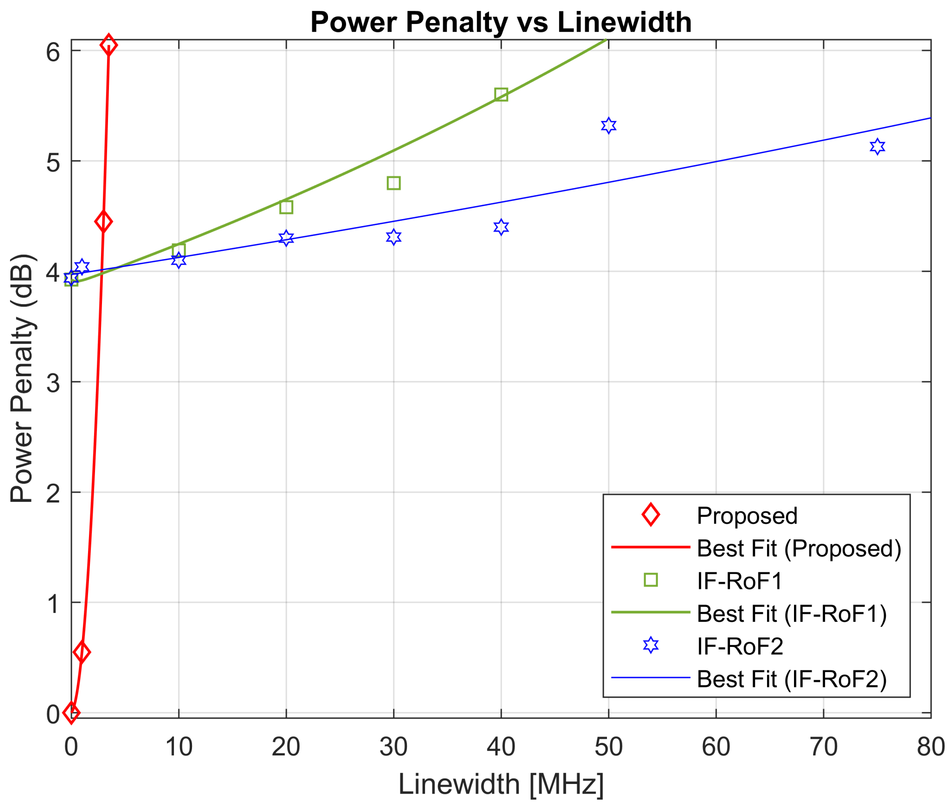

FIGURE 4.9: Power penalty incurred at different of laser linewidth

incurred by increasing laser linewidth on all three schemes. The laser linewidth of the first laser (E_1) is varied from 1 Hz to 75 MHz. Power penalty is calculated relative to the lowest optical receiving power at SER of 10^{-9}, which is the receiving power of the proposed scheme at SER of 10^{-9}. At a linewidth of less than 2.8 MHz, the proposed scheme performs better than both IF-RoF schemes. However, the proposed scheme's curve gradient increases much faster than other schemes. This is contributed by the increase in residue phase noise as the phase fluctuation increases with increasing laser linewidth. As shown in equation (4.10) and equation (4.11), the phase noise is reduced through the subtraction of $\Delta\phi_l(\Delta t_2)$ and $\Delta\phi_l(t)$. As the laser linewidth increases, phase noise at time Δt_2 and t can differ greatly. IF-RoF2 performs better than IF-RoF1 at higher phase noise as the power penalty curve is flatter than IF-RoF1. As discussed in section 4.3.2, while the laser diodes used in IF-RoF2 are unlocked, the detection of DSB+C and DSB+SC tones are carried out separately. Hence the tones within the DSB+C signal and DSB+SC signal are locked. Therefore, in IF-RoF2, the phase noise is reduced through heterodyning. Compared to DPSK, the power penalty experienced by the proposed DQPSK scheme with increasing phase noise is much higher, and the gradient of the curve is also much steeper. As discussed in section 4.2, the residue phase noise for QPSK is higher than DPSK at the same laser linewidth due to having a longer time delay τ_2.

4.5 Summary

An optical DQPSK RoF link is proposed and investigated. Results obtained through theoretical analysis and simulation show that the proposed DQPSK RoF scheme has the potential to reduce phase noise inherited from the optical transmitter. However, the proposed scheme experience a higher impairment compared to the DPSK schemes shown in Chapter 3 due to the longer time delay used in the detection process and a higher symbol rate. While the two IF-RoF schemes perform better than the proposed DQPSK scheme at high phase noise scenario, the proposed DQPSK scheme performs better at lower phase noise levels and has a higher tolerance towards RIN. The optimal point of operation for the proposed DQPSK link is when the total carrier power is equal to the total sideband power.

Chapter 5

Deep Learning based Coordinated Multipoint

5.1 Introduction

One of the significant challenges of future wireless networks, 5G and beyond, is the ever-increasing demand for higher data rate. Such demand has led to an increase in research in the millimeter-wave band (30 GHz - 300 GHz) and terahertz band for the upcoming 5G and 6G wireless communication respectively, due to congestion in the sub-3 GHz band [212]. However, radio signals propagating at high-frequency experience considerably higher path loss, which reduces reliable communication distance. Therefore, more base stations and the adoption of steerable high-gain antennas are required. However, millimeter-wave's short-wavelength nature allows stacking of multiple antenna elements within a relatively small footprint to form a massive antenna array, thus making it possible to exploit the benefit of beamforming [66–68].

Densification of both antenna arrays and base stations incurs new technical challenges. In wireless communication, coordinated multipoint (CoMP) is used to coordinate transmissions of network elements to minimize interference and increase overall data throughput of a network. The increase in the number of base stations increases network management complexity, especially for CoMP transmission. In addition, to benefit from the use of massive MIMO (mMIMO) antenna arrays, the base station has to align the high gain RF beam towards the user through beamforming. Therefore, the network has to be managed such that it aligns the high gain RF beam towards the user and at the same time coordinates the transmission of the base stations to mitigate interference and improve data throughput. Hence, significantly more overhead resources and processing capability are required from the baseband processing unit to perform large-scale coordination

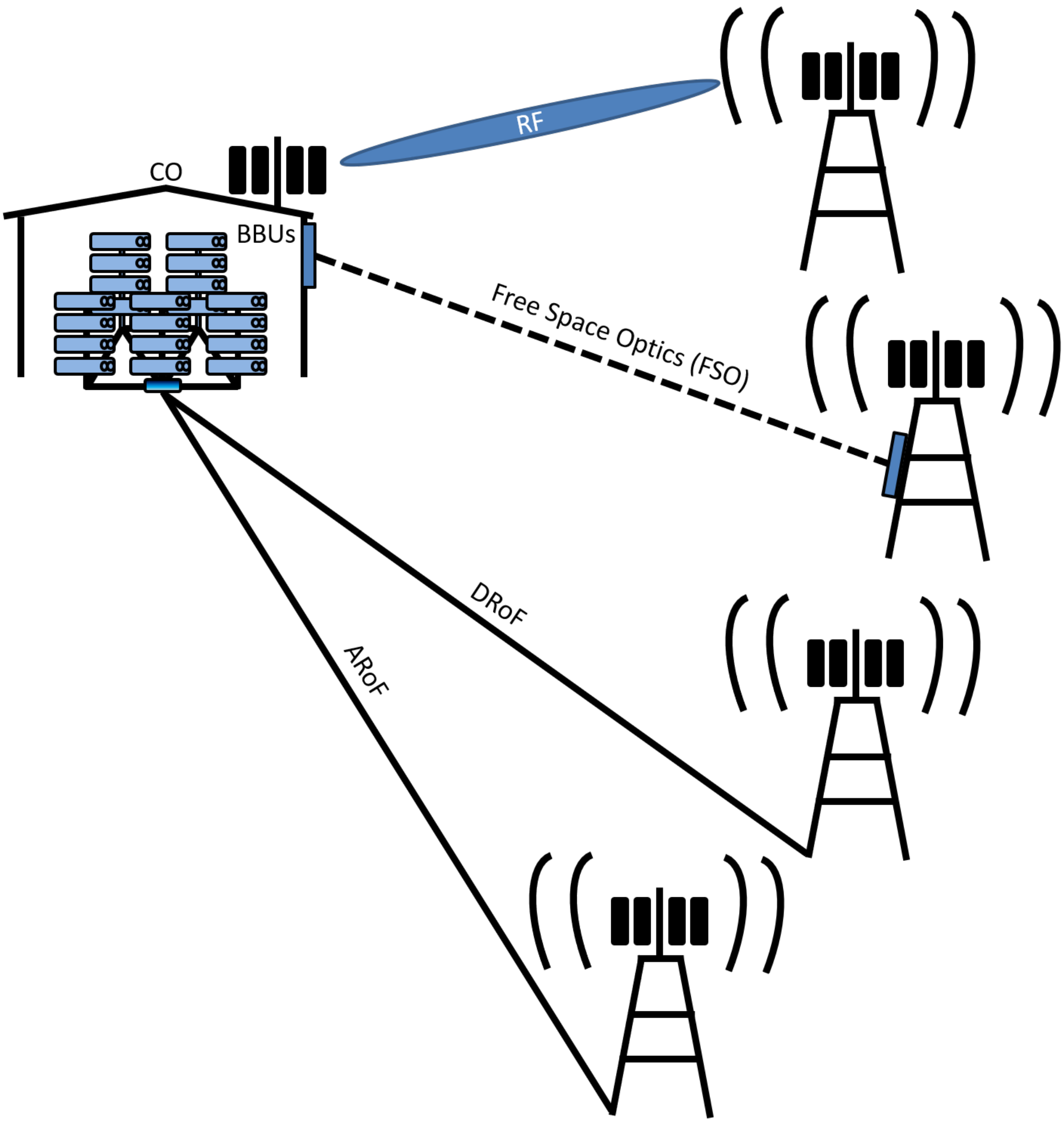

FIGURE 5.1: Illustration of CRAN with different CO to BS link.

and scheduling for a mMIMO millimeter-wave wireless communication network. Aside from higher data rate, energy efficiency and latency are three things to consider when deploying 5G systems. The increase in the number of base stations, overhead resources, and processing capability can lead to an increase in power consumption. Furthermore, a congested backhaul network might lead to an increase in latency.

The concept of centralization, as shown in Fig. 5.1, has been proposed to address the aforementioned challenges, whereby baseband units are located in a centralized pool in the central office separated from the base station (BS), e.g. centralized radio access network (C-RAN) [15]. In this configuration, all routing, control signal, and data processing are carried out centrally. This means that CoMP and beamforming of mMIMO array processing will be managed centrally. Downlink CoMP can be categorized into

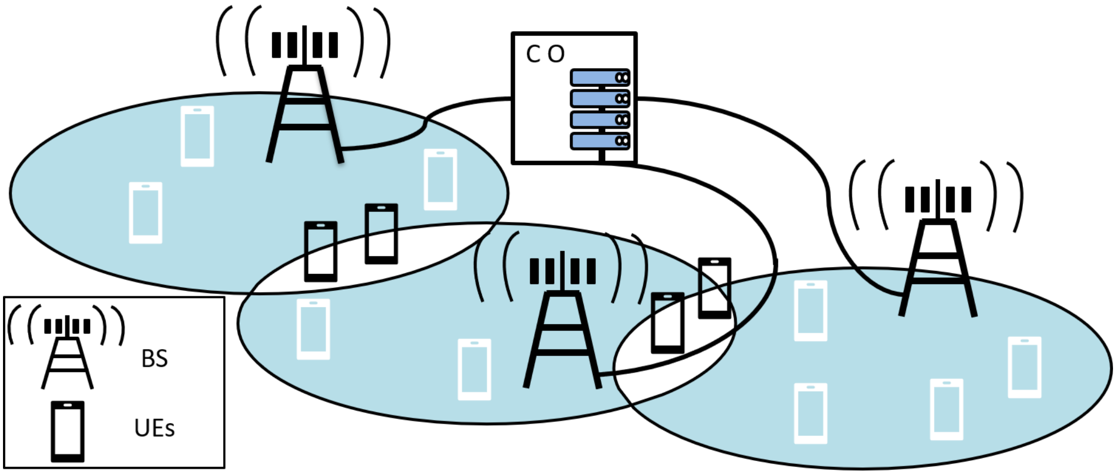

FIGURE 5.2: Illustration of a C-RAN based Coordinated Multipoint

three categories: joint transmission, dynamic point selection (DPS), and coordinated beamforming. In DPS, the user can only receive signals transmitted from a single base station. The base station is selected among the cooperating base stations within a cluster based on channel conditions. For coordinated beamforming, user data only exists in one base station, while users' channel state information is shared among base stations. Interference between base stations can be suppressed by either altering base station radiating pattern, zero-forcing beamforming (ZFBF), or joint leakage suppression (JLS). The focus of this chapter will be on downlink joint transmission coordinated multipoint as it allows for more efficient utilization of base stations transmission resources to improve cell edge throughput. Joint transmission CoMP requires user equipment (UE) multiplexed data to be available at multiple CoMP cooperating points for transmission, which in effect will form a distributed multiple-input multiple-output (MIMO) channel with multiple streams to improve overall data rate and cell edge reception. For a centrally managed CoMP, as shown in Fig. 5.2, UE multiplexed data is present in the central office. The CoMP cooperating cluster will be controlled and managed centrally based on UE multiplexed data and predefined CoMP connection rules.

The use of machine learning has been applied in telecommunication problems, including self-organizing network management, beam alignment, and physical layer optimizations [213–215]. The successful breakthrough in applying deep learning in other domains such as speech processing [216], image processing [217], and gaming [25] motivates the application of deep learning to communication problems [214, 218]. Looking at the development trend in various fields using machine learing, it is possible to have a future where the network is entirely controlled using machine learning algorithms. Therefore, in this chapter, we explore the use of deep learning in CoMP.

In this chapter, we extend the application of deep learning for CoMP triggering in [219].

We do this by including two different applications of deep learning for CoMP: to select an additional base station for downlink joint CoMP transmission, and to provide all possible base station options that meet the predefined criteria for downlink joint CoMP transmission. In the demonstrated deep learning based CoMP triggering [219], deep feed-forward neural network, with varying number of neurons, was used to determine non-linear boundaries for CoMP triggering. The performance of the deep neural network (DNN) was measured using downlink throughput and compared to SVM based triggering and static SNR triggering. The results shown in [219] suggests that using a simple dual-layered feed-forward neural network can improve system performance as it can define the non-linear boundary for CoMP triggering better than SVM. In addition, a recurrent neural network based deep learning algorithm has been demonstrated in predicting triggering conditions for enabling or disabling virtual cell based CoMP [220]. The results show that the recurrent neural network based deep learning algorithm achieves a 92% accuracy in predicting triggering conditions for enabling and disabling the virtual cell mode. However, there were no comparisons made to other deep learning algorithms.

The data collected from the constant exchange of telemetry data between network elements can be used for more than just triggering CoMP algorithm. In CRAN, the data collected will be available centrally. Hence, deep learning algorithms can be used to process the collected data to select additional base stations for downlink CoMP, perform large-scale beamforming and scheduling, and providing all possible base station options for CoMP joint downlink transmission.

In this chapter, a deep learning based CoMP is demonstrated using deep reinforcement learning and other deep learning algorithms such as multilayer perceptron (MLP) and long short-term memory (LSTM). The performance of these algorithms are explored and compared using three different approaches for two different scenarios with varying complexity. In the three different approaches, the task performed by the deep learning algorithm varies. The three approaches, namely AP1, AP2, and AP3, are:

- AP1: As a switch to trigger the downlink CoMP algorithm
- AP2: To select an additional base station for CoMP using predefined criteria.
- AP3: To provide all possible base station options that meet the predefined criteria for CoMP transmission.

The chapter is organized as follows. Section 5.2 provides a brief background on an mMIMO link and a description of the deep learning algorithm and deep reinforcement learning used. Results and performance comparison between algorithms used are provided in section 5.3. Section 5.4 summarizes this chapter.

5.2 Proposed Deep Learning Algorithm based Centrally Managed Millimeter-wave CoMP

This section is organized as follows. Section 5.2.1 provides a brief introduction to the link model of an mMIMO system. Section 5.2.2 describes the methods used to generate and collect data used for deep learning training and testing. A brief introduction and description of the proposed deep learning algorithms used and their application in a downlink CoMP problem is provided in Section 5.2.3. Section 5.2.4 describes the proposed reinforcement learning algorithm used and its application in CoMP.

5.2.1 Link Model

In a practical mMIMO millimeter-wave system, a codebook-based beam alignment would generally be used. Hence a MIMO channel can be estimated by

$$H_{MIMO} = \sqrt{N_{TX}N_{RX}}(\sum_{l=1}^{L} \alpha_l a_{RX}(\theta_l^A, \phi_l^A) a_{TX}^H(\theta_l^D, \phi_l^D)) \tag{5.1}$$

where α_l denotes the instantaneous random complex path gain, $\theta_l^A \in [0, \pi]$ and $\phi_l^A \in [0, \pi]$ are the angle of arrival, $\theta_l^D \in [0, \pi]$and $\phi_l^D \in [0, \pi]$ are the angle of departure, $a_{RX}(\theta_l^A, \phi_l^A)$ and $a_{TX}^H(\theta_l^D, \phi_l^D)$ are the antenna response or steering vectors at the receiver and transmitter for l-th path, L is the number of rays per transmitter and receiver pair, N_{TX} is the number of transmitting antenna, and N_{RX} is the number of antenna at the receiver. Since there are multiple stacked antenna elements within an mMIMO antenna, the beamforming gain depends on the number of transmitted and received beam pairs. Using the estimated MIMO channel, the average beam gain matrix can be calculated using

$$G_{q,p} = \mathbb{E}_{\alpha}[|w_q^H \cdot H_{MIMO} \cdot g_p|^2] \tag{5.2}$$

where the expectation is carried out over all channel path coefficients α with w_q and g_p being elements from the codebook pairs. The average beam gain matrix contains individual combined transmitter and receiver beam pair choice. The transmitting and receiving beam codebooks are denoted as:

$$V_{TX} = \{g_1, ..., g_{N_{TX}}\} \tag{5.3}$$

$$V_{RX} = \{w_1, ..., g_{N_{RX}}\} \tag{5.4}$$

where

$$g_p = a_{TX}(\theta_p^D, \phi_p^D),\ p \in \{1, ..., N_{TX}\} \tag{5.5}$$

$$w_q = a_{RX}(\theta_q^A, \phi_q^A),\ q \in \{1, ..., N_{RX}\} \tag{5.6}$$

The path loss of the transmitted signal can be calculated using:

$$\begin{aligned} L_P[\text{dB}] \quad = \quad & L_{FS}\ [\text{dB/meter}] + 10n\log_{10}(d) + \\ & L_A\ [\text{dB}] + F_S \end{aligned} \tag{5.7}$$

where L_{FS} is the free space path loss, d is the transmitter-receiver distance in meter, n is the path loss exponent where $n = 2$ for free space, F_S is the shadow fading, and L_A is the atmospheric loss due to adsorption.

Hence, the received signal can be represented by:

$$r = G_{Tot}s + n_i \tag{5.8}$$

where G_{Tot} is the total gain including average beam gain from multiple radiating elements from mMIMO array, path loss, and amplifying components; s is the transmitted signal, and n_i is the noise contributed by interference and thermal noise.

5.2.2 Data Generation

Data used for training and testing the deep learning based CoMP were generated using Vienna 5G System-Level Simulator [221], a MATLAB-based simulator. The training dataset is used to train the neural network model used. For example, in a feed-forward neural network model, the model's weights and biases are optimized based on this set of data. The test dataset is used to evaluate the trained model.

The simulator is used to simulate user equipment (UE) movements and the propagation channel model. From the simulator, results such as data throughput, UE and BS position, received signal power, channel quality index (CQI), and block-error rate (BLER) of each individual user were collected.

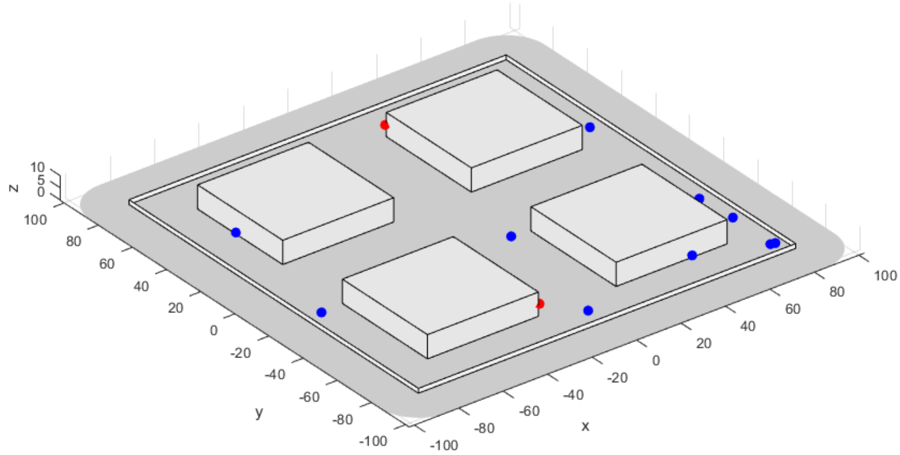

FIGURE 5.3: Scenario A with base station (red) and UEs (blue)

The simulator is configured to include both large and small-scale path losses and fading in an urban environment. The base stations are set to have a carrier frequency of 60 GHz, 20MHz bandwidth, and a maximum radiating power of 30 dBm. UEs are assumed to be pedestrians moving at a maximum speed of 5 km/h in random directions. The deep learning based CoMP is demonstrated using two scenarios: Scenario A (Fig. 5.3) and Scenario B (Fig. 5.4). Fig. 5.3 shows a simplistic urban street scenario with only two base stations. Fig. 5.4 shows a more complex scene with seven base station arranged in a hex grid formation in an open field. These two scenarios are configured in the simulator with the base stations in Scenario A and Scenario B having an inter base station distance of 139.2 meters and 100 meters respectively. Simulations were run $N+1$ times where N is the number of base stations in the region of interest. Hence, the simulation ran three times for Scenario A and eight times for Scenario B. In the first simulation, all base stations were turned on to obtain primary UE to BS connection and the UE's random movement pattern. The primary UE to BS connection is the connection with the highest channel quality index. In the event where joint downlink transmission is not activated, the primary connection will be the only connection that the UE will be receiving signals from. For the consecutive runs, only one base station will be turned on at a time, with UE moving in the same path and speed as in the first simulation run. Since the main focus of this chapter is on joint transmission CoMP, where multiple base stations in a cluster are transmitting to the receiver, the radiating pattern of antenna arrays within a base station is considered as a whole unit and evaluating individual beam radiating from a massive MIMO antenna base station is not within the scope of this chapter. Therefore, the base station is assumed to have a combined radiation pattern similar to a tri-sector antenna.

Simulations of each scenario are sampled at an interval of T_{samp}, such that T_{samp} stays

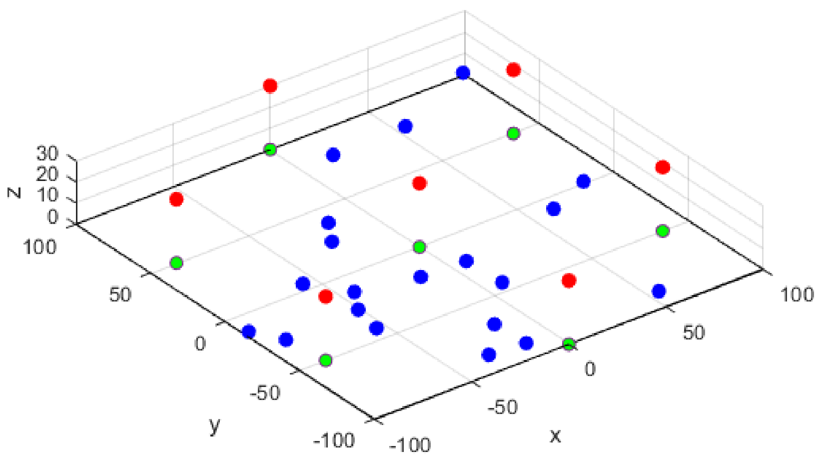

FIGURE 5.4: Scenario B with base station (red [actual position] and green [position at ground level]) and UEs (blue)

within the channel coherence time T_{cor} and the 5G radio frame duration T_{RF}. In the 3GPP Release 16 [222], the radio frame and subframe of 5G new radio (NR) are 10 ms and 1 ms respectively. Since the user is moving at 5 km/h and a 60 GHz carrier frequency is used, the coherence time is approximately 3.6 millisecond, using $T_{cor} \approx \frac{c}{v f_c}$, where c is the speed of light, v is the movement speed of the user, and f_c is the center frequency of the transmitter. Therefore, the sampling period T_{samp} is set to have a duration of 1 millisecond.

5.2.3 Deep Learning based CoMP

As mentioned in section 5.1, the use of MLP based DNN has been demonstrated for the use of triggering CoMP function [219]. The demonstration shows that the MLP based trigger outperforms conventional static SNR based triggering and SVM-based triggering. In this chapter, LSTM is proposed for the use in CoMP along with MLP. LSTM is a type of recurrent neural network (RNN) and has been demonstrated to solve problems involving sequential data. While the input data used in this chapter might not be sequential between each batch input, the columns of the input matrix (shown in equation (5.10)) are correlated. Hence, the unique structure of LSTM wherein includes memory blocks and forget gates, may allow LSTM to outperform MLP.

Following sections are organized as follows. Section 5.2.3.1 describes the input features and the label generation methods used for the proposed deep learning based CoMP. In section 5.2.3.2 and section 5.2.3.3, describes the proposed MLP and LSTM algorithms used.

5.2.3.1 Input and Label Generation

As mentioned in section 5.1, the proposed deep learning algorithms will be evaluated using three approaches. In these three approaches, deep learning algorithms are tasked to either trigger downlink joint transmission CoMP algorithm, select an additional base station for downlink joint transmission CoMP, or provide all possible base station options that meet the predefined CoMP transmission criteria. Each of the three approaches can be posed as classification tasks as listed below

- AP1: Binary Classification
- AP2: Multiclass Classification
- AP3: Multi-label Classification

Although the three approaches are different classification problems, the input matrix X is the same for all three approaches.

$$X = \begin{bmatrix} x_{1\_1} & ..... & x_{1\_N} \\ \vdots & \ddots & \vdots \\ x_{ft\_1} & ..... & x_{ft\_N} \end{bmatrix} \tag{5.9}$$

where ft being the number of features collected from UE from N number of base stations. The number of columns of the input matrix is determined by the number of base stations while the number of rows is determined by the number of input features collected. The input features can be channel state information (CSI) such as UE received power, location, transmitted and received beam angle pair, and CQI; as demonstrated in [214] for beam alignment and [219] for downlink CoMP. Hence, x_{1_1} to x_{ft_1} represents the CSI collected from the first base station; and x_{1_N} to x_{ft_N} represents the CSI collected from the N-th BS.

In this chapter, input X will have two features. The two features are SINR and the UE's receive power, denoted by x_{1_n} and x_{2_n} respectively, where $n = [1, ..., N]$. Hence, the input matrix X can be rewritten as

$$X = \begin{bmatrix} x_{1\_1} & ..... & x_{1\_N} \\ x_{2\_1} & ..... & x_{2\_N} \end{bmatrix} \tag{5.10}$$

where x_{1_1} and x_{2_1} represents the SINR and UE's received signal power for the first BS; x_{1_N} and x_{2_N} represents the SINR and UE's received signal power from the N-th BS. Since SINR and received signal power are measured from the UE's perspective, the measurement of these two features are relative to the position of the UE's position. Therefore, whenever the position of UE changes, the SINR and received signal power from each BS will change. As base stations remain stationary, the measurements taken will only change when UE's position changes.

In AP1, the deep learning CoMP algorithm acts as a trigger switch. Hence, the target output of the algorithm will be

$$Y_{AP1} = \begin{cases} 0 & \text{, CoMP off} \\ 1 & \text{, CoMP on} \end{cases} \tag{5.11}$$

which represents a switch with 1 representing turning the CoMP algorithm on, and 0 representing not turning on the CoMP algorithm. The decision target output label is processed based on the following criteria

$$y_s := 1_{\beta_s \leq \beta_{target}}, \ s = 1, ..., N_s \tag{5.12}$$

where $Y_{AP1} = [y_1, y_2, ..., y_{N_s}]^T$, N_s is the number of samples taken, and β_s and β_{target} are the BLER for s-th sample and the predetermined BLER threshold. When β_s is smaller than or equals to β_{target}, the output label is '1'.

In AP2, the deep learning algorithm is tasked with selecting an additional base station for CoMP where there is already an existing link between UE and one of the base stations. The deep learning algorithm's output will have a range of $[0, N]$. The additional BS is selected if it is not the existing BS that the UE is connected to, and its transmitted signal is above the predefined BLER threshold. If more than one BS fulfills these criteria, the BS with the highest power is selected. Using Scenario B as an example, the output of the deep learning algorithm will range from 0 to 7, and if one-hot encoding [223] is used, all of the possible output can be represented by Table 5.1.

TABLE 5.1: All possible outputs for AP2 using one-hot encoding

None	1	0	0	0	0	0	0	0
Base Station 1	0	1	0	0	0	0	0	0
Base Station 2	0	0	1	0	0	0	0	0
Base Station 3	0	0	0	1	0	0	0	0
Base Station 4	0	0	0	0	1	0	0	0
Base Station 5	0	0	0	0	0	1	0	0
Base Station 6	0	0	0	0	0	0	1	0
Base Station 7	0	0	0	0	0	0	0	1

In AP3, the deep learning algorithm provides all possible BS that meets the predefined criteria for CoMP transmission. A base station is labeled '1' if it transmits below the BLER threshold and if it is not the existing BS that the UE is connected to. For Scenario B, there will be 2^{7-1} possible combinations, ranging from [0 0 0 0 0 0 0] to [1 1 1 1 1 1 0], as shown in Table 5.2.

TABLE 5.2: Possible outputs for AP3

0	0	0	0	0	0	0
0	0	0	0	0	0	1
0	0	0	0	0	1	1
⋮			⋮			⋮
1	1	1	1	1	0	0
1	1	1	1	1	0	1
1	1	1	1	1	1	0

5.2.3.2 Multilayer Perceptron (MLP)

Multilayer Perceptron [224–227] is a type of feed-forward artificial neural network. Artificial neural network (ANN) is inspired by the biological nervous system. The basic unit of ANN is an artificial neuron. In MLP, these neurons are organized in layers and are trained through a backpropagation learning algorithm. A feed-forward neural network consists of three layers (Fig. 5.5): an input layer, a hidden layer, and an output layer. The output of one layer is the input of the consecutive layer, and neurons in each layer are not connected within a layer. Depending on the depth of hidden layers, a neural network can be categorized as a deep neural network or a shallow neural network. In MLP, the output of a single hidden layer can be defined as follows,

$$\mathbf{y}_h = A_f(W^T\mathbf{x} + \mathbf{b}) \tag{5.13}$$

with input vector $\mathbf{x}$, transposed weight matrix W^T, bias vector $\mathbf{b}$ and activation function A_f.

During the training phase of deep learning based CoMP, the deep learning algorithm is optimised to minimise the loss value returned from the loss function. For example, in AP1, where the output is either '0' or '1', the deep learning algorithm is tasked to determine the non-linear boundary separating '0' and '1', such that the neural network can return a value that is as close as possible to the targeted output based on the input vector. If the value deviates from the targeted output, a non-zero loss value is returned from the loss function. In MLP, the feed-forward neural networks' weight matrix and bias vector are updated throughout the training process until the loss curve converges or

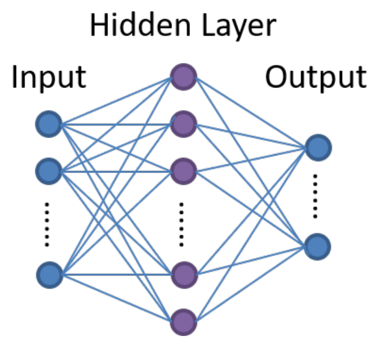

FIGURE 5.5: Feed-forward neural network

when the training process stops. Algorithm 1 shows the training process of the proposed MLP algorithm.

Algorithm 1 MLP Training Algorithm

1: **Input:** Data generated in Section 5.2.2 and arranged in the form of equation (5.10)
2: Data split using 4:1 ratio for training and testing sample
3: **Initialize**: W
4: **while** loss did not converge **do**
5: Calculate output of neural network using equation (5.13);
6: Applying activation function (Softmax or Sigmoid)
7: Calculate loss using BCE or CCE
8: Update weights and biasses of each neural network layer such that loss is being minimized;
9: **end while**

The proposed MLP algorithm is optimized using either binary cross-entropy (BCE) or categorical cross-entropy (CCE) [228]. The binary cross-entropy loss function can be defined as

$$L_{bce} = -\frac{1}{s_o}\sum_{i=1}^{s_o} y_{t\_i}\log\left(y_{p\_i}\right) + \left(1 - y_{t\_i}\right)\log\left(1 - y_{p\_i}\right) \tag{5.14}$$

where s_o is the output size of the deep learning model, y_{t_i} is the ground truth label,and y_{p_i} is the predicted output of the model. The categorical cross-entropy loss function can be defined as

$$L_{cce} = -\sum_{i=1}^{s_o} y_{t\_i}\log\left(y_{p\_i}\right) \tag{5.15}$$

The loss function used depends on the given task. In AP1, the loss function used can either be BCE or CCE depending on the output label. If one-hot encoding is used for AP1, then the loss function used would be CCE. If the output of the model in AP1 is binary, then BCE is used. In AP2, CCE loss function is used when the output labels are in the form of one-hot. For AP3, BCE loss function is used as binary target output is used.

5.2.3.3 Long-Short Term Memory (LSTM)

In contrast to feed-forward neural network, an LSTM layer is much more complex, as shown in Fig. 5.6. LSTM [229–231] is a type of recurrent neural network (RNN). The introduction of LSTM is motivated by the vanishing gradient problem faced by RNN [229, 232]. A single LSTM block unit has three gates: input gate, output gate, and forget gate. These gates within the LSTM blocks allow LSTM to add, prevent, and remove information within the cell state. Memory blocks in the LSTM have access to all gates, preventing irrelevant information from entering and important information from leaving the memory blocks. The forget gate weighs the information within the LSTM cell. For example, when a piece of information held within the LSTM memory block becomes irrelevant, the forget gate can reset the individual cell's state inside the block. Hence, the forget gate prevents prediction biasing by making cells "forget" previous states.

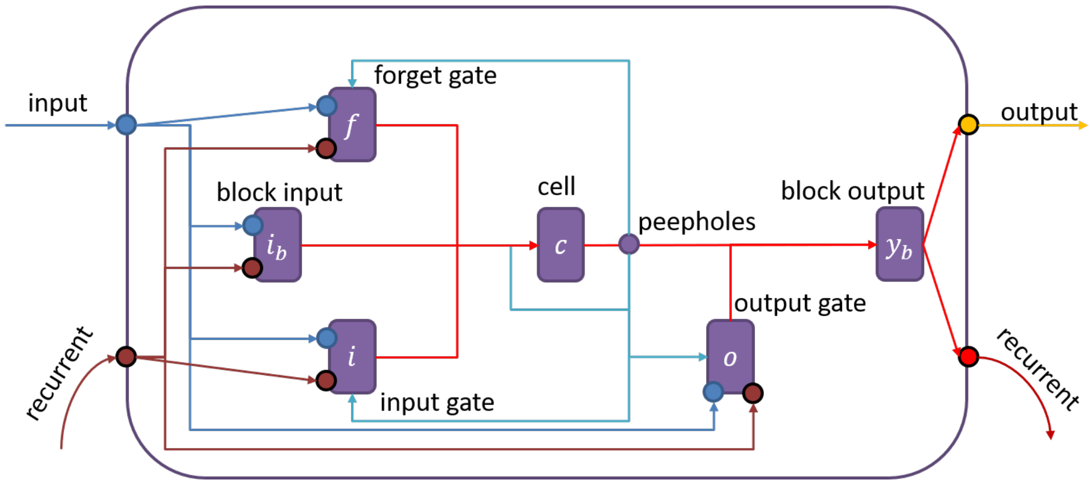

FIGURE 5.6: LSTM block as used in a recurrent neural network layer

An LSTM layer is made up of multiple LSTM blocks, and forward pass output of each blocks at time t can be represented by [233]

$$\mathbf{y}_{blk}(t) = A_{f\_b}(\mathbf{c}(t)) \odot \mathbf{o}(t) \tag{5.16}$$

where $\odot$ is the elemental-wise product and y_{blk} represents the output of an LSTM block with

$$\begin{aligned}
\mathbf{o}(t) &= A_{f_o}\left(W_o\mathbf{x}(t) + W_{r_o}\mathbf{y}_{blk}(t-1) + \mathbf{w}_{p_o} \odot \mathbf{c}(t) + \mathbf{b}_o\right) && \text{output gate}\\
\mathbf{c}(t) &= \mathbf{i}_{blk}(t) \odot \mathbf{i}(t) + \mathbf{c}(t-1) \odot \mathbf{f}(t) && \text{cell}\\
\mathbf{i}_{blk}(t) &= A_{f_i_b}(W_{i_b}\mathbf{x}(t) + W_{r_i_b}\mathbf{y}_{blk}(t-1) + \mathbf{b}_{i_b}) && \text{block input}\\
\mathbf{i}(t) &= A_{f_i}(W_i\mathbf{x}(t) + W_{r_i}\mathbf{y}_{blk}(t-1) + \mathbf{w}_{p_i} \odot \mathbf{c}(t-1) + \mathbf{b}_i) && \text{input gate}\\
\mathbf{f}(t) &= A_{f_f}(W_f\mathbf{x}(t) + W_{r_f}\mathbf{y}_{blk}(t-1) + \mathbf{w}_{p_f} \odot \mathbf{c}(t-1) + \mathbf{b}_f) && \text{forget gate}
\end{aligned} \tag{5.17}$$

with input weight matrices: W_{i_b}, W_i, W_f, W_o ; recurrent weight matrices: $W_{r\_i_b}$, W_{r_i}, W_{r_f}, W_{r_o}; peephole weight vectors: $\mathbf{w}_{p\_i}$, $\mathbf{w}_{p\_f}$, $\mathbf{w}_{p\_o}$; bias: $\mathbf{b}_{i_b}$, $\mathbf{b}_i$, $\mathbf{b}_f$, $\mathbf{b}_o$; and $\mathbf{x}(t)$ being the input vector at time t.

As discussed in section 5.2.3.2, during the training phase, the deep learning algorithm is optimized to minimize the loss value until the loss curve converges. While LSTM layers are more complicated compared to feed-forward neural networks, the training process of LSTM is similar to MLP. During training, the weights and biases of each individual gate within each LSTM block are updated based on the present input and the past hidden states. The LSTM algorithm is also optimized using BCE or CCE loss function. The training of the proposed LSTM algorithm stops when the loss curve converges. Algorithm 2 describes the training process of the proposed LSTM algorithm.

Algorithm 2 LSTM Training Algorithm

```
1: Input: Data generated in Section 5.2.2 and arranged in the form of equation (5.10)
2: Data split using 4:1 ratio for training and testing sample
3: Initialize weights: W_ib, W_i, W_f, W_o, W_r_ib, W_r_i, W_r_f, W_r_o, w_p_i, w_p_f, w_p_o
4: while loss did not converge do
5:     Calculate o(t), c(t), i_blk(t), i(t), f(t) (equations shown in (5.17))
6:     Calculate output of each LSTM block using equation (5.16)
7:     Applying activation function (Softmax or Sigmoid)
8:     Calculate loss using BCE or CCE
9:     Update weights and biasses of each gate and blocks within the LSTM neural
   network layer such that loss is being minimized
10: end while
```

5.2.4 Deep Reinforcement Learning Based CoMP

The method proposed in Section 5.2.3 trains deep learning algorithms using supervised learning where each input is mapped to a targeted output. The targeted output has to be generated based on the objective of the task. For example, if the task is to maximize data throughput, the targeted output for a CoMP problem would be base stations that can transmit at the highest rate based on the data collected. Different tasks would require different targeted labels and have to be generated before any training or testing can be carried out on a given deep learning model. The labels would also change based on the number of base stations within the cooperating CoMP cluster. In static clustering, the cluster size will remain the same. However, in dynamic clustering, cluster size changes according to network conditions. Hence, all possible combinations of dynamic clustering have to be considered before labels are generated.

In contrast, reinforcement learning does not require training with pre-generated labels. The desired output criteria of reinforcement learning can be defined within the reward system. Hence, no preprocessing is needed to map each input to a targeted output. In future generation communication networks where higher RF bands are used, the network's complexity will increase due to densification of network elements. The predefined criteria used to generate the targeted output might not be the best solution for a given CoMP problem.

In general, a simple reinforcement learning setup is composed of two components; an environment and an agent. The relationship between the environment and the agent is such that the agent's actions are a reaction to a given state of the environment. At the same time, the agent's action also creates an effect against the environment it has reacted to. An agent's reward is given based on its actions. The reward is dependent on the intended goal of the assigned problem. For example, if the goal is to escape from a maze, the agent can be rewarded if it successfully escapes from the maze and penalized if it meets a dead end. The agent's aim is to maximize the reward gained. Unlike traditional supervised learning, where training is carried out using training data tied to a corresponding ground-truth label, reinforcement learning learns through its "experience"(penalty and rewards) and can be trained in the absence of the ground truth label.

Deep reinforcement learning (DRL) combines reinforcement learning with deep learning. While RL has shown potential in its application in a wide range of fields [234–240], the performance of RL suffers when state and action spaces are of high dimension [241]. The addition of a deep learning algorithm in reinforcement learning can help efficiently overcome this problem [242]. Deep reinforcement learning has garnered attention when it was successfully demonstrated in playing a range of classic Atari 2600 games, with performance surpassing previous algorithms and comparable to a professional human game tester [241]. This demonstration shows deep reinforcement learning capability in learning challenging tasks with high-dimensional inputs and actions.

In a CoMP problem, the environment will be the area where UEs are present, the agent is the network management algorithm, and reward is given based on the agent's actions. In a real-world scenario, every single telemetry exchange between UE and base station can be used for reinforcement learning without prior bulk data collection. This means that it can be done in real-time and deployed for online learning of non-linear interactions of features from incoming data. Fig. 5.7 shows how a deep reinforcement learning CoMP problem can be formulated. The observer obtains channel state information of the users in a given environment and passes it on to the agent. The observer also rewards the agent based on current state of the environment that has been affected by the agent's previous actions. Rewards given are based on the criteria set within the reward system. The agent's actions are affected by past rewards awarded by the observer, and the current channel state information from the environment. In this chapter, the channel state information is X, and the agent's action will be the additional base station required for downlink CoMP joint transmission.

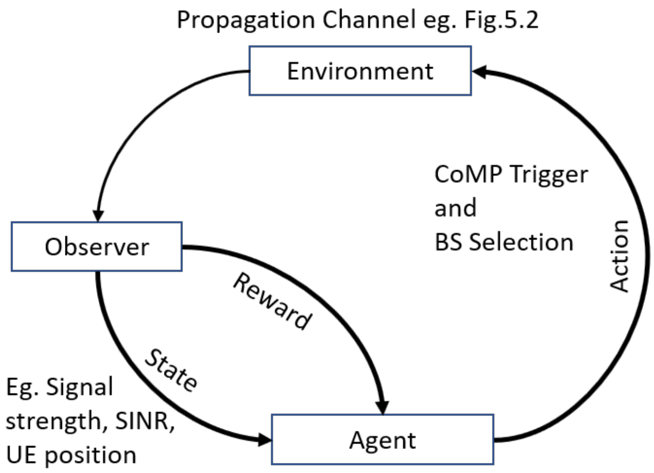

FIGURE 5.7: Deep reinforcement learning for CoMP

In our work, deep Q-network (DQN) is used. DQN combines the use of Q-learning with deep learning. Q-learning is an off-policy model-free reinforcement learning algorithm. An off-policy reinforcement learning algorithm learns from a different policy and not from its derived policy. The Q-learning algorithm is based on Bellman equation [243]. The goal of Q-learning is to maximize the Q value. The optimal Q value can be obtained using [242]

$$Q_{op}(\mathbf{s}, \mathbf{a}) = E_{\mathbf{s}_{t+1}}[r_{t+1} + f_D \max_{\mathbf{a}} Q(\mathbf{s}_{t+1}, \mathbf{a}_{t+1})] \tag{5.18}$$

where $f_D \in [0, 1]$ represents the discount factor, and $\mathbf{s}_t$, $\mathbf{a}_t$ and r_t represent the state, action and reward at time t. For DQN the optimal Q value is

$$Q_{op\_DRL}(\mathbf{s}, \mathbf{a}) = E_{\mathbf{s}_{t+1}}[r_{t+1} + f_D \max_{\mathbf{a}} Q(\mathbf{s}_{t+1}, \mathbf{a}_{t+1}; \theta_{DQN})] \tag{5.19}$$

where θ_{DQN} represents the parameters of the neural network used in DQN. If mean squred error (MSE) loss function is used, the DQN will be optimized using the function shown below [241, 244]

$$L_{mse\_DQN} = E((Q_{op\_DRL} - Q_{DRL})^2) \tag{5.20}$$

with the Q value being Q_{DRL}

$$Q_{DRL}(\mathbf{s}, \mathbf{a}) = E_{\mathbf{s}_{t+1}}[r_{t+1} + f_D Q(\mathbf{s}_{t+1}, \mathbf{a}_{t+1}; \theta_{DQN})] \tag{5.21}$$

Therefore, in this CoMP problem, the data collected will be fed iteratively to the agent in the form of equation (5.10). The agent's action will be selecting the additional base station for joint downlink CoMP transmission, and the agent will be rewarded or penalized based on the selection made. The award given to the agent will be based on the reward criteria of the DRL. For every iteration, the Q value of the DQN based DRL will be updated, the optimal Q value is obtained using equation (5.19), and the weights and biases within DQN will be optimized based on the L_{mse_DQN}.

5.3 Experiment and Results

The proposed deep learning and deep reinforcement learning algorithms are evaluated using three different CoMP approaches. The performance of the proposed MLP, LSTM, and DQN algorithms are compared to SVM in terms of prediction accuracy and computational cost. The training of machine learning algorithms is carried out using Matlab and Tensorflow. SVM training is carried out in MATLAB, and the training for deep learning and deep reinforcement learning is carried out using Keras Tensorflow. Deep reinforcement learning is implemented using Keras Tensorflow by modifying the base code provided in [245, 246].

5.3.1 Dataset

The datasets used were sampled from the data generated using methods described in Section 5.2.2. A dataset of one million points was generated for Scenario A, and two sets of data of the same size were generated for Scenario B. All three datasets have a size of one million data points each.

As shown in Fig. 5.3, Scenario A has only two BSs. To perform a joint downlink CoMP transmission when the predefined transmission criteria are met, and the scene only has two BS. Since UEs in the scene are already assigned to one BS, the option will only be the BS that was not transmitting to the UE. Therefore, only AP1 is applied to Scenario

A. Hence, the label in Scenario A dataset is prepared according to equation (5.11) and equation (5.12). Based on the generated dataset, the ground truth labels consist of 84.28% '1' and 15.72% '0'.

For Scenario B, we considered two datasets, where one is a static dataset, and the other is a dynamic dataset. Datasets generated for Scenario B are used for AP1, AP2, and AP3. The label generation criteria for these three approaches are detailed in Section 5.2.3. The static dataset is used in all three approaches, while the dynamic dataset is only used in AP2. The main difference between these two datasets is the proportion of labels between the training and testing samples. In the static dataset, both training and testing samples have a similar distributed proportion of ground truth labels. Using AP2 as an example, the proportion of label '0' to label '7' distributed between the training and testing sample are similar, as shown in Table 5.3. In the dynamic dataset, as shown in Table 5.4, the proportion of the labels distributed between the training and testing sample are different. In both tables, Table 5.3 and Table 5.4, the total number of labels within each training and testing sample are listed with its corresponding proportion with respect to the total number of data points within a sample.

The proportion of the distributed labels are calculated in percentage relative to the total number of samples as shown below

$$\text{Distribution of } N_{label} \text{ of } Y_{AP2} = \frac{\text{Total no. of } N_{label}}{\text{Total no. of Samples}} \tag{5.22}$$

where $N_{label} = \{\text{'0','1','2','3','4','5','6','7'}\}$ refers to the ground truth labels of AP2. The total number of samples refers to the total number of samples within the training sample or testing sample. The total number of N_{label} refers to the total number of N_{label} within the training or testing sample.

TABLE 5.3: Static Dataset Labels for AP2

	Training + Validation		Testing	
Label	Data Points	Distribution	Data Points	Distribution
0	81661	10.21%	20401	10.20%
1	70533	8.82%	17674	8.84%
2	45964	5.75%	11681	5.84%
3	57132	7.14%	14219	7.11%
4	253265	31.66%	63449	31.72%
5	84398	10.55%	21106	10.55%
6	62274	7.78%	15463	7.73
7	14473	18.10%	36007	18.00%
total	80000	100%	200000	100%

TABLE 5.4: Dynamic Dataset Labels for AP2

	Training + Validation		Testing	
Label	Data Points	Distribution	Data Points	Distribution
0	57790	7.22%	44272	22.14%
1	78169	9.77%	10038	5.02%
2	40962	5.12%	16683	8.34%
3	50194	6.27%	21157	10.58%
4	277632	34.70%	39082	19.54%
5	93951	11.74%	11553	5.78%
6	56358	7.04%	21379	10.69%
7	144944	18.12%	35836	17.92%
total	80000	100%	200000	100%

The dynamic dataset is used to mimic a scenario where the scene changes with time. For example, assuming that the distribution of labels reflects UEs' activity within a given area of a city for a certain period of time, let's say a year. As time goes by, the dynamic of the city will change, and so will the movements and distribution of UEs. An event that occurs within an area or neighboring area might influence the movements of users as well. The main reason for the generation of the dynamic dataset is to test how well the deep learning algorithms can perform in an 'unexpected' event where the algorithms have not been trained for.

For the static dataset, the maximum and minimum difference in label distribution between the training and testing set are 0.95% and 0.00325% respectively. The difference is much bigger for the dynamic dataset with a maximum and minimum label distribution difference of 15.163% and 0.2% respectively. A detailed training and testing label distribution difference for each label is provided in Table 5.5.

TABLE 5.5: Training and Testing Data Distribution Difference

	Static	Dynamic
Label	Differences	Differences
0	0.007125%	14.91%
1	0.020375%	4.75%
2	0.095%	3.22%
3	0.032%	4.30%
4	0.066375%	15.16%
5	0.00325%	5.96%
6	0.05275%	3.64%
7	0.09325%	0.20%
Average	0.04625%	6.52%
Max	0.095%	15.16%
Min	0.00325%	0.20%

5.3.2 Experimental Setup

Fig. 5.8 shows the general architecture of a neural network. Both MLP and LSTM have five layers: an input layer, three hidden layers, and an output layer. The proposed MLP and LSTM algorithms have three hidden layers because increasing the depth of the neural network architecture did not result in a noticeable performance improvement. For the proposed MLP algorithm, three densely connected neural network layers are used. Moreover, the proposed LSTM algorithm's hidden layers consist of two LSTM layers and a densely connected neural network layer. For DQN, two densely connected neural networks are used. Table 5.6 provides the settings used for different neural network layers.

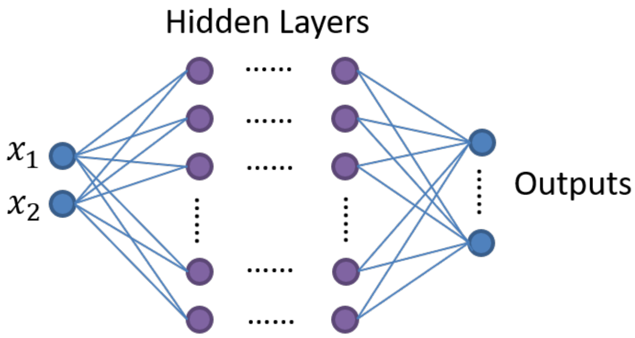

FIGURE 5.8: An example of the neural network architecture used for deep learning based CoMP

TABLE 5.6: Deep learning algorithm neural network parameters

Deep Learning Algorithms	Parameter Values
Densely connected neural network layer (MLP)	nodes: 250
LSTM	No of block(s): 50

The following table (Table 5.7) shows the parameters used for training the deep learning algorithms. An initial learning rate as low as 10^{-4} and up to 10^{-3} is used. The learning rate decay is set to have a constant decaying rate ranging from 10^{-4} to 10^{-3}. Adam optimizer is used for MLP, LSTM, and DQN. BCE loss function is used for AP1 and AP3, while CCE is used for AP2. DQN uses MSE loss function. All models are trained until the loss function converges. Hence, up to 4000 epochs were run to ensure that the loss function has fully converged.

TABLE 5.7: Training Parameters

Parameters	Values
Learning rate	10^{-4} - 10^{-3}
Learning rate decay	10^{-4} to 10^{-3}
Optimizer	Adam
Loss function	BCE, CCE, MSE
Batch size/ Steps	MLP/LSTM: 125 to 250 DQN :20
Epochs	200 - 4000

TABLE 5.8: AP1 (Prediction Accuracy)

Scenario	Scenario A	Scenario B
SVM	99.53%	89.59%
MLP	99.90%	96.95%
LSTM	96.18%	96.90%

5.3.3 Deep Learning Algorithm as a Trigger (AP1)

Results for AP1 are shown in Table 5.8. The test for AP1 is carried out in both Scenario A and Scenario B (static data) using SVM, MLP, and LSTM. The deep learning algorithm is trained until both its loss curve and accuracy curve converges, as shown in Fig. 5.9. The algorithms' performances are compared to observe their accuracy in triggering the CoMP algorithm "on" or "off". The accuracy of each algorithm is calculated using the equation below

$$\text{Accuracy} = \frac{\text{Total no. of True Predictions}}{\text{Total no. of Samples}} \tag{5.23}$$

For Scenario A, SVM, MLP, and LSTM achieves an accuracy of 99.53%, 99.9%, and 96.18% respectively. For Scenario B, an accuracy of 89.59%, 96.95%, and 96.9% is recorded for SVM, MLP, and LSTM respectively. For both scenarios, the results suggest that MLP performs better than both SVM and LSTM for AP1. While SVM performs better than LSTM in Scenario A, in Scenario B, LSTM performs better than SVM. In scenario A, MLP has a 3.72% advantage over LSTM. However, while MLP still performs better than LSTM in Scenario B, the advantage gap drops to 0.05%.

5.3.4 Selecting Base Station for Joint Downlink CoMP (AP2)

The test on AP2 is carried out on Scenario B using both static and dynamic dataset. Since both datasets have imbalanced labels, where label '4' takes up around 30% of the total number of labels, as shown in Table 5.4. The labels are weighted using the equation

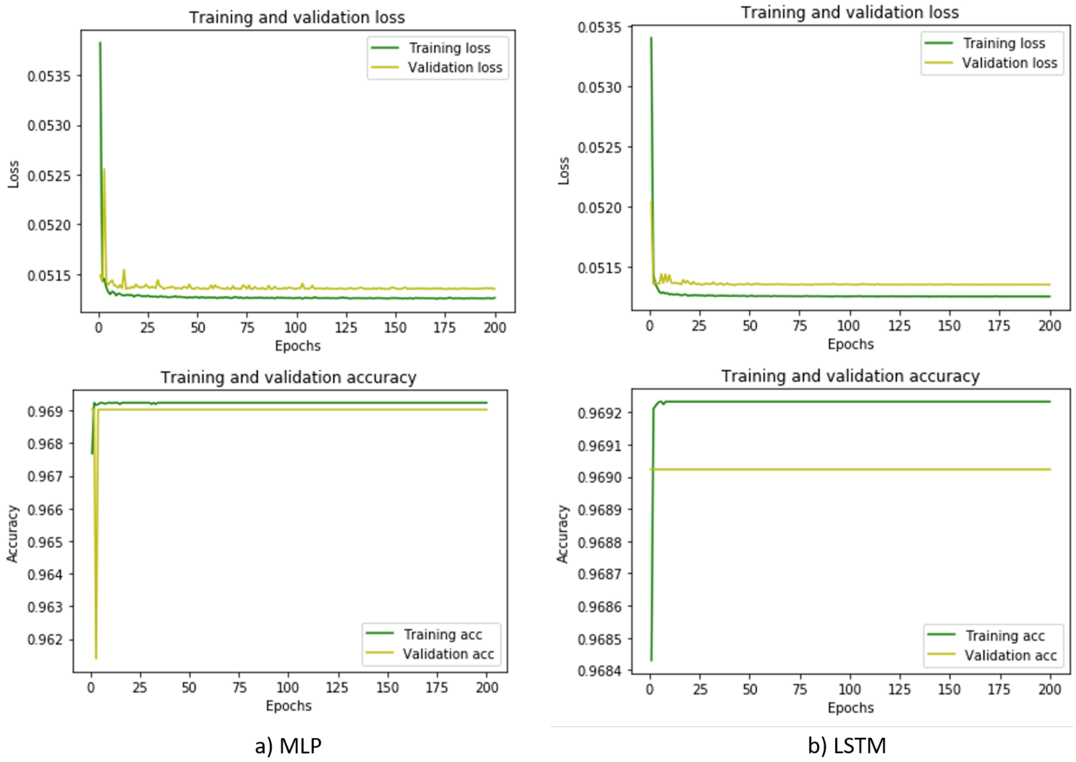

FIGURE 5.9: (AP1) Loss (top) and accuracy (bottom) curve for a) MLP and b) LSTM

below

$$\text{Weight of } N_{label} = \frac{\text{Total no. of Samples}}{\text{No. of Classes} \times \text{Total no. of } N_{label}} \tag{5.24}$$

Using equation (5.24), the labels are weighted such that the least frequent label will be weighted higher than the most frequently occurring label. In AP2, the total number of classes is eight. The neural networks are trained until both of the loss and accuracy curve converges, as shown in Fig. 5.10 and Fig. 5.11.

TABLE 5.9: DQN Agent reward

BS select	Reward/Penalty value
Correct	$+1$
Wrong (>BLER)	-1
Wrong (<BLER)	0

In AP2, the performance of DQN is added for comparison with SVM, MLP, and LSTM. The agent in the deep Q-network is awarded if it selects the correct BS. However, if the agent selects a BS that is not the intended BS, it will be penalized if the selected BS does not fulfill the predefined BLER threshold. If the selected BS transmits below the predefined BLER threshold, the agent will neither be rewarded nor penalized. Table 5.9 summarizes the reward criteria for DQN.

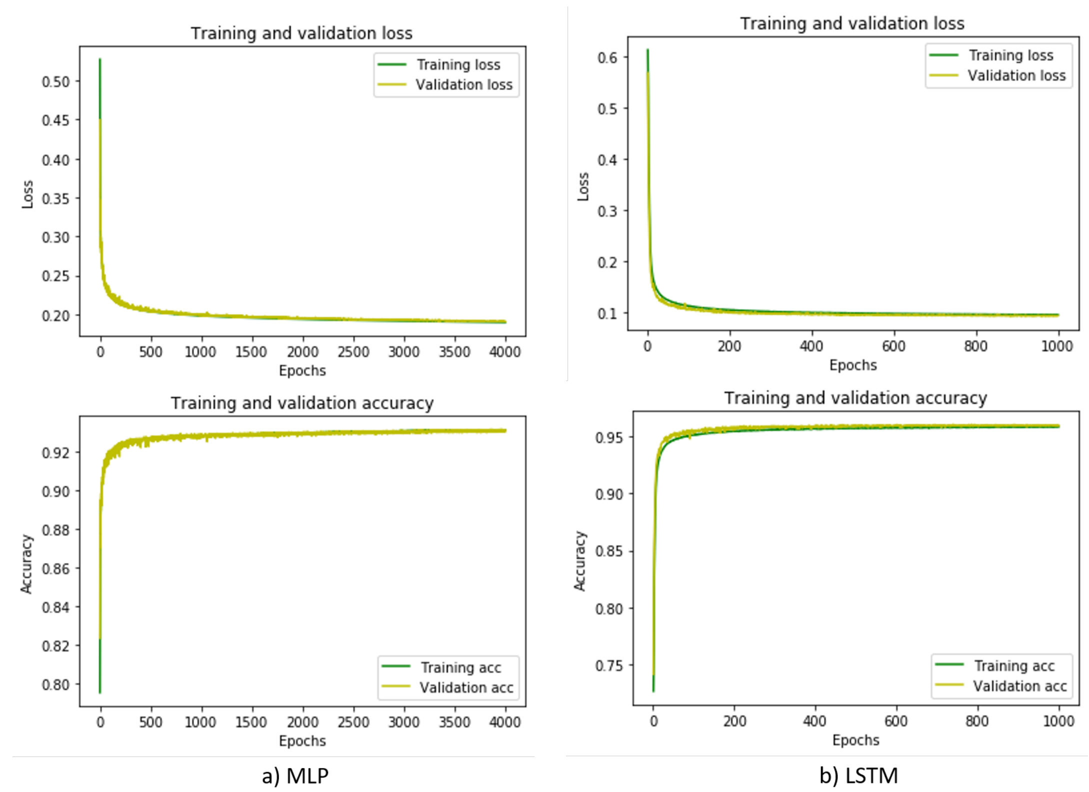

FIGURE 5.10: (AP2) Loss (top) and accuracy (bottom) curve for a) MLP and b) LSTM

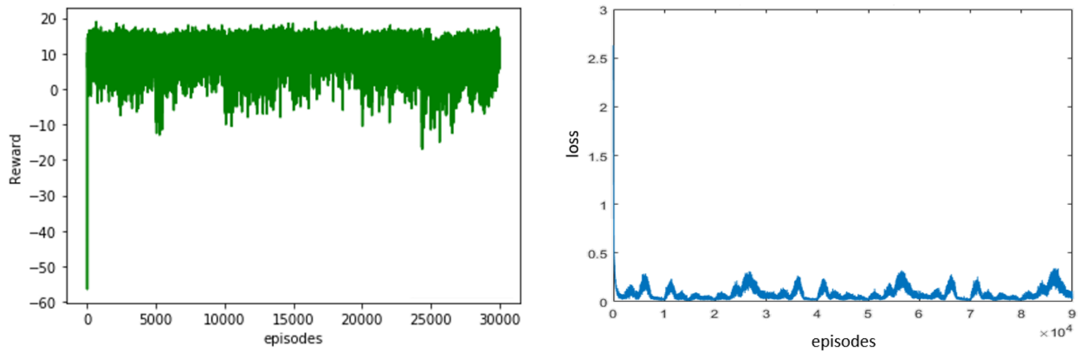

FIGURE 5.11: (AP2) Reward (left) and loss (right) curve for DRL

When both training and testing dataset have the same proportion of distributed labels (static), SVM, MLP, LSTM, and DRL achieves an accuracy of 69.05%, 93.94%, 95.95%, and 94.11% respectively. When the distribution differs between the training and testing set (dynamic), an accuracy of 55.53%, 56%, 68.60%, and 71.85% is achieved by SVM, MLP, LSTM, and DRL respectively. The results of both datasets are tabulated in Table 5.10.

Referring to Table 5.8 and Table 5.10, the results suggest that if the neural network output is not affected by the sequence of which the input is fed, the LSTM algorithm has no advantage against MLP. Taking Scenario B in AP1 as an example, if the column

Table 5.10: AP2 (Prediction Accuracy)

Scenario B	Static	Dynamic
SVM	69.05%	55.53%
MLP	94.65%	56.00%
LSTM	95.95%	68.60%
DRL	94.11%	71.85%

position of the input vector, as shown in equation (5.10), were to be switched in every single input, it will have no effect on the trigger output. The neural network output is not dependent on the sequence within the input vector. However, when the neural network output depends on the sequence within the input vector, LSTM performs better than MLP. In general, LSTM performs the best for static dataset, and the deep Q network used for DRL performs best for dynamic dataset. Since the dynamic set is sampled in time sequence, the DRL algorithm that is continuously updating and learning from the environment is expected to perform better.

5.3.5 Providing Possible Base Station Options for Joint Downlink CoMP (AP3)

AP3 is carried out using SVM, MLP, and LSTM using Scenario B's static data. While the input vector remains the same, the truth label is different from AP2 (shown in Table 5.3) as the target labels for AP3 provide all possible BS that fulfills the predefined requirements for CoMP transmission. The deep learning algorithms are trained until the loss and accuracy curve converges, similar to AP1 and AP2. The results obtained are shown in Table 5.11. The predicted output is considered correct only if it is an exact match to the target output. Using this rule, SVM, MLP, and LSTM achieved an accuracy of 70.52%, 78.8%, and 78.9% respectively. However, if the prediction accuracy is calculated based on the individual label, the prediction accuracy increases to more than 90%, with SVM achieving an accuracy of 94.3%, and 96.1% for both MLP and LSTM.

Table 5.11: AP3 (Prediction Accuracy)

Scenario B	AP3
SVM	70.52%
MLP	78.80%
LSTM	78.90%

5.3.6 Computational Cost

Table 5.12 compares the computation time taken by SVM, MLP, LSTM, and DQN to provide predicted outputs based on inputs from the static dataset's testing sample. The testing sample has a size of 200,000 data points. The test was performed on a workstation equipped with an Intel Xeon E5-2650v3 processor, 256GB of RAM, and an NVIDIA Geforce GTX 1080.

Overall, it can be seen that DQN demands the highest computational time with more than 25 minutes taken to process the entire testing sample, while other algorithms' computational time falls within the 10 second range. However, it is to note that rewards are still being calculated during the testing phase of DQN. Therefore, the DQN based DRL has to evaluate the agent's actions and reward the agent based on the actions taken. This would lead to a longer computational time as more processing is required. In a similar scenario, if the proposed deep learning algorithms' computational time includes evaluating the predicted output with the ground truth label, the computational time of MLP will increase from 1.43 seconds to 632.07 seconds, and the computational time of LSTM will increase from 8.34 seconds to 630.91 seconds. However, both algorithms still demand less than half of the computation time of DQN. In general, MLP demands the lowest computational time, followed by SVM, LSTM, and DQN.

TABLE 5.12: Computational cost per testing sample on Scenario B static dataset

Scenario B	Computational Time (s)
SVM	2.42
MLP	1.43
LSTM	8.34
DQN	1527.53

5.4 Summary

A deep learning and deep reinforcement learning based downlink joint transmission CoMP were demonstrated using MLP, LSTM, and DQN. The results obtained were compared with SVM. In general, the deep learning and deep reinforcement learning algorithms perform better than SVM. The results suggest that in situations where the sequence of the input vector matters, LSTM can perform better than MLP. However, when the input vector sequence is irrelevant, MLP performs better than LSTM. In an environment that is constantly changing, DQN based reinforcement learning algorithm can perform better than both LSTM and MLP. However, DQN demands the most computational time, followed by LSTM, SVM, and MLP.

Chapter 6

Deep Learning based Phase Noise Tolerant Millimeter-wave Radio-over-Fiber Receiver

6.1 Introduction

In chapter 3 and chapter 4, we demonstrated three different differential encoded millimeter-wave RoF schemes. Two optical baseband modulated DPSK millimeter-wave RoF links were demonstrated in chapter 3, and an optical baseband modulated DQPSK millimeter-wave RoF link was demonstrated in chapter 4. The proposal of the use of differential encoded signal in millimeter-wave RoF links were mainly motivated by three things: the simplicity of an uncorrelated millimeter-wave RoF transmitter, the phase noise tolerance of an SH receiver [133, 191], and the inability of an SH based receiver to directly detect phase modulated signal as explained in chapter 3.1. The results obtained from the demonstrated links in chapter 3 and chapter 4 suggest that the usage of differential encoded data with its DAM receiver enables the proposed schemes to have the ability to directly detect phase-modulated data while maintaining relatively tolerant to phase noise and bandwidth-efficient. While the delay used in a DAM receiver, as shown in Fig. 3.2 and Fig. 4.1, allows the detector to reduce the phase noise inherited from an uncorrelated optical transmitter, its presence prevents the use of non differentially encoded signal to be used. For higher-order modulation, the time delay used in the DAM receiver increases, which would cause the residual phase noise to increase, leading to a drop in detection performance as suggested by the results obtained in chapter 4. However, dynamic modulation format selection based on channel quality is supported in wireless communication, and this feature would be a problem for the incoherent DAM receiver proposed and demonstrated in chapter 3 and chapter 4 as it limits the choice of modulation format and the phase noise residual increases with increasing modulation order.

As discussed in chapter 2, the use of uncorrelated optical tones causes phase noise to propagate from the optical transmitter to the RF receiver due to unlock heterodyning. While conventional optical tone generation methods, as shown in Fig. 2.6 to Fig. 2.8, can generate phase correlated optical tones, these methods require high-speed optoelectronics and oscillators that operate in the millimeter-wave frequency range. Although optical tone generation using optical frequency multiplication reduces the reliance on high-speed components through varying advanced modulation techniques and/or optical filtering, it is limited by the harmonic generation efficiency of the modulator used, and the transmitter configuration is more complicated than unlocked heterodyning ARoF systems. To exploit the benefit of using a simple unlock heterodyning ARoF transmitter, SH-based receivers were proposed and demonstrated in [65, 192]. However, phase-modulated signals cannot be directly detected using SH receiver as the phase integrity of the signal will be corrupted. To maintain the phase integrity of phase-modulated signals, SH-based IF-RoF system [193] introduces an additional tone at the SH receiver. The additional tone causes the received millimeter-wave signal to be downconverted to IF so that the phase of the received signal is retained. However, the additional bandwidth required to transmit the additional RF tone will decrease the overall spectral efficiency of the system. Therefore, new transceivers for unlocked heterodyning ARoF systems that are more robust to phase noise has to be explored to enable low-cost unlock heterodyning RoF systems to be used in future generation high order modulation fiber-wireless communication.

In recent years, the application of machine learning (ML) in optical communication has been an active research topic. The use of ML has been demonstrated in optical performance monitoring [37, 38], link equipment failure prediction [247], and linear and non-linear noise estimation [248]. Besides, an ML-based classifier to mitigate nonlinear phase noise through applying nonlinear decision boundary using support vector machine (SVM) was demonstrated in [249]. In addition, feed-forward neural network has been applied as a nonlinear equalizer for nonlinear distortions of millimeter-wave RoF links. These demonstrations show that the feed-forward neural network can improve system sensitivity by up to 2 dB [172], and suppresses cross-modulation nonlinearity [173, 174]. Deep learning based decoder has been demonstrated in [175, 176], showing that the CNN based decoder can improve link sensitivity and perform better than multilayered feed-forward neural networks while requiring less computation. However, the CNN based decoder is carried out in a millimeter-wave RoF link that uses correlated optical tones, and as discussed in chapter 2, heterodyning of correlated tones can reduce nonlinear phase noise contributed by the optical source.

In this chapter, we propose two deep learning based RoF receiver that is capable of improving signal detection in the presence of phase noise. While ML-based phase noise receiver has been explored and demonstrated in [249], only SVM-based algorithm is used. Furthermore, phase noise reduction through SH-based receiver requires additional bandwidth and cannot be used directly on phase-modulated data. The proposed receiver is bandwidth-efficient, adaptable to various RoF setups, and flexible in terms of data rate and modulation format. The proposed receiver is demonstrated using a QPSK RoF link in two different scenarios as listed below:

- Deep learning based direct detection (DLDD)
- Deep learning based detection with reference tone (DLD-RT)

In DLDD, detection is carried out on sampled downconverted phase noise corrupted received signal; and DLD-RT detects signal using an additional reference tone in addition to the sampled received signal. The reference tone can be generated in the transmitter using an oscillator operating at a frequency close to the modulated IF signal. In this chapter, we propose the use of autoencoder-based deep learning architecture for DLDD and LSTM for DLD-RT. The contributions of the chapter are as follows:

- Propose, demonstrate and evaluate the use of autoencoder and LSTM deep learning based receiver for millimeter-wave RoF system
- Comparing proposed deep learning receiver with MLP and CNN based deep learning receiver.
- Improve overall spectral efficiency of RoF receivers relative to SH receiver based intermediate frequency radio-over-fiber (IF-RoF) link through reducing required frequency spacing between RF frequencies.

The chapter is organized as follows. Section 6.2 provides a theoretical analysis on an intermediate frequency radio-over-fiber link using an oscillator-based receiver, and describes the model of the proposed deep learning algorithm. Section 6.3 describes the experimental details and provides a discussion on the results obtained. Section 6.4 concludes the chapter.

6.2 Proposed Deep Learning based RoF Receivers

The proposed deep learning based receiver are demonstrated on an unlocked heterodyning intermediate frequency radio-over-fiber (IF-RoF) system with an oscillator-based receiver, as shown in Fig. 6.1. Heterodyning of unlocked optical tones will cause phase noise to propagate from the transmitter to the receiver as the base station has no additional processing capability. Unlike self-homodyning based receivers, oscillator based receiver used in this setup has no phase noise reduction capability. Hence, the deep learning based RoF receiver is proposed to improve signal detection in the presence of phase noise.

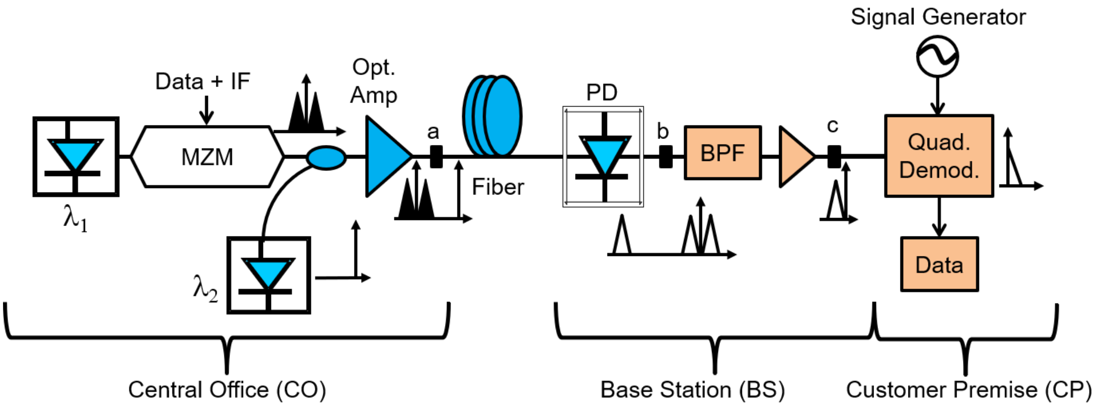

FIGURE 6.1: Intermediate frequency radio-over-fiber setup

This section is organized as follows. Section 6.2.1 provides a theoretical analysis on the IF-RoF system shown in Fig. 6.1. Section 6.2.2 describes the proposed autoencoder model for DLDD, and section 6.2.3 describes the deep learning model used for DLD-RT.

6.2.1 Oscillator based receiver on IF-RoF

For an IF-RoF link as shown in Fig. 6.2, the output of the Mach-Zehnder modulator (MZM) can be represented by:

$$E_{M_{osc}}(t) = AE_1(t)e^{j\frac{\pi}{V_{\pi RF}}v(t)} \tag{6.1}$$

where $v(t)$ is the IF signal, $V_{\pi RF}$ is the switching voltage of the modulator, $E_1(t)$ is the output of the first laser with a wavelength of λ_1, as shown in Fig. 6.2, and A is the gain of the modulator, and it is affected by the voltage supply, extinction ratio and the split ratio of the modulator. Let $v(t) = \cos(2\pi f_{IF}t)$,

$$E_{M_{osc}}(t) = AE_1(t)e^{j\frac{\pi}{V_{\pi RF}}\cos(2\pi f_{IF}t)} \tag{6.2}$$

Applying Jacobi-Anger expansion [250, 251]:

$$e^{jzcos(\theta)} \equiv J_0(a) + 2\sum_{n=1}^{\infty} j^n J_n(a)\cos(n\theta)$$

and let $a = \frac{\pi}{V_{\pi RF}}$, equation (6.2) could be written as follows

$$\begin{aligned} E_{M_{osc}}(t) &= AE_1(t)(J_0(a) + \\ & 2\sum_{n=1}^{\infty} j^n J_n(a)\cos(n2\pi f_{IF}t)) \end{aligned} \tag{6.3}$$

For simplicity, let $n = 1$ and ignore higher-order harmonics

$$\begin{aligned} E_{M_{osc}}(t) &= AE_1(t)(J_0(a) + j^1 2J_1(a)\cos(2\pi f_{IF}t)) \\ &= AE_1(t)(J_0(a) + jJ_1(a)[e^{j2\pi f_{IF}t} \\ &\qquad +e^{-j2\pi f_{IF}t}]) \end{aligned} \tag{6.4}$$

Substituting $E_1(t) = e^{j(\omega_1 t + \phi_1(t))}$,

$$\begin{aligned} E_{M_{osc}}(t) &= Ae^{j(\omega_1 t+\phi_1(t))}(J_0(a) + jJ_1(a)[e^{j2\pi f_{IF}t} \\ & +e^{-j2\pi f_{IF}t}]) \\ &= Ae^{j(\omega_1 t+\phi_1(t))}J_0(a) \\ & +jAJ_1(a)[e^{j(\omega_1 t+2\pi f_{IF}t+\phi_1(t))} \\ & \qquad +e^{j(\omega_1 t-2\pi f_{IF}t+\phi_1(t))}] \end{aligned} \tag{6.5}$$

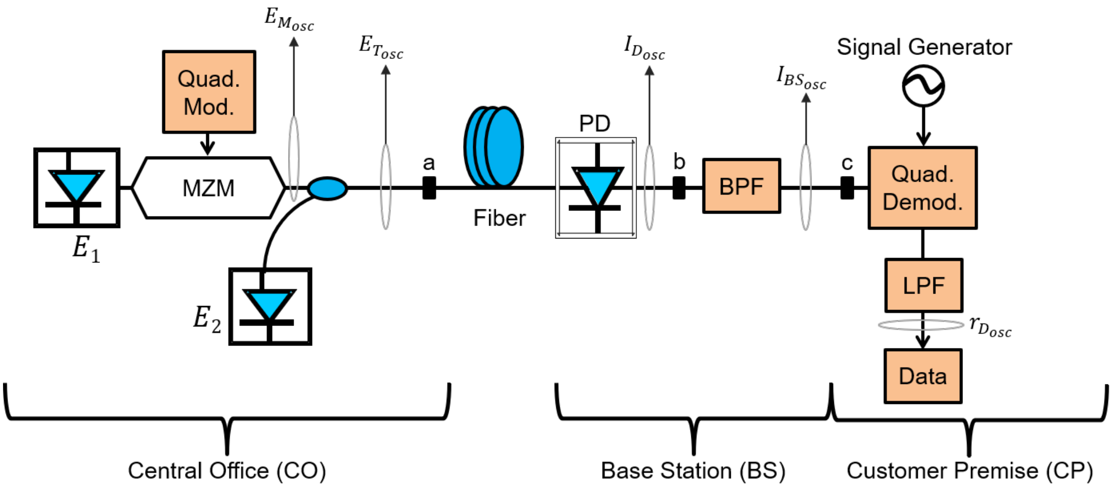

FIGURE 6.2: Intermediate frequency radio-over-fiber with oscillator based receiver with output labels

where $\phi_1(t)$ is the phase noise contributed by the first laser, and ω_1 is the angular frequency of the first laser. Before transmitting out from the central office (CO), the output of the modulator is coupled with a local oscillator (LO) laser $E_2(t)$. The output signal from the CO can be represented as follows

$$\begin{aligned}
E_{T_{osc}}(t) &= E_{M_{osc}}(t) + E_2(t) \\
E_{T_{osc}}(t) &= Ae^{j(\omega_1 t+\phi_1(t))}J_0(a) \\
&\quad +jAJ_1(a)[e^{j(\omega_1 t+2\pi f_{IF}t+\phi_1(t))} \\
&\quad +e^{j(\omega_1 t-2\pi f_{IF}t+\phi_1(t))}] + e^{j(\omega_2 t+\phi_2(t))}
\end{aligned} \tag{6.6}$$

where $\phi_2(t)$ is the phase noise of the LO laser. After heterodyning photodiode detection, the photocurrent can be represented as:

$$\begin{aligned}
I_{D_{osc}}(t) &= E_{T_{osc}}(t) \times E^*_{T_{osc}}(t) \\
I_{D_{osc}}(t) &= (Ae^{j(\omega_1 t+\phi_1(t))}J_0(a) \\
&\quad +jAJ_1(a)e^{j(\omega_1 t+2\pi f_{IF}t+\phi_1(t))} \\
&\quad +jAJ_1(a)e^{j(\omega_1 t-2\pi f_{IF}t+\phi_1(t))} + e^{j(\omega_2 t+\phi_2(t))}). \\
&\quad (Ae^{-j(\omega_1 t+\phi_1(t))}J_0(a) \\
&\quad -jAJ_1(a)e^{-j(\omega_1 t+2\pi f_{IF}t+\phi_1(t))} \\
&\quad -jAJ_1(a)e^{-j(\omega_1 t-2\pi f_{IF}t+\phi_1(t))} \\
&\quad +e^{-j(\omega_2 t+\phi_2(t))})
\end{aligned} \tag{6.7}$$

where $E^*_{T_{osc}}(t)$ is the conjugate of $E_{T_{osc}}(t)$. Expanding equation (6.7),

$$\begin{aligned}
I_{D_{osc}}(t) &= 1 + A^2J_0^2(a) - jA^2J_0(a)J_1(a)e^{-j(2\pi f_{IF}t)} \\
&\quad -jA^2J_0(a)J_1(a)e^{+j(2\pi f_{IF}t)} \\
&\quad +AJ_0(a)e^{j(\Delta\omega t+\Delta\phi(t))} \\
&\quad +jA^2J_0(a)J_1(a)e^{j(2\pi f_{IF}t)} + A^2J_1^2(a) \\
&\quad +A^2J_1^2(a)e^{j(4\pi f_{IF}t)} \\
&\quad +jAJ_1(a)e^{j(\Delta\omega t+2\pi f_{IF}t+\Delta\phi(t))} \\
&\quad +jA^2J_0(a)J_1(a)e^{-j(2\pi f_{IF}t)} \\
&\quad +A^2J_1^2(a)e^{-j(4\pi f_{IF}t)} + A^2J_1^2(a) \\
&\quad +jAJ_1(a)e^{j(\Delta\omega t-2\pi f_{IF}t+\Delta\phi(t))} \\
&\quad +AJ_0(a)e^{-j(\Delta\omega t+\Delta\phi(t))} \\
&\quad -jAJ_1(a)e^{-j(\Delta\omega t+2\pi f_{IF}t+\Delta\phi(t))} \\
&\quad -jAJ_1(a)e^{-j(\Delta\omega t-2\pi f_{IF}t+\Delta\phi(t))}
\end{aligned} \tag{6.8}$$

Simplifying equation (6.8),

$$
\begin{aligned}
I_{D_{osc}}(t) &= 1 + A^2 J_0^2(a) + 2A^2 J_1^2(a) \\
&\quad -j2A^2 J_0(a) J_1(a) \cos(2\pi f_{IF} t) \\
&\quad +2AJ_0(a) \cos(\Delta\omega t + \Delta\phi(t)) \\
&\quad +j2A^2 J_0(a) J_1(a) cos(2\pi f_{IF} t) \\
&\quad +2A^2 J_1^2(a) \cos(4\pi f t) \\
&\quad +jAJ_1(a)(2j \sin(\Delta\omega t + 2\pi f_{IF} t + \Delta\phi(t)) \\
&\quad +jAJ_1(a)(2j \sin(\Delta\omega t - 2\pi f_{IF} t + \Delta\phi(t)) \\
&= 1 + A^2 J_0^2(a) + 2A^2 J_1^2(a) \\
&\quad +2AJ_0(a) \cos(\Delta\omega t + \Delta\phi(t)) \\
&\quad +2A^2 J_1^2(a) \cos(4\pi f t) \\
&\quad +j2AJ_1(a)(j \sin(\Delta\omega t + 2\pi f_{IF} t + \Delta\phi(t)) \\
&\quad +j2AJ_1(a)(j \sin(\Delta\omega t - 2\pi f_{IF} t + \Delta\phi(t))
\end{aligned}
$$

Before the signal is transmitted wirelessly to the CP from the BS, the signal is bandpass filtered to obtain the desired millimeter-wave frequency signal at $\omega_{mm} = \Delta\omega - 2\pi f_{IF}$. The output signal from the BS can be represented by

$$
\begin{aligned}
I_{BS_{osc}}(t) &= -2AJ_1(a)(\sin(\Delta\omega t - 2\pi f_{IF} t + \Delta\phi(t))) \\
I_{BS_{osc}}(t) &\propto \cos(\Delta\omega t - 2\pi f_{IF} t + \Delta\phi(t) + \frac{\pi}{2})
\end{aligned} \tag{6.9}
$$

where $\Delta\omega t = \omega_1 t - \omega_2 t$, and $\Delta\phi(t) = \phi_1(t) - \phi_2(t)$. At the receiver located in the CP, the received signal from the base station (BS) will be downconverted to IF using an oscillator to extract the transmitted IF signal ($v(t)$):

$$
\begin{aligned}
r_{D_{osc}}(t) &\propto \cos(\Delta\omega t - 2\pi f_{IF} t + \Delta\phi(t) + \frac{\pi}{2}) \times \\
&\quad \cos(\Delta\omega t + \phi_{osc}(t)) \\
&\propto \frac{1}{2}(\cos(2\Delta\omega t - 2\pi f_{IF} t + \Delta\phi(t) \\
&\qquad\qquad + \phi_{osc}(t) + \frac{\pi}{2}) \\
&\quad + \cos(-2\pi f_{IF} t + \Delta\phi(t) - \phi_{osc}(t) \\
&\qquad\qquad + \frac{\pi}{2}))
\end{aligned} \tag{6.10}
$$

where $\phi_{osc}(t)$ is the phase noise of the RF oscillator. After lowpass filtering, the signal at IF can be represented by

$$
r_{D_{osc}}(t) \propto \frac{1}{2} cos(-2\pi f_{IF} t + \Delta\phi(t) - \phi_{osc}(t) + \frac{\pi}{2})) \tag{6.11}
$$

The received downconverted signal (6.11) inherits the phase noise $\Delta\phi(t)$ from the optical transmission system due to unlock heterodyning detection of uncorrelated optical tones. The inherited phase noise from the optical source can drastically degrade link performance during detection. The higher the order of modulation, the more sensitive it is to phase noise. This could pose a serious problem for 1024 QAM proposed to be used for 5G and Gigabit Long-Term Evolution (LTE) [8]. The proposed DLDD and DLD-RT receiver can be used to improve signal detection in the presence of phase noise. The proposed receivers can be used as an complementary solution together with existing hardware based phase noise reduction techniques to improve detection in the presence of residue phase noise, or as an alternative solution for SH based RoF system.

6.2.2 Deep learning based direct detection (DLDD)

Denoising autoencoder (DAE) and variational autoencoder (VAE) are proposed for DLDD. DAE has shown potential in reproducing signal from noise corrupted signal in electrocardiogram [252, 253], corrupted linguistic features in audio documents [30], and radar pulse streams [254]. VAE has also shown potential in recovering "clean" signal from a noisy signal in speech enhancement [31], and speech recognition [32]. Therefore in this problem, DAE and VAE are used to recover "clean" signal from the phase corrupted signal sampled from the received signal of the configuration shown in Fig. 6.3.

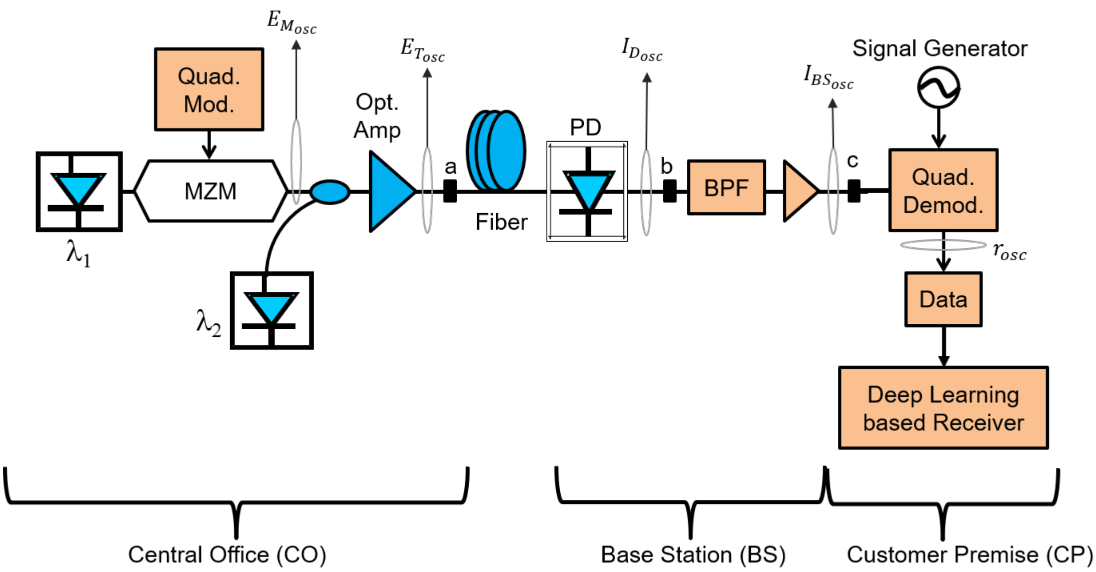

FIGURE 6.3: Deep learning based direct detection configuration

An autoencoder, as shown in Fig. 6.4, can be seperated into two parts: encoder and decoder. Conventionally, autoencoders are used in unsupervised learning where the ground truth values is also the input, $y_i = x_i$ where y_i is the ground truth and x_i is the

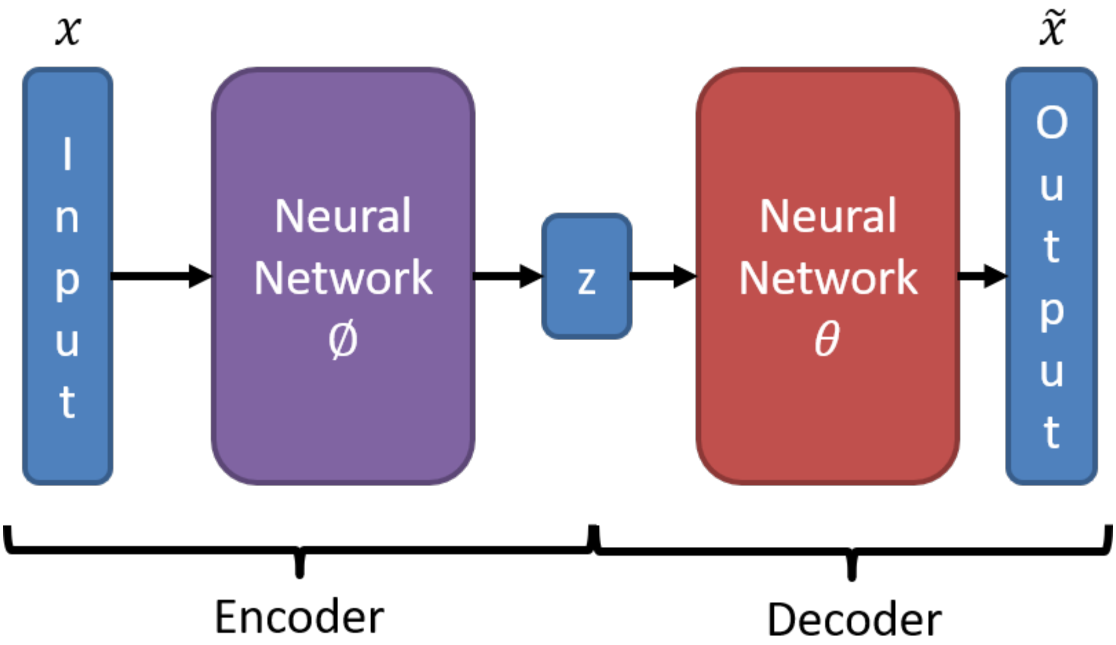

Figure 6.4: Basic Autoencoder

input. The autoencoder neural network tries to learn a function where $h_{\theta,\phi}(x_i) = \tilde{x_i}$ with $\tilde{x_i}$ being the output of the decoder, and will be optimized such that the output of the decoder is as close as possible to input of the autoencoder. An autoencoder takes the input $X = [x_1, x_2, ..., x_n]^T$, where n is the total number of input samples, and map it to a hidden representation z parameterized using $\phi = \{W, \boldsymbol{b}\}$. W and $\boldsymbol{b}$ are the weight and bias matrix respectively. The hidden representation z is then mapped to the reconstructed decoder output parameterized with $\theta = \{W', \boldsymbol{b'}\}$. The autoencoder is optimized to minimized the average squared reconstruction error:

$$\phi, \theta = \underset{\phi,\theta}{\arg\min} \frac{1}{n} \sum_{1}^{n} L(x_i, \tilde{x_i}) \tag{6.12}$$

where L is the mean squared error (MSE) loss function, $L(x_i, \tilde{x_i}) = ||x_i - \tilde{x_i}||^2$.

However, the purpose of DLDD is to detect signals that are phase corrupted. Therefore, the input of the proposed autoencoders will be the noisy phase corrupted QPSK signal, and the output of the autoencoders will be a "clean" uncorrupted version of the input. Hence, the proposed DAE and VAE are optimized differently compared to conventional autoencoder implementation.

6.2.2.1 Denoising Autoencoder (DAE)

In general, DAE has a similar structure as a basic autoencoder shown in Fig. 6.4. However, contrary to the most basic form of a basic autoencoder where feed-forward neural networks are used in the hidden layer of the encoder and decoder, the proposed DAE uses convolutional neural networks (CNN) in the hidden layer of the encoder and transposed convolution neural networks in the hidden layer of the decoder. Fig. 6.5 shows the proposed DAE architecture.

As mentioned in the previous section, the implementation of the proposed autoencoders are different for DLDD. Contrary to the conventional usage of autoencoder, for DLDD, the input to the autoencoder is a noisy input and the desired output of the autoencoder is a "clean" uncorrupted version of the input. Therefore, the neural networks in DAE will try to learn a slightly different function $h_{DAE}(x_i) = \tilde{x_i}$ such that the output $\tilde{x_i}$ is as close as possible to the "clean" uncorrupted version of the input. The input to DAE is the $r_{osc}(t)$ signal (shown in Fig. 6.3) sampled at 32 sample per bit, and the ground truth is denoted by $y = [I(t), Q(t)]^T$ assuming that $v(t) = I(t)\cos(2\pi f_{IF}t) + Q(t)\sin(2\pi f_{IF}t)$. The encoded feature z is defined to have a smaller size compared to the input feature and the regenerated output, so that the encoder neural network will only extract important features from the noisy input. Hence the decoder is forced to learn from a "compressed" version of the input to regenerate an uncorrupted version of the input. The dimension of z denoted by s_z is $2 \leq s_z < c$ as the input features consist of I and Q symbols, and c represents the input feature size. The proposed DAE is optimized using:

$$\phi, \theta = \arg\min_{\phi,\theta} \frac{1}{n}\sum_{1}^{n} L(y_i, \tilde{x_i}) \tag{6.13}$$

where the MSE loss function is $L(y_i, \tilde{x_i}) = ||y_i - \tilde{x_i}||^2$.

As shown in Fig. 6.5, CNN and densely connected neural network are used in DAE. During training of the DAE algorithm, weights and biases of the densely connected neural network, and the filter parameter and biases of the CNN are updated such that the MSE is minimized. The training process is stopped when the MSE returned from the loss function converges.

6.2.2.2 Variational Autoencoder (VAE)

VAE is different from basic autoencoder and denoising autoencoder. An example of the VAE architecture is shown in Fig 6.6. VAE is a maximum likelihood generative model which maximizes the Evidence Lower Bound (ELBO) through minimization of

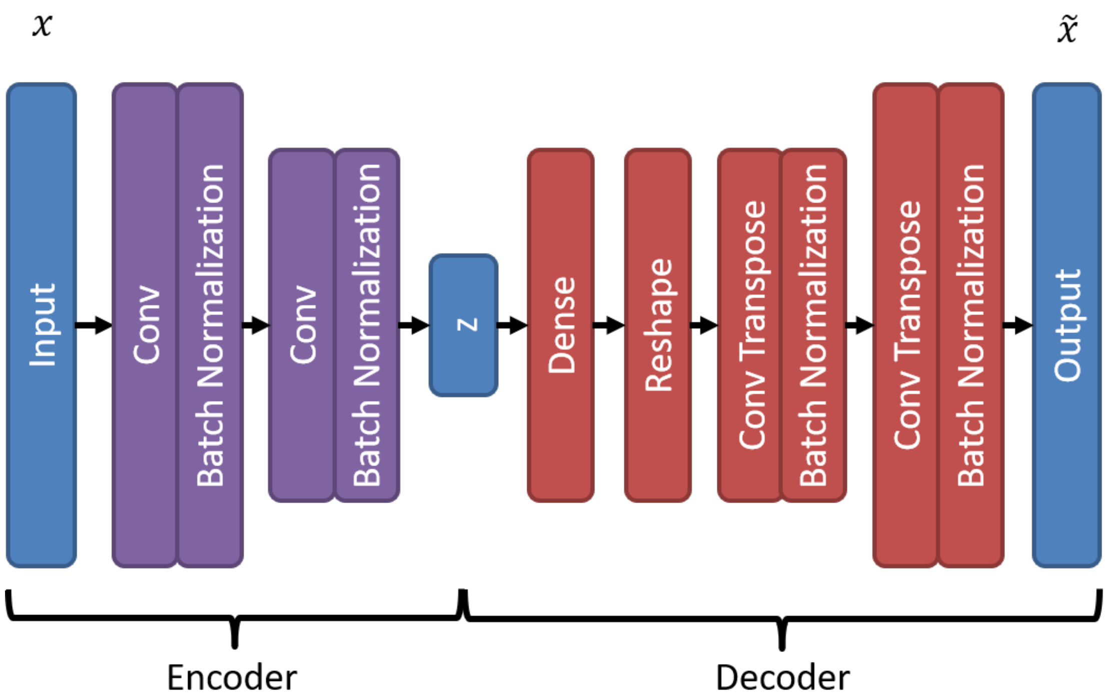

Figure 6.5: Denosing Autoencoder

the model's reconstruction error and the differences between the posterior distribution and the hypothesized prior using Kullback-Leibler (KL) divergence. The encoder portion of VAE is an inference model, while the decoder is a generative model. A simple VAE can be implemented using a single Gaussian distribution prior. However, over-regularization of the posterior distribution might occur, which may lead to posterior collapse and underfitting of the encoder. Hence, for the proposed VAE, a Gaussian mixture distribution prior is used.

For a single Gaussian distribution VAE, the ELBO can be defined as [255]:

$$ELBO = -D_{KL}(Q(z|X)||P(z)) + E[\log(P(X|z))] \tag{6.14}$$

where $P(z)$ is the prior distribution, $P(X|z)$ represents the generative model (decoder), and $Q(z|X)$ represents the inference model (encoder). Input x is fed into the encoder to be encoded with $Q(z|X)$ distribution and sampled with a latent representation of z. Sampled z is used by the decoder for reconstruction. $D_{KL}(Q(z|X)||P(z))$ can be defined

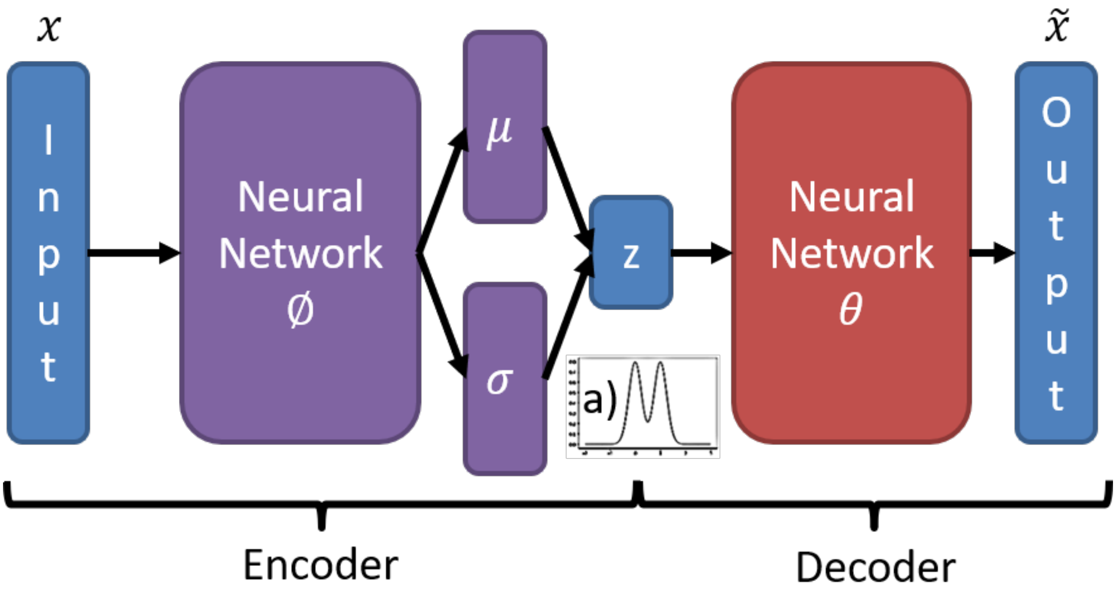

FIGURE 6.6: Variational Autoencoder where a) shows an example of a mix Gaussian prior for latent representation z.

as:

$$\begin{aligned} D_{KL}(Q(z|X)||P(z)) &= \mathcal{D}[\mathcal{N}(\mu_0, \Sigma_0)||\mathcal{N}(\mu_1, \Sigma_1)] \\ &= \frac{1}{2}(\mathrm{tr}(\Sigma_1^{-1}\Sigma_0) + \\ &\quad (\mu_1 - \mu_0)^T \Sigma_1^{-1}(\mu_1 - \mu_0) \\ &\quad -k + \log(\frac{\det \Sigma_1}{\det \Sigma_0})) \end{aligned} \tag{6.15}$$

If the prior is $\mathcal{N}(\mu_1, \Sigma_1) = \mathcal{N}(0, 1)$, then

$$\mathcal{D}[\mathcal{N}(\mu_0, \Sigma_0)||\mathcal{N}(0, 1)] = \frac{1}{2}(\Sigma_0 + (-\mu_0)^2 - 1 - \log(\det \Sigma_0)) \tag{6.16}$$

For DLDD, we defined a Gaussian mixture prior. The Guassian mixture can be defined as a sum of multiple individual Gaussian distributions. Hence $Q(z|X)$ and $P(z)$ can be defined as

$$Q(z|X) = \sum_{m}^{M} \pi_m q_m$$
$$P(z) = \sum_{m}^{M} \pi_m^{'} q_m^{'}$$

where $m = 1, 2, 3, 4, ...M$. M is the number of Gaussian distributions within the Gaussian mixture, and π_m,$\pi_m^{'}$ is the weight of the distribution. Since QPSK is used, I and Q are in binary form, the Gaussian mixture contains two Gaussian distributions (M=2) as shown in Fig. 6.7. Since the distribution of the prior has changed, the KL divergence equation for single Gaussian distribution as shown in (6.16) cannot be used. The KL divergence for the Gaussian mixture distribution prior can be represented as:

$$\begin{aligned} D_{KL}[Q(z|X)||P(z)] &= -\int Q(z|X)\log(\frac{P(z)}{Q(z|X)})dz \\ &= \int[\sum_{m}^{M}\pi_m q_m]\log(\frac{\sum_m^M \pi_m q_m}{\sum_m^M \pi_m^{'} q_m^{'}}) \\ &= \sum_{m}^{M}\pi_m \log(\frac{\sum_m^M \pi_m}{\sum_m^M \pi_m^{'}}) + \\ & \quad \sum_{m}^{M}\pi_m \mathcal{D}[q_m||q_m^{'}] \end{aligned} \tag{6.17}$$

where $\sum_m^M \pi_m \mathcal{D}[q_m||q_m^{'}]$ can be represented as:

$$\begin{aligned} \sum_{m}^{M}\pi_m \mathcal{D}[q_m||q_m^{'}] &= \frac{1}{2}\sum_{m}^{M}\pi_m(\mathrm{tr}(\Sigma_1^{-1}\Sigma_0) + \\ & \quad (\mu_1-\mu_0)^T\Sigma_1^{-1}(\mu_1-\mu_0) \\ & \quad -k + \log(\frac{\det\Sigma_1}{\det\Sigma_0})) \end{aligned} \tag{6.18}$$

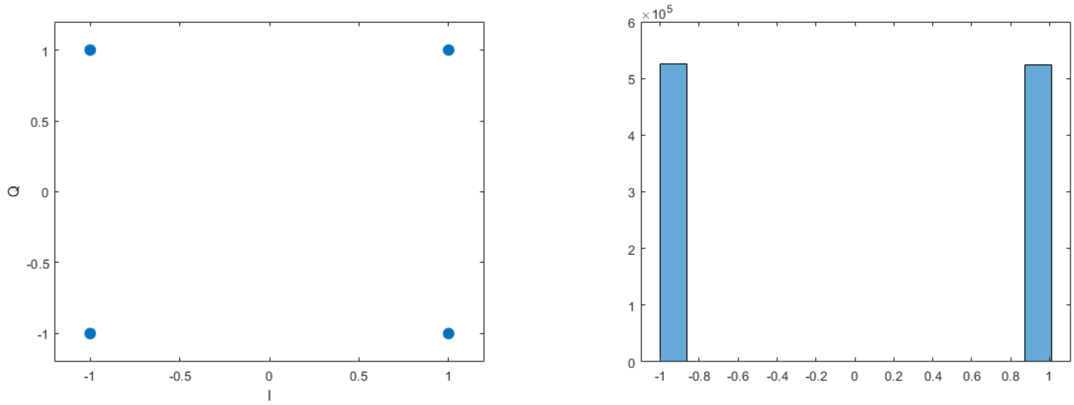

FIGURE 6.7: Constellation diagram of transmitted IQ symbols (left) and the distribution of the individual I and Q signals (right).

Therefore, after substituting equation (6.18) into equation (6.17), the KL divergence for a Gaussian mixture distribution prior can be rewritten as:

$$\begin{aligned}\mathcal{D}[Q(z|X)||P(z)] \quad = \quad & \sum_{m}^{M} \pi_m \log(\frac{\sum_m^M \pi_m}{\sum_m^M \pi_m^{'}}) + \\ & \frac{1}{2}\sum_{m}^{M} \pi_m (\mathrm{tr}(\Sigma_{1_{i,m}}^{-1}\Sigma_{0_{i,m}}) + \\ & (\mu_{1_{i,m}} - \mu_{0_{i,m}})^T \Sigma_{1_{i,m}}^{-1} \\ & (\mu_{1_{i,m}} - \mu_{0_{i,m}}) - k \\ & + \ \log(\frac{\det \Sigma_{1_{i,m}}}{\det \Sigma_{0_{i,m}}}))\end{aligned} \tag{6.19}$$

For DLDD, feed-forward neural networks are used in the encoder and decoder of the proposed VAE. Similar to DAE, the neural networks in VAE are optimized such that the output VAE is similar to the ground truth label. However, the loss function of VAE is different from DAE. In DAE, the neural networks are optimized using MSE loss function. For VAE, the loss function has two components: reconstruction loss and latent loss. The reconstruction loss of VAE is BCE (equation (5.14)), and the latent loss will be KL divergence loss shown in equation (6.19). The reconstruction loss of VAE calculates the difference between the output of the VAE and the ground truth label, while the latent loss penalizes VAE if the latent representation z deviates from the defined Gaussian mixture prior. Therefore, contrary to DAE and basic autoencoder where the latent representation z is defined by the encoder's output and can not be directly controlled, the latent representation of VAE can be optimized such that it is similar to the defined Gaussian mixture prior.

As mentioned in Section 6.2.2.1, the latent representation z is defined to have a smaller dimension than the autoencoder's input and output. Essentially, the DAE's encoder transforms the noisy input of a higher dimension to a small dimension latent representation z, and during that process, only "important" features that are used to reconstruct the "clean" uncorrupted version of the input is retained. However, the transformation process might produce a corrupted latent representation which will cause the decoder to generate an output that is different from the ground truth label. Hence, by defining the prior distribution of the latent variable in VAE such that it closely resembles the distribution of the "clean" uncorrupted ground truth labels, and have a smaller variance than the noise corrupted input, the defined prior distribution acts as a "guide" during the optimization process of the neural network within the VAE. By having a prior distribution with a smaller variance than the corrupted input, the encoder can estimate the posterior distribution such that it is sufficient for the decoder to reconstruct the "clean" version of the input, and at the same time is less noisy than the corrupted input.

As shown in Fig. 6.7, the I and Q components of the QPSK can be represented using two Gaussian distributions with zero variance. However, the proposed VAE prior Gaussian mixture distribution is defined to have a variance of more than zero. This is because having a variance that is very close to zero might lead to poor generalization of the neural networks within VAE. Therefore a test to determine the optimal variance for the prior distribution was carried out and discussed in Section 6.3.3.

6.2.3 Deep learning based detection with reference tone (DLD-RT)

For DLD-RT, an additional reference tone is used as an input to the proposed deep learning based receiver in addition to the phase corrupted signal as shown in Fig. 6.8. The additional reference tone input, highlighted in pink, is used as a reference for the deep learning based receiver to predict the transmitted IQ symbol. When phase noise is not present, the reference tone will stay constant for every IQ symbol. In the presence of phase noise, the reference tone will fluctuate. Since both the main data signal and the reference tone are corrupted from the same source, the deep learning based receiver can predict the transmitted QPSK IQ symbol based on the fluctuation in the reference tone.

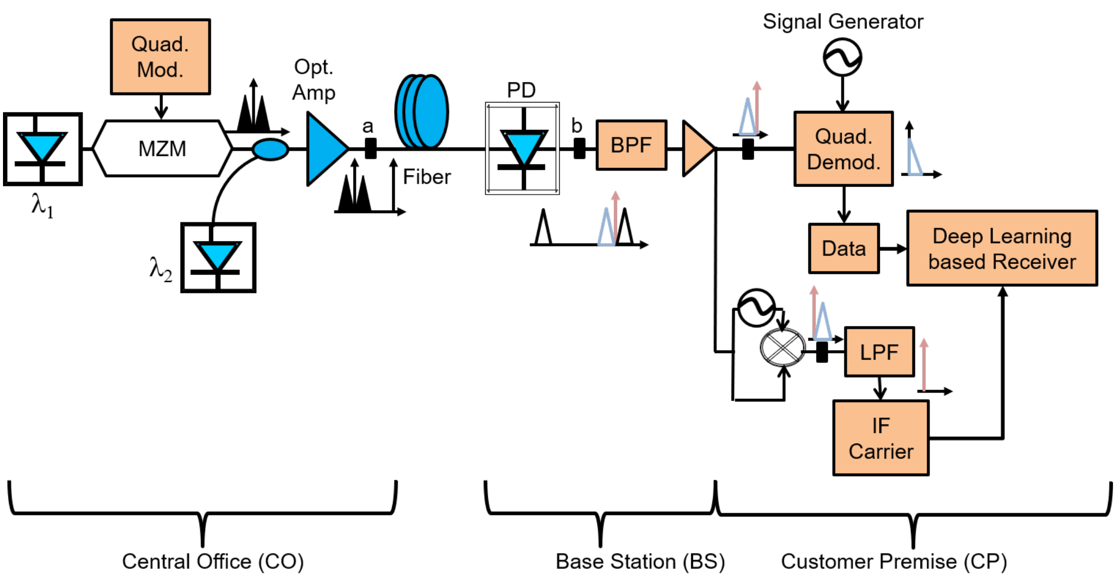

FIGURE 6.8: DLD-RT configuration

As discussed in chapter 4, in a self-homodyning-based IF-RoF (SH-IF-RoF) system, phase noise is reduced by mixing the reference tone (referred to as the carrier tone in chapter 4) and the main data signal. The reduction of phase noise is possible for an SH-IF-RoF system because the reference tone and the main data signal are modulated onto the same optical tone using the same modulator. However, for SH-IF-RoF, a certain gap between the reference tone and the main data signal has to be maintained to avoid signal-to-signal beating interference (SSBI), and to ensure that the downconverted IF signal has sufficient frequency such that it is more than or equal to the symbol period. An insufficient gap can affect system performance. Therefore, DLD-RT is proposed to increase bandwidth efficiency of unlocked heterodyning IF-RoF system by reducing the required frequency gap of SH IF-RoF, and replacing the SH receiver with a deep learning based phase noise tolerant receiver.

We proposed the use of LSTM neural network for DLD-RT as the input signals, the received phase corrupted signal, and the reference tone are sequence data, and both signals fluctuate with time. LSTM is a variant of RNN, and RNN has shown potential in solving challenging problems involving sequential data analysis such as speech recognition [33, 34], language modeling [256], and speech activity detection [257]. The structure of an LSTM block has been introduced in Section 5.2.3.

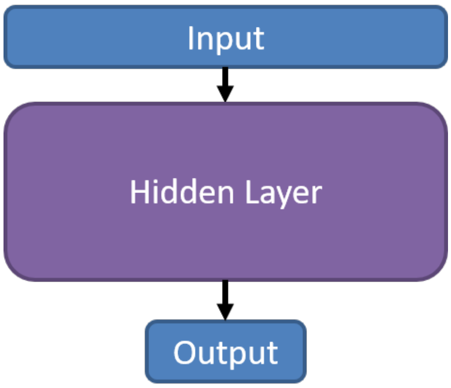

FIGURE 6.9: Deep learning architecture of DLD-RT

Fig. 6.9 shows the architecture of the deep learning architecture used in DLD-RT. The input of the deep learning based receiver contains the sampled I and Q components of the phase corrupted received signal, and the sampled reference tone. The input matrix has three rows and N_{sample} of columns. The number of columns of the input matrix is determined by the number of samples per bit. The output of the DLD-RT receiver is the number of bits represented by each symbol. Hence, the input has a larger size compared to the output. The hidden layer consists of multiple layers of the proposed LSTM neural network. The LSTM neural network in the hidden layer has to learn the correlation between the sampled IQ signal and the reference tone, and between past and present reference tone samples to predict the transmitted QPSK signal. During the training process of the proposed LSTM algorithm, the weights and biasses within the various gates of each LSTM blocks has to be updated, and the forget gates has to weigh past and present information within the memory blocks such that the loss returned from the loss function is minimized. The training process stops when the loss converges. The proposed LSTM algorithm is optimized using MSE loss function. Algorithm 3 shows the training process of the proposed LSTM based receiver.

Algorithm 3 Training of the proposed LSTM algorithm for DLD-RT receiver

1: **Input:** Sampled reference tone and phase corrupted IQ components of the received QPSK signal
2: Data split using 10:2:1 ratio for training, validation, and testing sample
3: **while** loss did not converge **do**
4: Calculate $\mathbf{o}(t)$, $\mathbf{c}(t)$, $\mathbf{i}_{blk}(t)$, $\mathbf{i}(t)$, $\mathbf{f}(t)$ (equations shown in (5.17))
5: Calculate output of each LSTM block using equation (5.16)
6: Applying activation function (Sigmoid)
7: Calculate MSE loss
8: Update weights and biasses of each gate and blocks within the LSTM neural network layer such that loss is being minimized;
9: **end while**

6.3 Experiments

The proposed algorithms for DLDD and DLD-RT are evaluated using varying levels of phase noise. A test comparing the performance of SH receiver based IF-RoF link to oscillator receiver based IF-RoF links is carried out to show the phase noise tolerance of SH-based RoF systems and as a baseline for comparison with the performance of the proposed deep learning based RoF receivers. Furthermore, a test comparing different variances used for VAE is carried out to optimize the performance of the VAE used in DLDD.

The training of the deep learning algorithm is completed using Keras Tensorflow. Simulations are carried out on a workstation equipped with an Intel Xeon E5-2650v3 processor, 256GB of RAM, and an NVIDIA Geforce GTX 1080.

This section is organized as follows. The data generation for deep learning algorithm training is described in Section 6.3.1. Section 6.3.2 describes the neural network architectures used. The results for both DLDD and DLD-RT are included in Section 6.3.3 and Section 6.3.4.

6.3.1 Data Generation

The data used for training the proposed algorithms are collected through simulations carried out using *OptiSystem 16*, using two configurations shown in Fig. 6.3 and Fig. 6.8.

The data collected is further processed using MATLAB before exporting for deep learning algorithm training and testing. For DLDD, the downconverted baseband phase corrupted IQ signal, and the transmitted uncorrupted IQ signal are collected and sampled at 32 sample/bit. For DLD-RT, an additional reference tone is sampled and collected in addition to the transmitted and received IQ symbols. Approximately 14 million bits are collected for 1 kHz, 100 kHz, and 1 MHz laser linewidth individually and divided into training, validation, and testing set with a ratio of 10:2:1 for both DLDD and DLD-RT receivers respectively. In a real-world scenario, the deep learning training data can be collected from the UE (phase corrupted signal) and the CO (uncorrupted signal). The following paragraphs describe the simulation setups used for data collection.

For DLDD, a free-running laser operating at 193.1 THz is externally modulated using an MZM with a 2.5 GHz IF carrier. The IF signal carries 1 Gbps QPSK signal generated using a quadrature modulator with oscillators operating at 2.5 GHz and a PRBS generator. The output of MZM is coupled with the optical output from the second free-running LO laser. An amplifier with a 20 dBm gain and a noise figure of 6 dBm is used to amplify the coupled optical signal before being transported over a 5 km single-mode fiber (SMF) to the BS. A 60 GHz millimeter-wave signal is generated at the BS after unlock heterodyning photodiode detection of the received optical tones. The millimeter-wave signal is amplified using a 50 dB gain amplifier with a current spectral density of $2.25 \times 10^{-11} \frac{A}{\sqrt{Hz}}$ and filtered using a Bessel bandpass filter with 1 GHz bandwidth (BW) centered around 60 GHz. At the CP, the received signal is downconverted to baseband using a quadrature demodulator with RF oscillators operating at 60 GHz.

For DLD-RT, the optical transmitter configuration is similar to DLDD. At the BS, the millimeter-wave signal is generated through unlocked heterodyning of received optical tones. The millimeter-wave signal is amplified using the same amplifier as DLDD and filtered using a Bessel bandpass filter with a filter bandwidth ranging from 1 GHz to 5 GHz. The bandpass filter's bandwidth is varied to extract the millimeter-wave QPSK signal and the reference tone at different frequency gaps. The different frequency spacing between the reference tone and the millimeter-wave QPSK signal requires different bandpass filter bandwidth. At the CP, the signal is split into two using a balance power divider, as shown in 6.8. At the first arm, the millimeter-wave QPSK signal is downconverted using a quadrature demodulator with RF oscillators operating at 60 GHz. A lowpass filter is used to extract the downconverted baseband signal. At the second arm, the reference tone at millimeter-wave frequency is downconverted to baseband using an oscillator with the same frequency. The frequency of the oscillator is varied according to the frequency spacing between the QPSK signal and the reference tone.

6.3.2 Experimental Setup

As mentioned in chapter 5, and shown in Fig. 5.8, the architecture of a deep learning neural network consists of an input layer, an output layer, and at least a hidden layer. The performance of the proposed autoencoders (DAE and VAE), measured in terms of prediction accuracy, is compared to various deep learning architectures such as MLP, CNN, CNN+LSTM, and a basic autoencoder. For a basic autoencoder, as shown in Fig. 6.4, the encoder and decoder each consist of two densely connected neural network layers. As shown in Fig. 6.5, the encoder of DAE consist of two sets of convolution and batch normalization layers, and the decoder consists of two sets of transposed convolution and batch normalization layers. For VAE, the encoder and decoder use the same layers as the basic autoencoder. For MLP, three layers of densely connected neural network are used in the hidden layer. For CNN, similar to DAE, two sets of convolution and batch normalization layers were used in addition to a densely connected neural network. For CNN+LSTM, the architecture is similar to CNN, with the exception of replacing the densely connected neural network with LSTM. Table 6.1 provides the settings used for different neural network layers.

Table 6.1: Deep learning algorithm parameters

Deep Learning Algorithms	Parameter Values
Densely connected neural network layer (MLP, VAE and basic autoencoder)	nodes: 256
Convolutional layer (CNN, DAE)	No. of filters: $10-64$ Kernel size: (r, c); $r \in [2, 8]$, $c \in [1, 3]$ Stride size: (2,1)
LSTM	No of block(s): 50

For the proposed LSTM based DLD-RT, the hidden layer consists of two LSTM layers and a densely connected neural network. The MLP and CNN added for comparison shares the same architecture as those described for DLDD. The settings of the hidden layers used are similar to those listed in Table 6.1. Table 6.2 provides a summary of the settings used for training the proposed DAE, VAE, and LSTM algorithms.

Table 6.2: Training Parameters

Parameters	Values
Learning rate	10^{-7} - 10^{-3}
Learning rate decay	10^{-6} to 10^{-1}
Optimizer	Adam
Loss function	MSE
Batch size	8 - 256
Epochs	10 - 400

6.3.3 Results for Deep Learning based Direct Detection (DLDD)

For VAE used in DLDD, the Gaussian mixture prior's variance used can be varied. For an uncorrupted QPSK, its I and Q components can each be represented as a Gaussian mixture distribution with mean at 1 and -1, and variance of approximately zero as shown in Fig. 6.7. Gaussian distribution with a zero variance can be represented as a Dirac delta distribution. However, the presence of phase and thermal noise would increase the variance of the distribution as shown in Fig. 6.10. Setting a small variance for the prior could lead to the deep learning algorithms in the VAE to not be able to 'learn' properly, which leads to a poor detection performance of the received signal.

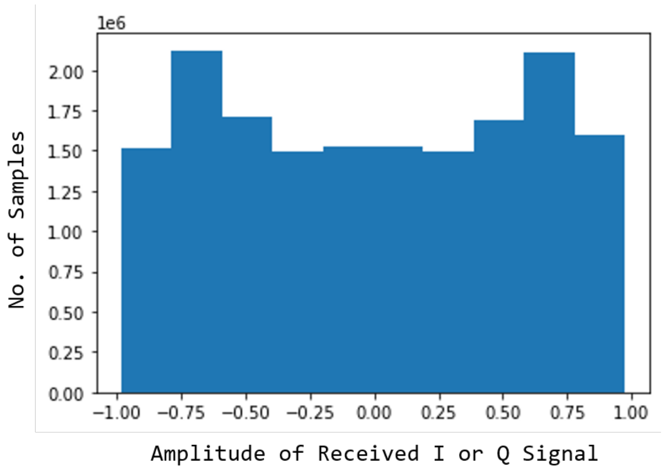

FIGURE 6.10: Distribution of I or Q symbols in the presence of phase and thermal noise

A test is carried out to search for the optimal variance for Gaussian mixture prior using a small dataset of one million samples for both 1 kHz and 1 MHz laser linewidth data set. The variance is varied from 0.005 to 0.2. The data is normalized to $[0, 1]$, and hence the threshold between the two signal peaks is at 0.5. Therefore, the variance of the prior is set such that the threshold value does not fall within one standard deviation of the mean of the Gaussian mixtures, and a variance of 0.2 has a standard deviation of 0.4472.

Fig. 6.11 shows the detection performance of VAE using different Gaussian mixture prior variance. From the obtained results, VAE performed the best at a variance of 0.01 for both 1 MHz and 1 kHz laser linewidth datasets. It is to be noted that during the training phase of variance 0.005 and 0.0055, 'NaN' is returned from the loss function. The model is unable to optimize properly and caused the detection accuracy to be low at 0.005 and 0.0055 variance. Therefore, for VAE, the Gaussian mixture prior variance is defined as 0.01 for DLDD.

Fig. 6.12 shows the performance degradation with increasing phase noise of an oscillator-based receiver (Fig. 6.1) and a SH-based receiver (Fig. 4.2) in an unlocked heterodyning

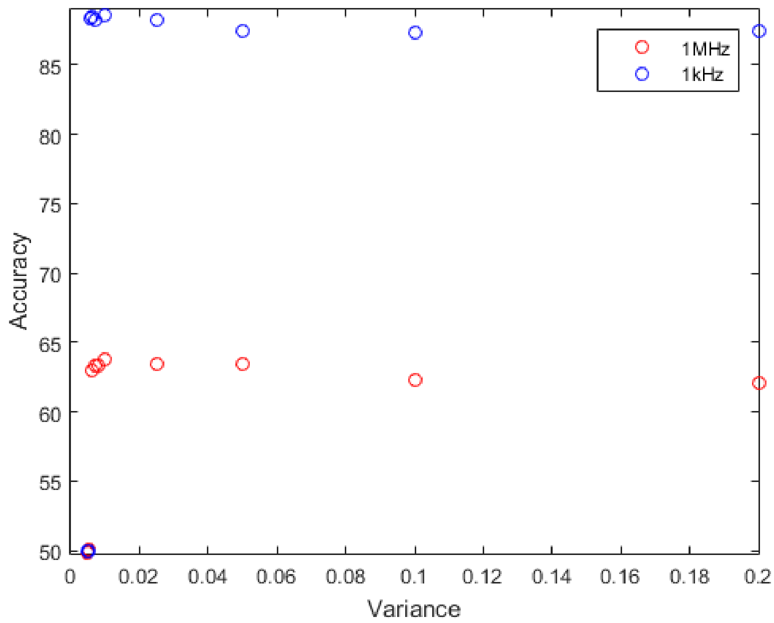

FIGURE 6.11: Detection Performance of VAE using different Gaussian mixture prior variance

IF-RoF link. The performance of each receiver is measured in terms of bit error rate (BER) with a fiber launch power of 0 dBm, and an optical receiving power of -11 dBm. The phase noise is varied through varying laser linewidth from 1 Hz to 80 MHz. The graph shows a rapid increase in BER for the oscillator-based receiver as the linewidth of the laser increases. The oscillator-based receiver performs better than the SH-based receiver below 100 Hz laser linewidth. However, the SH-based receiver is more resilient to phase noise as performance degradation of the receiver is much slower compared to the oscillator-based receiver. The SH-based receiver has virtually no performance degradation up to 1 MHz laser linewidth. In contrast, the error rate of the oscillator-based receiver increases exponentially with increasing phase noise.

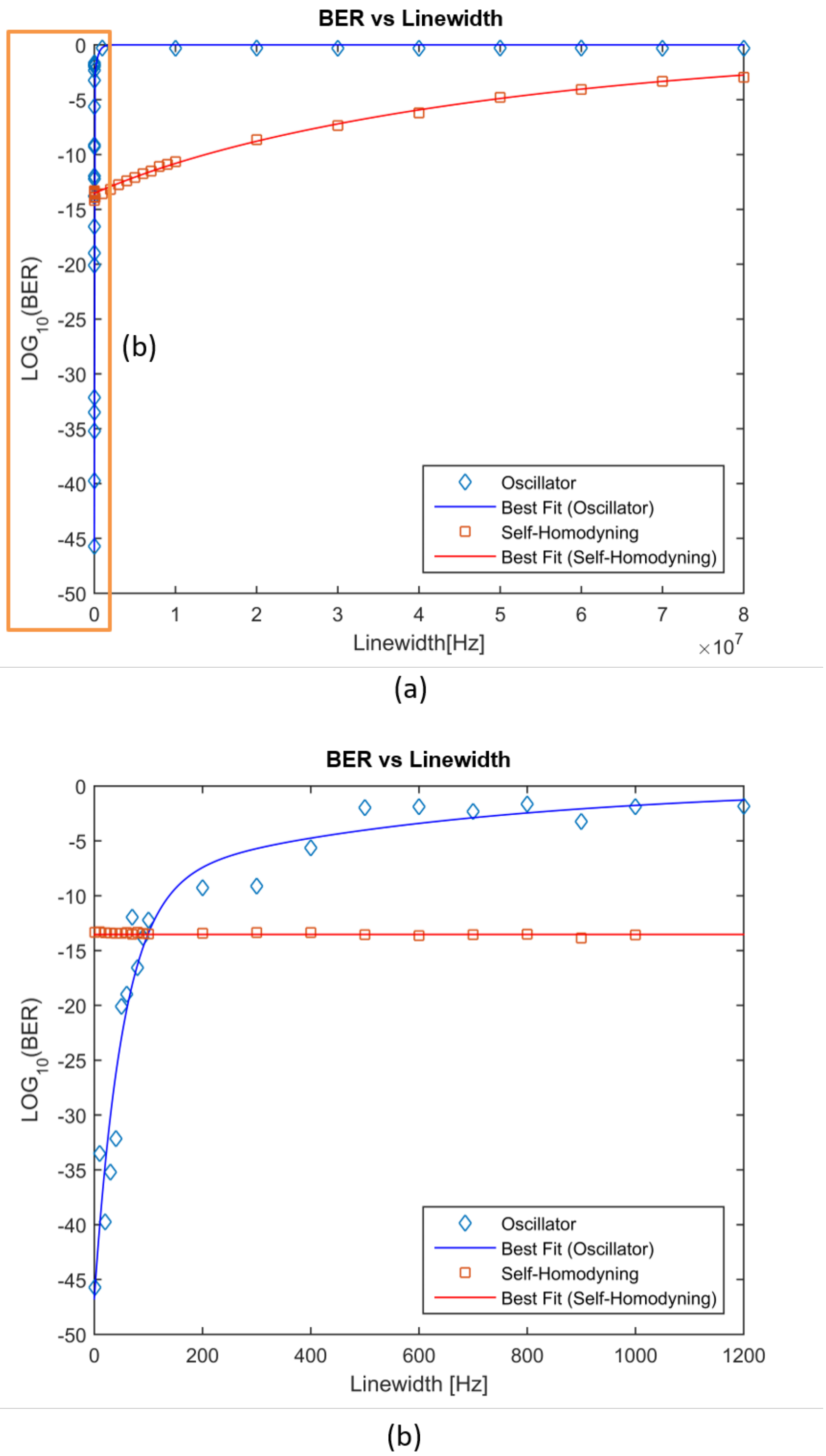

FIGURE 6.12: a) Receivers' detection performance with increasing linewidth measured using BER b) Zoom in portion of a)

Table 6.3:
DLDD (Detection Accuracy)

	1 kHz	1 MHz
Threshold Detection	61.95%	51.40%
MLP	81.00%	52.90%
CNN	82.00%	81.50%
CNN+LSTM	83.60%	82.50%
Basic Autoencoder (Feed-forward)	87.70%	58.17%
DAE (CNN)	96.00%	84.35%
VAE (Feed-forward)	91.76%	75.30%

Results obtained for DLDD are tabulated in Table 6.3. All the algorithms' performance is measured based on the accurate prediction of transmitted bits. The results are obtained by training each deep learning algorithm using two sets of data collected at different phase noise levels. Phase noise is varied through varying the laser linewidth of the lasers used, as shown in Fig. 6.3, to operate at 1 kHz and 1MHz respectively. All algorithms used were trained using the same sets of data. At 1 kHz laser linewidth, the autoencoder-based architectures, namely: Basic Autoencoder, DAE, and VAE, perform better than MLP and CNN based algorithms. At 1 MHz laser linewidth, the detection accuracy of basic autoencoder and VAE, which are both based on feed-forward neural network, decreases drastically. The detection accuracy of basic autoencoder dropped from 87.7% to 58.7%. For VAE, the detection accuracy dropped from 91.76% to 75.3%. Based on the results obtained, VAE outperforms basic autoencoder in terms of detection accuracy, which suggests that the user-configurable distribution of the latent representation can help improve the deep learning detection performance. On the other hand, the detection degradation of DAE and other CNN-based algorithms are smaller. Moving from 1 kHz to 1 MHz, the drop in detection accuracy of CNN and CNN+LSTM algorithms are both less than 1%. Although the drop in detection accuracy for DAE is much larger than CNN and CNN+LSTM, the detection accuracy of DAE for both laser linewidth levels remains higher than the rest.

6.3.4 Results for Deep Learning based Detection with Reference Tone (DLD-RT)

As mentioned in Section 6.2.3, a certain frequency gap has to be maintained between the reference tone and the main data signal in an SH-based IF-RoF link; an insufficient frequency gap can cause a drop in link performance. Fig. 6.13 shows the performance of the IF-RoF link with varying levels of frequency gap. The frequency gap Δf is varied through varying the IF carrier f_{IF} used, $\Delta f = f_{IF}$. Since the 1 Gbps data is transmitted in the form of QPSK at a symbol rate (SR) of 0.5×10^6 symbol/s, at $\Delta f = 0.5$ GHz, the reference tone is located right after the main frequency of the data signal. The results obtained suggest that the guard band (GB) has to be $GB \geq 2 \times SR$. The guard band is defined as $GB = f_{IF} - \frac{1}{2}BW_{signal}$, where BW_{signal} is the bandwidth of the QPSK signal at millimeter-wave frequency.

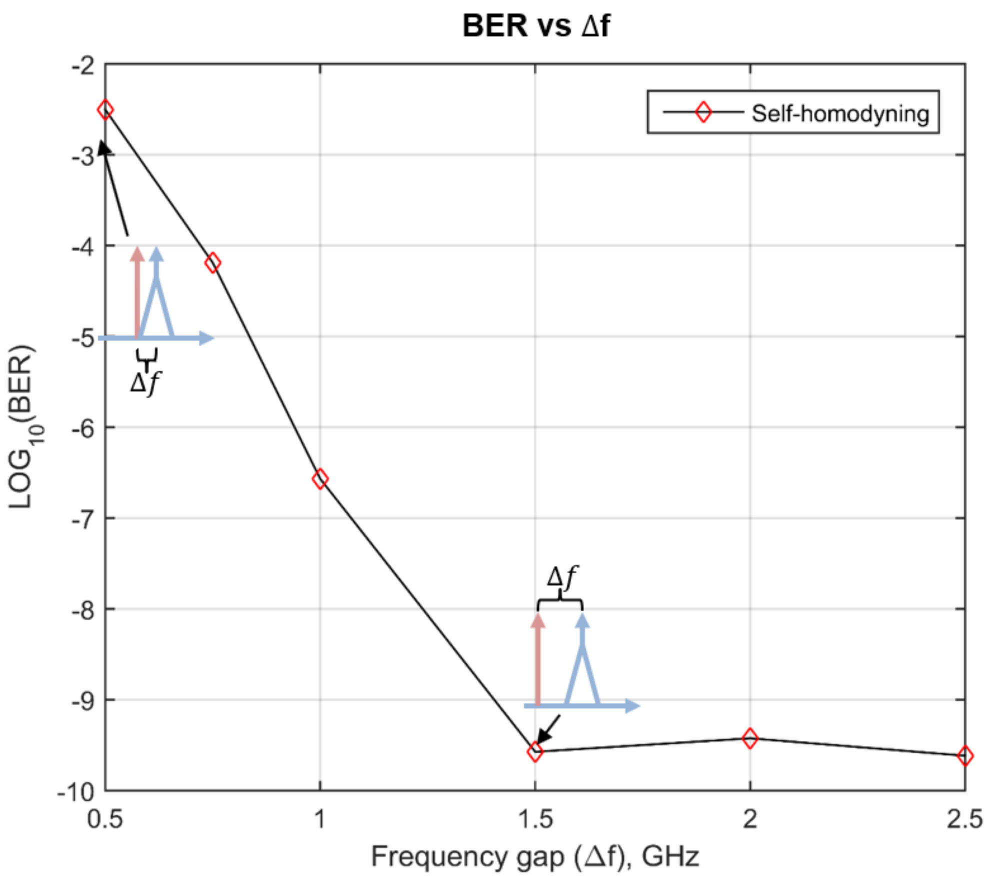

FIGURE 6.13: BER vs Frequency gap

TABLE 6.4:
Method 2 (BER)

Δf=2.5 GHz		
	100 KHz	1 MHz
SH Receiver	-9.6100	
Threshold Detection	-0.3134	-0.3027
MLP	-2.3645	-1.5217
LSTM	-5.3783	-4.3979
CNN	-1.9222	-1.8972
Δf=0.5 GHz		
SH	-2.5023	
MLP	-0.3680	-0.3200
LSTM	-4.2882	-3.1487
CNN	-1.4097	-1.2047

For DLD-RT, the performance of the proposed LSTM based receiver measured using bit error rate (BER) and is compared to SH receiver and deep learning algorithms such as MLP and CNN. Results obtained are tabulated in Table 6.4, and the BER in the table are calculated using $\log_{10}(BER)$. The proposed LSTM receiver's performance was compared to the SH-based RoF receiver at two different frequency gap values ($\Delta f = \{0.5\text{GHz}, 2.5\text{GHz}\}$), and two different levels of phase noise at each Δf. Hence, all the deep learning algorithms were trained using four different datasets. As shown in Fig. 6.12, an SH receiver has virtually no performance degradation up to 1MHz linewidth; the SH receiver's performance is measured at 1MHz for both frequency gaps.

Comparing results shown in Table 6.3 and Table 6.4, the overall results of the deep learning algorithms used in DLD-RT is better than DLDD. At $\Delta f = 2.5$ GHz, which means that the frequency gap is sufficient, the proposed LSTM algorithm achieves a BER of less than 10^{-4}, much better than the results obtained in DLDD, and outperforms MLP and CNN algorithms by a significant margin. However, the SH-based receiver achieves a much lower BER at 10^-9 compared to the proposed LSTM based deep learning receiver, which only has a BER of less than 10^{-4}. At $\Delta f = 0.5$ GHz, the BER obtained using the proposed LSTM algorithm is still lower than MLP and CNN. When the frequency gap is insufficient ($\Delta f = 0.5$ GHz), the proposed LSTM based receiver performs much better than SH based receiver, with the proposed LSTM based receiver achieving a BER of less than 10^{-3} while the SH based receiver has a BER of less than 10^{-2}. As shown in Table 6.4 and Fig. 6.13, the SH-based receiver's performance deteriorates quickly when the frequency gap is insufficient. In contrast, the performance degradation experienced by the proposed LSTM based receiver is much smaller. Using the results obtained at 1 MHz as an example, when the frequency gap decreases from $\Delta f = 2.5$ to $\Delta f = 0.5$, the LSTM based receiver's BER increases from 4×10^{-5} to 7.1×10^{-4} while the BER of the SH receiver increases from 2.5×10^{-10} to 3.1×10^{-3}. Fig. 6.14 shows changes in the output signal constellation of the proposed LSTM based receiver as it is gradually optimized during the training process. Each subplot within the figure is extracted during various stages of the training process until the MSE loss curve converges. As shown in Fig. 6.14, as the training process progresses, the ability of the proposed LSTM based receiver to be able to 'sort' the phase noise corrupted signal to its respective symbol improves. The last subplot, situated at the bottom right of Fig. 6.14, suggests that the detection of the phase corrupted signal should be error-free if an appropriate threshold is used. However, the results shown in Table 6.4 do not support that claim which suggests that an SER estimated using error vector magnitude cannot be used as a performance indicator for deep learning based receivers.

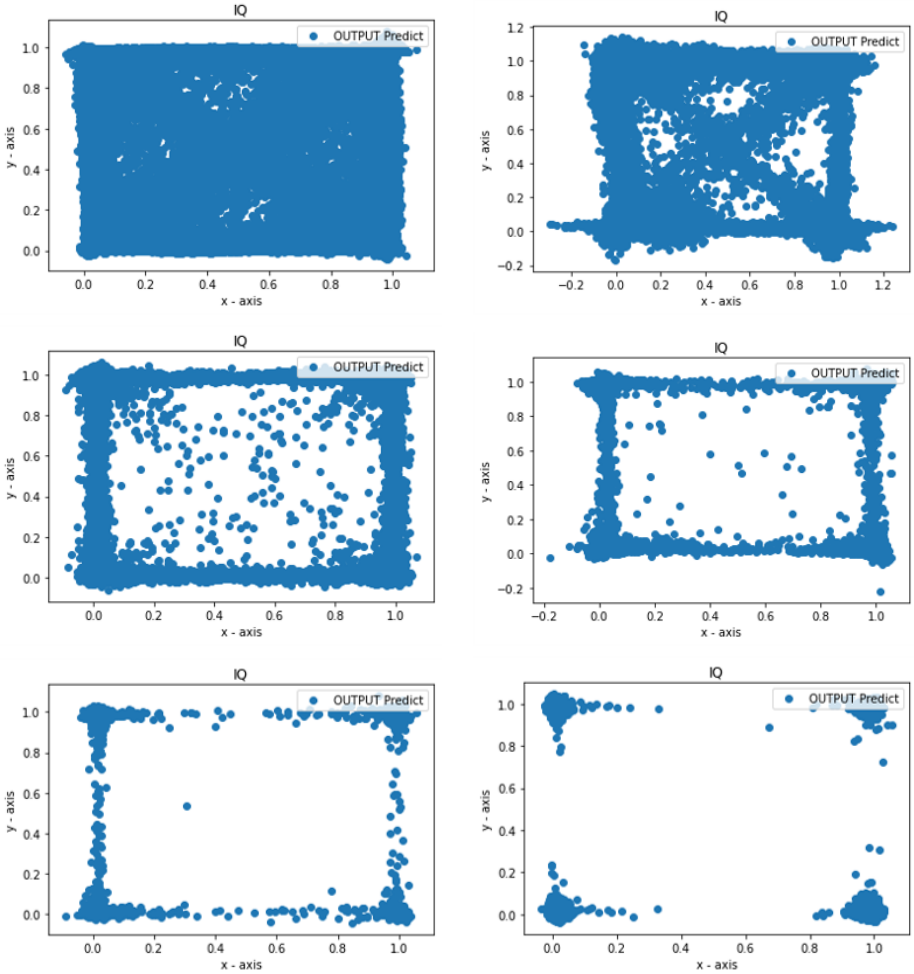

FIGURE 6.14: Proposed LSTM based millimeter-wave RoF receiver output changes as the network gradually optimize

6.4 Conclusions

Two novel implementations of deep learning based detection for millimeter-wave RoF, namely DLDD and DLD-RT has been demonstrated with three proposed deep learning algorithms. For DLDD, DAE and VAE were proposed, while LSTM was proposed for DLD-RT. Results obtained for DLDD show that CNN-based DAE can improve signal detection accuracy better than VAE, basic autoencoder, MLP, CNN, and CNN+LSTM based algorithms. While DLDD receivers as a whole have a BER of above 10^{-3}, the detection accuracy of these DLDD receivers is higher than direct threshold detection. This shows that DLDD receivers have the potential to be used in lower phase noise RoF links such as differential encoding based RoF link shown in chapter 3 and chapter 4 or a phase-locked optical tone RoF link, to minimize the performance impairment caused by residual phase noise. For DLD-RT, the LSTM based receiver performs better than MLP and CNN-based receivers. Results obtained for the LSTM based receiver show that the receiver has the potential to be used as a bandwidth-efficient alternative to an SH-based receiver in an uncorrelated RoF link. However, there are still room for improvement that can be explored in the future.

Chapter 7

Conclusions and Future Works

This thesis's focus is on ARoF systems with reduced complexity and reliance on high-speed optoelectronics and RF oscillators. In addition, this thesis explores the use of deep learning for future generation communication networks. From the literature review carried out in chapter 2, we know that while millimeter-wave frequency bands provide more bandwidth than lower RF bands, millimeter-wave have high propagation loss, high specific attenuation in the presence of oxygen, moisture, and rain, and high penetration loss. The high path loss of millimeter-wave can require more base stations to achieve similar coverage areas as lower RF bands, which would increase the network's deployment cost. Solutions proposed to overcome issues that arise with the use of millimeter-wave introduces new challenges and problems. The introduction of mMIMO antenna allows finer beamforming control and higher antenna gain to overcome the high path loss of millimeter-wave. However, significantly more overhead resources and processing capability are needed by the baseband units to perform large-scale coordination and scheduling for CoMP. While the introduction of fiber can increase fronthaul bandwidth, the signal transmitted through fiber is susceptible to impairments such as dispersion, phase noise, and intensity noise contributed by the optical transmission system. Phase-locked optical tones can reduce the impairments propagated from the optical transmitter, but conventional coherent optical tone generation methods rely on cutting-edge high-speed optoelectronics and RF oscillators. While the use of self-homodyning (SH) receivers with uncorrelated optical tones reduces the overall optical transmitter configuration, SH receiver cannot be used directly to detect phase-modulated signals. Therefore, in chapter 3, we proposed the use of differential encoding and differential demodulation method to enable direct detection of phase modulated signal in unlocked heterodyning RoF links. However, the time delay present in the differential demodulation method limits modulation choices and leads to higher phase noise residue. Hence, deep learning based phase noise tolerant RoF receivers were proposed in chapter 6 as an alternative to the DAM receiver proposed in chapter 3 and to replace the bandwidth inefficient self-homodyning-based receiver used in unlocked heterodyning IF-RoF schemes. In chapter 5, we explore and investigate the use of deep learning in joint downlink CoMP transmission. The following paragraphs discuss the contributions of the research topics explored in chapter 3, 4, 5, and 6.

In chapter 3, two DPSK baseband modulated millimeter-wave RoF fronthaul downlink schemes were proposed and demonstrated experimentally. The proposed links were analyzed theoretically and experimentally through software simulation and were evaluated through varying optical power, laser linewidth, and relative intensity noise. In addition, the proposed links are tested using different optical carrier-to-sideband power ratios, and different signal formats such as RZ-DPSK, CSRZ-DPSK, and NRZ-DPSK. Results obtained show that the optimal operating point for both proposed DPSK schemes is when the total carrier power is equal to the total sideband power. Furthermore, while RZ-DPSK and CSRZ-DPSK have a slight performance advantage over NRZ-DPSK, the transmission of signals in the form of RZ-DPSK and CSRZ-DPSK require more bandwidth and a more complex transmission configuration. Theoretical analysis performed on the proposed DPSK scheme and the optical demodulated DPSK scheme shows that these two schemes can directly detect phase-modulated signals and reduce phase noise contributed by the optical transmission system. Simulation results show that the proposed DPSK RoF scheme remains relatively phase noise tolerant up to 10 MHz range laser linewidth. However, conventional phase-locked optical DPSK link performs better than the proposed DPSK scheme and the optical demodulated DPSK scheme at lower RIN levels and high phase noise scenarios. Compared to oscillator receiver based unlocked heterodyned RoF scheme, at higher phase noise levels, the proposed DPSK RoF scheme and the optical demodulated DPSK scheme performs better whilst the oscillator receiver based unlocked heterodyned RoF scheme perform better than the two DPSK schemes at lower phase noise levels.

In chapter 4, the investigation on the use of differential encoding and differential demodulation methods on RoF links was extended to include DQPSK signals. From the findings in chapter 3, we discover that while the DAM receiver used in the proposed DPSK RoF scheme can reduce the phase noise impairment caused by the optical transmitter, the time delay present in the DAM receiver causes detection accuracy to drop due to phase fluctuations between time t and $t-\tau_1$. In DQPSK, the DAM receiver's time delay used to demodulate the DQPSK signal is twice as long. The longer time delay will cause the phase noise residual to increase due to higher phase fluctuation between time t and $t-\tau_2$. Hence, chapter 4 investigates the feasibility of the proposed differential encoding RoF link using DQPSK signal in the presence of a relatively higher phase noise residual. Results obtained through theoretical analysis and simulation show that the proposed DQPSK RoF scheme can reduce phase noise inherited from the optical transmitter. Compared to the DPSK schemes demonstrated in chapter 3, the proposed DQPSK RoF scheme experienced a higher detection impairment in the presence of phase noise caused by the longer time delay used in the demodulation process. Compared to SH IF-RoF schemes, the proposed DQPSK scheme performs better at lower phase noise levels and has a higher tolerance towards RIN.

A deep learning based CoMP is explored and demonstrated in chapter 5. The deep learning algorithms were tested in two different scenarios with varying cell sizes. Deep learning algorithms were tasked as a trigger to activate or deactivate a CoMP algorithm, to provide all possible base stations for CoMP joint transmission, and to select an additional base station that fulfills predefined criteria for CoMP transmission. In addition, varying user distributions were used to test the performance of different deep learning algorithms used in the deep learning based CoMP. The proposed deep learning based CoMP was demonstrated using MLP, LSTM, and DQN, and the results obtained were compared with SVM. In general, the deep learning and deep reinforcement learning algorithms perform better than SVM in all tests. In situations where the sequence of the input vector matters, LSTM performs better than MLP. However, when the sequence of the input vector is irrelevant, MLP can perform better than LSTM. In addition, MLP demands a lower computational time compared to LSTM. In an environment that is constantly changing, DQN based deep reinforcement learning can perform better than both LSTM and MLP. However, DQN demands more computational time compared to LSTM and MLP.

The use of incoherent detection for M-DPSK signals in chapter 3 and chapter 4 allows phase noise to be reduced through delayed and phase-shifted multiplication of the signal while remaining spectrally efficient. However, the presence of the time delay in the DAM receiver prevents the use of non-differentially encoded signals. The time delay used in the DAM receiver increases with the order of modulation, which would cause an increase in phase noise residual and lead to a drop in detection performance. Furthermore, alternative RoF schemes discussed in chapter 2 and chapter 3 require either additional bandwidth, high-speed optoelectronics and oscillators, or a more complex transceiver configuration. Therefore, transceivers for unlocked heterodyning ARoF systems that are more robust to phase noise have to be explored to enable low-cost unlock heterodyning RoF systems to be used in future generation high order modulation fiber-wireless communication. Hence, two deep learning based phase noise tolerant receivers have been proposed and demonstrated in chapter 6. The proposed receivers use autoencoder and LSTM based deep learning architecture and are demonstrated using unlocked heterodyning RoF downlink with oscillator-based baseband downconversion method. Contrary to conventional implementation of autoencoder where it is trained to have the output be the same as the input, the autoencoder-based receiver is tasked to predict the uncorrupted signal from a phase corrupted input. For the LSTM based receiver, an additional reference input is used. The LSTM based receiver detects the signal based on the phase corrupted input and the reference input. The reference input is used as a reference point for the LSTM based receiver to predict the phase rotation caused by the optical transmitter's phase noise. Based on the results, both deep learning based receivers have the ability to detect signal in the presence of phase noise. The proposed autoencoder and LSTM receivers achieve a higher detection accuracy compared to MLP and CNN based receivers. Compared to SH-based receivers, the LSTM based receiver performed better than the SH-based receiver when the frequency gap between the main data signal and the reference signal is small (or insufficient), while the inverse is true when the frequency gap is sufficient. Therefore, based on the results obtained, the LSTM based receiver has the potential to be used as a bandwidth-efficient alternative to an SH-based receiver in an uncorrelated RoF link.

In summary, the proposed differential encoding optical baseband M-DPSK schemes demonstrated in chapter 3 and chapter 4 can directly detect phase-modulated signals, improve overall bandwidth efficiency, and is more tolerant to RIN compared to self-homodyning receiver based RoF schemes. The results obtained from applying deep learning in CoMP and phase noise tolerant RoF receivers have demonstrated the ability of deep learning algorithms and the possibility of implementing machine learning algorithms in future generation cognitive-communication networks.

7.1 Future Research

This thesis presented investigations and comparisons on analog millimeter-wave RoF systems using variations of differential encoding and DAM receivers, explored the use of deep learning in CoMP, and developed phase noise tolerant receivers for millimeter-wave ARoF systems. However, the proposed differential encoding and DAM receiver demonstrated in chapter 3 and chapter 4 considered the impairments incurred by the fiber link; the impairments contributed by wireless transmission were not included in the investigation. In addition, the proposed link in which used OSSB signal format generated using optical baseband modulation and unlocked laser sources exhibited performance fluctuations due to chromatic dispersion, wherein OSSB signals generated through locked optical tones are generally known to be immune to chromatic dispersion. Besides, as discussed in chapter 6, there are other higher-order modulation formats that are used in wireless communication, which were not included in the investigations carried out in this thesis. The results obtained and discussed in chapter 3 and chapter 4 showed that the bit-delay introduced in the DAM receiver caused the receiver performance to degrade with increasing phase noise, and the effect is more evident when the bit-delay increases when the order of modulation increases. In chapter 5, the scope of investigation for CRAN CoMP was confined to triggering, base station selection, and providing possible base station options for CoMP joint transmission. However, there are other optimization issues that are of concern, such as clustering policy, backhaul bandwidth, power usage, fault detection, and fault mitigation, that have to be addressed to exploit the full benefit of CoMP in a millimeter-wave centralized radio access network. In chapter 6, the investigation focused on evaluating the proposed phase noise tolerant deep learning based receivers in varying levels of phase noise induced by unlocked heterodyning. However, the maximum linewidth of the laser sources used are only up to 1 MHz, and while fiber impairments are considered, the performance of the proposed deep learning based receivers was not evaluated and quantified in varying levels fiber induced impairments such as nonlinear phase noise and dispersion which can significantly degrade link performance. Therefore, more research can be carried out to fill in research gaps that were not covered in this thesis's investigations, and more research has to be carried out to work towards a fully AI-controlled future generation communication network. The following list includes future pursuable works

- Further investigations on the effects of chromatic dispersion on OSSB like optical signals generated using uncorrelated ARoF systems can be carried out, especially on differential encoded and DAM receiver based ARoF systems. While OSSB signals are generally known to be immune to chromatic dispersion, during the investigation of DQPSK ARoF links presented in Chapter 4, the ARoF based DQPSK link performance exhibited signs of fluctuation in detection performance with different fiber lengths. Hence, a thorough investigation on the effects of chromatic dispersion on differentially encoded based ARoF systems and comparisons with conventional phase-locked OSSB tones and phase uncorrelated OSSB tones can be carried out.

- An investigation into the limits of differentially encoded and DAM receiver based ARoF systems can be carried out. As shown in Chapter 3 and Chapter 4, for M-DPSK modulation, the system sensitivity towards phase noise increases with increasing M. Hence, the limits of M for differential PSK and differential QAM based modulation can be investigated to explore how high M can be before the phase noise reduction effect of the DAM receiver is no longer sufficient for error-free detection.

- Explore and compare different deep reinforcement learning algorithms, algorithms other than Q- learning based algorithms for CoMP applications for problems such as:
  - Optimization for maximum network throughput
  - Achieving a balance between network throughput and power consumption
  - Optimization for clustering policies to balance between overhead bandwidth, network throughput, and power consumption
- Develop a feasible real-world framework for training and testing deep reinforcement learning algorithms for communication network management without affecting user experience.
- Evaluate the developed deep learning based ARoF receivers in Chapter 6:
  - In the presence of other distortion contributed by the optical transmitter
  - In a wider range of optical phase noise, including laser phase noise and non-linear phase noise
  - Implementing the DLDD receiver with proposed differentially encoded ARoF schemes, and evaluate its feasibility and quantify the performance benefit of such implementation
- Develop a deep learning based encoder that is capable of generating encoded signals that are resistant towards optical transmitter impairments to improve the performance of ARoF links and to enable higher transmission speeds.

Appendix A

Theoretical Analysis

A.1 Optical Demodulated DPSK Link (Scheme B)

Continuing from equation (3.25)

$$
\begin{aligned}
r_{D2}(t) &= I_{BS_2}^2 \\
r_{D2}(t) &\propto \cos(A)^2 + \cos(B)^2 + \cos(C)^2 + \cos(D)^2 + 2\cos(A)\cos(B) + \\
&\quad 2\cos(A)\cos(C) + 2\cos(B)\cos(C) + 2\cos(A)\cos(D) + 2\cos(B)\cos(D) + \\
&\quad 2\cos(C)\cos(D)
\end{aligned}
$$

where

$$
\begin{aligned}
A &= 2\pi f_{mm}t + \frac{\pi s_D(t)}{V_{\pi_{RF}}} + \Delta\phi(t) \\
B &= 2\pi f_{mm}t + 2\pi f_2\tau_1 + \frac{\pi s_D(t)}{V_{\pi_{RF}}} + \phi_1(t) - \phi_2(\Delta t) \\
C &= -2\pi f_{mm}t + 2\pi f_1\tau_1 - \frac{\pi s_D(\Delta t)}{V_{\pi_{RF}}} + \phi_2(t) - \phi_1(\Delta t) \\
D &= 2\pi f_{mm}\Delta t + \frac{\pi s_D(\Delta t)}{V_{\pi_{RF}}} + \phi_d(\Delta t)
\end{aligned}
$$

Rewriting $r_{D2}(t)$

$$
\begin{aligned}
r_{D2}(t) \;\propto\; & \cos(2\pi f_{mm}t + \frac{\pi s_D(t)}{V_{\pi_{RF}}} + \Delta\phi(t))^2 \\
& + \cos(2\pi f_{mm}t + 2\pi f_2\tau_1 + \frac{\pi s_D(t)}{V_{\pi_{RF}}} + \phi_1(t) - \phi_2(\Delta t))^2 \\
& + \cos(-2\pi f_{mm}t + 2\pi f_1\tau_1 - \frac{\pi s_D(\Delta t)}{V_{\pi_{RF}}} + \phi_2(t) - \phi_1(\Delta t))^2 \\
& + \cos(2\pi f_{mm}\Delta t + \frac{\pi s_D(\Delta t)}{V_{\pi_{RF}}} + \phi_d(\Delta t))^2 \\
& +2\cos(2\pi f_{mm}t + \frac{\pi s_D(t)}{V_{\pi_{RF}}} + \Delta\phi(t)) \\
& \quad \cos(2\pi f_{mm}t + 2\pi f_2\tau_1 + \frac{\pi s_D(t)}{V_{\pi_{RF}}} + \phi_1(t) - \phi_2(\Delta t)) \\
& +2\cos(2\pi f_{mm}t + \frac{\pi s_D(t)}{V_{\pi_{RF}}} + \Delta\phi(t)) \\
& \quad \cos(-2\pi f_{mm}t + 2\pi f_1\tau_1 - \frac{\pi s_D(\Delta t)}{V_{\pi_{RF}}} + \phi_2(t) - \phi_1(\Delta t)) \\
& +2\cos(2\pi f_{mm}t + 2\pi f_2\tau_1 + \frac{\pi s_D(t)}{V_{\pi_{RF}}} + \phi_1(t) - \phi_2(\Delta t)) \\
& \quad \cos(-2\pi f_{mm}t + 2\pi f_1\tau_1 - \frac{\pi s_D(\Delta t)}{V_{\pi_{RF}}} + \phi_2(t) - \phi_1(\Delta t)) \\
& +2\cos(2\pi f_{mm}t + \frac{\pi s_D(t)}{V_{\pi_{RF}}} + \Delta\phi(t)) \\
& \quad \cos(2\pi f_{mm}\Delta t + \frac{\pi s_D(\Delta t)}{V_{\pi_{RF}}} + \phi_d(\Delta t)) \\
& +2\cos(2\pi f_{mm}t + 2\pi f_2\tau_1 + \frac{\pi s_D(t)}{V_{\pi_{RF}}} + \phi_1(t) - \phi_2(\Delta t)) \\
& \quad \cos(2\pi f_{mm}\Delta t + \frac{\pi s_D(\Delta t)}{V_{\pi_{RF}}} + \phi_d(\Delta t)) \\
& +2\cos(-2\pi f_{mm}t + 2\pi f_1\tau_1 - \frac{\pi s_D(\Delta t)}{V_{\pi_{RF}}} + \phi_2(t) - \phi_1(\Delta t)) \\
& \quad \cos(2\pi f_{mm}\Delta t + \frac{\pi s_D(\Delta t)}{V_{\pi_{RF}}} + \phi_d(\Delta t))
\end{aligned} \tag{A.1}
$$

Expanding equation (A.1)

$$
\begin{aligned}
r_{D2}(t) \propto\ & 2 + \cos(\Delta\phi(t) - \phi_1(t) + \phi_2(\Delta t) - 2\pi f_2 \tau_1) \\
& + \cos(\Delta\phi(t) + \phi_2(t) - \phi_1(\Delta t) + \frac{\pi s_D(t)}{V_{\pi_{RF}}} + 2\pi f_1 \tau_1 - \frac{\pi s_D(\Delta t)}{V_{\pi_{RF}}}) \\
& + \cos(\phi_1(t) - \phi_2(\Delta t) + \phi_2(t) - \phi_1(\Delta t) + \frac{\pi s_D(t)}{V_{\pi_{RF}}} + 2\pi f_2 \tau_1 + 2\pi f_1 \tau_1 - \\
& \quad \frac{\pi s_D(\Delta t)}{V_{\pi_{RF}}}) \\
& + \frac{1}{2} \cos(2\phi_2(t) - 2\phi_1(\Delta t) + 4\pi f_1 \tau_1 - 2\frac{\pi s_D(\Delta t)}{V_{\pi_{RF}}} - 4\pi f_{mm} t) \\
& + \frac{1}{2} \cos(2\Delta\phi(t) + 2\frac{\pi s_D(t)}{V_{\pi_{RF}}} + 4\pi f_{mm} t) \\
& + \cos(\Delta\phi(t) + \phi_1(t) - \phi_2(\Delta t) + 2\frac{\pi s_D(t)}{V_{\pi_{RF}}} + 2 f_2 \tau_1 \pi + 4\pi f_{mm} t) \\
& + \frac{1}{2} \cos(2\phi_1(t) - 2\phi_2(\Delta t) + 2\frac{\pi s_D(t)}{V_{\pi_{RF}}} + 4 f_2 \tau_1 \pi + 4\pi f_{mm} t) \\
& + \cos(\Delta\phi(t) - \phi_2(t) + \phi_1(\Delta t) + \frac{\pi s_D(t)}{V_{\pi_{RF}}} - 2 f_1 \tau_1 \pi + \frac{\pi s_D(\Delta t)}{V_{\pi_{RF}}} + 4\pi f_{mm} t) \\
& + \cos(\phi_1(t) - \phi_2(\Delta t) - \phi_2(t) + \phi_1(\Delta t) + \frac{\pi s_D(t)}{V_{\pi_{RF}}} + 2 f_2 \tau_1 \pi - 2 f_1 \tau_1 \pi + \\
& \quad \frac{\pi s_D(\Delta t)}{V_{\pi_{RF}}} + 4\pi f_{mm} t) \\
& + \cos(\phi_2(t) - \phi_1(\Delta t) - \phi_d(\Delta t) + 2 f_1 \tau_1 \pi - 2\frac{\pi s_D(\Delta t)}{V_{\pi_{RF}}} - 2\pi f_{mm} t - \\
& \quad 2\pi f_{mm} \Delta t) \\
& + \cos(\Delta\phi(t) - \phi_d(\Delta t) + \frac{\pi s_D(t)}{V_{\pi_{RF}}} - \frac{\pi s_D(\Delta t)}{V_{\pi_{RF}}} + 2\pi f_{mm} t - 2\pi f_{mm} \Delta t) \\
& + \cos(\phi_1(t) - \phi_2(\Delta t) - \phi_d(\Delta t) + \frac{\pi s_D(t)}{V_{\pi_{RF}}} + 2 f_2 \tau_1 \pi - \frac{\pi s_D(\Delta t)}{V_{\pi_{RF}}} + \\
& \quad 2\pi f_{mm} t - 2\pi f_{mm} \Delta t) \\
& + \cos(\phi_2(t) - \phi_1(\Delta t) + \phi_d(\Delta t) + 2 f_1 \tau_1 \pi - 2\pi f_{mm} t + 2\pi f_{mm} \Delta t) \\
& + \cos(\Delta\phi(t) + \phi_d(\Delta t) + \frac{\pi s_D(t)}{V_{\pi_{RF}}} + \frac{\pi s_D(\Delta t)}{V_{\pi_{RF}}} + 2\pi f_{mm} t + 2\pi f_{mm} \Delta t) \\
& + \cos(\phi_1(t) - \phi_2(\Delta t) + \phi_d(\Delta t) + \frac{\pi s_D(t)}{V_{\pi_{RF}}} + 2 f_2 \tau_1 \pi + \frac{\pi s_D(\Delta t)}{V_{\pi_{RF}}} + \\
& \quad 2\pi f_{mm} t + 2\pi f_{mm} \Delta t) \\
& + \frac{1}{2} \cos(2\phi_d(\Delta t) + 2\frac{\pi s_D(\Delta t)}{V_{\pi_{RF}}} + 4\pi f_{mm} \Delta t)
\end{aligned}
\tag{A.2}
$$

After lowpass filtering, the baseband signal before sampling $Y_2(t)$ will be

$$
\begin{aligned}
Y_2(t) \;\propto\;\; & 2 + \cos(\Delta\phi(t) - \phi_1(t) + \phi_2(\Delta t) - 2\pi f_2 \tau_1) \\
& + \cos(\Delta\phi(t) + \phi_2(t) - \phi_1(\Delta t) + \frac{\pi s_D(t)}{V_{\pi_{RF}}} + 2\pi f_1 \tau_1 - \frac{\pi s_D(\Delta t)}{V_{\pi_{RF}}}) \\
& + \cos(\phi_1(t) - \phi_2(\Delta t) + \phi_2(t) - \phi_1(\Delta t) + \frac{\pi s_D(t)}{V_{\pi_{RF}}} + 2\pi f_2 \tau_1 + 2\pi f_1 \tau_1 - \\
& \qquad \frac{\pi s_D(\Delta t)}{V_{\pi_{RF}}}) \\
& + \cos(\Delta\phi(t) - \phi_d(\Delta t) + \frac{\pi s_D(t)}{V_{\pi_{RF}}} - \frac{\pi s_D(\Delta t)}{V_{\pi_{RF}}} + 2\pi f_{mm} t - 2\pi f_{mm} \Delta t) \\
& + \cos(\phi_1(t) - \phi_2(\Delta t) - \phi_d(\Delta t) + \frac{\pi s_D(t)}{V_{\pi_{RF}}} + 2 f_2 \tau_1 \pi - \frac{\pi s_D(\Delta t)}{V_{\pi_{RF}}} + \\
& \qquad 2\pi f_{mm} t - 2\pi f_{mm} \Delta t) \\
& + \cos(\phi_2(t) - \phi_1(\Delta t) + \phi_d(\Delta t) + 2 f_1 \tau_1 \pi - 2\pi f_{mm} t + 2\pi f_{mm} \Delta t) \\
\propto\;\; & 2 + \cos(\Delta\phi(t) - \phi_1(t) + \phi_2(\Delta t) - 2\pi f_2 \tau_1) \\
& + \cos(\Delta\phi(t) + \phi_2(t) - \phi_1(\Delta t) + \frac{\pi s_D(t)}{V_{\pi_{RF}}} + 2\pi f_1 \tau_1 - \frac{\pi s_D(\Delta t)}{V_{\pi_{RF}}}) \\
& + \cos(\phi_1(t) - \phi_2(\Delta t) + \phi_2(t) - \phi_1(\Delta t) + \frac{\pi s_D(t)}{V_{\pi_{RF}}} + 2\pi f_2 \tau_1 + 2\pi f_1 \tau_1 - \\
& \qquad \frac{\pi s_D(\Delta t)}{V_{\pi_{RF}}}) \\
& + \cos(\Delta\phi(t) - \phi_d(\Delta t) + \frac{\pi s_D(t)}{V_{\pi_{RF}}} - \frac{\pi s_D(\Delta t)}{V_{\pi_{RF}}} + 2\pi f_{mm} \tau_1) \\
& + \cos(\phi_1(t) - \phi_2(\Delta t) - \phi_d(\Delta t) + \frac{\pi s_D(t)}{V_{\pi_{RF}}} + 2 f_2 \tau_1 \pi - \frac{\pi s_D(\Delta t)}{V_{\pi_{RF}}} + \\
& \qquad 2\pi f_{mm} \tau_1) \\
& + \cos(\phi_2(t) - \phi_1(\Delta t) + \phi_d(\Delta t) + 2 f_1 \tau_1 \pi - 2\pi f_{mm} \tau_1) \qquad \text{(A.3)}
\end{aligned}
$$

Bibliography

[1] "This week in tech," Apr 2017. [Online]. Available: https://www.telegraph.co.uk/technology/connecting-britain/guglielmo-marconi-birth/

[2] R. Steele and L. jos Hanzo, *Mobile RadioCommunications: Second and ThirdGeneration Cellular and WATM Systems.* Chichester, U.K: Wiley, 1999.

[3] E. Dahlman, S. Parkvall, and J. Skold, *4G LTE / LTE-Advance for Mobile Broadband.* Massachusetts, U.S.: Academic Press, 2011.

[4] "Gsa confirms lte subscriptions are now more than 25% of all global mobile subscriptions," Mar 2017. [Online]. Available: https://gsacom.com/paper/gsa-confirms-lte-subscriptions-now-25-global-mobile-subscriptions/

[5] "Gsa joins regional commonwealth in the field of communications (rcc)," May 2017. [Online]. Available: https://gsacom.com/paper/gsa-joins-regional-commonwealth-field-communications-rcc/

[6] T. Casaccia, "Demystifying 3gpp – an insider's perspective to how 4g and 5g standards get created," Aug 2017. [Online]. Available: https://www.telegraph.co.uk/technology/connecting-britain/guglielmo-marconi-birth/

[7] "Key outcomes of the world radiocommunication conference 2019," 2019. [Online]. Available: https://www.google.com/url?sa=t&rct=j&q=&esrc=s&source=web&cd=&ved=2ahUKEwiXlt6H-L3uAhWSzjgGHfoICL4QFjABegQIBxAC&url=https%3A%2F%2Fwww.itu.int%2Fmyitu%2F-%2Fmedia%2FPublications%2FITU-News-Magazine%2F2019%2FEn---Key-outcomes-of-the-WRC-2019.pdf&usg=AOvVaw13A__ZVc_HPEQdqLj0HzCF

[8] 3GPP, "Technical specification group services and system aspects; summary of rel-15 work items (release 15)," 3rd Generation Partnership Project (3GPP), Tech. Rep. TR 21.915, version 15.0.0.

[9] "Milestones: First millimeter-wave communication experiments by j.c. bose," Sept 2012. [Online]. Available: http://www.ieeeghn.org/wiki/index.php/Milestones:First_Millimeter-wave_Communication_Experiments_by_J.C._Bose.

[10] P. Lebedew, "Ueber die dopplbrechung der strahlen electrischer kraft," *Annalen der Physik*, vol. 292, pp. 1 – 17, 03 2006.

[11] P. T. Dat, A. Kanno, K. Inagaki, and T. Kawanishi, "High-capacity wireless backhaul network using seamless convergence of radio-over-fiber and 90-ghz millimeter-wave," *Journal of Lightwave Technology*, vol. 32, no. 20, pp. 3910–3923, 2014.

[12] I. Humar, X. Ge, L. Xiang, M. Jo, M. Chen, and J. Zhang, "Rethinking energy efficiency models of cellular networks with embodied energy," *IEEE Network*, vol. 25, no. 2, pp. 40–49, 2011.

[13] "Energy-saving solutions helping mobile operators meet commercial and sustainability goals worldwide," 2007. [Online]. Available: http://www.mobilontelecom.com/upload/Ericsson-Energy-Efficiency-White-Paper.pdf

[14] C. Schaefer, C. Weber, and A. Voss, "Energy usage of mobile telephone services in germany," *Energy*, vol. 28, no. 5, pp. 411–420, 2003. [Online]. Available: https://www.sciencedirect.com/science/article/pii/S0360544202001548

[15] C. M. R. Institute, "C-ran: The road towards green ran," White Paper, Tech. Rep., 2011.

[16] L. Zhang, A. Udalcovs, R. Lin, O. Ozolins, X. Pang, L. Gan, R. Schatz, M. Tang, S. Fu, D. Liu, W. Tong, S. Popov, G. Jacobsen, W. Hu, S. Xiao, and J. Chen, "Toward terabit digital radio over fiber systems: Architecture and key technologies," *IEEE Communications Magazine*, vol. 57, no. 4, pp. 131–137, 2019.

[17] F. Lu, M. Xu, L. Cheng, J. Wang, S. Shen, H. J. Cho, and G.-K. Chang, "Adaptive digitization and variable channel coding for enhancement of compressed digital mobile fronthaul in pam-4 optical links," *Journal of Lightwave Technology*, vol. 35, no. 21, pp. 4714–4720, 2017.

[18] J. Wang, Z. Yu, K. Ying, J. Zhang, F. Lu, M. Xu, L. Cheng, X. Ma, and G.-K. Chang, "Digital mobile fronthaul based on delta-sigma modulation for 32 lte carrier aggregation and fbmc signals," *IEEE/OSA Journal of Optical Communications and Networking*, vol. 9, no. 2, pp. A233–A244, 2017.

[19] H. Li, X. Li, and M. Luo, "Improving performance of differential pulse coding modulation based digital mobile fronthaul employing noise shaping," *Opt. Express*, vol. 26, no. 9, pp. 11 407–11 417, Apr 2018. [Online]. Available: http://www.opticsexpress.org/abstract.cfm?URI=oe-26-9-11407

[20] L. Zhang, X. Pang, O. Ozolins, A. Udalcovs, R. Schatz, U. Westergren, G. Jacobsen, S. Popov, L. Wosinska, S. Xiao, W. Hu, and J. Chen,

"Digital mobile fronthaul employing differential pulse code modulation with suppressed quantization noise," *Opt. Express*, vol. 25, no. 25, pp. 31 921–31 936, Dec 2017. [Online]. Available: http://www.opticsexpress.org/abstract.cfm?URI=oe-25-25-31921

[21] L. Zhang, X. Pang, O. Ozolins, A. Udalcovs, S. Popov, S. Xiao, W. Hu, and J. Chen, "Spectrally efficient digitized radio-over-fiber system with k-means clustering-based multidimensional quantization," *Opt. Lett.*, vol. 43, no. 7, pp. 1546–1549, Apr 2018. [Online]. Available: http://ol.osa.org/abstract.cfm?URI=ol-43-7-1546

[22] "Specification: Specification overview." [Online]. Available: http://www.cpri.info/spec.html

[23] A. Udalcovs, M. Levantesi, P. Urban, D. A. A. Mello, R. Gaudino, O. Ozolins, and P. Monti, "Total cost of ownership of digital vs. analog radio-over-fiber architectures for 5g fronthauling," *IEEE Access*, vol. 8, pp. 223 562–223 573, 2020.

[24] D. Silver, A. Huang, C. Maddison, A. Guez, L. Sifre, G. Driessche, J. Schrittwieser, I. Antonoglou, V. Panneershelvam, M. Lanctot, S. Dieleman, D. Grewe, J. Nham, N. Kalchbrenner, I. Sutskever, T. Lillicrap, M. Leach, K. Kavukcuoglu, T. Graepel, and D. Hassabis, "Mastering the game of go with deep neural networks and tree search," *Nature*, vol. 529, pp. 484–489, 01 2016.

[25] D. Silver, J. Schrittwieser, K. Simonyan, I. Antonoglou, A. Huang, A. Guez, T. Hubert, L. Baker, M. Lai, A. Bolton, Y. Chen, T. Lillicrap, F. Hui, L. Sifre, G. Driessche, T. Graepel, and D. Hassabis, "Mastering the game of go without human knowledge," *Nature*, vol. 550, pp. 354–359, 10 2017.

[26] A. M. TURING, "I.—COMPUTING MACHINERY AND INTELLIGENCE," *Mind*, vol. LIX, no. 236, pp. 433–460, 10 1950. [Online]. Available: https://doi.org/10.1093/mind/LIX.236.433

[27] T. Hwang, "Computational power and the social impact of artificial intelligence," *ArXiv*, vol. abs/1803.08971, 2018.

[28] E. Gong, J. Pauly, M. Wintermark, and G. Zaharchuk, "Deep learning enables reduced gadolinium dose for contrasenhanced brain mri," *Journal of Magnetic Resonance Imaging*, vol. 48, 2018.

[29] V. Kearney, S. Haaf, A. Sudhyadhom, G. Valdes, and T. Solberg, "An unsupervised convolutional neural network-based algorithm for deformable image registration." *Physics in medicine and biology*, vol. 63 18, p. 185017, 2018.

[30] K. Janod, M. Morchid, R. Dufour, G. Linarès, and R. Mori, “Denoised bottleneck features from deep autoencoders for telephone conversation analysis,” *IEEE/ACM Transactions on Audio, Speech, and Language Processing*, vol. 25, pp. 1505–1516, 2017.

[31] S. Leglaive, X. Alameda-Pineda, L. Girin, and R. Horaud, “A recurrent variational autoencoder for speech enhancement,” *ICASSP 2020 - 2020 IEEE International Conference on Acoustics, Speech and Signal Processing (ICASSP)*, pp. 371–375, 2020.

[32] P. Agrawal and S. Ganapathy, “Modulation filter learning using deep variational networks for robust speech recognition,” *IEEE Journal of Selected Topics in Signal Processing*, vol. 13, pp. 244–253, 2019.

[33] A. Graves, A. rahman Mohamed, and G. E. Hinton, “Speech recognition with deep recurrent neural networks,” *2013 IEEE International Conference on Acoustics, Speech and Signal Processing*, pp. 6645–6649, 2013.

[34] A. Graves and N. Jaitly, “Towards end-to-end speech recognition with recurrent neural networks,” *31st International Conference on Machine Learning, ICML 2014*, vol. 5, pp. 1764–1772, 01 2014.

[35] M. K. M. Ali and F. Kamoun, “Neural networks for shortest path computation and routing in computer networks,” *IEEE transactions on neural networks*, vol. 4 6, pp. 941–954, 1993.

[36] S. Zander, T. T. Nguyen, and G. Armitage, “Self-learning ip traffic classification based on statistical flow characteristics,” in *PAM*, 2005.

[37] X. Wu, J. Jargon, R. Skoog, L. Paraschis, and A. Willner, “Applications of artificial neural networks in optical performance monitoring,” *Journal of Lightwave Technology*, vol. 27, pp. 3580–3589, 2009.

[38] F. N. Khan, K. Zhong, X. Zhou, W. H. Al-Arashi, C. Yu, C. Lu, and A. Lau, “Joint osnr monitoring and modulation format identification in digital coherent receivers using deep neural networks.” *Optics express*, vol. 25 15, pp. 17 767–17 776, 2017.

[39] Z. Wang, M. Zhang, D. Wang, C. Song, M. Liu, J. Li, L. Lou, and Z. Liu, “Failure prediction using machine learning and time series in optical network.” *Optics express*, vol. 25 16, pp. 18 553–18 565, 2017.

[40] F. Boitier, V. Lemaire, J. Pesic, L. Chavarría, P. Layec, S. Bigo, and E. Dutisseuil, “Proactive fiber damage detection in real-time coherent receiver,” *2017 European Conference on Optical Communication (ECOC)*, pp. 1–3, 2017.

[41] C. Lim, K. Lee, A. Nirmalathas, D. Novak, and R. Waterhouse, "Impact of chromatic dispersion on 60 ghz radio-over-fiber transmission," *LEOS 2008 - 21st Annual Meeting of the IEEE Lasers and Electro-Optics Society*, pp. 89–90, 2008.

[42] L. Goldberg, H. Taylor, J. Weller, and D. Bloom, "Microwave signal generation with injection-locked laser diodes," *Electronics Letters*, vol. 19, pp. 491–493, 1983.

[43] L. Goldberg, A. Yurek, H. Taylor, and J. Weller, "35 ghz microwave signal generation with an injection-locked laser diode," *Electronics Letters*, vol. 21, pp. 814–815, 1985.

[44] J. O'Reilly and P. Lane, "Remote delivery of video services using mm-waves and optics," *Journal of Lightwave Technology*, vol. 12, pp. 369–375, 1994.

[45] H. Schmuck, T. Pfeiffer, and H. Bülow, "Design optimisation of erbium ring laser regarding output power and spectral properties," *Electronics Letters*, vol. 28, pp. 1637–1639, 1992.

[46] K. Williams, L. Goldberg, R. Esman, M. Dagenais, and J. Weller, "6-34 ghz offset phase-locking of nd:yag 1319 nm nonplanar ring lasers," *Electronics Letters*, vol. 25, pp. 1242–1243, 1989.

[47] R. Ramos and A. Seeds, "Fast heterodyne optical phase-lock loop using double quantum well laser diodes," *Electronics Letters*, vol. 28, pp. 82–83, 1992.

[48] F. Fan and M. Dagenais, "Optical generation of a megahertz-linewidth microwave signal using semiconductor lasers and a discriminator-aided phase-locked loop," *IEEE Transactions on Microwave Theory and Techniques*, vol. 45, pp. 1296–1300, 1997.

[49] E. Lau, X. Zhao, H.-K. Sung, D. Parekh, C. Chang-Hasnain, and M. Wu, "Strong optical injection-locked semiconductor lasers demonstrating ¿ 100-ghz resonance frequencies and 80-ghz intrinsic bandwidths." *Optics express*, vol. 16 9, pp. 6609–18, 2008.

[50] Y. Okajima, S.-K. Hwang, and J. Liu, "Experimental observation of chirp reduction in bandwidth-enhanced semiconductor lasers subject to strong optical injection," *Optics Communications*, vol. 219, pp. 357–364, 2003.

[51] L. Chrostowski, C. Chang, and C. Chang-Hasnain, "Reduction of relative intensity noise and improvement of spur-free dynamic range of an injection locked vcsel," *The 16th Annual Meeting of the IEEE Lasers and Electro-Optics Society, 2003. LEOS 2003.*, vol. 2, pp. 706–707, 2003.

[52] G. Yabre and J. Bihan, "Reduction of nonlinear distortion in directly modulated semiconductor lasers by coherent light injection," *IEEE Journal of Quantum Electronics*, vol. 33, pp. 1132–1140, 1997.

[53] D. Parekh, W. Yang, A. Ng'oma, D. Fortusini, M. Sauer, S. Benjamin, W. Hofmann, M. Amann, and C. Chang-Hasnain, "Multi-gbps ask and qpsk-modulated 60 ghz rof link using an optically injection locked vcsel," *2010 Conference on Optical Fiber Communication (OFC/NFOEC), collocated National Fiber Optic Engineers Conference*, pp. 1–3, 2010.

[54] A. Ng'oma, D. Fortusini, D. Parekh, W. Yang, M. Sauer, S. Benjamin, W. Hofmann, M. Amann, and C. Chang-Hasnain, "Performance of a multi-gb/s 60 ghz radio over fiber system employing a directly modulated optically injection-locked vcsel," *Journal of Lightwave Technology*, vol. 28, pp. 2436–2444, 2010.

[55] T. Kuri, K. Kitayama, and Y. Takahashi, "A single light-source configuration for full-duplex 60-ghz-band radio-on-fiber system," *IEEE Transactions on Microwave Theory and Techniques*, vol. 51, pp. 431–439, 2003.

[56] S. T. Choi, K. S. Yang, S. Nishi, S. Shimizu, K. Tokuda, and Y. H. Kim, "A 60-ghz point-to-multipoint millimeter-wave fiber-radio communication system," *IEEE Transactions on Microwave Theory and Techniques*, vol. 54, pp. 1953–1960, 2006.

[57] M. Huang, J. Yu, Z. Jia, and G. Chang, "Simultaneous generation of centralized lightwaves and double/single sideband optical millimeter-wave requiring only low-frequency local oscillator signals for radio-over-fiber systems," *Journal of Lightwave Technology*, vol. 26, pp. 2653–2662, 2008.

[58] J. Pan, "21 ghz wideband fiber optic link," *1988., IEEE MTT-S International Microwave Symposium Digest*, pp. 977–978, 1988.

[59] H. Wen, L. Chen, J. He, and S. Wen, "Simultaneously realizing optical millimeter-wave generation and photonic frequency down-conversion employing optical phase modulator and sidebands separation technique," *2007 Asia Optical Fiber Communication and Optoelectronics Conference*, pp. 427–429, 2007.

[60] J. Park, W. Sorin, and K. Lau, "Elimination of the fibre chromatic dispersion penalty on 1550 nm millimetre-wave optical transmission," *Electronics Letters*, vol. 33, pp. 512–513, 1997.

[61] M. Attygalle, C. Lim, G. Pendock, A. Nirmalathas, and G. Edvell, "Transmission improvement in fiber wireless links using fiber bragg gratings," *IEEE Photonics Technology Letters*, vol. 17, pp. 190–192, 2005.

[62] G. H. Smith, D. Novak, and Z. Ahmed, "Technique for optical ssb generation to overcome dispersion penalties in fibre-radio systems," *Electronics Letters*, vol. 33, pp. 74–75, 1997.

[63] E. Vergnol, F. Devaux, D. Tanguy, and E. Penard, "Integrated lightwave millimetric single side-band source: design and issues," *Journal of Lightwave Technology*, vol. 16, pp. 1276–1284, 1998.

[64] P. Shen, N. Gomes, P. A. Davies, W. Shillue, P. Huggard, and B. Ellison, "High-purity millimetre-wave photonic local oscillator generation and delivery," *MWP 2003 Proceedings. International Topical Meeting on Microwave Photonics, 2003.*, pp. 189–192, 2003.

[65] A. Islam, M. Bakaul, and A. Nirmalathas, "Multi-level ask demonstrations in millimeter-wave radio-over-fiber system using free-running lasers and rf self-homodyning," *2012 IEEE International Topical Meeting on Microwave Photonics*, pp. 95–98, 2012.

[66] B. Biglarbegian, M. Fakharzadeh, D. Busuioc, M. Nezhad-Ahmadi, and S. Safavi-Naeini, "Optimized microstrip antenna arrays for emerging millimeter-wave wireless applications," *IEEE Transactions on Antennas and Propagation*, vol. 59, pp. 1742–1747, 2011.

[67] P. Dat, A. Kanno, N. Yamamoto, and T. Kawanishi, "Performance evaluation of full-duplex mimo seamless fiber–wireless system in \$w\$ -band," *IEEE Photonics Technology Letters*, vol. 30, pp. 1175–1178, 2018.

[68] T. G. Hao, M. Bakaul, and M. Boroon, "Incoherent heterodyning of phase modulated signal for low-cost millimeter-wave rof link," *2018 IEEE International RF and Microwave Conference (RFM)*, pp. 159–161, 2018.

[69] QualcommResearch, "Hyper-dense small cell deployment trial in NASCAR environment," Tech. Rep., 2014.

[70] FCC, "Code of federal regulations title 47 part 30 section 202 (47 cfr § 30.202), power limits,"
http://https://www.law.cornell.edu/cfr/text/47/30.202.

[71] Federal Communications Commissions, "Fcc-16-89, use of spectrum bands above 24 ghz for mobile radio services: Report and order and further notice of proposed rule making,"
https://www.fcc.gov/document/spectrum-frontiers-ro-and-fnprm.

[72] FCC, "Code of federal regulations title 47 part 2 section 1091 (47 cfr § 2.1091), radio frequency radiation exposure evaluation: mobile devices." https://www.govinfo.gov/content/pkg/CFR-2011-title47-vol1/pdf/CFR-2011-title47-vol1-part2-subpartJ-subjectgroup-id922.pdf.

[73] ——, "Code of federal regulations title 47 part 2 section 1093 (47 cfr § 2.1093), radio frequency radiation exposure evaluation: portable devices," https://www.law.cornell.edu/cfr/text/47/2.1093.

[74] ——, "Code of federal regulations title 47 part 15 section 255 (47 cfr § 15.255), operation within the band 57-71 ghz." https://www.law.cornell.edu/cfr/text/47/15.255.

[75] ——, "Code of federal regulations title 47 part 30 section 405 (47 cfr § 30.405), transmitter power limitations." https://www.law.cornell.edu/cfr/text/47/30.405.

[76] Federal Communications Commissions, "Fcc-17-152, use of spectrum bands above 24 ghz for mobile radio services: Second report and order, second further notice of proposed rulemaking, order on reconsideration, and memorandum opinion and order." https://www.fcc.gov/document/fcc-takes-next-steps-facilitating-spectrum-frontiers-spectrum.

[77] 3GPP, "Technical specification group radio access network; new radio; base station radio transmission and reception (release 16)," 3rd Generation Partnership Project (3GPP), Tech. Rep. TS 38.104, version 16.6.0.

[78] ——, "Technical specification group radio access network; new radio; user equipment radio transmission and reception; part 2: Range 2 standalone (release 16)," 3rd Generation Partnership Project (3GPP), Tech. Rep. TS 38.101-2, version 16.6.0.

[79] ITU, "Attenuation by atmospheric gases and related effects," International Telecommunication Union (ITU), Tech. Rep., 2019, recommendation ITU-R P.676-12.

[80] T. Wu, T. Rappaport, and C. M. Collins, "Safe for generations to come: Considerations of safety for millimeter waves in wireless communications," *IEEE Microwave Magazine*, vol. 16, pp. 65–84, 2015.

[81] C. Cho, M. Maloy, S. Devlin, O. Aras, H. Castro-Malaspina, L. Dauer, A. Jakubowski, R. O'reilly, E. Papadopoulos, M. Perales, T. Rappaport,

R. Tamari, M. Brink, and S. Giralt, “Characterizing ionizing radiation exposure after t-cell depleted allogeneic hematopoietic cell transplantation,” *Biology of Blood and Marrow Transplantation*, vol. 24, 2018.

[82] T. Wu, T. Rappaport, and C. M. Collins, “The human body and millimeter-wave wireless communication systems: Interactions and implications,” *2015 IEEE International Conference on Communications (ICC)*, pp. 2423–2429, 2015.

[83] Federal Communications Commissions, “Guidelines for evaluating the environmental effects of radio frequency radiation, document fcc 96-326,” https://www.fcc.gov/document/guidelines-evaluating-environmental-effects-radiofrequency.

[84] I. C. on Non-Ionizing Radiation Protection, “Icnirp statement on the ”guidelines for limiting exposure to time-varying electric, magnetic, and electromagnetic fields (up to 300 ghz)”.” *Health physics*, vol. 97 3, pp. 257–8, 2009.

[85] FCC, “Wireless devices and health concerns,” https://www.fcc.gov/consumers/guides/wireless-devices-and-healthconcerns.

[86] “Belgium adopts new regulations to promote cell phone radiation safety,” Oct 2013. [Online]. Available: https://www.prlog.org/12231532-belgium-adopts-newregulations-to-promote-cell-phone-radiation-safety.html.

[87] “Guidelines for limiting exposure to electromagnetic fields (100 khz to 300 ghz).” *Health physics*, 2020.

[88] “Ieee standard for safety levels with respect to human exposure to electric, magnetic, and electromagnetic fields, 0 hz to 300 ghz,” *IEEE Std C95.1-2019 (Revision of IEEE Std C95.1-2005/ Incorporates IEEE Std C95.1-2019/Cor 1-2019)*, pp. 1–312, 2019.

[89] FCC, “Code of federal regulation title 47 section 1.1310 (47 cfr § 1.1310) radio frequency radiation exposure limits,” https://www.law.cornell.edu/cfr/text/47/1.1310#:~:text=CFR-,%C2%A7%201.1310%20Radiofrequency%20radiation%20exposure%20limits.,to%206%20GHz%20(inclusive).

[90] Jake Novicky, “Rf exposure procedures,” https://transition.fcc.gov/oet/ea/presentations/files/apr19/4.0-RF-Exposure-Panel-FINAL.pdf.

[91] FCC, “Resolution of notice of inquiry second report and order notice of proposed rulemaking and memorandum opinion and order,” Dec 2019, https://docs.fcc.gov/public/attachments/FCC-19-126A1.pdf.

[92] CCIR, “Attenuation by hydrometeors, in particular precipitation, and other atmospheric particles,” Consultative Committee on International Radio (CCIR), Tech. Rep., 1986, report 721-2.

[93] ——, “Attenuation by atmospheric gases,” Consultative Committee on International Radio (CCIR), Tech. Rep., 1990, doc. Rep. 719-3.

[94] L. Ippolito, “Attenuation by atmospheric gases,” 1986.

[95] E. K. Smith, “Centimeter and millimeter wave attenuation and brightness temperature due to atmospheric oxygen and water vapor,” *Radio Science*, vol. 17, pp. 1455–1464, 1982.

[96] L. J. I. Jr, *Radiowave Propagation in satellite Communications.* Berlin: Springer, 1986, ch. Radio Noise in Satellite Communications, pp. 122–138.

[97] F. O. of Engineering and Technology, “Millimeter wave propagation: Spectrum management implications,” Federal Communications Commissionn (FCC), Tech. Rep., 1997, oET Bulletin No. 70.

[98] D. Cama-Pinto, M. Damas, J. A. Holgado-Terriza, F. Gómez-Mula, and A. Cama-Pinto, “Path loss determination using linear and cubic regression inside a classic tomato greenhouse,” *International Journal of Environmental Research and Public Health*, vol. 16, 2019.

[99] H. Xu, T. Rappaport, R. Boyle, and J. Schaffner, “Measurements and models for 38-ghz point-to-multipoint radiowave propagation,” *IEEE Journal on Selected Areas in Communications*, vol. 18, pp. 310–321, 2000.

[100] S. Swarup and R. Tewari, “Propagation characteristics of vhf/uhf signals in tropical moist deciduous forest,” *Iete Journal of Research*, vol. 21, pp. 123–125, 1975.

[101] ——, “Depolarization of radio waves in jungle environment,” *IEEE Transactions on Antennas and Propagation*, vol. 27, pp. 113–116, 1979.

[102] S. Ju, S. Shah, M. A. Javed, J. Li, G. Palteru, J. Robin, Y. Xing, O. Kanhere, and T. Rappaport, “Scattering mechanisms and modeling for terahertz wireless communications,” *ICC 2019 - 2019 IEEE International Conference on Communications (ICC)*, pp. 1–7, 2019.

[103] A. Goulianos, A. L. Freire, T. H. Barratt, E. Mellios, P. Cain, M. Rumney, A. Nix, and M. Beach, “Measurements and characterisation of surface scattering at 60 ghz,” *2017 IEEE 86th Vehicular Technology Conference (VTC-Fall)*, pp. 1–5, 2017.

[104] J. Ma, R. Shrestha, L. Moeller, and D. Mittleman, "Invited article: Channel performance for indoor and outdoor terahertz wireless links," 2018.

[105] C. Anderson and T. Rappaport, "In-building wideband partition loss measurements at 2.5 and 60 ghz," *IEEE Transactions on Wireless Communications*, vol. 3, pp. 922–928, 2004.

[106] K. Allen, "Building penetration loss measurements at 900 mhz, 11.4 ghz, and 28.8 ghz," 1994, nTIA rep. 94-306.

[107] H. Zhao, R. Mayzus, S. Sun, M. Samimi, J. K. Schulz, Y. Azar, K. Wang, G. N. Wong, F. Gutierrez, and T. Rappaport, "28 ghz millimeter wave cellular communication measurements for reflection and penetration loss in and around buildings in new york city," *2013 IEEE International Conference on Communications (ICC)*, pp. 5163–5167, 2013.

[108] A. Alejos, M. Sánchez, and I. Cuiñas, "Measurement and analysis of propagation mechanisms at 40 ghz: Viability of site shielding forced by obstacles," *IEEE Transactions on Vehicular Technology*, vol. 57, pp. 3369–3380, 2008.

[109] A. Malik and P. Singh, "Free space optics: Current applications and future challenges," *International Journal of Optics*, vol. 2015, pp. 1–7, 2015.

[110] R. A. Alsemmeari, S. T. Bakhsh, and H. Alsemmeari, "Free space optics vs radio frequency wireless communication," *International Journal of Information Technology and Computer Science*, vol. 8, pp. 1–8, 2016.

[111] J. Juarez, A. Dwivedi, A. R. Hammons, S. Jones, V. Weerackody, and R. Nichols, "Free-space optical communications for next-generation military networks," *IEEE Communications Magazine*, vol. 44, 2006.

[112] A. Demir, "Nonlinear phase noise in optical-fiber-communication systems," *Journal of Lightwave Technology*, vol. 25, pp. 2002–2032, 2007.

[113] E. Ip, A. Lau, D. Barros, and J. Kahn, "Coherent detection in optical fiber systems." *Optics express*, vol. 16 2, pp. 753–91, 2008.

[114] C. fei Li, *Nonlinear Optics: Principles and Applications.* Singapore: Springer, 2017, ch. Optical Kerr Effect and Self-focusing, pp. 109–147.

[115] J. Harris, M. Wistey, S. Bank, L. Goddard, V. Lordi, H. Bae, and H. Yuen, "Chapter 17 - long-wavelength dilute nitride-antimonide lasers," in *Dilute Nitride Semiconductors*, M. Henini, Ed. Amsterdam: Elsevier, 2005, pp. 507–578. [Online]. Available: https://www.sciencedirect.com/science/article/pii/B9780080445021500172

[116] R. Poggiani, *Encyclopedia of Physical Science and Technology*, 3rd ed. U.S: Academic Press, 2003, ch. Gravitational Wave Detectors, pp. 49–65.

[117] S. Yamamoto, N. Edagawa, H. Taga, Y. Yoshida, and H. Wakabayashi, "Analysis of laser phase noise to intensity noise conversion by chromatic dispersion in intensity modulation and direct detection optical-fiber transmission," *Journal of Lightwave Technology*, vol. 8, pp. 1716–1722, 1990.

[118] V. Urick, K. Williams, and J. McKinney, *Fundamentals of Microwave Photonics*, ser. Wiley Series in Microwave and Optical Engineering. Wiley, 2015. [Online]. Available: https://books.google.com.my/books?id=mg91BgAAQBAJ

[119] G. Meslener, "Analysis of mode-partition noise for subcarrier modulated transmission systems," in *Digest of Conference on Optical Fiber Communication.* Optical Society of America, 1992, p. TuD3. [Online]. Available: http://www.osapublishing.org/abstract.cfm?URI=OFC-1992-TuD3

[120] ——, "Mode-partition noise in microwave subcarrier transmission systems," *Journal of Lightwave Technology*, vol. 12, pp. 118–126, 1994.

[121] X. Lu, C. Su, R. Lauer, G. Meslener, and L. Ulbricht, "Analysis of relative intensity noise in semiconductor lasers and its effect on subcarrier multiplexed lightwave systems," *Journal of Lightwave Technology*, vol. 12, pp. 1159–1166, 1994.

[122] P. Laurêncio, S. Simoes, and M. Medeiros, "Impact of the combined effect of rin and intermodulation distortion on ossb/scm systems," *Journal of Lightwave Technology*, vol. 24, pp. 4250–4262, 2006.

[123] J. Morgado and A. Cartaxo, "New semi-analytical method of estimating the influence of laser noise on direct detection system performance," *Technical Digest. CLEO/Pacific Rim 2001. 4th Pacific Rim Conference on Lasers and Electro-Optics (Cat. No.01TH8557)*, vol. 2, pp. II–II, 2001.

[124] R. Poggiani, *Optical Fiber Telecommunication IIA*, 3rd ed. U.S: Academic Press, 1997, ch. Lightwave Analog Video Transmission, pp. 523–559.

[125] G. Meslener, "Chromatic dispersion induced distortion of modulated monochromatic light employing direct detection," *IEEE Journal of Quantum Electronics*, vol. 20, pp. 1208–1216, 1984.

[126] G. Smith, D. Novak, and Z. Ahmed, "Overcoming chromatic-dispersion effects in fiber-wireless systems incorporating external modulators," *IEEE Transactions on Microwave Theory and Techniques*, vol. 45, pp. 1410–1415, 1997.

[127] H. Schmuck, "Comparison of optical millimetre-wave system concepts with regard to chromatic dispersion," *Electronics Letters*, vol. 31, pp. 1848–1849, 1995.

[128] U. Gliese, S. Norskov, and T. Nielsen, "Chromatic dispersion in fiber-optic microwave and millimeter-wave links," *IEEE Transactions on Microwave Theory and Techniques*, vol. 44, pp. 1716–1724, 1996.

[129] D.-H. Kim, J.-Y. Lee, H.-J. Choi, and J.-I. Song, "All-optical single-sideband frequency upconversion utilizing the xpm effect in an soa-mzi." *Optics express*, vol. 24 18, pp. 20 309–17, 2016.

[130] R. Braun, G. Großkopf, D. Rohde, and F. Schmidt, "Optical millimetre-wave generation and transmission experiments for mobile 60 ghz band communications," *Electronics Letters*, vol. 32, pp. 626–628, 1996.

[131] F. Timofeev, S. Bennett, R. Griffin, P. Bayvel, A. Seeds, R. Wyatt, R. Kashyap, and M. Robertson, "High spectral purity millimetre-wave modulated optical signal generation using fibre grating lasers," *Electronics Letters*, vol. 34, pp. 668–669, 1998.

[132] A. Malcoci, A. Stohr, R. Heinzelmann, K. Hagedorn, R. Gusten, F. Schafer, H. Stuer, F. Siebe, P. van der Wal, V. Krozer, M. Feiginov, and D. Jager, "Photonic (sub)millimeterwave local oscillators," *14th International Conference on Microwaves, Radar and Wireless Communications. MIKON - 2002. Conference Proceedings (IEEE Cat.No.02EX562)*, vol. 3, pp. 722–734, 2002.

[133] I. G. Insua, D. Plettemeier, and C. Schaffer, "Simple remote heterodyne rof system for gbps wireless access," *2009 International Topical Meeting on Microwave Photonics*, pp. 1–4, 2009.

[134] A. Islam, M. Bakaul, A. Nirmalathas, and G. Town, "Simplification of millimeter-wave radio-over-fiber system employing heterodyning of uncorrelated optical carriers and self-homodyning of rf signal at the receiver." *Optics express*, vol. 20 5, pp. 5707–24, 2012.

[135] M. Huang, J. Yu, Z. Jia, and G. Chang, "Simultaneous generation of centralized lightwaves and double/single sideband optical millimeter-wave requiring only low-frequency local oscillator signals for radio-over-fiber systems," *Journal of Lightwave Technology*, vol. 26, pp. 2653–2662, 2008.

[136] P. Shen, N. Gomes, P. A. Davies, W. Shillue, P. Huggard, and B. Ellison, "High-purity millimetre-wave photonic local oscillator generation and delivery," *MWP 2003 Proceedings. International Topical Meeting on Microwave Photonics, 2003.*, pp. 189–192, 2003.

[137] J. Yu, Z. Jia, T. Wang, and G. Chang, "A novel radio-over-fiber configuration using optical phase modulator to generate an optical mm-wave and centralized lightwave for uplink connection," *IEEE Photonics Technology Letters*, vol. 19, pp. 140–142, 2007.

[138] G. Qi, J. Yao, J. Seregelyi, S. Paquet, and C. Bélisle, "Generation and distribution of a wide-band continuously tunable millimeter-wave signal with an optical external modulation technique," *IEEE Transactions on Microwave Theory and Techniques*, vol. 53, pp. 3090–3097, 2005.

[139] S. E. Alavi, I. Amiri, M. Khalily, N. Fisal, A. Supa'at, H. Ahmad, and S. M. Idrus, "W-band ofdm for radio-over-fiber direct-detection link enabled by frequency nonupling optical up-conversion," *IEEE Photonics Journal*, vol. 6, pp. 1–7, 2014.

[140] S. Li, X. Zheng, H. Zhang, and B. Zhou, "Highly linear radio-over-fiber system incorporating a single-drive dual-parallel mach–zehnder modulator," *IEEE Photonics Technology Letters*, vol. 22, pp. 1775–1777, 2010.

[141] C.-T. Lin, P. Shih, J. Chen, P. Peng, S.-P. Dai, W.-Q. Xue, and S. Chi, "Generation of carrier suppressed optical mm-wave signals using frequency quadrupling and no optical filtering," *OFC/NFOEC 2008 - 2008 Conference on Optical Fiber Communication/National Fiber Optic Engineers Conference*, pp. 1–3, 2008.

[142] 3GPP, "Requirements for further advancements for evolved universal terrestrial radio access (e-utra) (lte-advanced)," 3rd Generation Partnership Project (3GPP), Tech. Rep. TR 36.913, 2009, version 9.0.0.

[143] ——, "Evolved universal terrestrial radio access (e-utra); further advancements for e-utra physical layer aspects," 3rd Generation Partnership Project (3GPP), Tech. Rep. TR 36.814, 2010, version 9.0.0.

[144] ——, "Coordinated multi-point operation for lte physical layer aspects," 3rd Generation Partnership Project (3GPP), Tech. Rep. TR 36.819, 2013, version 11.2.0.

[145] P. Marsch and G. Fettweis, "Static clustering for cooperative multi-point (comp) in mobile communications," *2011 IEEE International Conference on Communications (ICC)*, pp. 1–6, 2011.

[146] A. S. Rodriguez and A. G. Armada, "Analysis of the cluster size in coordinated multipoint transmission," *2011 IEEE 19th Signal Processing and Communications Applications Conference (SIU)*, pp. 1197–1200, 2011.

[147] G. Cili, H. Yanikomeroglu, and F. Yu, "Cell switch off technique combined with coordinated multi-point (comp) transmission for energy efficiency in beyond-lte cellular networks," *2012 IEEE International Conference on Communications (ICC)*, pp. 5931–5935, 2012.

[148] I. Garcia, N. Kusashima, K. Sakaguchi, K. Araki, S. Kaneko, and Y. Kishi, "Impact of base station cooperation on cell planning," *EURASIP Journal on Wireless Communications and Networking*, vol. 2010, pp. 1–17, 2010.

[149] 3GPP, "Evolved universal terrestrial radio access network (e-utran); self-configuring and self-optimizing network (son) use cases and solutions," 3rd Generation Partnership Project (3GPP), Tech. Rep. TR 36.902, 2011, version 9.3.1.

[150] ——, "Telecommunication management; self-configuration of network elements; concepts and requirements," 3rd Generation Partnership Project (3GPP), Tech. Rep. TS 32.501, 2013, version 12.1.0.

[151] ——, "Telecommunication management; self-organizing networks (son) policy network resource model (nrm) integration reference point (irp); requirements," 3rd Generation Partnership Project (3GPP), Tech. Rep. TS 32.521, 2012, version 11.1.0.

[152] ——, "Telecommunication management; self-organizing networks (son); self-healing concepts and requirements," 3rd Generation Partnership Project (3GPP), Tech. Rep. TS 32.541, 2014, version 12.0.0.

[153] S. Ali and N. Saxena, "A novel static clustering approach for comp," *2012 7th International Conference on Computing and Convergence Technology (ICCCT)*, pp. 757–762, 2012.

[154] H. Shimodaira, G. Tran, K. Araki, K. Sakaguchi, S. Konishi, and S. Nanba, "Diamond cellular network — optimal combination of small power basestations and comp cellular networks-," *2013 IEEE 24th International Symposium on Personal, Indoor and Mobile Radio Communications (PIMRC Workshops)*, pp. 163–167, 2013.

[155] S. Nam, J. Oh, and Y. Han, "A dynamic transmission mode selection scheme for comp systems," *2012 IEEE 23rd International Symposium on Personal, Indoor and Mobile Radio Communications - (PIMRC)*, pp. 483–487, 2012.

[156] B. Makki, T. Eriksson, and T. Svensson, "On an harq-based coordinated multi-point network using dynamic point selection," *EURASIP Journal on Wireless Communications and Networking*, vol. 2013, pp. 1–11, 2013.

[157] X.-H. You, D. Wang, B. Sheng, X.-Q. Gao, X. Zhao, and M. Chen, "Cooperative distributed antenna systems for mobile communications [coordinated and distributed mimo]," *IEEE Wireless Communications*, vol. 17, 2010.

[158] D. Liu, S. Han, C. Yang, and Q. Zhang, "Semi-dynamic user-specific clustering for downlink cloud radio access network," *IEEE Transactions on Vehicular Technology*, vol. 65, pp. 2063–2077, 2016.

[159] F. Huang, Y. Wang, J. Geng, M. Wu, and D. cheng Yang, "Clustering approach in coordinated multi-point transmission/reception system," *2010 IEEE 72nd Vehicular Technology Conference - Fall*, pp. 1–5, 2010.

[160] V. Pichapati and P. Gupta, "Practical considerations in cluster design for coordinated multipoint (comp) systems," *2013 IEEE International Conference on Communications (ICC)*, pp. 5860–5865, 2013.

[161] H. Sun, X. Zhang, and W. Fang, "Dynamic cell clustering design for realistic coordinated multipoint downlink transmission," *2011 IEEE 22nd International Symposium on Personal, Indoor and Mobile Radio Communications*, pp. 1331–1335, 2011.

[162] S. Feng, W. Feng, H. Mao, and J. Lu, "Overlapped clustering for comp transmissions in massively dense wireless networks," *2014 IEEE International Conference on Communication Systems*, pp. 308–312, 2014.

[163] F. Guidolin, L. Badia, and M. Zorzi, "A distributed clustering algorithm for coordinated multipoint in lte networks," *IEEE Wireless Communications Letters*, vol. 3, pp. 517–520, 2014.

[164] A. Papadogiannis, D. Gesbert, and E. Hardouin, "A dynamic clustering approach in wireless networks with multi-cell cooperative processing," *2008 IEEE International Conference on Communications*, pp. 4033–4037, 2008.

[165] H. Li, H. Tian, C. Qin, and Y. Pei, "A novel distributed cluster combination method for comp in lte-a system," *The 15th International Symposium on Wireless Personal Multimedia Communications*, pp. 614–618, 2012.

[166] J.-M. Moon and D. Cho, "Formation of cooperative cluster for coordinated transmission in multi-cell wireless networks," *2013 IEEE 10th Consumer Communications and Networking Conference (CCNC)*, pp. 528–533, 2013.

[167] V. Kotzsch and G. Fettweis, "Interference analysis in time and frequency asynchronous network mimo ofdm systems," *2010 IEEE Wireless Communication and Networking Conference*, pp. 1–6, 2010.

[168] L. Cheng, M. Gul, F. Lu, M. Zhu, J. Wang, M. Xu, X. Ma, and G. Chang, "Coordinated multipoint transmissions in millimeter-wave radio-over-fiber systems," *Journal of Lightwave Technology*, vol. 34, pp. 653–660, 2016.

[169] J.-H. Yan, J.-K. Huang, Y.-Y. Lin, J. Hsu, and K. Feng, "A mmw coordinate multi-point transmission system for 5g mobile fronthaul networks based on a polarization-tracking-free pdm-rof mechanism," *2020 Optical Fiber Communications Conference and Exhibition (OFC)*, pp. 1–3, 2020.

[170] J. Li, M. Peng, A. Cheng, Y. Yu, and C. Wang, "Resource allocation optimization for delay-sensitive traffic in fronthaul constrained cloud radio access networks," *IEEE Systems Journal*, vol. 11, pp. 2267–2278, 2017.

[171] J. Zhang, H. Yu, Y. Ji, H. Li, X. Yu, Y. Zhao, and H. Li, "Demonstration of radio and optical orchestration for improved coordinated multi-point (comp) service over flexible optical fronthaul transport networks," *2017 Optical Fiber Communications Conference and Exhibition (OFC)*, pp. 1–3, 2017.

[172] S. Liu, X. Wang, W. Zhang, G. Shen, and H. Tian, "An adaptive activated ann equalizer applied in millimeter-wave rof transmission system," *IEEE Photonics Technology Letters*, vol. 29, pp. 1935–1938, 2017.

[173] S. Liu, Y. M. Alfadhli, S. Shen, H. Tian, and G. Chang, "Mitigation of multi-user access impairments in 5g a-rof-based mobile fronthaul utilizing machine learning for an artificial neural network nonlinear equalizer," *2018 Optical Fiber Communications Conference and Exposition (OFC)*, pp. 1–3, 2018.

[174] S. Liu, Y. M. Alfadhli, S. Shen, M. Xu, H. Tian, and G. Chang, "A novel ann equalizer to mitigate nonlinear interference in analog-rof mobile fronthaul," *IEEE Photonics Technology Letters*, vol. 30, pp. 1675–1678, 2018.

[175] J.-H. Lee, J. He, Y. Wang, C. Fang, and K. Wang, "Experimental demonstration of millimeter-wave radio-over-fiber system with convolutional neural network (cnn) and binary convolutional neural network (bcnn)," *arXiv: Signal Processing*, 2020.

[176] J. Lee, J. He, and K. Wang, "Neural networks and fpga hardware accelerators for millimeter-wave radio-over-fiber systems," *2020 22nd International Conference on Transparent Optical Networks (ICTON)*, pp. 1–4, 2020.

[177] D. Wang, M. Zhang, M. Fu, Z. Cai, Z. Li, H. Han, Y. Cui, and B. Luo, "Nonlinearity mitigation using a machine learning detector based on k -nearest neighbors," *IEEE Photonics Technology Letters*, vol. 28, no. 19, pp. 2102–2105, 2016.

[178] Y. Cui, M. Zhang, D. Wang, S. Liu, Z. Li, and G. Chang, "Bit-based support vector machine nonlinear detector for millimeter-wave radio-over-fiber mobile fronthaul systems." *Optics express*, vol. 25 21, pp. 26 186–26 197, 2017.

[179] Y. Huang, Y. Chen, and J. Yu, "Nonlinearity mitigation of rof signal using machine learning based classifier," *2017 Asia Communications and Photonics Conference (ACP)*, pp. 1–3, 2017.

[180] L. Guesmi and M. Menif, "Modulation formats recognition technique using artificial neural networks for radio over fiber systems," *2015 17th International Conference on Transparent Optical Networks (ICTON)*, pp. 1–4, 2015.

[181] M. Alharbi, A. Alhuseini, A. Ragheb, M. Altamimi, T. A. Alshawi, and S. Alshebeili, "Automatic modulation classification: Investigation for millimeter wave over fiber channels," *IEEE Photonics Technology Letters*, vol. 31, pp. 1092–1095, 2019.

[182] Y. Wu, M. Tornatore, Y. Zhao, and B. Mukherjee, "Traffic classification and sifting to improve tdm-epon fronthaul upstream efficiency," *IEEE/OSA Journal of Optical Communications and Networking*, vol. 10, pp. 15–26, 2018.

[183] A. M. Mikaeil, W. Hu, and S. B. Hussain, "A low-latency traffic estimation based tdm-pon mobile front-haul for small cell cloud-ran employing feed-forward artificial neural network," *2018 20th International Conference on Transparent Optical Networks (ICTON)*, pp. 1–4, 2018.

[184] W. Mo, C. L. Gutterman, Y. Li, G. Zussman, and D. Kilper, "Deep neural network based dynamic resource reallocation of bbu pools in 5g c-ran roadm networks," *2018 Optical Fiber Communications Conference and Exposition (OFC)*, pp. 1–3, 2018.

[185] W.-C. Chien, C.-F. Lai, and H. Chao, "Dynamic resource prediction and allocation in c-ran with edge artificial intelligence," *IEEE Transactions on Industrial Informatics*, vol. 15, pp. 4306–4314, 2019.

[186] H. Yang, B. Wang, Q. Yao, A. Yu, and J. Zhang, "Efficient hybrid multi-faults location based on hopfield neural network in 5g coexisting radio and optical wireless networks," *IEEE Transactions on Cognitive Communications and Networking*, vol. 5, pp. 1218–1228, 2019.

[187] M. Xu, J.-H. Yan, J. Zhang, F. Lu, J. Wang, L. Cheng, D. Guidotti, and G. Chang, "Bidirectional fiber-wireless access technology for 5g mobile spectral aggregation and cell densification," *IEEE/OSA Journal of Optical Communications and Networking*, vol. 8, pp. B104–B110, 2016.

[188] M. Bakaul, A. Nirmalathas, C. Lim, D. Novak, and R. Waterhouse, "Experimental characterization of single and cascaded wdm optical interfaces in a mm-wave fiber-radio network," *IEEE Photonics Technology Letters*, vol. 18, pp. 115–117, 2006.

[189] T. Umezawa, P. Dat, K. Kashima, A. Kanno, N. Yamamoto, and T. Kawanishi, "100-ghz radio and power over fiber transmission through multicore fiber using optical-to-radio converter," *Journal of Lightwave Technology*, vol. 36, pp. 617–623, 2018.

[190] K. Ikeda, T. Kuri, and K. Kitayama, "Simultaneous three-band modulation and fiber-optic transmission of 2.5-gb/s baseband, microwave-, and 60-ghz-band signals on a single wavelength," *Journal of Lightwave Technology*, vol. 21, pp. 3194–3202, 2003.

[191] A. Islam, M. Bakaul, A. Nirmalathas, and G. Town, "Millimeter-wave radio-over-fiber system based on heterodyned unlocked light sources and self-homodyned rf receiver," *IEEE Photonics Technology Letters*, vol. 23, pp. 459–461, 2011.

[192] ——, "Simplified generation, transport, and data recovery of millimeter-wave signal in a full-duplex bidirectional fiber-wireless system," *IEEE Photonics Technology Letters*, vol. 24, pp. 1428–1430, 2012.

[193] M. Chen, J. Yu, and X. Xiao, "Real-time q-band ofdm-rof systems with optical heterodyning and envelope detection for downlink transmission," *IEEE Photonics Journal*, vol. 9, pp. 1–7, 2017.

[194] C. Lim, M. Attygalle, A. Nirmalathas, D. Novak, and R. Waterhouse, "Analysis of optical carrier-to-sideband ratio for improving transmission performance in fiber-radio links," *IEEE Transactions on Microwave Theory and Techniques*, vol. 54, pp. 2181–2187, 2006.

[195] J. Cartledge, "Performance of 10 gb/s lightwave systems based on lithium niobate mach-zehnder modulators with asymmetric y-branch waveguides," *IEEE Photonics Technology Letters*, vol. 7, pp. 1090–1092, 1995.

[196] J. Ma, J. Yu, C. Yu, X. Xin, X. Sang, and Q. Zhang, "64 ghz optical millimeter-wave generation by octupling 8 ghz local oscillator via a nested linbo3 modulator," *Optics and Laser Technology*, vol. 42, pp. 264–268, 2010.

[197] G. Keiser, *Optical Fiber Communications*, 3rd ed. McGraw-Hill, Higher Education, 2000.

[198] C. K. Madsen and J. H. Zhao, *Optical Filter Design and Analysis, A Signal Processing Approach*. John Wiley & Sons, 1999.

[199] B. Hraimel, X. Zhang, Y. Pei, K. Wu, T. Liu, T. Xu, and Q. Nie, “Optical single-sideband modulation with tunable optical carrier to sideband ratio in radio over fiber systems,” *Journal of Lightwave Technology*, vol. 29, pp. 775–781, 2011.

[200] M. Xue, S. Pan, and Y. Zhao, “Optical single-sideband modulation based on a dual-drive mzm and a 120° hybrid coupler,” *Journal of Lightwave Technology*, vol. 32, pp. 3317–3323, 2014.

[201] M. Bakaul, A. Nirmalathas, C. Lim, D. Novak, and R. Waterhouse, “Investigation of performance enhancement of wdm optical interfaces for millimeter-wave fiber-radio networks,” *IEEE Photonics Technology Letters*, vol. 19, pp. 843–845, 2007.

[202] J. Wang and J. Kahn, “Impact of chromatic and polarization-mode dispersions on dpsk systems using interferometric demodulation and direct detection,” *Journal of Lightwave Technology*, vol. 22, pp. 362–371, 2004.

[203] Y. Zhu and A. Hadjifotiou, “Nonlinear tolerance benefit of modified-csrz dpsk modulation format,” *Electronics Letters*, vol. 40, pp. 903–904, 2004.

[204] M. Sakib, B. Hraimel, X. Zhang, M. Mohamed, W. Jiang, K. Wu, and D. Shen, “Impact of optical transmission on multiband ofdm ultra-wideband wireless system with fiber distribution,” *Journal of Lightwave Technology*, vol. 27, pp. 4112–4123, 2009.

[205] L. Johansson and A. Seeds, “Millimeter-wave modulated optical signal generation with high spectral purity and wide-locking bandwidth using a fiber-integrated optical injection phase-lock loop,” *IEEE Photonics Technology Letters*, vol. 12, pp. 690–692, 2000.

[206] I. Garrett and G. Jacobsen, “The effect of laser linewidth on coherent optical receivers with nonsynchronous demodulation,” *Journal of Lightwave Technology*, vol. 5, pp. 551–560, 1987.

[207] J. Barry and E. Lee, “Performance of coherent optical receivers,” *Proceedings of the IEEE*, vol. 78, no. 8, pp. 1369–1394, 1990.

[208] T. Bogale, X. Wang, and L. Le, “Chapter 9 - mmwave communication enabling techniques for 5g wireless systems: A link level perspective,” in *mmWave Massive MIMO*, S. Mumtaz, J. Rodriguez, and L. Dai, Eds. Academic Press, 2017, pp. 195–225. [Online]. Available: https://www.sciencedirect.com/science/article/pii/B9780128044186000091

[209] J. Wang and J. Kahn, “Impact of chromatic and polarization-mode dispersions on dpsk systems using interferometric demodulation and direct detection,” *Journal of Lightwave Technology*, vol. 22, pp. 362–371, 2004.

[210] S. Hladik, S. Chennakeshu, and G. Saulnier, “On acipr of pi /4 shifted dqpsk for us digital land mobile radio systems,” *[1991] IEEE Pacific Rim Conference on Communications, Computers and Signal Processing Conference Proceedings*, pp. 530–533 vol.2, 1991.

[211] M. Daikoku, I. Morita, H. Taga, H. Tanaka, T. Kawanishi, T. Sakamoto, T. Miyazaki, and T. Fujita, “100-gb/s dqpsk transmission experiment without otdm for 100g ethernet transport,” *Journal of Lightwave Technology*, vol. 25, pp. 139–145, 2007.

[212] Z. Chen, X. Ma, B. Zhang, Y. Zhang, Z. Niu, N. Kuang, W. Chen, L. Li, and S. Li, “A survey on terahertz communications,” *China Communications*, vol. 16, pp. 1–35, 2019.

[213] C. Jiang, H. Zhang, Y. Ren, Z. Han, K.-C. Chen, and L. Hanzo, “Machine learning paradigms for next-generation wireless networks,” *IEEE Wireless Communications*, vol. 24, pp. 98–105, 2017.

[214] A. Klautau, P. Batista, N. G. Prelcic, Y. Wang, and R. Heath, “5g mimo data for machine learning: Application to beam-selection using deep learning,” *2018 Information Theory and Applications Workshop (ITA)*, pp. 1–9, 2018.

[215] P. V. Klaine, M. Imran, O. Onireti, and R. Souza, “A survey of machine learning techniques applied to self-organizing cellular networks,” *IEEE Communications Surveys & Tutorials*, vol. 19, pp. 2392–2431, 2017.

[216] D. Wang and J. Chen, “Supervised speech separation based on deep learning: An overview,” *IEEE/ACM Transactions on Audio, Speech, and Language Processing*, vol. 26, pp. 1702–1726, 2018.

[217] F. C. Ghesu, E. Krubasik, B. Georgescu, V. Singh, Y. Zheng, J. Hornegger, and D. Comaniciu, “Marginal space deep learning: Efficient architecture for volumetric image parsing.” *IEEE transactions on medical imaging*, vol. 35 5, pp. 1217–1228, 2016.

[218] D. Côté, “Using machine learning in communication networks [invited],” *IEEE/OSA Journal of Optical Communications and Networking*, vol. 10, pp. D100–D109, 2018.

[219] F. B. Mismar and B. Evans, “Deep learning in downlink coordinated multipoint in new radio heterogeneous networks,” *IEEE Wireless Communications Letters*, vol. 8, pp. 1040–1043, 2019.

[220] M. Elkourdi, A. Mazin, and R. Gitlin, "Performance analysis for virtual-cell based comp 5g networks using deep recurrent neural nets," *2019 Wireless Telecommunications Symposium (WTS)*, pp. 1–6, 2019.

[221] M. K. Müller, F. Ademaj, T. Dittrich, A. Fastenbauer, B. R. Elbal, A. Nabavi, L. Nagel, S. Schwarz, and M. Rupp, "Flexible multi-node simulation of cellular mobile communications: the Vienna 5G System Level Simulator," *EURASIP Journal on Wireless Communications and Networking*, vol. 2018, no. 1, p. 17, Sep. 2018.

[222] 3GPP, "Technical specification group radio access network; evolved universal terrestrial radio access; physical channel and modulation (release 16)," 3rd Generation Partnership Project (3GPP), Tech. Rep. TS 36.211, 2020, version 16.3.0.

[223] D. M. Harris and S. L. Harris, *Sequential Logic Design*. Massachusetts, United States: Kaufmann, 2013, ch. Digital Design and Computer Architecture, pp. 108–171.

[224] H. S. Hippert, C. E. Pedreira, and R. Souza, "Neural networks for short-term load forecasting: a review and evaluation," *IEEE Transactions on Power Systems*, vol. 16, pp. 44–55, 2001.

[225] S. Skansi, *Introduction to Deep Learning*. Berlin: Springer, 2018, ch. Feedforward Neural Networks, pp. 79–105.

[226] S. Abirami and P. Chitra, *Advances in Computers*. Amsterdam: Elsevier, 2019, ch. Energy-efficient edge based real-time healthcare support system, pp. 339–368.

[227] H. Iba and N. Noman, *Deep Neural Evolution*. Berlin: Springer, 2020.

[228] A. Semenov, V. Boginski, and E. L. Pasiliao, *Neural Networks with Multidimensional Cross-Entropy Loss Functions*. Berlin: Springer, 2019, ch. Computational Data and Social Networks, pp. 57–62.

[229] S. Hochreiter and J. Schmidhuber, "Long short-term memory," *Neural computation*, vol. 9, pp. 1735–80, 12 1997.

[230] A. Graves, "Generating sequences with recurrent neural networks," *ArXiv*, vol. abs/1308.0850, 2013.

[231] A. Graves and J. Schmidhuber, "Framewise phoneme classification with bidirectional lstm and other neural network architectures," *Neural networks : the official journal of the International Neural Network Society*, vol. 18 5-6, pp. 602–10, 2005.

[232] S. Hochreiter and J. Schmidhuber, "Lstm can solve hard long time lag problems," 01 1996, pp. 473–479.

[233] K. Greff, R. Srivastava, J. Koutník, B. R. Steunebrink, and J. Schmidhuber, "Lstm: A search space odyssey," *IEEE Transactions on Neural Networks and Learning Systems*, vol. 28, pp. 2222–2232, 2017.

[234] R. Sutton and A. Barto, *Reinforcement Learning: An Introduction.* Massachusetts, United States: MIT Press, 1998.

[235] C. Szepesvari, *Algorithms for Reinforcement Learning.* California: Morgan & Claypool, 2010.

[236] W. B. Powell, *Approximate Dynamic Programming: Solving the curses of dimensionality.* New Jersey: John Wiley and Sons,, 2011.

[237] G. Tesauro, "Temporal difference learning and td-gammon," *Commun. ACM*, vol. 38, pp. 58–68, 1995.

[238] M. Kearns, D. Litman, S. Singh, and M. Walker, "Optimizing dialogue management with reinforcement learning: Experiments with the njfun system," *ArXiv*, vol. abs/1106.0676, 2002.

[239] A. Ng, A. Coates, M. Diel, V. Ganapathi, J. Schulte, B. Tse, E. Berger, and E. Liang, "Autonomous inverted helicopter flight via reinforcement learning," in *ISER*, 2004.

[240] N. Kohl and P. Stone, "Policy gradient reinforcement learning for fast quadrupedal locomotion," *IEEE International Conference on Robotics and Automation, 2004. Proceedings. ICRA '04. 2004*, vol. 3, pp. 2619–2624 Vol.3, 2004.

[241] V. Mnih, K. Kavukcuoglu, D. Silver, A. A. Rusu, J. Veness, M. G. Bellemare, A. Graves, M. A. Riedmiller, A. Fidjeland, G. Ostrovski, S. Petersen, C. Beattie, A. Sadik, I. Antonoglou, H. King, D. Kumaran, D. Wierstra, S. Legg, and D. Hassabis, "Human-level control through deep reinforcement learning," *Nature*, vol. 518, pp. 529–533, 2015.

[242] K. Arulkumaran, M. Deisenroth, M. Brundage, and A. Bharath, "Deep reinforcement learning: A brief survey," *IEEE Signal Processing Magazine*, vol. 34, pp. 26–38, 2017.

[243] R. Bellman, "On the theory of dynamic programming." *Proceedings of the National Academy of Sciences of the United States of America*, vol. 38 8, pp. 716–9, 1952.

[244] Y. Su, R. Fan, X. Fu, and Z. Jin, "Dqelr: An adaptive deep q-network-based energy- and latency-aware routing protocol design for underwater acoustic sensor networks," *IEEE Access*, vol. 7, pp. 9091–9104, 2019.

[245] M. Plappert, "keras-rl," https://github.com/keras-rl/keras-rl, 2016.

[246] G. Brockman, V. Cheung, L. Pettersson, J. Schneider, J. Schulman, J. Tang, and W. Zaremba, "Openai gym," *ArXiv*, vol. abs/1606.01540, 2016.

[247] Z. Wang, M. Zhang, D. Wang, C. Song, M. Liu, J. Li, L. Lou, and Z. Liu, "Failure prediction using machine learning and time series in optical network." *Optics express*, vol. 25 16, pp. 18 553–18 565, 2017.

[248] F. J. Caballero, D. Ives, C. Laperle, D. Charlton, Q. Zhuge, M. O'sullivan, and S. Savory, "Machine learning based linear and nonlinear noise estimation," *IEEE/OSA Journal of Optical Communications and Networking*, vol. 10, pp. D42–D51, 2018.

[249] D. Wang, M. Zhang, Z. Li, Y. Cui, J.-D. Liu, Y. Yang, and H. Wang, "Nonlinear decision boundary created by a machine learning-based classifier to mitigate nonlinear phase noise," *2015 European Conference on Optical Communication (ECOC)*, pp. 1–3, 2015.

[250] F. Oliver, *Handbook of Mathematical Functions with Formulas, Graphs, and Mathematical Tables.* Washington D.C: Dover Publication, 1965, ch. Bessel Functions of Integer Order, pp. 355–434.

[251] D. L. Colton and R. Kress, *Inverse acoustic and electromagnetic scattering theory.* Berlin: Springer, 1997.

[252] P. Xiong, H. Wang, M. Liu, and X. Liu, "Denoising autoencoder for eletrocardiogram signal enhancement," *Journal of Medical Imaging and Health Informatics*, vol. 5, pp. 1804–1810, 12 2015.

[253] H.-T. Chiang, Y.-Y. Hsieh, S.-W. Fu, K.-H. Hung, Y. Tsao, and S.-Y. Chien, "Noise reduction in ecg signals using fully convolutional denoising autoencoders," *IEEE Access*, vol. 7, pp. 60 806–60 813, 2019.

[254] X. Li, Z. Liu, and Z.-T. Huang, "Denoising of radar pulse streams with autoencoders," *IEEE Communications Letters*, vol. 24, pp. 797–801, 2020.

[255] D. P. Kingma and M. Welling, "Auto-encoding variational bayes," 2014.

[256] M. Sundermeyer, H. Ney, and R. Schlüter, "From feedforward to recurrent lstm neural networks for language modeling," *IEEE/ACM Transactions on Audio, Speech, and Language Processing*, vol. 23, pp. 517–529, 2015.

[257] G. Gelly and J. Gauvain, "Optimization of rnn-based speech activity detection," *IEEE/ACM Transactions on Audio, Speech, and Language Processing*, vol. 26, pp. 646–656, 2018.